Numerical Analysis of the Relation between Interactions and Structure in a Molecular Fluid

Dissertation
zur Erlangung des Grades
“Doktor der Naturwissenschaften”
am Fachbereich Physik, Mathematik und Informatik
der Johannes Gutenberg-Universität
in Mainz

Dmitry Ivanizki
geb. in Winsili (Russland)
Mainz 2015

1. Berichterstatter:
2. Berichterstatter:

Datum der mündlichen Prüfung: 11. Dezember 2015

D77 - Mainzer Dissertation

Abstract

Coarse graining is a popular technique used in physics to speed up the computer simulation of molecular fluids. An essential part of this technique is a method that solves the inverse problem of determining the interaction potential or its parameters from the given structural data [PK-2010]. Due to discrepancies between model and reality, the potential is not unique, such that stability of such method and its convergence to a meaningful solution are issues.

In this work, we investigate empirically whether coarse graining can be improved by applying the theory of inverse problems from applied mathematics. In particular, we use the singular value analysis to reveal the weak interaction parameters, that have a negligible influence on the structure of the fluid and which cause non-uniqueness of the solution. Further, we apply a regularizing Levenberg-Marquardt method, which is stable against the mentioned discrepancies [Hanke-1997]. Then, we compare it to the existing physical methods – the Iterative Boltzmann Inversion [Soper-1996] and the Inverse Monte Carlo method [LL-1995], which are fast and well adapted to the problem, but sometimes have convergence problems [RJLKA-2009], [MFKV-2007].

From analysis of the Iterative Boltzmann Inversion, we elaborate a meaningful approximation of the structure and use it to derive a modification of the Levenberg-Marquardt method. We engage the latter for reconstruction of the interaction parameters from experimental data for liquid argon and nitrogen. We show that the modified method is stable, convergent and fast. Further, the singular value analysis of the structure and its approximation allows to determine the crucial interaction parameters, that is, to simplify the modeling of interactions. Therefore, our results build a rigorous bridge between the inverse problem from physics and the powerful solution tools from mathematics.

Acknowledgment

In the first place, I want to thank my advisors for the highly interesting topic and the guidance during all these years of work.

Further, I thank the numerical and functional analysis groups for a friendly environment in both cooperative and social aspects. I am also very grateful to my colleagues for many fruitful discussions and for improving my english writing skills.

Finally, I acknowledge the "Computational Science Mainz" for funding the first year of my promotion and offering the opportunity to meet other PhD-students in various interdisciplinary workshops. I also want to give a credit to The Mathworks, Inc., whose product MATLAB® was used for implementation of the algorithms and for creation of all pictures in this work.

Preface

For the beginning, we want to highlight the interdisciplinary character of this work motivated by *coarse graining*. Two completely different sciences, the statistical physics and the applied mathematics, contribute equally to the topic. While the motivation of the topic lies in the advanced levels of modern physics, we treat the problem arising there from a viewpoint of equally modern mathematical theory. Even if we can apply the mathematical solution methods without studying the entire physical background of the problem, we need a basic physical understanding for interpretation of the results. Since each of the two sciences requires an appropriate introduction, we shield in Chapter 1 only the terms, which are necessary for weaving the sciences together. We sketch many ambient concepts, like *interactions* and *structure*, just to return to them later in the work, when we elaborate more rigorous definitions. Amongst other things, we introduce the *inverse problem* of determining the interaction *potential* from the structural data given by the *radial distribution function* (RDF).

In Chapter 2, we explain the mathematical concept of an *ill-posed* inverse problem and discuss the solution theory. We stress that an ill-posed problem describes a model with instable relation between input and output, such that a *regularization* is required. We show how the *singular value decomposition* can be used to reveal the instabilities of the model. Finally, we present the regularizing *Levenberg-Marquardt* method (LM), solving such problems iteratively, and a condition for its convergence.

We start Chapter 3 with a rigorous derivation of the functional spaces for potentials and RDFs, in order to apply the theory to the particular inverse problem. We motivate why the problem is ill-posed and adapt the LM to the previously derived spaces. We also keep in mind the physical background of the problem by discussing the *direct problem*, where the RDF is computed from the given potential by molecular simulation. We test the LM in a well-posed, two-dimensional setting and then successfully apply the method on realistic problems where the experimentally measured RDFs are given as data.

In order to improve our method, we turn in Chapter 4 to the existing, physically motivated methods, the *Iterative Boltzmann Inversion* and the *Inverse Monte Carlo* method. We show that the reason for their success is a clever approximation of the RDF, and modify the LM in a similar way. Then, we prove the convergence condition for the LM in the framework of this approximation and apply the modified method to the realistic inverse problems we studied earlier. Further, we discuss a suitable approximation of the underlying potential and its parameters. We conclude the work by illustrating our results in Chapter 5.

We supply this work with two appendices. Appendix A introduces the basics of statistical physics needed for understanding the concept of the RDF. We follow the classical terminology and do not pretend to cover a complete state of art, but we define a simple rigorous framework sufficient for showing some useful theorems. Appendix B focuses of the crucial points of molecular simulation, which play an important role in our discussion.

A Word about Notation

In fact, notation deserves a separate section in this work, because every science has its own preferences about notations, and conflicts cannot be avoided where two sciences come together. For instance, σ is a parameter in physics, a singular value in analysis and a standard deviation in statistics. Therefore, we make many subjective conventions and shield them here.

We denote with d the dimension of the Euclidean space, that is, for the most part, it equals three, with exception of some theoretical considerations, where the dimension can be general, and some illustrative special cases, where the lower dimensions become interesting. Throughout the work, the letter D denotes the derivative operator and $\mathbb{1}$ the identity operator, where the relevant variables and their number are clear from the context. We also use the notation of the gradient operator $\vec{\nabla}$, if the derivative is taken in $\mathbb{R}^d$. Further, we write $\frac{\partial}{\partial v}$ for the partial derivative with respect to variable v, such that lower indices never mean derivatives and always mean indices, components and labels. We supply the vectors from $\mathbb{R}^d$ with arrows, and, in order to distinguish between vector's index and component, we put the index in parentheses above the vector, for instance, $\{\vec{\mathrm{e}}^{(i)} | 1 \leq i \leq d\}$ is the standard base of the Euclidean space. $B(r)$ denotes the open ball of the radius r around origin in $\mathbb{R}^d$. $\partial\Omega$ designates the boundary of a domain Ω, that is, $\partial B(r)$ is the sphere of the radius r around origin. We want to be able to distinguish between the same variable/space/map in the continuous and the discrete formulations, x, X, F and $\mathrm{x}, \mathbb{X}, \mathrm{F}$, respectively. However, since the discretization is always straight-forward, one can also ignore the differences of the formulations and typefonts, if not specified otherwise. For a function f of variables $s_1, \ldots, s_J$ and parameters $x_1, \ldots, x_I$, we write

$$f(s_1, \ldots, s_J; x_1, \ldots, x_I)$$

or

$$f[x_1, \ldots, x_I](s_1, \ldots, s_J)$$

and omit some of the letters, if they do not matter in the current consideration. Further, we label the analytical theorems with A1, A2, etc. and the physical theorems with P1, P2, etc. Both kinds are proven, but the mathematical ones are bound to our model, while the physical theorems refer to different models used in physics simultaneously.

Due to an immense number of variables in the appendices devoted to statistical physics, we deviate from the above notations in the following cases. Since the components of vectors are never mentioned, we put the vector indices below the vectors. For vector families $\{\vec{X}_i\}_{1 \leq i \leq N} \subset \mathbb{R}^d$, we consequently use the notations

$$\begin{aligned} \underline{X} &:= \begin{pmatrix} \vec{X}_1 \\ \ldots \\ \vec{X}_N \end{pmatrix}, \\ \vec{X}_{ij} &:= \vec{X}_i - \vec{X}_j. \end{aligned}$$

We omit multiple integrals and integrate over the usual domain, if not specified otherwise. In other words, for variables $\vec{X}, \vec{Y} \in \Omega \subseteq \mathbb{R}^d$, we define

$$\int \ldots d\vec{X} d\vec{Y} := \int_\Omega \int_\Omega \ldots d\vec{X} d\vec{Y}.$$

For an even better readability, we supply this work with lists of all symbols (see p. 149) and abbreviations (see p. 153), as well as with an index where every namebearing concept appears.

Contents

Chapter 1

Introduction

1.1 Coarse Graining

The motivation for this work comes from the *coarse graining* – a popular technique, designed to reduce the number of the degrees of freedom in a *soft matter* system like fluid [Schmid-2006], mixture [MVYPBMM-2009] or polymer melt [PDK-2008]. The mentioned reduction appears particularly useful in a computer simulation, where one considers processes on very different time and length scales [PK-2009]. For example, the dynamics of a polymer chain, like the polystyrene (see Figure 1.1), is a slow process (long time scale), compared with the vibration of atoms (short time scale). If one would simulate a melt of several polymer chains over a long time by taking the interactions of every single atom into account, this would claim a large amount of expensive CPU time. But, if one studies only the coarse dynamics of the melt, it should suffice to consider *effective interactions* between certain atom groups, which respresent the shape of the polymer well enough (see Figure 1.2). One applies coarse graining by replacing the polymer parts by *effective particles*, such that the simulation of the simplified melt involves fewer degrees of freedom and requires significantly less resources.

Regarding the length scales, the coarse graining can be explained as zooming out of the detailed model. The change of the length of a vibrating bond can be only seen on

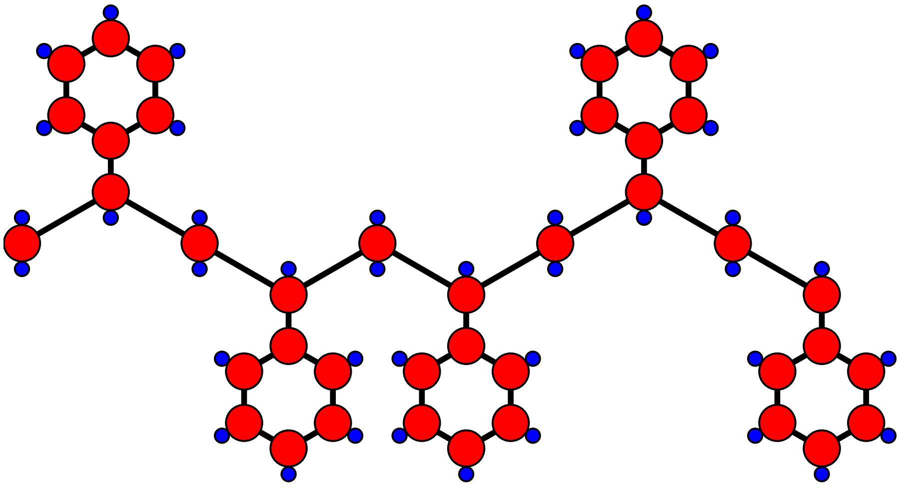

Figure 1.1: Sketch of the atomistic model for a polystyrene chain. Red and blue circles represent carbon and hydrogen atoms, respectively. Black lines represent the bonds.

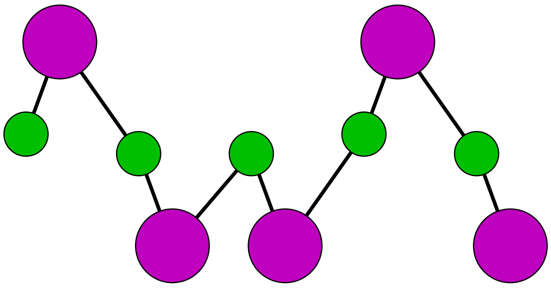

Figure 1.2: Sketch of the *bead-spring* model for a polystyrene chain. Purple and green circles represent effective particles (*beads*), substituted for phenyl ring and backbone part, respectively. Black lines represent the effective bonds (*springs*).

the finest (or *microscopic*) length scale (see Figure 1.1). During one looks at the polymer chain and zooms out, more and more details become lost. On some intermediate (or *mesoscopic*) scale, one cannot see the bond vibrations anymore, but still can recognize whether two neighbouring phenyl rings take the same or the opposite sides:

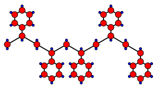

$\approx$

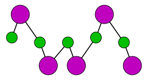

Finally, on the coarsest (or *macroscopic*) scale, one can only observe the overall chain conformation (see Figure 1.3) – stretched, bent, knotted etc. Clearly, the definitions of the length scales depend on the relevant (or available) assortment of models. For example, the conformational description of single polymer chains is coarse in the context of the statistical mechanics, but too detailed from the viewpoint of the hydrodynamics studying the flow properties of a melt.

The length and time scales are naturally coupled:

- On a coarser length scale one should consider larger effective particles.
- A larger effective particle has a higher mass.
- A particle with a higher mass moves slower.
- One should consider the motion of slower particles on a longer time scale.

That is, the *transition* to a mesoscopic time scale allows one to simulate the soft matter over a longer time interval and observe the relevant processes without wasting CPU time for the microscopic dynamics. However, it is only possible with a clever choice of the effective interactions, which must be consistent with experimental data.

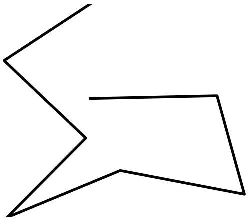

Figure 1.3: Sketch of the *swollen chain* model for a polymer chain. Black lines represent segments of the polymer, containing many repeating units.

In this work, we analyze various models for interactions in a fluid by employing the theory of inverse problems from the applied mathematics. We base our analysis on the same data from experiment/simulation, which is used to derive the effective interactions. Therefore, our results help to improve the coarse graining procedure. In the following, we motivate briefly our models for interactions and data, which provide a basis for mathematical analysis and help us to tackle the subtleties of the coarse graining.

1.2 Interactions and Structure

We model a *fluid* as a system of particles (*atoms*) in $d \in \mathbb{N}$ dimensions, whose motion is totally determined by pair interactions of two kinds (see Figure 1.4) – one between particles belonging to different molecules (*non-bonded* interactions), and one between constituents of the same molecule (*bonded* interactions).

We use the simplest model for the bonded interaction – a potential of the form

$$v_\ell(\ell) = \frac{1}{2} k_\ell (\ell - \ell_0)^2$$

describes a spring with certain stiffness $k_\ell > 0$ and length $\ell_0 > 0$, and ensures that the energy $v_\ell(\ell)$ changes, when the *bond length* ℓ for atom pairs deviates from ℓ_0. In a nutshell, atoms move into configuration with minimal energy, therefore, on the interval $(0, \ell_0)$, where the function v_ℓ decays, a *repulsion* (*repulsive* interaction) between the atoms takes place. Vice versa, there is an *attraction* (*attractive* interaction) on (ℓ_0, ∞), because v_ℓ grows there. In a similar way, potentials of the form

$$\begin{aligned} v_\theta(\theta) &= \frac{1}{2} k_\theta (\theta - \theta_0)^2, \\ v_\phi(\phi) &= \frac{1}{2} k_\phi (\phi - \phi_0)^2 \end{aligned}$$

allow us to control the *bending angle* θ for triplets and the *torsion angle* ϕ for quartets of atoms, respectively (see Figure 1.5).

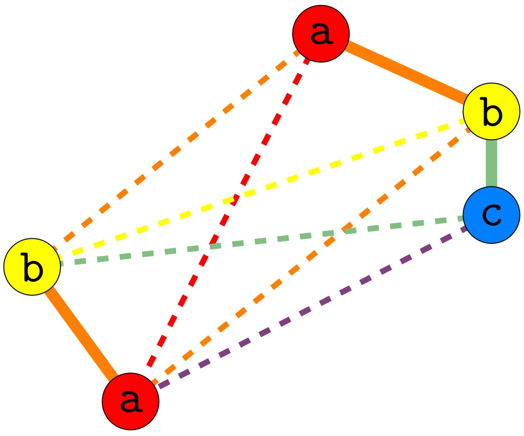

Figure 1.4: Interactions between atoms of fictive molecules `ab` and `abc` (solid lines for bonded and dashed lines for non-bonded interactions, respectively).

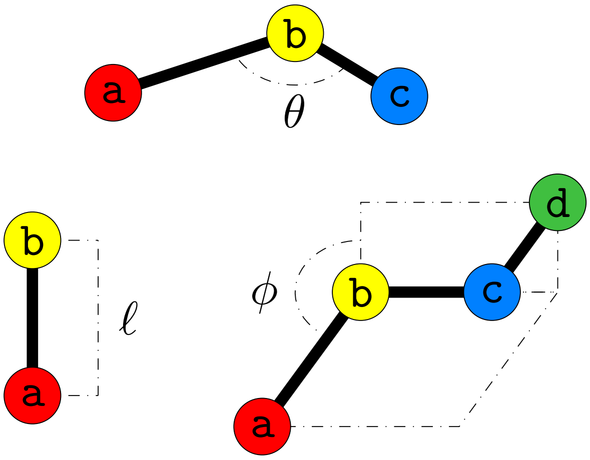

Figure 1.5: Bonded interactions between atoms of fictive molecules `ab`, `abc` and `abcd`.

The non-bonded interaction *potential* is usually (see Appendices A.2 and B.2 for details) described by some smooth function $u : (0, \infty) \to \mathbb{R}$ of the distance between two particles:

(U1) the interaction is strongly repulsive at short distances:

$$\lim_{r \to 0} u(r) = \infty,$$

(U2) the interaction is weak at long distances:

$$\lim_{r \to \infty} u(r) = 0,$$

(U3) the interaction allows particles to have a preferred distance $r^{\min} \in (0, \infty)$:

$$\min_{r \in (0,\infty)} u(r) = u(r^{\min}) < 0.$$

A popular representative is the *Lennard-Jones potential*

$$u^{\mathrm{LJ}}(r) = 4\varepsilon \left(\left(\frac{\sigma}{r} \right)^{12} - \left(\frac{\sigma}{r} \right)^{6} \right),$$

whose shape is governed by parameters $\varepsilon > 0$ and $\sigma > 0$ (see Figure 1.6).

For the sake of simplicity, we consider in the following a *simple fluid*, where only one type of particles is present and there are no bonded interactions, in contrast to a *molecular fluid*. In this case, the non-bonded interactions completely determine the motion of particles in the fluid. Considering the time-dependent coordinate vectors (*trajectories*)

$$\begin{array}{rcl} \vec{r}_i : [0, \infty) & \to & \mathbb{R}^d, \\ t & \mapsto & \vec{r}_i(t) \end{array}$$

of the particles, we can determine the *force*

$$\vec{F}_{ij}(t) = - \left. \frac{\partial u(|\vec{s}|)}{\partial \vec{s}} \right|_{\vec{s} = \vec{r}_i(t) - \vec{r}_j(t)}$$

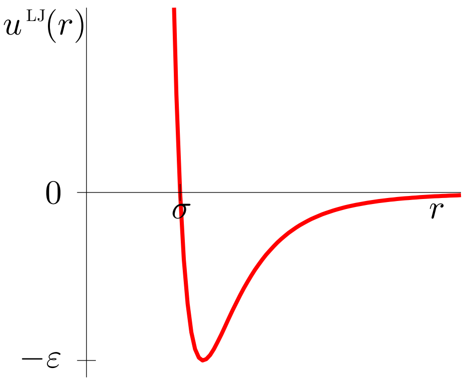

Figure 1.6: The Lennard-Jones potential.

acting on the i-th particle at time t due to interaction with the j-th particle. Theoretically, for any given initial positions $(\vec{r}_i(0))_{i=1}^N$ of the particles, we can obtain their trajectories from the *Newton equations*

$$m_i \frac{d^2}{dt^2}\vec{r}_i(t) = \sum_{j\neq i} \vec{F}_{ij}(t), \quad 1 \leq i \leq N.$$

A computer simulation method called *molecular dynamics* solves numerically the above system of ordinary differential equations. In principle, the method works in a very intuitive way by moving the particles in small timesteps along their force vectors (see Appendix B.1). One can show that the corresponding solution is unstable, because a small uncertainty in the initial positions of the particles leads to a completely different trajectory. However, the computational scientists believe that the collective dynamics of the particles is physically meaningful and can be used to calculate statistical properties of the fluid with a quality of a real experiment [FS-2002].

One of these reliably computable properties is the *radial distribution function (RDF)*, representing the distribution of the distance in each particle pair (see Appendix A for details). The reason, why we choose the RDF from all available statistical properties, is the prominent *Henderson theorem* [Henderson-1974], which is applicable (only) to the simple fluids and states that two interaction potentials yielding the same RDF cannot differ by more than an additive constant $C \in \mathbb{R}$. Due to (U2), all potentials converge to zero, so that $C = 0$ and the statement of the theorem becomes: for each RDF, there is a unique potential. In other words, the interaction potential and the RDF are equivalent descriptions of the fluid.

We postpone the rigorous discussion of the relation between the potential and the corresponding RDF to Section 4.1.1, because it is not very valuable at this point. Here we prefer to give an intuitive illustration of the RDF and describe its numerical computation. In a computer simulation, one takes from time to time a snapshot of actual particle positions. In each snapshot, the procedure considers concentric spheres around a fixed particle and counts the neighbouring particles in the layers between the spheres (see Figure 1.7). Afterwards, the neighbour counts are divided by the corresponding layer volumes and the resulting ratios form a histogram. The average of such histograms, which runs over all snapshots and fixed particles, gives the discretized approximation of the RDF (see Figure 1.8). The figure suggests that a typical RDF of a fluid is a smooth function $y : (0, \infty) \to (0, \infty)$ with the following properties:

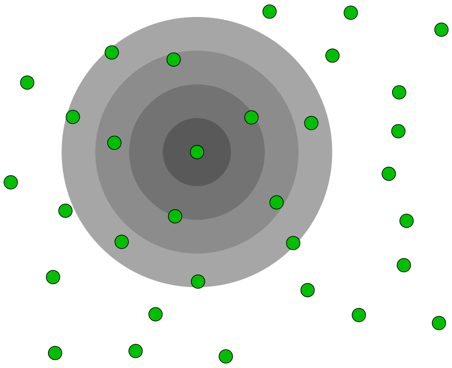

Figure 1.7: Spherical layers (gray areas) around a fixed particle and neighbouring particles (green circles).

(Y1) no particle pair holds a short distance (due to the repulsive nature of interaction):

$$\lim_{r\to 0} y(r) = 0,$$

(Y2) there is no correlation at long distances (due to the vanishing interaction):

$$\lim_{r\to \infty} y(r) = 1,$$

(Y3) the function shows a noticeable correlation at some distance (because the particles have a preferred distance):

$$\max_{r\in(0,\infty)} y(r) > 1.$$

The above properties underline how close is the correspondence between potentials and RDFs. Moreover, the numerical procedure described above can be interpreted as a map G, which assigns a unique RDF y to each interaction potential u, and, according to the Henderson theorem, there is no other potential with the same RDF. In other words, G is injective and one can (theoretically) invert the procedure, that is, for each $y \in \operatorname{ran}(G)$, one can find the solution $u \in \operatorname{dom}(G)$ of the equation

$$y = G[u].$$

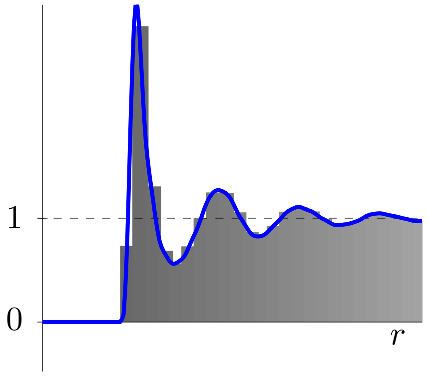

Figure 1.8: One histogram (gray area) and a typical RDF, averaged from many histograms (blue line). r denotes the distance between two particles.

A task of this form is called an *inverse problem* in the applied mathematics. The simplest way to solve it, is to discretize the problem: according to a certain *parameterization* H, one represents the potential $u = H[x]$ as a vector $x \in \mathbb{R}^n$ of few parameters, in order to fit these afterwards to the available data y by solving the equation

$$y = (G \circ H)[x],$$

typically with some numerical iterative method. For example, the Lennard-Jones potential has only two parameters, $x = (\varepsilon, \sigma)^T$, which are physically uncorrelated and they can be adjusted (even manually) to fit the experimental RDF. A similar fitting procedure is an essential part of the *structure-based* coarse graining, where the close relation of the interaction potential and the RDF (*structure*) is used.

1.3 Subtleties of the Coarse Graining

We finish this introduction with a more detailed discussion of the coarse graining and line out the crucial points, which could benefit from a mathematical analysis of the map G. We split the whole technique in few steps and visualize them by using the motivation example with polystyrene $[\mathtt{C_6H_5\text{-}CH\text{-}CH_2}]_k$ from the beginning of the chapter.

In the first step, one chooses the *mapping scheme* replacing the atoms $(\vec{r}^{(1)}, \ldots, \vec{r}^{(n)})$ of the repeating unit of the polymer by *effective particles* $(\vec{R}^{(1)}, \ldots, \vec{R}^{(N)})$. In other words, one looks for a matrix $\Lambda \in \mathbb{R}^{N \times n}$ with

$$\Lambda \begin{pmatrix} \vec{r}^{(1)} \\ \ldots \\ \vec{r}^{(n)} \end{pmatrix} = \begin{pmatrix} \vec{R}^{(1)} \\ \ldots \\ \vec{R}^{(N)} \end{pmatrix},$$

that reduces the number of degrees of freedom to $N \ll n$. Clearly, a mapping scheme performs a model reduction and should find a balance between the most simple and the most informative models. Since the information carried by the model as well as the underlying polymer can vary in applications, there is no general choice strategy. Therefore, the mapping scheme is often restricted to a particular polymer, and the concrete choice is reserved for experts in the computer simulation of soft matter.

A natural approach is to choose the effective particles to represent the geometric structure and physical properties of the polymer. For example, the chain-like geometry of the polystyrene molecule suggests to replace the whole repeating unit by one effective particle in its center of mass. One recognizes soon that the masses of hydrogen atoms make a nearly negligible contribution to the positions of the effective particles. If one fades out these light atoms, the polymer chain appears as a kind of backbone made of carbon atoms and supplied with phenyl rings (see Figure 1.1). Considering that physical properties of polystyrene depend on the orientations of the phenyl rings with respect to the backbone, the mapping scheme suggested above appears rather naive. The resulting model looses control about flips of the phenyl rings from one side to the other, because both the rings and the backbone are hidden in spherical effective particles. Thus, one needs one effective particle to represent the building block of the backbone and one to represent the ring, but there are many different possibilities, even if the centers of mass are chosen again as a reference point. For instance, one could split the repeating unit, according to

$$\mathtt{C_6H_5\text{-}CH\text{-}CH_2} \quad = \quad \mathtt{C_6H_5\text{-}CH} \quad \text{-} \quad \mathtt{CH_2},$$

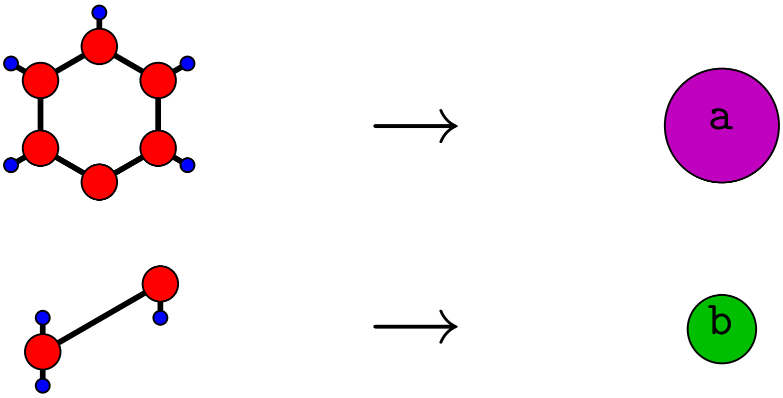

Figure 1.9: Sketch of the chosen mapping scheme for polystyrene.

which would be a reasonable model [HAVK-2006]. However, it can be shown that the splitting

$$\mathtt{C_6H_5\text{-}CH\text{-}CH_2} \quad = \quad \mathtt{C_6H_5} \quad \text{-} \quad \mathtt{CH\text{-}CH_2}$$

provides a better model in the sense of representation of chain conformations [HRVK-2007]. The corresponding mapping scheme is sketched in Figure 1.9. The same scheme was used to obtain the bead-spring model in Figure 1.2 from the atomistic model in Figure 1.1.

In the second step of the coarse graining, one calculates the *effective interaction* potentials, which determine the general behaviour of the effective particles. Indeed, a mapping scheme suggests a *transition* from the microscopic to a mesoscopic scale, but yields only the initial positions of the effective particles in the coarse grained polymer. In order to ensure the consistency of the effective interactions $U(\vec{R}^{(1)}, \ldots, \vec{R}^{(N)})$ with the scale transition, these have to describe the fluid nearly equally well as the atomistic interactions $u(\vec{r}^{(1)}, \ldots, \vec{r}^{(n)})$. As we mentioned before, the concrete dynamics of particles is irrelevant and the fluid is well-described by rather statistical properties. The latter can be derived from the *partition functions*

$$\begin{aligned} z &:= \int \exp\left(-\frac{1}{k_B T} u(\vec{r}^{(1)}, \ldots, \vec{r}^{(n)})\right) d\vec{r}^{(1)} \ldots d\vec{r}^{(n)}, \\ Z &:= \int \exp\left(-\frac{1}{k_B T} U(\vec{R}^{(1)}, \ldots, \vec{R}^{(N)})\right) d\vec{R}^{(1)} \ldots d\vec{R}^{(N)}, \end{aligned}$$

where k_B denotes the *Boltzmann constant*. z and Z characterize the fluid at temperature T on the microscopic and the mesoscopic scales, respectively (see Appendix A). Therefore, we demand $z \overset{!}{=} Z$ and obtain the following expression for the effective interactions,

$$\begin{aligned} U(\vec{R}^{(1)}, \ldots, \vec{R}^{(N)}) &= -k_B T \ln\left(\int \exp\left(-\frac{1}{k_B T} u(\vec{r}^{(1)}, \ldots, \vec{r}^{(n)})\right) \quad \times \right. \\ &\left. \times \prod_{I=1}^{N} \delta(\Lambda_I(\vec{r}^{(1)}, \ldots, \vec{r}^{(n)}) - \vec{R}^{(I)}) d\vec{r}^{(1)} \ldots d\vec{r}^{(n)}\right) + \text{const}, \end{aligned}$$

which is per definition consistent with the given mapping scheme Λ [NCAKIVDA-2008]. Although this explicit formula shows the existence of the effective description for the given fluid, its direct evaluation is impossible for relevant n. Therefore, instead of matching the partition function itself, one aims some property of the fluid, which can be derived from the partition function. According to the aimed property, one can distinguish the following kinds of the coarse graining:

- *energy-based*, where the energy arising from the effective potentials reproduces the energy of the atomistic fluid;
- *structure-based*, where the effective potentials lead to an RDF matching the atomistic RDF;
- *force-matching*, where the effective force field (derivatives of the effective potentials) fits the atomistic force field.

Since we discuss in this work the dependence of the RDF from the underlying interactions, we present here the details of the structure-based approach. For each type of the effective particle, one simulates the fluid consisting of the corresponding polymer parts on the microscopic scale. The simulations are relatively short, because the unchained parts of the polymer can move freely, and yield the center-of-mass RDFs $y^{(1)}, \dots, y^{(N)}$. If some (non-bonded) interaction potentials $u^{(1)}, \dots, u^{(N)}$ fit these RDFs on the mesoscopic scale, that is, if they solve the equations

$$y^{(I)} = G[u^{(I)}], \quad 1 \le I \le N,$$

(approximately), then these potentials are unique due to the Henderson theorem. From this point of view, the structure-based coarse graining uses the RDF as a bridge between the different scales (see Figure 1.10). The solution methods for the above equations vary

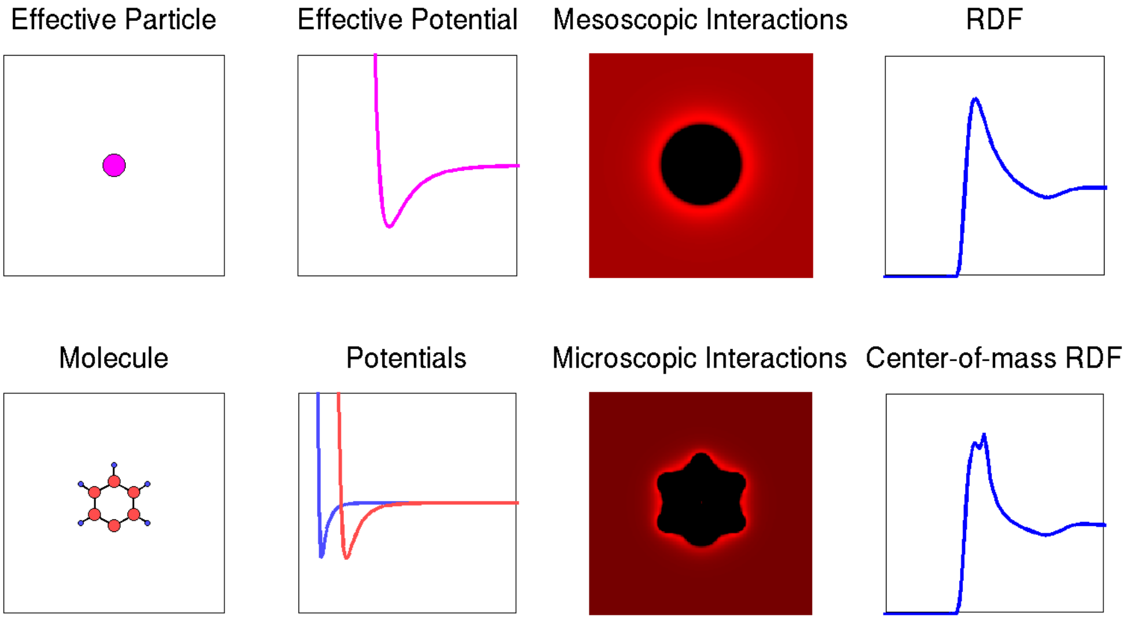

Figure 1.10: A visualization of the difference between the microscopic (bottom row) and the mesoscopic (upper row) scales. The left four pictures show atoms and potentials for hydrogen (blue), carbon (red) and effective (magenta) particles. The corresponding interactions on the right are represented by energy values in the vicinity of the molecule (red scale, the lower the value, the lighter the color). The right two pictures show the corresponding, approximately equal RDFs (blue).

from iterative methods, which provide tabulated potentials, to the simple fitting of the parameters of the preferred model for interactions (see Section 4.1.2 for details). In the polystyrene example, one can assume that the effective non-bonded interaction has a form of the generalized Lennard-Jones potential, in particular,

$$u_{\mathtt{a},\mathtt{a}}(r) = 4\varepsilon_{\mathtt{a},\mathtt{a}} \left(\left(\frac{\sigma_{\mathtt{a},\mathtt{a}}}{r} \right)^{\mu_{\mathtt{a},\mathtt{a}}} - \left(\frac{\sigma_{\mathtt{a},\mathtt{a}}}{r} \right)^{\nu_{\mathtt{a},\mathtt{a}}} \right).$$

Then, one simulates the fluid of `a`-particles and fits the parameters to the simulated RDF, that is, one demands

$$y_{\mathtt{C_6H_5},\mathtt{C_6H_5}} \overset{!}{\approx} y_{\mathtt{a},\mathtt{a}} = G[u_{\mathtt{a},\mathtt{a}}],$$

in order to obtain a potential mirroring the size $\sigma_{\mathtt{a},\mathtt{a}}$ and the attractiveness $\varepsilon_{\mathtt{a},\mathtt{a}}$ of the effective particle `a` (see Figure 1.11).

Further, one derives the effective bonded interactions from the conformational statistics of the polymer. More precisely, one simulates a single polymer chain on the microscopic scale and samples the probability densities $\mathcal{P}_\ell(\ell)$, $\mathcal{P}_\theta(\theta)$ and $\mathcal{P}_\phi(\phi)$ of the bond length, bending angle and torsion angle, respectively. Then, the corresponding *potentials of mean force*,

$$\begin{aligned} v_\ell(\ell) &= -k_B T \ln \left(\frac{\mathcal{P}_\ell(\ell)}{\ell^2} \right) + \text{const}, \\ v_\theta(\theta) &= -k_B T \ln \left(\frac{\mathcal{P}_\theta(\theta)}{\sin\theta} \right) + \text{const}, \\ v_\phi(\phi) &= -k_B T \ln \mathcal{P}_\phi(\phi) + \text{const}, \end{aligned}$$

can eventually be used as the bonded interaction potentials in the coarse grained chain.

In the next step, one can simulate the system of simplified chains $[\mathtt{-ab-}]_k$ much faster (compared to the detailed system). As we mentioned before, such a simulation runs on the mesoscopic scale and allows to investigate the slow processes in a polymer melt by taking snapshots of the trajectory on a coarser time grid. However, the snapshots are also coarse with respect to the length scale.

In the final step, one reinserts the atoms into the final configuration or into all coarse snapshots. Since an effective particle is typically softer than a real atom, a mesoscopic

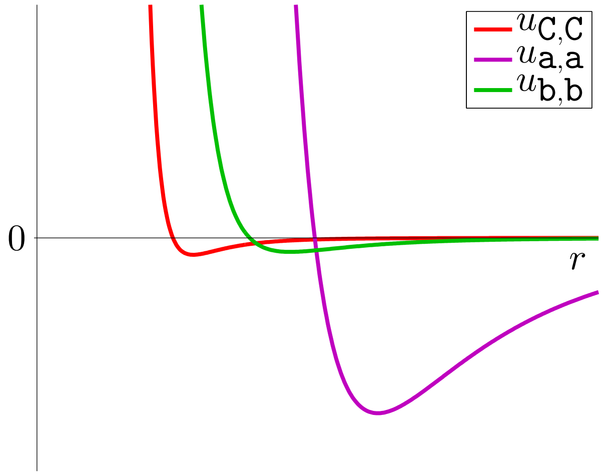

Figure 1.11: Sketch of the effective non-bonded interaction potentials.

configuration of the polymer chain tolerates overlaps between the substituted groups of atoms. In order to get rid of these overlaps, one uses some gradient method for the geometric optimization of the reconstructed chains and a short simulation of the detailed system for the energetic optimization. The procedure of reinsertion, or *backmapping*, is established by now and its fundamentals can be found in [TKHBB-1998].

In [PK-2010], the authors review the typical challenges in the coarse graining. In particular, they state a difficulty to derive representative effective interactions in the case of strong model reduction. Further, they emphasize the need for a systematic choice of a physically meaningful mapping scheme. We want to contribute to these two, evidently interrelated topics, by studying the inverse problem in the second step of the coarse graining. There, an effective interaction potential, consistent with the mapping scheme, is derived from the given RDF. However, disregarding this consistency, the mapping scheme replaces a non-spherical molecule (polymer part) by a spherical effective particle, such that the inversion procedure yields a mesoscopic interaction potential, which is only valid for spherical particles (see Figure 1.10). That is, some important microscopic details of the original molecule could be lost and the effective interactions do not necessarily represent the fluids properties, which depend on that details. The natural questions arising here are fully in line with the challenges in the mentioned review paper.

Question I: Can we develop a better inversion method?

Question II: Can we measure/lower/minimize the loss of microscopic details owing to inversion?

In order to answer these questions, we have to deal with the theory of inverse problems.

Chapter 2

Theory of Inverse Problems

2.1 Ill-posed Problems

In the introduction, we already used the term *inverse problem* to describe an equation of the form

$$y = F[x], \tag{2.1}$$

where the map $F : X \to Y$ between Hilbert spaces $(X, \langle\cdot|\cdot\rangle_X)$ and $(Y, \langle\cdot|\cdot\rangle_Y)$ is not linear in the general case. We call elements $x \in X$ and $y \in Y$ *parameter* and *data*, respectively. The word "inverse" comes from the assumption that for historical or technical reasons, the problem of evaluation of the map F is well-studied and can be considered as the original or the *direct problem*. For example, it is much easier to obtain the value $y = p(x)$ of a polynomial p for the given variable value x (direct problem), than to find the vanishing points of p, that is, all variable values x, for which $0 = p(x)$ (inverse problem). This chapter provides a short overview of the modern theory of inverse problems, as it can be found in [EHN-1996].

In principle, equation (2.1) is the question: given the data, what is the parameter? However, mathematical questions, just as questions in the real life, can be good (well-posed) or bad (ill-posed). An inverse problem is called *well-posed* (in the sense of Hadamard), if all following conditions are fulfilled:

(H1) a solution $x \in X$ exists,

(H2) the solution $x \in X$ is unique,

(H3) the solution $x \in X$ depends continuously on the data $y \in Y$.

If one of the conditions is not satisfied, the problem is referred to as *ill-posed*.

In the general case, the *exact data* $\overline{y}$ is unknown – we have only the noisy measured data $y^{(\delta)}$ and an estimate of the *noise level* $\delta > 0$, such that

$$\|y^{(\delta)} - \overline{y}\|_Y \leq \delta \ll \|y^{(\delta)}\|_Y. \tag{2.2}$$

It can make the inverse problem (2.1) ill-posed – if the noisy data is not in the range of F, the equation has no solution and (H1) is not met. Especially, we cannot retrieve the *exact parameter* $\overline{x}$ from $y^{(\delta)}$. Resigned to this fact, we replace equation (2.1) by the minimization problem

$$\min_{x \in X} \|y^{(\delta)} - F[x]\|_Y, \tag{2.3}$$

which has at least one solution. Even if we obtain a set of solutions, we can reduce it to a unique solution by imposing additional requirements, such that (H2) is also met. Of course, we have to be careful, but, roughly speaking, the first two Hadamard conditions are harmless, in contrast to the third one.

In order to discuss the dependence between solution and data in accordance with (H3), we look first at the actual solution method. If there is no noise in the data ($\delta = 0$), one can solve a nonlinear minimization problem of the form (2.3) with a *Newton-type* method. One assumes that F is Fréchet-differentiable and its derivative

$$A^{(k)} := DF[x^{(k)}]$$

as *operator* (linear map) from X to Y is continuous. Then, one chooses an initial guess $x^{(0)} \in X$ and improves it in the k-th step via

$$x^{(k+1)} = x^{(k)} + h^{(k)},$$

where the *update* $h^{(k)}$ should ideally have the value $\overline{h}^{(k)} := \overline{x} - x^{(k+1)}$. Since $\overline{x}$ is unknown, one can only obtain an approximate $h^{(k)}$, for instance, from the Taylor expansion

$$\overline{y} = F[\overline{x}] \overset{!}{=} F[x^{(k)} + h^{(k)}] = F[x^{(k)}] + DF[x^{(k)}]h^{(k)} + \Xi(\overline{x}; x^{(k)}). \tag{2.4}$$

This is a local linearization of the map F, where the actual iterate $x^{(k)}$ should be close enough to the solution $\overline{x}$, such that the (unknown) Taylor remainder $\Xi(\overline{x}; x^{(k)})$ is small and can be omitted in the corresponding linear equation

$$\overline{y} - F[x^{(k)}] - \cancel{\Xi(\overline{x}; x^{(k)})} =: b^{(k)} = A^{(k)}h^{(k)}. \tag{2.5}$$

In presence of noise, one does not posess the exact data, such that one solves rather

$$y^{(\delta)} - F[x^{(k)}] - \cancel{\Xi(\overline{x}; x^{(k)})} =: b^{(k,\delta)} = A^{(k)}h^{(k)}. \tag{2.6}$$

The left hand side of this equation is noisy due to

$$\|b^{(k,\delta)} - b^{(k)}\|_Y = \|y^{(\delta)} - \overline{y}\|_Y \leq \delta,$$

that is, its solution is different from that of (2.5). One can hope that the difference is small for small δ, however, if condition (H3) is not met, already small uncertainties in the data can cause a large error in the solution. We show how it happens in the following sections where we consider a general framework for solution of **linear** inverse problems, that is, problems of the form (2.1) with linear F. At the end of the chapter, we return to the original nonlinear setting and discuss a Newton-type method, which determines an approximate solution iteratively by solving linear problems (2.6).

2.2 Moore-Penrose Inverse

We consider the linear inverse problem

$$y^{(\delta)} = Ax, \tag{2.7}$$

where the operator $A \in B(X, Y)$ and the noisy data $y^{(\delta)} \in Y$ are given and $x \in X$ is the unknown solution. If the problem is well-posed for $\delta = 0$, then A is bijective, A^{-1} exists and the solution of the above problem is given by

$$x := A^{-1}y^{(\delta)}, \tag{2.8}$$

for all *attainable* data $y^{(\delta)}$, that is, for $y^{(\delta)} \in \operatorname{ran}(A)$. Since A^{-1} is continuous, this solution is stable to the noise in the data, as long as the noisy data is attainable. Otherwise, there are many difficulties on the same way. For instance, if the data $y^{(\delta)}$ is not attainable, then $y^{(\delta)} \notin \operatorname{dom}(A^{-1})$ and $A^{-1}y^{(\delta)}$ is not even defined. Thus, we generalize the definition of "solution", in order to have any solution. We call an $x \in X$ a *least-squares solution* of (2.7), if

$$\|y^{(\delta)} - Ax\|_Y = \inf_{z \in X} \|y^{(\delta)} - Az\|_Y. \tag{2.9}$$

There is at least one such x, that is, the Hadamard condition (H1) is met. In the well-posed case where the data is attainable, the unique solution (2.8) would also be a least-squares solution. However, if A is not injective, that is, if $\ker(A) \neq \{0\}$, we obtain suddenly a whole solution set $x + \ker(A)$. In order to repair the lack of uniqueness, we impose constraints on the generalized solution. We call $x \in X$ a *best-approximate solution* of (2.7), if x is a least-squares solution of (2.7) and

$$\|x\|_X = \inf\{\|z\|_X | z \text{ is a least-squares solution of (2.7)}\}. \tag{2.10}$$

One can show that such x is unique, that is, condition (H2) is also fulfilled.

The best-approximate solution can also be obtained by the generalization of the term "inverse" for an operator. The *Moore-Penrose inverse* $A^\dagger$ of $A \in B(X,Y)$ is defined as the unique linear extension of $(A|_{\ker(A)^\perp})^{-1}$ to

$$\operatorname{dom}(A^\dagger) := \operatorname{ran}(A) \oplus \operatorname{ran}(A)^\perp$$

with

$$\ker(A^\dagger) = \operatorname{ran}(A)^\perp.$$

If the inverse A^{-1} exists, we have

$$A^{-1}A = AA^{-1} = \mathbb{1}.$$

Similarly, the Moore-Penrose inverse fulfills the generalized equations

$$\begin{aligned} AA^\dagger A &= A, \\ A^\dagger AA^\dagger &= A^\dagger. \end{aligned}$$

Further, one can show that for all $y^{(\delta)} \in \operatorname{dom}(A^\dagger)$, the problem (2.7) has the unique best-approximate solution

$$x^{(\delta)} := A^\dagger y^{(\delta)} \tag{2.11}$$

and for $x \in X$, the following statements are equivalent:

- x is a least-squares solution of (2.7),
- $x \in x^{(\delta)} + \ker(A)$,
- x solves the *normal equation*

$$A^* y^{(\delta)} = A^* Ax. \tag{2.12}$$

This result promises a unique solution for all attainable data. Indeed, the domain of the Moore-Penrose inverse is dense in Y. That is, if $\operatorname{ran}(A)$ is closed, then the best-approximate solution is obtainable for any data in Y. Moreover, the continuous dependence of the solution (2.11) from the data is equivalent to the boundedness of $A^\dagger$ and one can show that $A^\dagger$ is bounded, if and only if $\operatorname{ran}(A)$ is closed. In summary, if this range is closed, everything is fine.

From now on we assume that the operator A is *compact*, that is, the sequence $(Ax_n)_{n\in\mathbb{N}}$ in Y has a convergent subsequence in Y, for each bounded sequence $(x_n)_{n\in\mathbb{N}}$ in X. In this case, which is common for inverse problems, one can show that the range $\operatorname{ran}(A)$ is closed, if and only if $\dim(\operatorname{ran}(A)) < \infty$. That is, in the general case where the range is of infinite dimension, the Moore-Penrose inverse $A^\dagger$ is unbounded and the Hadamard condition (H3) is not fulfilled. Even worse, the range of A is "small", because a compact operator maps bounded sets (there are "many" bounded sets) to compact sets (there are "few" compact sets). Therefore, the "most" data from Y are not attainable.

The compactness of A allows us to use the *singular value decomposition* (SVD) – a powerful tool from functional analysis, which provides us an insight into the nature of $A^\dagger$ and its domain. Indeed, let $(\psi^{(j)}, \sigma_j, \varphi^{(j)})_{j\in\mathbb{N}}$ be the SVD of a compact operator A, where σ_j are the *singular values*, while $\psi^{(j)}$ and $\varphi^{(j)}$ denote the *left* and the *right singular vectors*, respectively. Since $(\varphi^{(j)})_{j\in\mathbb{N}}$ is an orthonormal basis of X, any $x \in X$ is given by

$$x = \sum_{j=1}^{\infty} \langle \varphi^{(j)} | x \rangle_X \varphi^{(j)}. \tag{2.13}$$

Further, $(\psi^{(j)})_{j\in\mathbb{N}}$ provides an orthonormal basis of $\operatorname{ran}(A)$, so that we can write any y in this range as

$$y = \sum_{j=1}^{\infty} \langle \psi^{(j)} | y \rangle_Y \psi^{(j)}.$$

On the other hand, the singular value expansion of A yields

$$y = Ax = \sum_{j=1}^{\infty} \sigma_j \langle \varphi^{(j)} | x \rangle_X \psi^{(j)}.$$

Comparing the coefficients of the two series, we see that

$$\langle \psi^{(j)} | y \rangle_Y = \sigma_j \langle \varphi^{(j)} | x \rangle_X$$

and

$$x = \sum_{j=1}^{\infty} \frac{\langle \psi^{(j)} | y \rangle_Y}{\sigma_j} \varphi^{(j)}$$

is a solution to the equation $y = Ax$. One can show that

$$x = A^\dagger y,$$

if $y \in \operatorname{dom}(A^\dagger)$, and this is the case, if and only if

$$\sum_{j=1}^{\infty} \frac{|\langle \psi^{(j)} | y \rangle_Y|^2}{\sigma_j^2} < \infty. \tag{2.14}$$

The latter condition is called the *Picard criterion*. It says that the best-approximate solution $A^\dagger y$ exists, if and only if the projections $\langle \psi^{(j)} | y \rangle_Y$ of the data decay faster than the singular values σ_j. However, the SVD characterizes only A, so, if we have noisy data $y^{(\delta)}$, the error projections $\langle \psi^{(j)} | y - y^{(\delta)} \rangle_Y$ do not have to decay in the general case. That is, due to the form of the terms $\frac{|\langle\psi^{(j)}|y^{(\delta)}\rangle_Y|^2}{\sigma_j^2}$, the large singular values damp the propagated noise in $x^{(\delta)} = A^\dagger y^{(\delta)}$, while the small ones amplify it. This allows us to classify inverse problems – from *modestly ill-posed*, where the singular values decay polynomially, to the *severely ill-posed*, where the decay is exponential.

A similar characterization exists for the case of a finite-dimensional range $\operatorname{ran}(A)$. Such inverse problems are evidently well-posed from the theoretical point of view, but in applications, we observe a behaviour similar to ill-posedness. Consider a linear equation

$$\mathrm{y}^{(\delta)} = \mathrm{Ax},$$

where $\mathrm{x} \in \mathbb{X} \simeq \mathbb{R}^n$, $\mathrm{y}^{(\delta)} \in \mathbb{Y} \simeq \mathbb{R}^m$, and $\mathrm{A} \in B(\mathbb{X}, \mathbb{Y}) \simeq \mathbb{R}^{m\times n}$ is a matrix with rank $n < m$, that is, A is a compact operator. Theoretically, we can determine the best-approximate solution from the corresponding normal equation

$$\mathrm{A}^*\mathrm{y}^{(\delta)} = \mathrm{A}^*\mathrm{Ax},$$

because the matrix $\mathrm{M} := \mathrm{A}^*\mathrm{A}$ is invertible due to the full rank of A. But practically, the solution $\mathrm{x}^{(\delta)}$ can be meaningless, if the matrix is *ill-conditioned*, that is, if the *condition number*

$$\mathrm{cond}(\mathrm{M}) := \|\mathrm{M}\|_2\|\mathrm{M}^{-1}\|_2 = \frac{\sigma_1}{\sigma_n}$$

is too large. The reason for this are the singular values again – even though they do not converge to zero, their decay still can be very fast, such that the condition number, as the ratio between the largest and the smallest singular value, can be very large. From the practical viewpoint, the Hadamard condition (H3) is not satisfied for such *ill-conditioned* problem – the operator $\mathrm{A}^\dagger = \mathrm{M}^{-1}\mathrm{A}$ is bounded, but the bound (the norm of the operator) is too large for a meaningful numerical treatment of the above equations. We illustrate this issue on a small linear system.

Example 2.1. "(3×2)**-system":**
Let us consider

$$\mathrm{A} = \begin{pmatrix} 1 & 102 \\ 1 & 101 \\ 1 & 100 \end{pmatrix}, \quad \overline{\mathrm{x}} = \begin{pmatrix} 1 \\ 1 \end{pmatrix}, \quad \overline{\mathrm{y}} = \mathrm{A}\overline{\mathrm{x}} = \begin{pmatrix} 103 \\ 102 \\ 101 \end{pmatrix}$$

and relatively small noise

$$\mathrm{e} = \begin{pmatrix} 1 \\ 1 \\ 1 \end{pmatrix} \quad \Rightarrow \quad \mathrm{y}^{(\delta)} = \overline{\mathrm{y}} + \mathrm{e} = \begin{pmatrix} 104 \\ 103 \\ 102 \end{pmatrix}.$$

The solution

$$\mathrm{x}^{(\delta)} = \begin{pmatrix} 2 \\ 1 \end{pmatrix}$$

to the corresponding normal equation is quite wrong, while the residual $\mathrm{y}^{(\delta)} - \mathrm{Ax}^{(\delta)}$ is exactly zero. We should not be surprised, because the matrix $\mathrm{M} = \mathrm{A}^*\mathrm{A}$ is ill-conditioned – the condition number

$$\mathrm{cond}(\mathrm{M}) \approx 2 \cdot 10^8$$

as well as the norm of $\mathrm{A}^\dagger = \mathrm{M}^{-1}\mathrm{A}^*$ are quite large. In a nutshell, due to machine arithmetic, the matrix

$$\mathrm{M} = \begin{pmatrix} 3 & 303 \\ 303 & 30605 \end{pmatrix} \approx \begin{pmatrix} 3 & 300 \\ 300 & 30000 \end{pmatrix}$$

is almost singular, the norm $\|\mathrm{A}^\dagger\|_2$ is almost infinite and the error

$$\overline{\mathrm{x}} - \mathrm{x}^{(\delta)} = \mathrm{M}^{-1}\mathrm{A}^*\mathrm{e} = \mathrm{A}^\dagger \mathrm{e}$$

arises from the noise amplification due to inversion of M. $\diamond$

The decay of the singular values σ_j and the corresponding projections $\langle \psi^{(j)} | \mathrm{y}^{(\delta)} \rangle_{\mathbb{Y}}$ can be easily compared in a *Picard plot*. [Hansen-2010] uses this plot in order to deduce a kind of Picard criterion for the finite-dimensional case. Figure 2.1 shows an example of a Picard plot for a certain ill-posed inverse problem. First, one determines the level τ, at which the singular values level off due to machine arithmetic (see the gap at $j \approx 10$). Then, one says that the *discrete Picard criterion* is satisfied, if the ratios $\frac{|\langle \psi^{(j)} | \mathrm{y}^{(\delta)} \rangle_{\mathbb{Y}}|}{\sigma_j}$ are (approximately) non-increasing for all $\sigma_j > \tau$. Obviously, this is an analogue of the necessary condition for the series in (2.14) to converge. In the Picard plot, we observe that the terms of the series rather increase for $j \gtrsim 5$. That is, the best-approximate solution

$$\mathrm{x}^{(\delta)} = \sum_{j=1}^{16} \frac{\langle \psi^{(j)} | \mathrm{y}^{(\delta)} \rangle_{\mathbb{Y}}}{\sigma_j} \varphi^{(j)} \tag{2.15}$$

is wrong in the last twelve terms. In contrast to (2.14), the discrete Picard criterion carries a heuristical character and should be used only for sufficiently large n. The length n of the solution vector can be easily justified in the inverse problems arising from discretization of an infinite-dimensional problems, as in the following example from [Varah-1983].

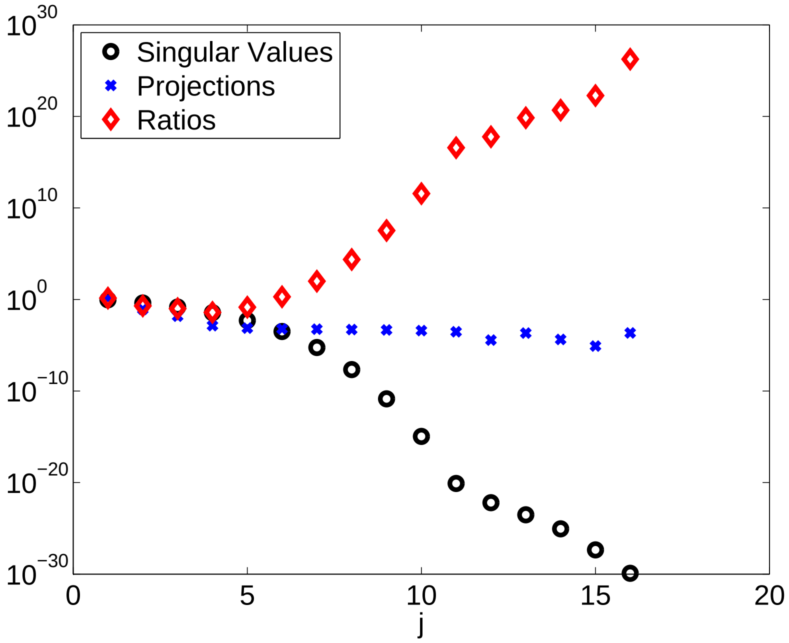

Figure 2.1: An example of the Picard plot. Circles represent the singular values σ_j, crosses – the projections $|\langle \psi^{(j)} | \mathrm{y}^{(\delta)} \rangle_{\mathbb{Y}}|$ and diamonds – their ratios $\frac{|\langle \psi^{(j)} | \mathrm{y}^{(\delta)} \rangle_{\mathbb{Y}}|}{\sigma_j}$.

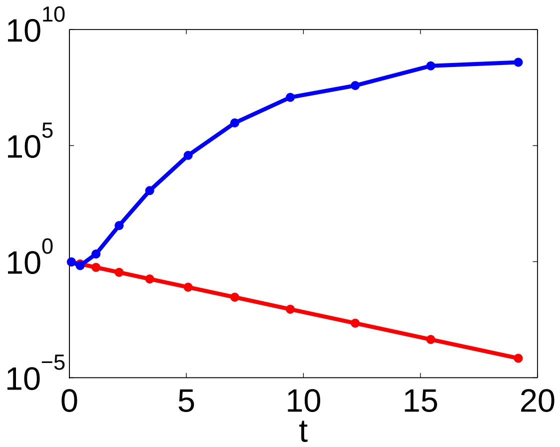

Figure 2.2: The exact solution (red curve) and the best-approximate solution (blue curve) from Example 2.2.

Example 2.2. "Inverse Laplace transformation":
We consider the linear equation $y = Ax$, where

$$(Ax)(s) = \int_0^\infty e^{-st}x(t)dt, \quad 0 \leq s < \infty,$$

describes the *Laplace transformation* of a function $x \in L^2([0,\infty))$. The operator $A : L^2([0,\infty)) \to L^2([0,\infty))$ is compact, because its *kernel* e^{-st} belongs to $L^2([0,\infty)^2)$ (see, for example, [Cheney-2001]). For the fixed exact parameter $\overline{x}(t) := e^{-t/2}$, one obtains the corresponding exact data

$$\overline{y}(s) = \frac{1}{s+\frac{1}{2}}.$$

In order to invert the transformation, one solves the above equation numerically by discretizing it by means of the Gauss-Laguerre quadrature with certain knots $(t_i)_{i=1}^n$ [Hansen-1994]. After discretization of A and $\overline{y}$, the equation turns to an $(n \times n)$-system $\overline{\mathrm{y}} = \mathrm{Ax}$, where the left hand side differs from $\mathrm{A}\overline{x}$. The best-approximate solution is wrong – it has negative values, while the exact solution is strictly positive. In Figure 2.2, we compare the absolute values of the two solutions on the relevant interval. They agree in the vicinity of zero, but their disagreement grows exponentially with t. The reason for this tremendous discrepancy is the compactness of the operator A. We already studied the Picard plot for this inverse problem in Figure 2.1, and this example demonstrates the usefulness of such study. We could foresee that only few terms of the series expansion (2.15) of the solution are trustworthy. Moreover, the rapid decay of the singular values classifies the inverse problem as severely ill-posed and points out that the underlying operator is probably compact. $\diamond$

In the above examples, we sketched situations where the Moore-Penrose inverse of a compact operator A is continuous, but the best-approximate solution is worthless. Also in the general case, we have $A\varphi \approx 0$ for any singular vector φ corresponding to a very small singular value. That is, instead of the best-approximate solution $x^{(\delta)}$, the normal equation yields just a least-squares solution from $x^{(\delta)} + \mathrm{span}(\varphi)$. It means also that a small residual norm $\|y^{(\delta)} - Ax\|_{\mathrm{Y}}$ does not necessarily imply that x is a good solution approximation. This effect can obviously ruin any classical solution method based on the minimization of the residual norm. Therefore, a least squares solution should not be considered as a proper solution of an ill-posed inverse problem. We should rather use a more modern approach, the *regularization* methods, which denoise (regularize) the Moore-Penrose inverse, so that a meaningful solution can be achieved.

2.3 Regularization

We visualize the regularization of an inverse problem by the diagram in Figure 2.3, where we consider the same problem in both ideal and noisy settings. That is, the ideal equation with exact data does not describe properly the real world, where the data contains noise and we can only obtain an approximate (and noisy) solution $x^{(\delta)}$. The "regularization" is a parametric modification of the noisy equation, which allows to find a unique solution $x^{(\lambda,\delta)}$, which is "near" to $\overline{x}$ for a proper choice

$$\lambda = \lambda(\delta, y^{(\delta)}).$$

Clearly, the regularization can also be applied to the ideal equation, and it is natural to demand a kind of "stability", in the sense that the regularization of the ideal equation yields a similar solution $x^{(\lambda)}$, that is,

$$x^{(\lambda,\delta)} \to x^{(\lambda)}, \quad \delta \to 0.$$

After coupling these assumptions via

$$\lambda(\delta) \to 0, \quad \delta \to 0,$$

one can expect a kind of "convergence" described by

$$x^{(\lambda,\delta)} \to \overline{x}, \quad \delta \to 0.$$

$$\begin{tikzcd}
\boxed{\text{Ideal}} & \boxed{\overline{y} = A\overline{x}} \arrow[r, "\text{``regularization''}"] \arrow[d, "\text{noise}"'] & \boxed{\overline{y} = A^{(\lambda)}x^{(\lambda)}} \arrow[d, leftrightarrow, "\text{``stability''}"'] \\
\boxed{\text{Noisy}} & \boxed{y^{(\delta)} \approx Ax^{(\delta)}} \arrow[r, "\text{``regularization''}"] & \boxed{y^{(\delta)} = A^{(\lambda)}x^{(\lambda,\delta)}} \arrow[ul, "\text{``convergence''}"]
\end{tikzcd}$$

Figure 2.3: Modifications of an inverse problem and the roles of the noise, stability, regularization and convergence.

This "convergence" **does not** mean that one can obtain the exact solution $\overline{x}$ from the noisy data. The term means that the approximate solution $x^{(\lambda,\delta)}$, no matter how good it is, becomes better as soon as the precision of the data measurement gets better. In the following, we provide mathematical definitions of the concepts we just introduced.

A family $(R^{(\lambda)})_{\lambda>0}$ of operators is called a *regularization* (of the Moore-Penrose inverse $A^\dagger$), if

(R1) $R^{(\lambda)}$ are continuous for all $\lambda > 0$,

(R2) $R^{(\lambda)} \to A^\dagger$ for $\lambda \to 0$ pointwise on $\mathrm{dom}(A^\dagger)$.

If A is compact, then one can show that $\|R^{(\lambda)}\| \xrightarrow{\lambda\to 0} \infty$. Further, if

$$\|AR^{(\lambda)}\| \leq C, \quad \forall \lambda > 0, \tag{2.16}$$

then $\|R^{(\lambda)}y\| \xrightarrow{\lambda\to 0} \infty$ for all $y \notin \mathrm{dom}(A^\dagger)$.

Example 2.3. "Truncated SVD":
In the previous section, we motivated that the Moore-Penrose inverse $A^\dagger$ cannot handle the noisy data $y^{(\delta)}$ due to the terms in the expansion

$$A^\dagger y^{(\delta)} = \sum_{j=1}^{\infty} \frac{\langle \psi^{(j)} | y^{(\delta)} \rangle_Y}{\sigma_j} \varphi^{(j)}, \tag{2.17}$$

that correspond to the small singular values σ_j. The simplest way to regularize $A^\dagger$ is to truncate the SVD, such that the bad terms do not appear in the series (2.17). More precisely, we define the operator family $(R^{(\lambda)})_{\lambda>0}$ with

$$\begin{aligned} R^{(\lambda)} y^{(\delta)} &:= \sum_{j=1}^{k(\lambda)} \frac{\langle \psi^{(j)} | y^{(\delta)} \rangle_Y}{\sigma_j} \varphi^{(j)}, \qquad (2.18) \\ k(\lambda) &:= \max \left\{ j \in \mathbb{N} \,\middle|\, j \leq \frac{1}{\lambda} \right\}. \end{aligned}$$

Evidently, for $\lambda > 1$, $R^{(\lambda)} \equiv 0$ is continuous, and otherwise, we have

$$\|R^{(\lambda)}\| = \frac{1}{\sigma_{k(\lambda)}} < \infty, \tag{2.19}$$

therefore (R1) is fulfilled. Further, according to the Picard criterion, the partial sums of the series (2.14) converge for all $y \in \mathrm{dom}(A^\dagger)$, that is,

$$R^{(\lambda)} y^{(\delta)} \xrightarrow{\lambda\to 0} \sum_{j=1}^{\infty} \frac{\langle \psi^{(j)} | y^{(\delta)} \rangle_Y}{\sigma_j} \varphi^{(j)} = A^\dagger y^{(\delta)}.$$

Thus, (R2) is satisfied and we conclude that (2.18), called the *truncated SVD* (TSVD), is a regularization. Moreover, condition (2.16) is fulfilled, because

$$\begin{aligned} \|AR^{(\lambda)}\| &= \sup_{\|y\|_Y=1} \left\| \sum_{j=1}^{k(\lambda)} \frac{\langle \psi^{(j)} | y \rangle_Y}{\sigma_j} A\varphi^{(j)} \right\|_Y = \sup_{\|y\|_Y=1} \left\| \sum_{j=1}^{k(\lambda)} \langle \psi^{(j)} | y \rangle_Y \psi^{(j)} \right\|_Y \\ &\leq \sup_{\|y\|_Y=1} \|y\|_Y = 1. \end{aligned}$$

That is, the series expansion of $A^\dagger$ diverges outside of the domain. ◇

Surely, for a fixed $\lambda > 0$, the regularized solution $x^{(\lambda)} := R^{(\lambda)}y$ depends continuously on the data. However, it may happen that the operator $R^{(\lambda)}$ has not much to do with the original problem. If we compare the exact solution $\overline{x} = A^\dagger\overline{y}$ with the more realistic solution $x^{(\lambda,\delta)} = R^{(\lambda)}y^{(\delta)}$, we can write the total error

$$x^{(\lambda,\delta)} - \overline{x} = R^{(\lambda)}y^{(\delta)} - A^\dagger\overline{y} = (R^{(\lambda)}\overline{y} - A^\dagger\overline{y}) + R^{(\lambda)}(y^{(\delta)} - \overline{y})$$

as a sum of the *regularization error* and the *propagated noise*, respectively. Due to (R2),

$$\|R^{(\lambda)}\overline{y} - A^\dagger\overline{y}\|_X \to 0, \quad \lambda \to 0,$$

that is, we can keep the first term under control by setting the *regularization parameter* λ very small. Even though $R^{(\lambda)}$ is bounded, the bound $\|R^{(\lambda)}\|$ may become very large. In the general case, the noise $y^{(\delta)} - \overline{y} \notin \operatorname{dom}(A^\dagger)$ and hence, $R^{(\lambda)}$ amplifies the noise in the second term, such that the propagated noise becomes very large,

$$\|R^{(\lambda)}(y^{(\delta)} - \overline{y})\|_X \to \infty, \quad \lambda \to 0.$$

For these reasons, we should choose a regularization parameter $\lambda > 0$, for that the two error terms are in balance (see Figure 2.4).

A function

$$\begin{array}{rcl} \lambda : (0,\infty) \times Y & \to & (0,\infty), \\ (\delta, y^{(\delta)}) & \mapsto & \lambda(\delta, y^{(\delta)}) \end{array}$$

is called a *parameter choice strategy*. A combination $((R^{(\lambda)})_{\lambda>0}, \lambda(\delta, y^{(\delta)}))$ of a regularization with a parameter choice strategy is called a *regularization method*, if

$$R^{\lambda(\delta,y^{(\delta)})}y^{(\delta)} \xrightarrow{\delta\to 0} A^\dagger\overline{y}$$

for all $y^{(\delta)}$ with $\|y^{(\delta)} - \overline{y}\| \le \delta$. In the general case, a parameter choice strategy takes both the noise level δ and the noisy data $y^{(\delta)}$ into account. It can be shown that there is no regularization method where λ depends only on $y^{(\delta)}$. The knowledge about the noise level δ is so important, that we can provide an example with $\lambda = \lambda(\delta)$.

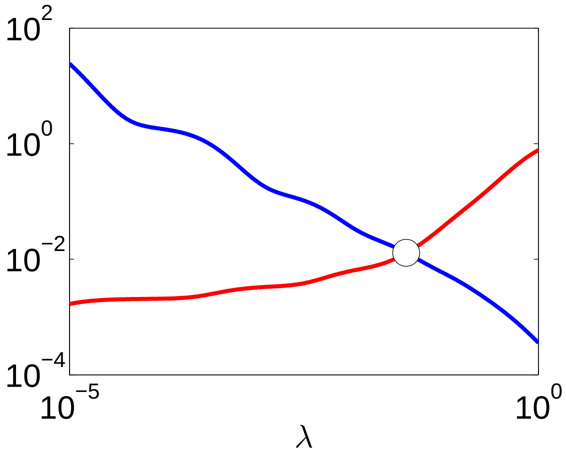

Figure 2.4: The regularization error (red curve) and the propagated noise (blue curve) for the problem from Example 2.2 “Inverse Laplace transformation”. The curves are in balance (white circle) for a certain value of the regularization parameter λ.

Example 2.4. "TSVD":
The parameter choice strategy $\lambda(\delta) := \min\{\mu | \sigma_{k(\mu)} \geq \sqrt{\delta}\}$ yields that for $\delta \to 0$,

$$\lambda(\delta) \to 0 \quad \text{and} \quad \|R^{(\lambda(\delta))}\|\delta \overset{(2.19)}{=} \frac{\delta}{\sigma_{k(\lambda(\delta))}} \leq \sqrt{\delta} \to 0.$$

Then, the second term on the right of

$$\|R^{(\lambda(\delta))}y^{(\delta)} - A^{\dagger}\overline{y}\|_X \leq \|R^{(\lambda(\delta))}\overline{y} - A^{\dagger}\overline{y}\|_X + \|R^{(\lambda(\delta))}\| \cdot \|y^{(\delta)} - \overline{y}\|_Y$$

vanishes for $\delta \to 0$. The first term also tends to zero due to the property (R2) of the regularization, that is, we have a regularization method. $\diamond$

2.4 Tikhonov Regularization

In this section, we present an intuitive derivation of the *Tikhonov regularization*. We remind that in the general case, we solve the linear equation (2.7), where A is a compact operator with infinite-dimensional range. We already motivated that such an operator is almost singular, in the sense that the inverses of the operators A and $M := A^*A$ are not continuous. However, M is a positive semidefinite operator. The basic idea of the Tikhonov regularization is to add to M a positively scaled identity, such that the sum

$$M^{(\lambda)} := M + \lambda^2 \mathbb{1}$$

is far from singular (more regular). More precisely, the operator $M^{(\lambda)}$ is invertible with a continuous inverse, that is,

$$\|(M^{(\lambda)})^{-1}\| = \frac{1}{\lambda^2}$$

for every value of the regularization parameter $\lambda > 0$. This technique is equivalent to replacing the normal equation (2.12) by

$$A^*y^{(\delta)} = \left(A^*A + \lambda^2 \mathbb{1}\right)x. \tag{2.20}$$

In order to derive the solutions to the normal equation (2.20), we use the SVD $(\psi^{(j)}, \sigma_j, \varphi^{(j)})_{j\in\mathbb{N}}$ of the compact operator A. The singular value expansion of $A^* \in B(Y, X)$ yields

$$A^*y = \sum_{j=1}^{\infty} \sigma_j \langle \psi^{(j)} | y \rangle_Y \varphi^{(j)},$$

and

$$A^*y = (A^*A + \lambda^2 \mathbb{1})x \overset{(2.13)}{=} \sum_{j=1}^{\infty} (\sigma_j^2 + \lambda^2) \langle \varphi^{(j)} | x \rangle_X \varphi^{(j)}$$

suggests that the series have equal coefficients. This leads to

$$\sigma_j \langle \psi^{(j)} | y \rangle_Y = (\sigma_j^2 + \lambda^2) \langle \varphi^{(j)} | x \rangle_X$$

and we see that

$$x = \sum_{j=1}^{\infty} \frac{\sigma_j^2}{\sigma_j^2 + \lambda^2} \frac{\langle \psi^{(j)} | y \rangle_Y}{\sigma_j} \varphi^{(j)}$$

is a solution to the normal equation $A^*y = (A^*A + \lambda^2 \mathbb{1})x$. From this point of view, the Tikhonov regularization yields a filtered solution

$$x^{(\lambda,\delta)} = \sum_{j=1}^{\infty} \chi_j(\lambda) \frac{\langle \psi^{(j)} | y^{(\delta)} \rangle_Y}{\sigma_j} \varphi^{(j)}, \tag{2.21}$$

where the functions given by

$$\chi_j(\lambda) := \frac{\sigma_j^2}{\sigma_j^2 + \lambda^2} \in [0, 1]$$

ensure that the coefficients of the above series decay properly with respect to the Picard criterion. At this place, the SVD helps us to interpret the regularization as filtering out the noisy coefficients, such that an alternative choice of the functions $(\chi_j)_{j\in\mathbb{N}}$ also makes sense.

Example 2.5. "TSVD":
By setting the filter functions

$$\chi_j(\lambda) := \begin{cases} 1, & 1 \leq j \leq k(\lambda), \\ 0, & j > k(\lambda), \end{cases}$$

in the regularized solution (2.21), we can derive the TSVD regularization as a special case of the Tikhonov regularization. ◇

Similar to the TSVD, we can show that the family of operators

$$R^{(\lambda)} := \left(A^*A + \lambda^2 \mathbb{1}\right)^{-1} A^* \tag{2.22}$$

is a regularization of $A^\dagger$ and every parameter choice strategy $\lambda(\delta)$ with

$$\lambda(\delta) \to 0 \quad \text{and} \quad \frac{\delta}{\lambda} \to 0, \quad \delta \to 0$$

in combination with the Tikhonov regularization (2.22) yields a regularization method. Indeed, since

$$(A^*A + \lambda^2 \mathbb{1})^{-1} A^* = A^*(AA^* + \lambda^2 \mathbb{1})^{-1},$$

we obtain

$$\begin{aligned}
\|R^{(\lambda)}\|^2 &= \sup_{\|y\|_Y = 1} \|(A^*A + \lambda^2 \mathbb{1})^{-1} A^* y\|_X^2 \\
&= \sup_{\|y\|_Y = 1} \langle (A^*A + \lambda^2 \mathbb{1})^{-1} A^* y | (A^*A + \lambda^2 \mathbb{1})^{-1} A^* y \rangle_X \\
&= \sup_{\|y\|_Y = 1} \langle A^*(AA^* + \lambda^2 \mathbb{1})^{-1} y | A^*(AA^* + \lambda^2 \mathbb{1})^{-1} y \rangle_X \\
&\leq \sup_{\|y\|_Y = 1} \big(\langle (AA^* + \lambda^2 \mathbb{1})^{-1} y | AA^*(AA^* + \lambda^2 \mathbb{1})^{-1} y \rangle_Y \\
&\qquad + \lambda^2 \langle (AA^* + \lambda^2 \mathbb{1})^{-1} y | (AA^* + \lambda^2 \mathbb{1})^{-1} y \rangle_Y \big) \\
&= \sup_{\|y\|_Y = 1} \langle (AA^* + \lambda^2 \mathbb{1})^{-1} y | (AA^* + \lambda^2 \mathbb{1})(AA^* + \lambda^2 \mathbb{1})^{-1} y \rangle_Y \\
&\overset{\text{CSI}}{\leq} \sup_{\|y\|_Y = 1} \|(AA^* + \lambda^2 \mathbb{1})^{-1} y\|_Y \cdot \|y\|_Y \\
&= \|(AA^* + \lambda^2 \mathbb{1})^{-1}\| = \frac{1}{\lambda^2},
\end{aligned}$$

that is, $R^{(\lambda)}$ is continuous for any $\lambda > 0$. Further, for any $y \in \operatorname{dom}(A^\dagger)$ and $\lambda > 0$,

$$\|R^{(\lambda)}y\|_X \leq \|R^{(\lambda)}\| \cdot \|y\|_Y \leq \frac{\text{const}}{\lambda}$$

is bounded and for $\lambda \to 0$, we have

$$R^{(\lambda)}y = \sum_{j=1}^{\infty} \frac{\sigma_j^2}{\sigma_j^2 + \lambda^2} \frac{\langle \psi^{(j)} | y \rangle_Y}{\sigma_j} \varphi^{(j)} \to \sum_{j=1}^{\infty} \frac{\langle \psi^{(j)} | y \rangle_Y}{\sigma_j} \varphi^{(j)} = A^\dagger y,$$

such that all prerequisites of a regularization are fulfilled. Finally, we estimate the error via

$$\|R^{(\lambda(\delta))}y^{(\delta)} - A^\dagger \overline{y}\|_X \leq \|R^{(\lambda(\delta))}\overline{y} - A^\dagger \overline{y}\|_X + \|R^{(\lambda(\delta))}\| \cdot \|y^{(\delta)} - \overline{y}\|_Y,$$

and let $\delta \to 0$. The first term on the right tends to zero due to the above consideration, if $\lambda(\delta) \to 0$. The second term is bounded,

$$\|R^{(\lambda(\delta))}\| \cdot \|y^{(\delta)} - \overline{y}\|_Y \leq \frac{1}{\lambda}\delta,$$

and vanishes, if $\frac{\delta}{\lambda} \to 0$. That is, $((R^{(\lambda)})_{\lambda>0}, \lambda(\delta, y^{(\delta)}))$ is a regularization method.

2.5 Parameter Choice Strategies

According to the Tikhonov regularization (or any other regularization), we obtain a whole family of possible solutions

$$x^{(\lambda,\delta)} = R^{(\lambda)}y^{(\delta)}, \quad \lambda > 0.$$

Intuitively, the regularization parameter should not be too small, otherwise we face the inverted noise again. In the contrary, if we choose a too large λ, then we solve a minimization problem that has nothing to do with the original one. Let us illustrate these two extreme cases on a familiar finite-dimensional problem.

Example 2.6. “(3×2)-system”:
We resume the simple problem from Example 2.1 and write down the regularized solution explicitly,

$$\mathrm{x}^{(\lambda,\delta)} = \left(\frac{309\lambda^4 + 939\lambda^2 + 36}{(3+\lambda^2)(\lambda^4 + 30608\lambda^2 + 6)}, \frac{31211\lambda^2 + 6}{\lambda^4 + 30608\lambda^2 + 6} \right)^T.$$

We see that it vanishes for $\lambda \to \infty$ and tends to $\mathrm{x}^{(\delta)} = (2,1)^T$ for $\lambda \to 0$. Since the exact solution $\overline{\mathrm{x}} = (1,1)^T$ is given, we can implement a test of all values of $\lambda \in [10^{-10}, 10^5]$ on a logarithmically equidistant grid. Then, we can find the one optimal λ^{opt}, such that the distance between $\mathrm{x}^{(\lambda^{\text{opt}},\delta)}$ and $\overline{\mathrm{x}}$ is minimal (see Figure 2.5). The family of all regularized solutions defines a curve in $\mathbb{R}^2$, and the optimal solution should be the orthogonal projection of the exact solution on this curve. Indeed, for a certain choice of the regularization parameter, we reach

$$\mathrm{x}^{(\lambda^{\text{opt}},\delta)} \approx (1,1)^T = \overline{\mathrm{x}}.$$

Further, we can see that the noise affects primarily the first component of the solution, while a too agressive regularization is able to ruin also the second component. ◇

In the general case, it is not clear how to choose the regularization parameter λ, and any concrete parameter choice strategy depends on the nature of the actual inverse problem. However, there are some common approaches, from simple and purely heuristic to rigorous and sophisticated. In order to motivate some of them, we consider the normal equation (2.20) in the equivalent formulation as the minimization problem

$$\min_{x\in X} T^{(\lambda,\delta)}(x), \tag{2.23}$$

where

$$T^{(\lambda,\delta)}(x) := \|y^{(\delta)} - Ax\|_Y^2 + \lambda^2 \|x\|_X^2 \tag{2.24}$$

is called the *Tikhonov functional*. The term $\|x\|_X^2$ plays the role of a penalty function, which prevents the noisy components of the solution from growing uncontrollably. In this regard, the factor λ^2 corresponds to the weight of the penalty. If the noise is small, we trust more in the residual and set λ small (almost no penalty). If the noise is large, we set λ large – the minimization will force the solution $x^{(\lambda,\delta)}$ to be small (damped noisy components).

More rigorously, we can show that

$$\begin{aligned}\frac{d}{d\lambda}\left(\left\|x^{(\lambda,\delta)}\right\|_X^2\right) &\overset{(2.21)}{=} \sum_{j=1}^{\infty} \frac{d}{d\lambda}\left(\left|\chi_j(\lambda)\frac{\langle\psi^{(j)}|y^{(\delta)}\rangle_Y}{\sigma_j}\right|^2\right)\\ &= -\sum_{j=1}^{\infty} \sigma_j^2 |\langle\psi^{(j)}|y^{(\delta)}\rangle_Y|^2 \frac{4\lambda}{(\sigma_j^2+\lambda^2)^3} < 0.\end{aligned}$$

Therefore, the solution norm is a monotonically decreasing function of λ. Before we analyze in a similar way the distance between $Ax^{(\lambda,\delta)}$ and the noisy data $y^{(\delta)} \in Y$, we note that the latter is generally not in the range of A. However, $Y = \overline{\operatorname{ran}(A)} \oplus \operatorname{ran}(A)^{\perp}$, such that we can split the data in two parts

$$y^{(\delta)} = y^{(\delta,\|)} \dotplus y^{(\delta,\perp)},$$

where

$$y^{(\delta,\|)} := \sum_{j=1}^{\infty} \langle\psi^{(j)}|y^{(\delta)}\rangle_Y \psi^{(j)}$$

is the projection of the data on $\operatorname{ran}(A)$ and $y^{(\delta,\perp)}$ is the part, orthogonal to this projection, that is, $\langle y^{(\delta,\|)}|y^{(\delta,\perp)}\rangle_Y = 0$. Then, we can derive that

$$\begin{aligned}\frac{d}{d\lambda}\left(\left\|y^{(\delta)} - Ax^{(\lambda,\delta)}\right\|_Y^2\right) &= \frac{d}{d\lambda}\left(\left\|y^{(\delta,\|)} + y^{(\delta,\perp)} - \sum_{j=1}^{\infty}\chi_j(\lambda)\langle\psi^{(j)}|y^{(\delta)}\rangle_Y\psi^{(j)}\right\|_Y^2\right)\\ &\overset{\text{Pythagoras}}{=} \frac{d}{d\lambda}\left(\sum_{j=1}^{\infty}\left|(1-\chi_j(\lambda))\langle\psi^{(j)}|y^{(\delta)}\rangle_Y\right|^2 + \left\|y^{(\delta,\perp)}\right\|_Y^2\right)\\ &= \sum_{j=1}^{\infty} |\langle\psi^{(j)}|y^{(\delta)}\rangle_Y|^2 \frac{4\sigma_j^2\lambda^3}{(\sigma_j^2+\lambda^2)^3} > 0.\end{aligned}$$

It proves the residual norm to grow monotonically with λ.

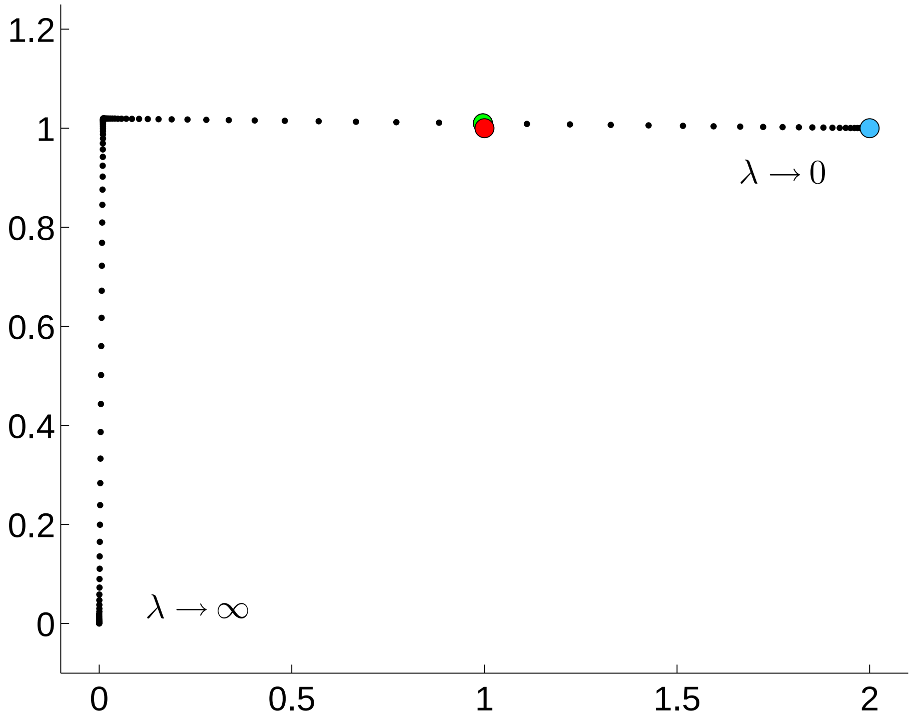

Figure 2.5: An illustration to Example 2.6. Black dots represent the regularized solutions $\mathrm{x}^{(\lambda,\delta)}$ for all test values of λ. The red circle is the exact solution $\overline{\mathrm{x}}$. The blue circle is the noisy solution $\mathrm{x}^{(\delta)}$ of the normal equation. The green circle is the optimal solution $\mathrm{x}^{(\lambda^{\mathrm{opt}},\delta)}$.

The latter result is used in the *Morozov discrepancy principle* – a parameter choice strategy, where the regularization parameter is the solution $\lambda = \lambda^{\mathrm{MDP}}$ of the equation

$$\|y^{(\delta)} - Ax^{(\lambda,\delta)}\|_Y = \delta. \tag{2.25}$$

On the one hand, for $\lambda \to \infty$, we have $\|x^{(\lambda,\delta)}\|_X \to 0$ due to (2.21), such that

$$\|Ax^{(\lambda,\delta)}\|_Y \leq \|A\| \cdot \|x^{(\lambda,\delta)}\|_X \to 0$$

and thus

$$\|y^{(\delta)} - Ax^{(\lambda,\delta)}\|_Y \geq \big|\|y^{(\delta)}\|_Y - \|Ax^{(\lambda,\delta)}\|_Y\big| \to \|y^{(\delta)}\|_Y \overset{(2.2)}{\gg} \delta.$$

On the other hand, for $\lambda \to 0$, we have

$$x^{(\lambda,\delta)} = R^{(\lambda)} y^{(\delta)} \to A^{\dagger} y^{(\delta)} = x^{(\delta)}$$

and, since $x = x^{(\delta)}$ is a minimizer of the functional $\|y^{(\delta)} - Ax\|_Y$, we obtain

$$\|y^{(\delta)} - Ax^{(\lambda,\delta)}\|_Y \to \|y^{(\delta)} - Ax^{(\delta)}\|_Y \leq \|y^{(\delta)} - A\overline{x}\|_Y = \|y^{(\delta)} - \overline{y}\|_Y \overset{(2.2)}{\leq} \delta.$$

This functional is continuous, such that the two estimates imply the existence of a solution of (2.25) and, since the norm grows strictly monotonically with λ, the solution is unique. One can show that the Tikhonov regularization combined with the Morozov discrepancy principle yields a regularization method [Groetsch-1993].

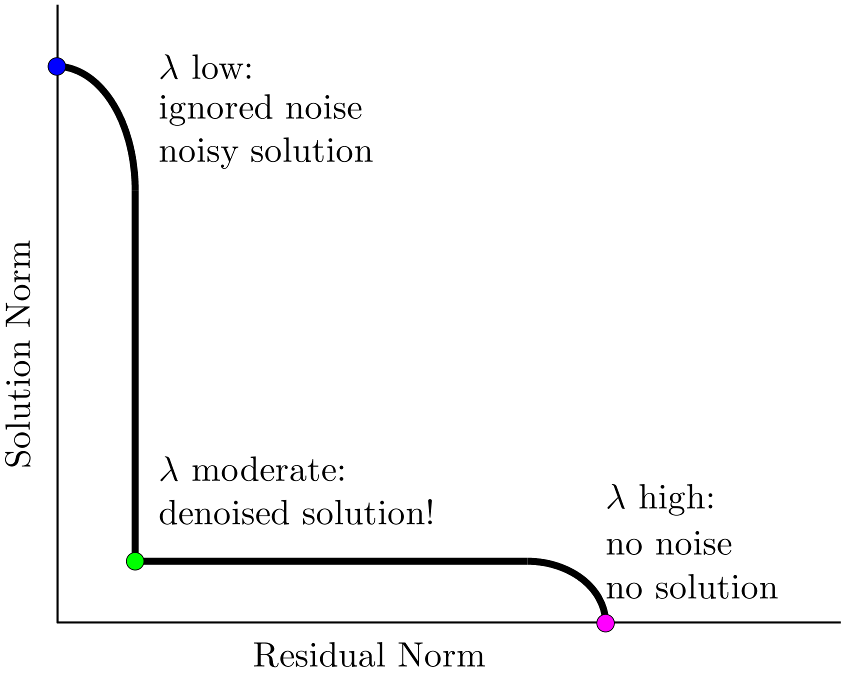

Figure 2.6: An illustration of the L-Curve criterion.

We can also use the monotonicity of the single terms of the Tikhonov functional, in order to reason that the curve

$$c(\lambda) := \begin{pmatrix} \ln \|y^{(\delta)} - Ax^{(\lambda)}\|_Y \\ \ln \|x^{(\lambda)}\|_X \end{pmatrix}$$

is the graph of a monotonically decreasing function, which has often a shape of the letter L (see Figure 2.6). Any point on the curve is characterized by the residual and solution norms and yields a unique value of the regularization parameter. We already stressed, from the intuitive point of view, how important it is to hit a moderate value λ, which is not too large and not too small. The *L-Curve criterion* is a heuristical parameter choice strategy that sets the regularization parameter λ to the value corresponding to the "corner" of the *L-Curve* $c = c(\lambda)$. In terms of the analytical geometry, the corner is the point with maximal *curvature*, that is, the regularization parameter is given by

$$\lambda^{\mathrm{LCC}} := \arg\max_{\lambda} \kappa(\lambda),$$
$$\kappa(\lambda) := \frac{\det(Dc(\lambda), D^2c(\lambda))}{|c(\lambda)|^3}.$$

Let us show how this simple criterion solves an ill-posed problem we considered earlier.

Example 2.7. "Inverse Laplace transformation":
The heuristical idea of the L-Curve criterion presented in Figure 2.6 is usually not met in practice. Considering the L-Curve for the inverse problem from Example 2.2 (see Figure 2.7), we recognize a "corner", which corresponds to the choice $\lambda^{\mathrm{LCC}} \approx 2 \cdot 10^{-3}$. We observe also that it is quite close to the optimal value $\lambda^{\mathrm{opt}} \approx 4 \cdot 10^{-2}$ of the regularization parameter. The comparison

$$\begin{aligned} \|x^{(\delta)} - \overline{x}\|_X &\approx 7 \cdot 10^{16}, \\ \|x^{(\lambda^{\mathrm{LCC}},\delta)} - \overline{x}\|_X &\approx 1 \cdot 10^{-1}, \\ \|x^{(\lambda^{\mathrm{opt}},\delta)} - \overline{x}\|_X &\approx 6 \cdot 10^{-3}, \end{aligned}$$

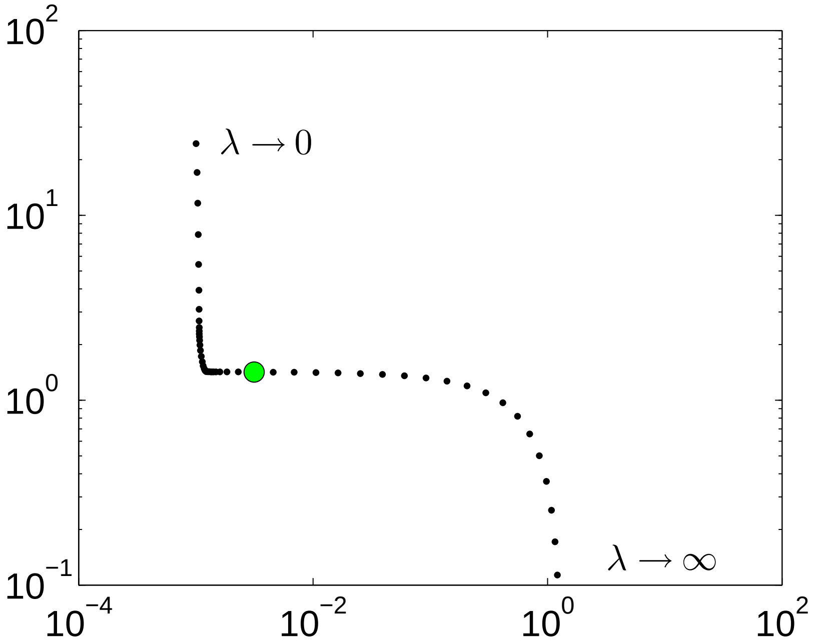

Figure 2.7: The discrete L-Curve (black dots) and the optimal choice (green circle) from Example 2.7.

shows that the regularized solution is much better than the best-approximate solution. Still, the heuristic of the criterion is coarse and far from optimal with regard to this problem. ◇

2.6 Nonlinear Problems

Let us now come back to the nonlinear minimization problem (2.3). Summarizing the considerations of the last few sections, a numerical solution method can have the following form

$$\begin{aligned} b^{(k,\delta)} &:= y^{(\delta)} - F[x^{(k)}], \\ A^{(k)} &:= DF[x^{(k)}], \\ h^{(k,\lambda)} &:= \left(A^{(k)*}A^{(k)} + \lambda^2 \mathbb{1}\right)^{-1} A^{(k)*} b^{(k,\delta)}, \\ x^{(k+1)} &:= x^{(k)} + h^{(k,\lambda)}, \quad k \geq 0, \end{aligned} \tag{2.26}$$

where the regularization parameter λ can be obtained from some parameter choice strategy. This method has a noticeable similarity with the *Levenberg-Marquardt* method – another Newton-type method, developed for solution of well-posed problems, where $\delta = 0$ and $y^{(\delta)} = y^{(0)} = \overline{y}$ actually, but the derivative $DF[x^{(k)}]$ may be an ill-conditioned matrix. If this is the case, one can "trust" in the linearization

$$\min_{h \in X} \|y^{(0)} - F[x^{(k)}] - DF[x^{(k)}]h\|_Y$$

of the problem (2.3) only in a small ball around the iterate $x^{(k)}$. Therefore, one supplies the norm to be minimized with a constraint, in order to stay in this ball called the *trust region*. In other words, one computes the update as a solution $h = h^{(k,\lambda)}$ of the minimization problem

$$\min_{h \in X} \|y^{(0)} - F[x^{(k)}] - DF[x^{(k)}]h\|_Y^2 + \lambda^2 \|h\|_X^2,$$

where the parameter λ justifies the update with respect to the given radius ρ of the trust region. For instance, the larger the value of λ, the smaller must be the norm $\|h\|_X^2$ to ensure the minimization of the whole expression above. More precisely,

$$\|h^{(k,\lambda)}\|_X^2 = \rho^2$$

must hold. Knowing the corresponding update $h^{(k,\lambda)}$, one should be able to decide whether the next iterate $x^{(k+1)} := x^{(k)} + h^{(k,\lambda)}$ can be trusted or not. The *Armijo-Goldstein criterion* uses the quotient

$$\mu := \frac{\|b^{(k,0)}\|_Y^2 - \|y^{(0)} - F[x^{(k+1)}]\|_Y^2}{2\langle A^{(k)} h^{(k,\lambda)} | b^{(k,0)} \rangle_Y} \tag{2.27}$$

to measure the quality of the linearization for the actual iterate. One must provide just two parameters $0 < \mu_1 < \mu_2 < 1$ that describe personal expectations respective linearity. If the function is "not linear enough" ($\mu < \mu_1$) in the current trust region, one repeats the previous step with a smaller radius (a larger λ). Eventually, one can also increase the radius ρ, if the iterate reaches the area, where the function is "pretty linear" ($\mu > \mu_2$).

While the radius adjustment reminds us on a parameter choice strategy, the above minimization problem is exactly the one we considered for the Tikhonov functional (2.24). Indeed, our regularization method (2.26) can be interpreted as an adaptation of the Levenberg-Marquardt method for ill-posed problems. The choice of the trust region radius takes place in the Morozov discrepancy principle by choosing λ, such that

$$\|b^{(k,\delta)} - A^{(k)} h^{(k,\lambda)}\|_Y = \mu \|y^{(\delta)} - F[x^{(k)}]\|_Y, \tag{2.28}$$

where the number $0 < \mu \lesssim 1$ remains constant. The norm on the left is an estimate of the residual norm of the next iterate,

$$\|y^{(\delta)} - F[x^{(k+1)}]\|_Y \approx \|y^{(\delta)} - F[x^{(k)}] - DF[x^{(k)}]h^{(k,\lambda)}\|_Y = \|b^{(k,\delta)} - A^{(k)} h^{(k,\lambda)}\|_Y.$$

Via the parameter μ, we control the reduction rate of the residual norm: for μ near one, we obtain a larger value of λ and correspondingly, a smaller update.

The intuition from the classical Newton-type methods, that the residual norm converges monotonically to zero, is not appropriate for an ill-posed problem, where the solution does not need to exist, such that a method eventually cannot converge. We could try to stop, when the residual norm begins to grow, in which case we risk to experience the *semiconvergence* – the iterates $x^{(k)}$ move towards the exact solution for $0 \le k \le k^{\text{stop}}$ and then, for $k > k^{\text{stop}}$, they drift away again (see Figure 2.8). Since we do not know the exact solution, we need a smart *stopping rule* – a kind of parameter choice strategy that analyzes the behaviour of the residuals and decides when the iteration should be stopped. From this point of view, the step number k^{stop} can be seen as a regularization parameter. The residual of our iterative method contains noise of the magnitude δ, that is, intuitively, the method should not minimize the residual norm below that value. We choose k^{stop} as the minimal k, such that

$$\|y^{(\delta)} - F[x^{(k)}]\|_Y \le \tau\delta \tag{2.29}$$

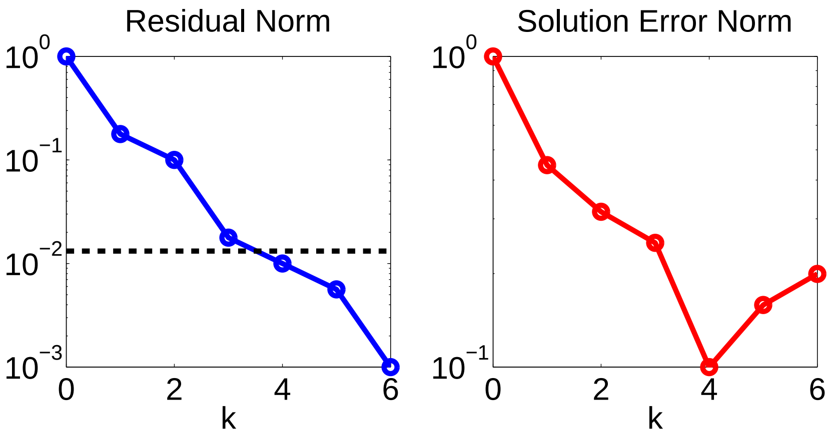

Figure 2.8: Crossing the noise level (dashed line) at $k^{\text{stop}} = 4$, the residual norm (blue line) decays further, but the solution (red line) drifts away.

is fulfilled, where $\tau \geq 1$ is a safety factor for the case that our noise model is too optimistic. Naturally, we should approach the noise level δ (that is, $\tau \approx 1$) only with small updates. Thus, by a rule of thumb, we can set the safety factor $\tau := 1/\mu$.

The numerical treatment of a nonlinear problem has also a positive effect. We remind that the map $F : X \to Y$ yields data $y = F[x] \in Y$ in dependence of the given parameter $x \in X$, where x and y are generally elements of some functional spaces X and Y. In practice, all spaces must be reduced to finite dimensions, such that in principle, the data is a vector $\mathrm{y} \in \mathbb{R}^m$ depending on a finite family of parameters $\mathrm{x} = (\mathrm{x}_1, \ldots, \mathrm{x}_n)^T$. Consequently, the operator $DF[x]$ becomes a matrix $\mathrm{A} \in \mathbb{R}^{m\times n}$ with rank $n < m$, which can be explored by using its SVD $(\psi^{(j)}, \sigma_j, \varphi^{(j)})_{j=1}^n$. The right singular vectors $(\varphi^{(j)})_{j=1}^n$ yield an orthonormal basis of $\mathbb{R}^n$, and the singular values $(\sigma_j)_{j=1}^n$ give an impression of the importance of the single basis vectors. The larger the singular value σ_j, the more important is the corresponding singular vector $\varphi^{(j)}$, the larger is the impact of a variation of the parameter vector x in the direction $\varphi^{(j)}$ on the map value $\mathrm{F}[\mathrm{x}]$. In this way, we can sneak into the nature of the (nonlinear) map F in the vicinity of x – the closer is the ℓ-th component of $\varphi^{(j)}$ to one, the easier we can deduce the importance of the parameter x_ℓ from the magnitude of the singular value σ_j. In the general case, the components of a singular vector are mixed and far from one, but if there is $1 \leq j \leq n$ with

$$\frac{\sigma_j}{\sigma_1} \approx 1, \qquad \frac{|\varphi_s^{(j)}|^2}{\|\varphi^{(j)}\|_2^2} \approx 1, \tag{2.30}$$

we can call the parameter x_s *strong*. Similarly, if there is $1 \leq j \leq n$ with

$$\frac{\sigma_j}{\sigma_1} \approx 0, \qquad \frac{|\varphi_w^{(j)}|^2}{\|\varphi^{(j)}\|_2^2} \approx 1, \tag{2.31}$$

we can call the parameter x_w *weak*. Further, the matrix $\Phi = (\varphi^{(1)}, \ldots, \varphi^{(n)}) \in \mathbb{R}^{n\times n}$ reveals correlations between the parameters $(\mathrm{x}_\ell)_{\ell=1}^n$. Typically, we are not interested in the concrete values of the entries (especially for large n), but in their relative magnitudes. Since

$$\begin{array}{rcl} |\varphi_1^{(j)}|^2 + \ldots + |\varphi_n^{(j)}|^2 & = & 1 \quad \Rightarrow \\ |\varphi_1^{(j)}|^2, \ldots, |\varphi_n^{(j)}|^2 & \leq & 1, \end{array}$$

we prefer to consider the componentwise squared matrix $\Phi.\hat{}2$ and represent it as a pictogram. The entries correspond to blocks in grayscale colors, for instance,

$$\Phi = \begin{pmatrix} 1 & 0 & 0 \\ 0 & 1/2 & \sqrt{3}/2 \\ 0 & -\sqrt{3}/2 & 1/2 \end{pmatrix} \quad \Rightarrow \quad \Phi.\hat{}2 = \begin{pmatrix} 1 & 0 & 0 \\ 0 & 1/4 & 3/4 \\ 0 & 3/4 & 1/4 \end{pmatrix} =$$

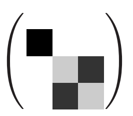

We show in the following example how such pictogram should be interpreted with respect to the definitions (2.30) and (2.31).

Example 2.8. "Singular Value Analysis":

We consider the matrix

$$\Phi.\hat{}2 = \qquad \in \mathbb{R}^{7\times 7}$$

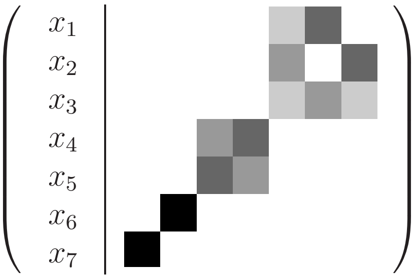

of the componentwise squared singular vectors corresponding to an ill-conditioned matrix A $\in \mathbb{R}^{20\times 7}$, which arises from discretization of a certain operator $DF[x]$. For the sake of simplicity, the parameter of the underlying map F has originally a finite length, that is, $x \in \mathbb{R}^7$. The columns of the above pictogram visualize the singular vectors and, for a better readability, we fade in an additional (zeroth) column with parameters corresponding to the rows. The first column is the most important, its last component is black, thus we conclude that x_7 is the strongest parameter in the map F. The second column reveals that x_6 is somewhat weaker than x_7. The next two columns show that x_4 and x_5 are weaker and correlated with each other – a repeated study of these parameters could improve the model. The last three columns represent the weakest parameters x_1, x_2, x_3, which are highly correlated – in this case, one can think about excluding these unimportant parameters from the model. $\diamond$

Through the chapter, we explained why only regularization methods **can** deliver a meaningful solution of an ill-posed problem. Until now we did not discuss under which conditions they **do** deliver such solution. The classical Newton-type methods require that the derivative $DF[x]$ is Lipschitz continuous (see, for example, [Hanke-Bourgeois-2006]), that is, the Taylor remainder of the linearization (2.4) can be estimated by

$$\|\Xi(\overline{x}; x)\|_Y \leq C\|\overline{x} - x\|_X^2,$$

where $C > 0$ is constant and $x \in \operatorname{dom}(F)$. However, for the ill-posed problem, even though the right-hand side is small (near the solution), the left-hand side can be considerably smaller, such that the above condition does not describe the local behaviour of the map properly and the error of the linearization can go out of control. The usual practice is to replace the parameter distance by the data distance, that is, to demand

$$\|\Xi(\overline{x}; x)\|_Y \leq C\|F[\overline{x}] - F[x]\|_Y$$

or

$$\|\Xi(\overline{x};x)\|_Y \leq C\|\overline{x}-x\|_X\|F[\overline{x}]-F[x]\|_Y. \tag{2.32}$$

Under the latter condition, one can show that the Levenberg-Marquardt method (2.26), combined with the parameter choice strategy (2.28) and the stopping rule (2.29), converges monotonically [Hanke-1997].

2.7 Summary

So far we made progress only in the mathematical specification of the terms appearing in the key questions of this work. We understand now that an “inversion method” is typically an iterative method for numerical solution of the given inverse problem. In the following, we want to measure the quality of such a method according to its theoretical and practical properties. Therefore, we formulate these properties as subquestions of the Question I (see p. 11), more precisely, from the purely theoretical viewpoint, we can ask two questions:

Question I.1: Does the inversion method contain regularization?

Question I.2: Does the inversion method converge?

We already answered the first one for the Levenberg-Marquardt method (2.26), by demonstrating how it is derived by the Tikhonov regularization of the classical Newton method. Moreover, inequality (2.32) is a rigorous condition for the method to converge. Unfortunately, we cannot just check this condition for the particular inverse problem presented in Chapter 1. As we saw, the problem has a complex physical background, such that we cannot treat the corresponding mathematical definition of the map F explicitly. But we can test our method on some well-studied cases where the solution is already obtained by other means.

Chapter 3

Application of the Theory

3.1 The Particular Inverse Problem

3.1.1 Functional Spaces

In Chapter 1, we discussed briefly the direct problem of interest and the associated map G, which yields for each interaction potential u the corresponding radial distribution function (RDF). In other words, the particular inverse problem is to solve the equation

$$y = G[u]$$

for the given RDF y. Sometimes, the unknown potential u is parameterized via $u = H[x]$, where x is an unknown parameter, and the equation takes the form

$$y = F[x]$$

with $F := G \circ H$. In this chapter, we want to apply the (general) theory of inverse problems to this particular problem. Even though we never discussed the mathematical structure of the sets $\mathrm{dom}(G)$ and $\mathrm{ran}(G)$, we identified their elements with potentials and RDFs, respectively, and specified some typical features. That is, a potential was any smooth function $u : (0, \infty) \to \mathbb{R}$ that posesses the properties

$$\begin{aligned} &(\mathrm{U1}) \qquad \lim_{r\to 0} u(r) = \infty, \\ &(\mathrm{U2}) \qquad \lim_{r\to \infty} u(r) = 0, \\ &(\mathrm{U3}) \qquad \min_{r\in(0,\infty)} u(r) < 0. \end{aligned}$$

We called an RDF any smooth function $y : (0, \infty) \to (0, \infty)$ with

$$\begin{aligned} &(\mathrm{Y1}) \qquad \lim_{r\to 0} y(r) = 0, \\ &(\mathrm{Y2}) \qquad \lim_{r\to \infty} y(r) = 1, \\ &(\mathrm{Y3}) \qquad \max_{r\in(0,\infty)} y(r) > 1. \end{aligned}$$

However, the preliminary description of the potentials and RDFs by properties (U1-3) and (Y1-3), respectively, lacks rigorosity from the viewpoints of computer simulation and mathematics. In the following, we discuss the mentioned lack and revise the properties, in order to elaborate more rigorous definitions, which cover our needs.

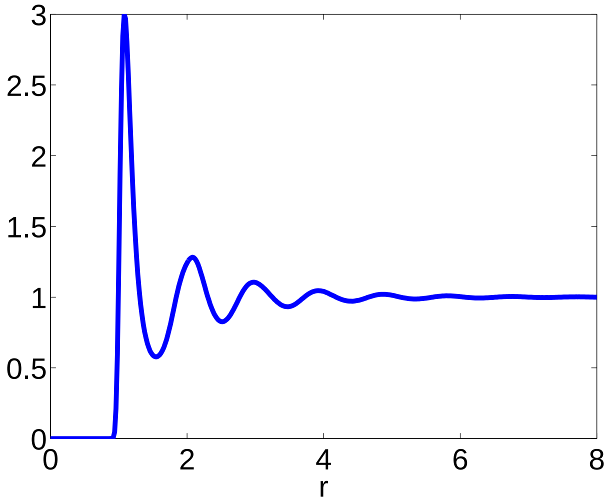

Figure 3.1: A typical RDF.

Figure 3.1 shows a typical RDF y obtained by computer simulation. We see that the property (Y1) holds and even more, the number

$$r^{\text{core}} := \max\{r > 0 | y(s) = 0, \forall s \in (0, r]\}$$

exists. The reason for this is the strongly repulsive interaction between particles at short distances, which is stated by the property (U1) of the underlying potential u. Due to repulsion, each particle has a "core" region $(0, r^{\text{core}}]$, which is rarely entered by other particles. Thus, the sampling procedure for the RDF never finds a particle pair at this short distance and we observe in simulations, that

$$y(r) = 0, \quad \forall r \in (0, r^{\text{core}}]. \tag{3.1}$$

In other words, the actual behaviour of the potential in the core region does not matter as long as the repulsion energy is high enough. In principle, this indefiniteness allows us to claim that the singularity of a potential at zero has a polynomial character, that is,

1. property of potentials:
There exist $A_0^{\text{inf}}, A_0^{\text{sup}} \in (0, \infty)$, $\alpha_0 \in [0, \infty)$, $\Delta\alpha_0 \in [0, \alpha_0]$ and $r^{\text{core}} \in (0, \infty)$, such that

$$A_0^{\text{inf}} r^{-\alpha_0 + \Delta\alpha_0} \leq u(r) \leq A_0^{\text{sup}} r^{-\alpha_0 - \Delta\alpha_0}, \quad \forall r \in (0, r^{\text{core}}].$$

This property is particularly useful in the computer simulation, where the values of the potential cannot be infinite. In the core region, which is a priori never visited by particles, we can replace the potential values by a (very large) constant $A_0^{\text{inf}} = A_0^{\text{sup}}$ while choosing $\alpha_0 = \Delta\alpha_0 = 0$. However theoretically, the probability for a short distance between the particles is not zero, it rather decays exponentially with growing repulsion energy (see Figure 3.2). Thus, we claim

1. property of RDFs:
There exist $B_0^{\text{inf}}, B_0^{\text{sup}} \in (0, \infty)$, $\beta_0 \in [0, \infty)$, $\Delta\beta_0 \in [0, \beta_0]$ and $r^{\text{core}} \in (0, \infty)$, such that

$$\exp\left(-B_0^{\text{inf}} r^{-\beta_0 - \Delta\beta_0}\right) \leq y(r) \leq \exp\left(-B_0^{\text{sup}} r^{-\beta_0 + \Delta\beta_0}\right), \quad \forall r \in (0, r^{\text{core}}].$$

According to this statement, we observe (3.1) in simulation due to rounding errors in the sampling procedure.

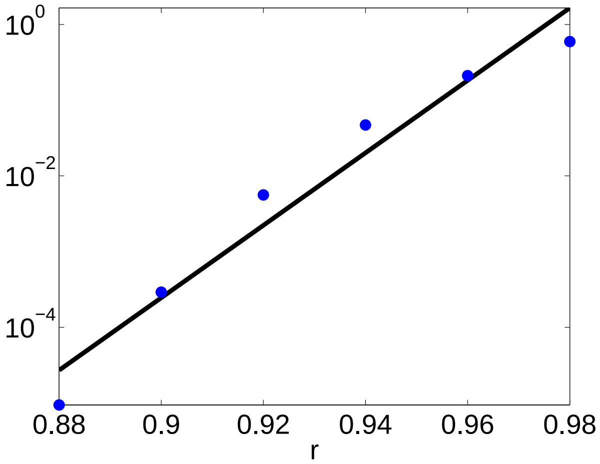

Figure 3.2: A logarithmic plot of the typical RDF (blue dots) near the core region, that is, for $r \to r^{\text{core}} + 0$. The black line represents the corresponding linear fit of the points.

Figure 3.3 shows a typical potential u used to describe the nonbonded interactions in a fluid. We confirm the property (U2) and even more, we see that $u(r) \approx 0$ for finitely large distances. This approximation is used in the computer simulation, in order to reduce the computational effort in a large system. Cutting off the potential at some appropriate distance $r^{\text{cut}} < \infty$ and continuating it with zero allows to consider only interactions in small subregions of the system. However, the resulting uncertainties in the energy and the pressure can only be estimated and corrected, if the convergence of the potential to zero is fast enough (see Appendix B). Such potentials are called *short-ranged* and the Lennard-Jones potential is one of them. In this work, we do not consider electrostatic interactions between particles, because they are modeled by the *Coulomb* potential, which is *long-ranged*. Therefore, we claim that our potentials are short-ranged:

2. property of potentials:
There exist $A_\infty \in (0, \infty)$, $\alpha_\infty \in (d, \infty)$ and $r^{\text{cut}} \in (r^{\text{core}}, \infty)$, such that

$$|u(r)| \leq A_\infty r^{-\alpha_\infty}, \quad \forall r \in (r^{\text{cut}}, \infty).$$

This model also covers the case where the potential is cut off.

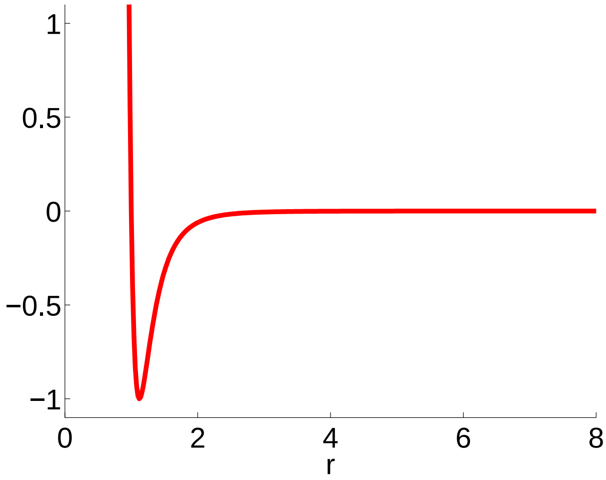

Figure 3.3: A typical nonbonded interaction potential.

As the property (Y2) states, the RDF has a similar asymptotic behaviour – it converges to one for large distances. We see in Figure 3.1 that the deviations of the function's extremal values from the limit decay very fast and become vague due to the statistical noise as the distance grows. We can model the decay on the interval (r^{cut}, ∞) polynomially

$$|y(r) - 1| \leq r^{-\beta_\infty^{\text{poly}}}$$

or exponentially

$$|y(r) - 1| \leq \exp\left(-r^{\beta_\infty^{\text{exp}}}\right).$$

Obviously, the first version is a safer estimate, no matter how large the power is. Regarding the good correspondence between RDF and potential promised by Henderson theorem, we expect that the power of the polynomial estimate is comparable with the number $d = 3$ of dimensions, like in the 2. property of potentials. We plot the power as a function of the distance

$$\beta_\infty^{\text{poly}}(r) \approx -\frac{\ln(|y(r) - 1|)}{\ln(r)}$$

and observe that the mentioned decay becomes faster with growing r (see Figure 3.4). Even more, for large r, the power reaches the desired level near d. Probably, we cannot observe $\beta_\infty^{\text{poly}} > d$ just because the data has finite length and becomes noisy in the last components. The best polynomial fit confirms our hypothesis. Therefore, we claim that in the absence of noise, the convergence has the polynomial behaviour:

2. property of RDFs:
There exist $B_\infty \in (0, \infty)$, $\beta_\infty \in (d, \infty)$ and $r^{\text{cut}} \in (r^{\text{core}}, \infty)$, such that

$$|y(r) - 1| \leq B_\infty r^{-\beta_\infty}, \quad \forall r \in (r^{\text{cut}}, \infty).$$

Finally, we discuss the shape of the potential well, which is essential for attraction between particles in a fluid. The term "fluid" covers both liquids (high density) and gases (low density). At high density, the particles are kept together by pressure, such that interactions are mainly repulsive. However, if we simulate a liquid at moderate density

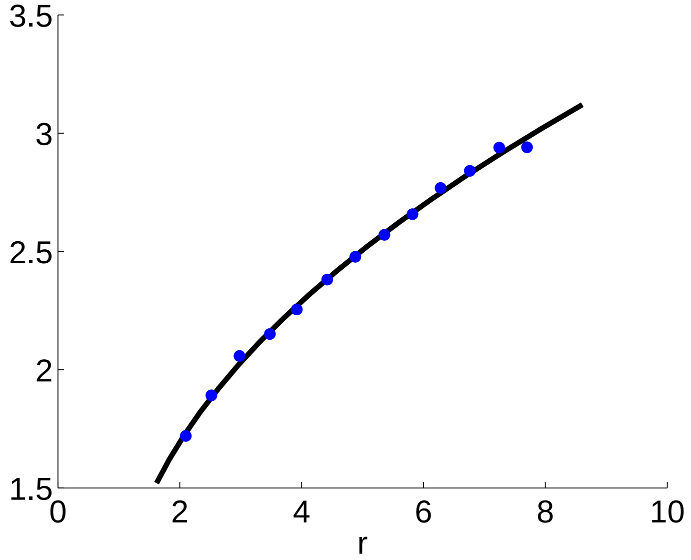

Figure 3.4: The power $\beta_\infty^{\text{poly}}(r)$ (blue dots) and the best polynomial fit (black line).

and without attractive forces, the particles could diffuse to the whole container (like a gas), which would be unusual for a liquid. Roughly speaking, the particles try to minimize the energy, such that the potential should have a well, which defines a preferred distance, as we indicated in the property (U3) and specify now:

3. property of potentials:
There exists a unique $r^{\min} \in (r^{\text{core}}, r^{\text{cut}}]$, such that

$$-\infty < u(r^{\min}) = \min_{r\in(0,\infty)} u(r) < 0.$$

Due to this attractive feature of the interaction, the sampling procedure for the RDF counts very many neighbours in a relatively small layer around a reference particle. The consequence is, as the property (Y3) states, that a noticeable peak emerges in the histogram:

3. property of RDFs:
There exists a unique $r^{\text{peak}} \in (r^{\text{core}}, \infty)$, such that

$$1 < y(r^{\text{peak}}) = \max_{r\in(0,\infty)} y(r) < \infty.$$

In the above discussion, we developed new formal properties describing the sets of potentials and RDFs. While some old properties remained, other were generalized or specified, but both the old and the new descriptions have a nearly equivalent physical interpretation. However, the corresponding mathematical statements are not equivalent, especially, the constants α_0 and β_0 establish the accurate behaviour of the functions near zero. We summarize the results of our study in the following definitions.

Definition:
For any $\alpha_0 \in [0,\infty)$ and $\Delta\alpha_0 \in [0,\alpha_0]$, let the set $S_U(\alpha_0,\Delta\alpha_0)$ contain all piecewise smooth functions $u : (0,\infty) \to \mathbb{R}$ with the following properties:

(SU1) there exist $A_0^{\inf}, A_0^{\sup} \in (0,\infty)$ and $r^{\text{core}} \in (0,\infty)$, such that

$$A_0^{\inf} r^{-\alpha_0+\Delta\alpha_0} \le u(r) \le A_0^{\sup} r^{-\alpha_0-\Delta\alpha_0}, \quad \forall r \in (0, r^{\text{core}}], \tag{3.2}$$

(SU2) there exist $A_\infty \in (0,\infty)$, $\alpha_\infty \in (d,\infty)$ and $r^{\text{cut}} \in (r^{\text{core}},\infty)$, such that

$$|u(r)| \le A_\infty r^{-\alpha_\infty}, \quad \forall r \in (r^{\text{cut}},\infty), \tag{3.3}$$

(SU3) there exists a unique $r^{\min} \in (r^{\text{core}}, r^{\text{cut}}]$, such that

$$-\infty < u(r^{\min}) = \min_{r\in(0,\infty)} u(r) < 0. \tag{3.4}$$

We call an element of the set

$$S_U := \bigcup_{\alpha_0\ge 0} \bigcup_{\Delta\alpha_0\le\alpha_0} S_U(\alpha_0,\Delta\alpha_0) = \bigcup_{\alpha_0\ge 0} S_U(\alpha_0,\alpha_0)$$

a *potential*.

Definition:
For any $\beta_0 \in [0, \infty)$ and $\Delta\beta_0 \in [0, \beta_0]$, let the set $S_Y(\beta_0, \Delta\beta_0)$ contain all piecewise smooth functions $y : (0, \infty) \to (0, \infty)$ with the following properties:

(SY1) there exist $B_0^{\text{inf}}, B_0^{\text{sup}} \in (0, \infty)$ and $r^{\text{core}} \in (0, \infty)$, such that

$$\exp\left(-B_0^{\text{inf}} r^{-\beta_0-\Delta\beta_0}\right) \le y(r) \le \exp\left(-B_0^{\text{sup}} r^{-\beta_0+\Delta\beta_0}\right), \quad \forall r \in (0, r^{\text{core}}], \tag{3.5}$$

(SY2) there exist $B_\infty \in (0, \infty)$, $\beta_\infty \in (d, \infty)$ and $r^{\text{cut}} \in (r^{\text{core}}, \infty)$, such that

$$|y(r) - 1| \le B_\infty r^{-\beta_\infty}, \quad \forall r \in (r^{\text{cut}}, \infty). \tag{3.6}$$

(SY3) there exists a unique $r^{\text{peak}} \in (r^{\text{core}}, r^{\text{cut}}]$, such that

$$1 < y(r^{\text{peak}}) = \max_{r \in (0,\infty)} y(r) < \infty. \tag{3.7}$$

We call an element of the set

$$S_Y := \bigcup_{\beta_0 \ge 0} \bigcup_{\Delta\beta_0 \le \beta_0} S_Y(\beta_0, \Delta\beta_0) = \bigcup_{\beta_0 \ge 0} S_Y(\beta_0, \beta_0)$$

a *radial distribution function* (RDF).

Even though the definitions are strictly derived from their physical motivation, the sets S_U and S_Y do not suffice for a mathematically rigorous discussion of the problem. For instance, if we intend to solve the problem by the Levenberg-Marquardt method presented in the previous chapter, then each set should be embedded in a Hilbert space, say, $S_U \hookrightarrow U$ and $S_Y \hookrightarrow Y$. Especially, the method makes use of the derivative $DG \in L(U, Y)$ of $G : U \to Y$, but its definition via

$$DG[u] := \lim_{t \to 0} \frac{1}{t}\bigg(G[u + tv] - G[u] \bigg), \quad u, v \in U,$$

makes sense only for linear spaces U and Y. Each of the sets $\{S_U(\alpha_0, \Delta\alpha_0)\}$ of potentials already posesses some structure, namely

$$u, v \in S_U(\alpha_0, \Delta\alpha_0), \quad c > 0 \quad \Rightarrow \quad u + v, cu \in S_U(\alpha_0, \Delta\alpha_0),$$

but none of them is a linear space. Likewise, none of the sets $\{S_Y(\beta_0, \Delta\beta_0)\}$ is a linear space, because all RDFs converge to one at infinity. Further, we have to supply each space with an appropriate norm $\|\cdot\|$, in order to justify the common definition of the term "limit" via

$$a = \lim_{k\to\infty} a^{(k)} \quad :\Leftrightarrow \quad \lim_{k\to\infty} \|a - a^{(k)}\| = 0,$$

and to measure the quality of the iterates and of the approximate solution. A popular norm in the physical literature is the root mean square distance given by

$$\text{RMSD}(f) := \left(\int |f(r)|^2 dr \right)^{1/2}$$

for a function f. However, the integral diverges for $y \in S_Y(\beta_0, \Delta\beta_0)$ due to (3.6) and for $u \in S_U(\alpha_0, \Delta\alpha_0)$, $0 < \Delta\alpha_0 < \alpha_0$, due to (3.2). Even for $u \in S_U(0, 0)$, the most part of $\text{RMSD}(u) < \infty$ comes from the integration over the core region where the potential values are apparently unimportant. In other words, the norms for potentials and RDFs need at least a fair reweighting. A popular approach in functional analysis is to embed a set into a weighted Lebesgue space $L^2((0,\infty), w)$, where $w \in C^\infty(0,\infty)$ is a bounded weight function. This space is a Hilbert space of all measurable functions $f : (0,\infty) \to \mathbb{R}$ that are *square-integrable* with the weight w, that is, $\|f\| < \infty$. The norm is induced by the weighted inner product

$$\langle f|g\rangle := \int_0^\infty f(r)g(r)w(r)dr$$

defined for any functions f and g from the Hilbert space.

Theorem A1:
S_U is a subset of the weighted Lebesgue space $U := L^2((0,\infty), w_U)$, if $w_U \in C^\infty((0,\infty))$ is a bounded weight function, such that

$$\begin{aligned} \lim_{r\to 0} u(r)^2 w_U(r) &= 0, & (3.8)\\ \lim_{r\to\infty} w_U(r) &= 1, & (3.9)\end{aligned}$$

for any $u \in S_U$.

Proof: Let $u \in S_U(\alpha_0, \Delta\alpha_0)$ be arbitrary. According to (3.8), there exists $r_0 \in (0, r^{\text{core}}]$ with

$$|u(r)^2 w_U(r)| \le 1, \quad \forall r \in (0, r_0),$$

because $u, w_U \in C^\infty(0, r^{\text{core}})$. Then, we have

$$\left|\int_0^{r_0} u(r)^2 w_U(r)dr\right| \le \int_0^{r_0} |u(r)^2 w_U(r)|dr \le r_0 \le r^{\text{core}} < \infty.$$

Further, due to (3.3), there exist $A_\infty \in (0,\infty)$, $\alpha_\infty \in (d,\infty)$ and $r^{\text{cut}} \in (r^{\text{core}},\infty)$ with

$$|u(r)| \le A_\infty r^{-\alpha_\infty}, \quad \forall r \in (r^{\text{cut}}, \infty).$$

Moreover, according to (3.9), we can assume that $r_1 \in (r^{\text{cut}},\infty)$ exists with

$$|w_U(r)| \le 2, \quad \forall r \in (r_1, \infty).$$

Thus, we have

$$\begin{aligned} \left|\int_{r_1}^\infty u(r)^2 w_U(r)dr\right| &\le \int_{r_1}^\infty |u(r)^2 w_U(r)|dr \\ &\le 2A_\infty \int_{r_1}^\infty r^{-2\alpha_\infty} dr \\ &= 2A_\infty \frac{1}{-2\alpha_\infty+1} r^{-2\alpha_\infty+1}\Big|_{r_1}^\infty \\ &= 2A_\infty \frac{1}{2\alpha_\infty - 1} r_1^{-2\alpha_\infty+1} < \infty. \end{aligned}$$

Finally, since u and w_U are bounded on the interval (r_0, r_1), we have

$$|u(r)^2 w_U(r)| \leq C, \quad \forall r \in (r_0, r_1)$$

for a constant $C < \infty$, that is,

$$\left| \int_{r_0}^{r_1} u(r)^2 w_U(r) dr \right| \leq C(r_1 - r_0) < \infty.$$

Summarizing the above estimates, we obtain

$$\begin{aligned} \|u\|_U^2 &= \left| \int_0^\infty u(r)^2 w_U(r) dr \right| \\ &\leq \left| \int_0^{r_0} u(r)^2 w_U(r) dr \right| + \left| \int_{r_0}^{r_1} u(r)^2 w_U(r) dr \right| + \left| \int_{r_1}^{\infty} u(r)^2 w_U(r) dr \right| < \infty, \end{aligned}$$

that is, $u \in U$. $\square$

Theorem A2:
S_Y is a subset of the weighted Lebesgue space $Y := L^2((0,\infty), w_Y)$, if $w_Y \in C^\infty((0,\infty))$ is a bounded weight function, such that

$$|w_Y(r)| \leq C_1 r^{-\beta}, \quad \forall r > r_\infty, \tag{3.10}$$

for certain $C_1 \in (0,\infty)$, $\beta \in (1,\infty)$ and $r_\infty \in (0,\infty)$.

Proof: Let $y \in S_Y(\beta_0, \Delta\beta_0)$ be arbitrary. According to (3.6), we can assume

$$|y(r)| \leq 2, \quad \forall r > r_\infty,$$

without loss of generality. Then, we have

$$\begin{aligned} \left| \int_{r_\infty}^{\infty} y(r)^2 w_Y(r) dr \right| &\leq 4 \int_{r_\infty}^{\infty} |w_Y(r)| dr \\ &\overset{(3.10)}{\leq} 4C_1 \int_{r_\infty}^{\infty} r^{-\beta} dr \\ &= 4C_1 \frac{1}{-\beta+1} r^{1-\beta} \Big|_{r_\infty}^{\infty} \\ &= 4C_1 \frac{1}{\beta-1} r_\infty^{1-\beta} < \infty. \end{aligned}$$

Finally, since y and w_Y are bounded on the interval $(0, r_\infty)$, there exists a constant $C_2 \in (0,\infty)$ with

$$|y(r)^2 w_Y(r)| \leq C_2, \quad \forall r \in (0, r_\infty),$$

that is

$$\left| \int_0^{r_\infty} y(r)^2 w_Y(r) dr \right| \leq C_2 r_\infty < \infty.$$

Summarizing the above estimates, we obtain

$$\|y\|_Y^2 = \left| \int_0^\infty y(r)^2 w_Y(r) dr \right| \leq \left| \int_0^{r_\infty} y(r)^2 w_Y(r) dr \right| + \left| \int_{r_\infty}^{\infty} y(r)^2 w_Y(r) dr \right| < \infty,$$

that is, $y \in Y$. □

In this work, we use the weight functions

$$w_U(r) := \exp\left(-\frac{1}{r}\right), \tag{3.11}$$
$$w_Y(r) := \exp(-r), \tag{3.12}$$

which satisfy the requirements of the theorems A1 and A2, respectively. These functions establish norms and limits on the spaces U and Y. It remains to discuss the structure of the set S_X of possible interaction parameters. Disregarding the concrete parameterization H, there are typically only few parameters, which are positive, such that we can embed $S_X := (0,\infty)^n$ into the Euclidean space $X := \mathbb{R}^n$ for some finite $n \in \mathbb{N}$. X is a Hilbert space with the standard inner product

$$\langle x|\xi\rangle_X := \langle x|\xi\rangle_2 = \sum_{j=1}^{n} x_j \xi_j, \quad \forall x, \xi \in X.$$

Following the above considerations, we work with the map

$$F : X \xrightarrow{H} U \xrightarrow{G} Y$$

and write the particular inverse problem in the usual form as equation

$$\overline{y} = F[\overline{x}], \tag{3.13}$$

where $\overline{x} \in X$ is the unknown exact parameter vector and $\overline{y} \in Y$ is the given exact data (RDF). In the future discussions, we will occassionally consider the inverse problem

$$\overline{y} = G[\overline{u}], \tag{3.14}$$

where the unknown exact potential $\overline{u} \in U$ appears without being parameterized.

3.1.2 Inversion Method

We explained earlier why an inverse problem of the form (3.13) is ill-posed in practice, for instance, if we do not know the exact data $\overline{y}$. This is the case for our problem – we have only the noisy RDF $y^{(\kappa)}$ measured experimentally with a certain noise level $\kappa > 0$, that is,

$$\|y^{(\kappa)} - \overline{y}\|_Y \leq \kappa.$$

Further, there are always model errors, for example, G does not perfectly describe the RDF as a physical quantity, and the parameterization H or the space U are not good enough to represent an interaction potential. In other words, it may happen that there is no $\overline{x} \in X$ with $\overline{u} = H[\overline{x}]$ or no $\overline{u} \in U$ with $\overline{y} = G[\overline{u}]$. Finally, the exact maps G and F are not available – we have only the approximate computational implementations $G^{(\nu)}$ and $F^{(\nu)} := G^{(\nu)} \circ H$, such that

$$\|G^{(\nu)}[u] - G[u]\|_Y \leq \nu \tag{3.15}$$

holds for a certain $\nu > 0$. Therefore, our inverse problems become

$$y^{(\delta)} = F^{(\nu)}[x], \tag{3.16}$$
$$y^{(\delta)} = G^{(\nu)}[u], \tag{3.17}$$

where we assume that the noise level δ takes into account all uncertainties of our model, that is, $\delta := \kappa + \nu$ and $y^{(\delta)} := y^{(\kappa)}$.

We already discussed in Chapter 2 ill-posed problems of the above form and presented the Levenberg-Marquardt method (2.26) as a good numerical solution approach. However, due to the chosen functional spaces U and Y, we have to take a closer look on the normal equation corresponding to the inverse problem (3.17). Simplifying our usual notations to $b := y^{(\delta)} - G[u]$ and $A := DG[u]$ in this paragraph, we see that the update h to the actual approximate potential u fulfills

$$(A^*A + \lambda^2 \mathbb{1})h = A^*b$$

for some $\lambda > 0$. Here, $A^* : Y \to U$ is the adjoint operator to $A : U \to Y$ with respect to the inner products of the weighted Lebesgue spaces U and Y, and it is defined by

$$\langle Au|y\rangle_Y = \langle u|A^*y\rangle_U.$$

The resulting operator differs from the usual $L^2((0,\infty))$-adjoint operator A^{*_2}, which is an infinite-dimensional analogon of a transposed matrix. For A^{*_2}, it rather holds

$$\langle Au|y\rangle_{L^2((0,\infty))} = \langle u|A^{*_2}y\rangle_{L^2((0,\infty))},$$

but its relation to A^* can be derived. Introducing the multiplication operators

$$\begin{aligned} W_U &: L^2((0,\infty)) \to L^2((0,\infty)), \qquad u \mapsto w_U u,\\ W_Y &: L^2((0,\infty)) \to L^2((0,\infty)), \qquad y \mapsto w_Y y, \end{aligned}$$

we obtain on the one hand,

$$\langle AW_U u|y\rangle_Y = \langle AW_U u|W_Y y\rangle_{L^2((0,\infty))} = \langle W_U u|A^{*_2}W_Y y\rangle_{L^2((0,\infty))} = \langle u|A^{*_2}W_Y y\rangle_U,$$

that is, $(AW_U)^* = A^{*_2}W_Y$. On the other hand, the equality

$$\langle AW_U u|y\rangle_Y = \langle W_U u|A^*y\rangle_U = \langle W_U u|W_U A^*y\rangle_{L^2((0,\infty))} = \langle u|W_U A^*y\rangle_U$$

reveals that $(AW_U)^* = W_U A^*$. Due to the uniqueness of the adjoint operator, we have

$$W_U A^* = A^{*_2} W_Y$$

and by multiplying the normal equation with W_U from the left, we obtain

$$(A^{*_2}W_Y A + \lambda^2 W_U \mathbb{1})h = A^{*_2}W_Y b,$$

what is more suitable for further discretization and implementation. This modified equation can also be used for problem (3.16). W_U then corresponds to the (non-present) weighting of the space X and can be omitted.

In order to implement the Levenberg-Marquardt method on the computer, we write it for finite-dimensional spaces, that is, we discretize the participating functions. Discretization is quite natural for our inverse problem, because experiments usually provide the data $y^{(\delta)}$ on some equidistant grid

$$r_i := i\Delta r, \quad 1 \le i \le m,$$

with a grid step $\Delta r > 0$. Thus, any data is actually a vector from the set

$$\mathbb{S}_Y := \{\mathrm{y} \in \mathbb{R}^m \,|\, \mathrm{y}_i = y(r_i), y \in S_Y, 1 \leq i \leq m\}$$

embedded in the space $\mathbb{Y} := \mathbb{R}^m$ with the inner product

$$\begin{aligned} \left\langle \mathrm{y}^{(1)} | \mathrm{y}^{(2)} \right\rangle_{\mathbb{Y}} &:= \Delta r \sum_{i=1}^{m} \mathrm{y}_i^{(1)} \mathrm{y}_i^{(2)} w_Y(r_i) = \Delta r \left\langle \mathrm{y}^{(1)} | \mathrm{W}_Y \mathrm{y}^{(2)} \right\rangle_2, \\ \mathrm{W}_Y &:= \mathrm{diag}(w_Y(r_1), \ldots, w_Y(r_m)). \end{aligned}$$

Conveniently, we use the same grid for the underlying potential by writing it as a vector from the set

$$\mathbb{S}_U := \{\mathrm{u} \in \mathbb{R}^m \,|\, \mathrm{u}_i = u(r_i), u \in S_U, 1 \leq i \leq m\}$$

embedded in the space $\mathbb{U} := \mathbb{R}^m$ with the inner product

$$\begin{aligned} \left\langle \mathrm{u}^{(1)} | \mathrm{u}^{(2)} \right\rangle_{\mathbb{U}} &:= \Delta r \sum_{i=1}^{m} \mathrm{u}_i^{(1)} \mathrm{u}_i^{(2)} w_U(r_i) = \Delta r \left\langle \mathrm{u}^{(1)} | \mathrm{W}_U \mathrm{u}^{(2)} \right\rangle_2, \\ \mathrm{W}_U &:= \mathrm{diag}(w_U(r_1), \ldots, w_U(r_m)). \end{aligned}$$

The space of parameters is already finite-dimensional and we define

$$\mathbb{S}_X := S_X = (0, \infty)^n \hookrightarrow \mathbb{X} := X = \mathbb{R}^n, \quad \langle \cdot | \cdot \rangle_{\mathbb{X}} := \langle \cdot | \cdot \rangle_X = \langle \cdot | \cdot \rangle_2.$$

The discretization of the maps between these spaces is obvious and leads to the discrete inverse problems

$$\mathrm{y}^{(\delta)} = \mathrm{F}^{(\nu)}[\mathrm{x}], \tag{3.18}$$

$$\mathrm{y}^{(\delta)} = \mathrm{G}^{(\nu)}[\mathrm{u}]. \tag{3.19}$$

The Levenberg-Marquardt method solves (3.18) by linearization, which requires discretization of the operator $A^{(k)}$ that represents the derivative of the RDF with respect to the parameter. In Chapter 1, we mentioned the complexity of the formal expression for the RDF and naturally, its derivative shows even more complexity. That is, while every serious software package (GROMACS, ESPResSo++, NAMD etc.) can run a molecular simulation and obtain the corresponding RDF from the snapshots of the systems trajectory, a computational procedure for the derivative is not included there by default. Therefore, we prefer to use a solution algorithm with a lower requirement – the ability to solve the direct problem, that is, to compute an RDF for the given interaction potential. Consequently, in our method, we discretize the operator D itself by approximating the derivative $DF^{(\nu)}$ by *finite differences*

$$\mathrm{D}_j \mathrm{F}_i^{(\nu)}[\mathrm{x}] := \frac{\mathrm{F}_i^{(\nu)}[\mathrm{x} + \Delta \mathrm{x}_j \mathrm{e}^{(j)}] - \mathrm{F}_i^{(\nu)}[\mathrm{x}]}{\Delta \mathrm{x}_j}, \quad 1 \leq i \leq m, 1 \leq j \leq n,$$

where the components of the variation vector $\Delta \mathrm{x} \in \mathbb{R}^n$ should be justified according to the following consideration. On the one hand, the map $\mathrm{F}^{(\nu)}$ is still noisy:

$$\begin{aligned} \|\mathrm{F}^{(\nu)}[\mathrm{x}] - \mathrm{F}^{(\nu)}[\xi]\|_{\mathbb{Y}} &= \|\mathrm{F}^{(\nu)}[\mathrm{x}] - \mathrm{F}^{(\nu)}[\xi] + \mathrm{F}[\mathrm{x}] - \mathrm{F}[\mathrm{x}] \\ &\qquad + \mathrm{F}[\xi] - \mathrm{F}[\xi]\|_{\mathbb{Y}} \\ &\leq \|\mathrm{F}[\mathrm{x}] - \mathrm{F}[\xi]\|_{\mathbb{Y}} + \|\mathrm{F}^{(\nu)}[\mathrm{x}] - \mathrm{F}[\mathrm{x}]\|_{\mathbb{Y}} \\ &\qquad + \|\mathrm{F}[\xi] - \mathrm{F}^{(\nu)}[\xi]\|_{\mathbb{Y}} \\ &\overset{(3.15)}{\leq} \|\mathrm{F}[\mathrm{x}] - \mathrm{F}[\xi]\|_{\mathbb{Y}} + 2\nu, \end{aligned}$$

so we have to choose $\Delta \mathrm{x}_i$ large enough to guarantee that the actually important information, $\mathrm{F}[\mathrm{x}] - \mathrm{F}[\xi]$, does not disappear in the noise of magnitude 2ν. On the other hand, the variations should be small enough to take the local behaviour of $\mathrm{F}^{(\nu)}$ into account. In these circumstances, we make a compromise by imposing the following *variation condition*,

$$2\nu < \|\mathrm{F}^{(\nu)}[\mathrm{x} + \Delta \mathrm{x}_j \mathrm{e}^{(j)}] - \mathrm{F}^{(\nu)}[\mathrm{x}]\|_{\mathbb{Y}} < 4\nu, \tag{3.20}$$

which should provide a reasonable choice of the variation vector $\Delta \mathrm{x}$. In our iterative regularization method, we ignore small perturbations in the operator $A^{(k)}$, consider the difference between discretizations of DF and $DF^{(\nu)}$ as negligible and take

$$\mathrm{A}^{(k)} := \mathrm{DF}^{(\nu)}[\mathrm{x}^{(k)}].$$

Since the number ν is an important part of the variation condition, we have to model the noise in the map $\mathrm{F}^{(\nu)}$ in a way, which allows us to estimate the noise level. We assume that each component $\mathrm{F}_i^{(\nu)}$ of the noisy map is normally distributed with mean F_i and standard deviation η_i^2. The mean RDF F is unknown, but we can estimate the vector $\eta \in \mathbb{R}^m$ of standard deviations in each step from ten samples of the map $\mathrm{F}^{(\nu)}$ via the *sample variance*

$$\eta_i^2 = \mathbf{Var}[\mathrm{F}_i^{(\nu)}], \quad 1 \leq i \leq m.$$

Then, the noise level ν can be estimated by using the properties of the *sample mean* via

$$\begin{aligned} \nu^2 &\approx \mathbf{E}\left[\|\mathrm{F}^{(\nu)}[\mathrm{x}] - \mathrm{F}[\mathrm{x}]\|_{\mathbb{Y}}^2\right] \\ &= \sum_{i=1}^{m} \mathbf{E}\left[|\mathrm{F}_i^{(\nu)}[\mathrm{x}] - \mathrm{F}_i[\mathrm{x}]|^2\right] w_Y(r_i)\Delta r \\ &= \sum_{i=1}^{m} \mathbf{Var}[\mathrm{F}_i^{(\nu)}] w_Y(r_i)\Delta r \\ &= \|\eta\|_{\mathbb{Y}}^2. \end{aligned} \tag{3.21}$$

According to the above discussion, the Levenberg-Marquardt method takes the form

$$\begin{aligned} \mathrm{b}^{(k,\delta)} &:= \mathrm{y}^{(\delta)} - \mathrm{F}^{(\nu)}[\mathrm{x}^{(k)}], \\ \mathrm{A}^{(k)} &:= \mathrm{DF}^{(\nu)}[\mathrm{x}^{(k)}], \\ \mathrm{h}^{(k,\lambda)} &:= \left(\mathrm{A}^{(k)*_2}\mathrm{W}_Y\mathrm{A}^{(k)} + \lambda^2 \mathbb{1}\right)^{-1} \mathrm{A}^{(k)*_2}\mathrm{W}_Y\mathrm{b}^{(k,\delta)}, \\ \mathrm{x}^{(k+1)} &:= \mathrm{x}^{(k)} + \mathrm{h}^{(k,\lambda)}, \quad k \geq 0, \end{aligned} \tag{3.22}$$

for the inverse problem (3.18), and

$$\begin{aligned} \mathrm{b}^{(k,\delta)} &:= \mathrm{y}^{(\delta)} - \mathrm{G}^{(\nu)}[\mathrm{u}^{(k)}], \\ \mathrm{A}^{(k)} &:= \mathrm{DG}^{(\nu)}[\mathrm{u}^{(k)}], \\ \mathrm{h}^{(k,\lambda)} &:= \left(\mathrm{A}^{(k)*_2}\mathrm{W}_Y\mathrm{A}^{(k)} + \lambda^2 \mathrm{W}_U\right)^{-1} \mathrm{A}^{(k)*_2}\mathrm{W}_Y\mathrm{b}^{(k,\delta)}, \\ \mathrm{u}^{(k+1)} &:= \mathrm{u}^{(k)} + \mathrm{h}^{(k,\lambda)}, \quad k \geq 0, \end{aligned} \tag{3.23}$$

for the inverse problem (3.19). In this chapter, we always assume that $\mathrm{x}^{(0)}$, $\mathrm{u}^{(0)}$, $\mathrm{y}^{(\delta)}$, ν and δ are given or can be estimated, such that the regularization parameter λ can be chosen via the Morozov discrepancy principle (2.28) and the iteration can be terminated due to the stopping rule (2.29).

3.1.3 Direct Problem

Since our inversion method's primary requirement is the ability to solve the direct problem, we briefly address the subtleties of the computer simulation, where the RDF is computed from the underlying potential or its parameters. For instance, in Chapter 1, we explained that it is done by *molecular dynamics*, which moves the particles of a fluid in accordance with the Newton equations. The corresponding solution method must be energy-conserving, otherwise the particles are either accelerated until the system blows up (due to energy gain), or slowed down until the system freezes (due to energy loss). But, in an experiment, where a total energy conservation is nearly impossible, the RDF is usually measured rather at constant temperature than at constant energy. Therefore, all our simulations are performed in the *canonical ensemble* (also called *NVT-ensemble*), that is, for fixed number N of particles, volume V and temperature T of the system. The source term of the Newton equations can be extended with a *thermostat* – a friction force, which speeds up or slows down the particles, such that the temperature remains constant (see Appendix B.1).

On the other hand, the parameters N, V and T allow a completely statistical description of the system by a distribution of particles, where their actual trajectories do not matter. This distribution is based exclusively on these three parameters and the interaction potential, and totally determines the fluid's statistical properties, including the RDF. Therefore, disregarding the popularity of the molecular dynamics in the physical community, a computer simulation can also be performed via the *Monte Carlo* method, which describes the fluid directly from the statistical viewpoint (see Appendix B.1). In a nutshell, the method picks out in each step a random particle, moves it slightly along a random vector, determines the change in the energy and depending on the temperature, decides whether this change is compatible with the canonical distribution (step accepted) or not (particle is moved back). Evidently, one can implement this procedure much easier than the molecular dynamics, therefore we use the Monte Carlo method in our preliminary tests in the next section.

A further subtlety we want to discuss here are the units used in a computer simulation. In the literature, one can find the tabulated RDF accompanied by all necessary experimental settings, including the temperature T in [K] and the density $\rho := \frac{N}{V}$ in [Å^{-3}]. Considering that, in SI units, we have

$$1 \quad [\text{Å}] \quad = \quad 10^{-10} \quad [\text{m}],$$

it is clear that no numerical method should work with numbers of that order. One usually introduces the *reduced units* by setting a unit mass M^{unit}, a unit length σ^{unit} and a unit energy $\varepsilon^{\text{unit}}$. Then, the computer simulation works with the more suitable quantities

$$\begin{aligned} T^* &= \frac{k_B T}{\varepsilon^{\text{unit}}}, \\ \rho^* &= \rho \left(\sigma^{\text{unit}}\right)^3, \\ \varepsilon^* &= \frac{\varepsilon}{\varepsilon^{\text{unit}}}, \\ \sigma^* &= \frac{\sigma}{\sigma^{\text{unit}}}, \end{aligned}$$

which are all of the same order and nearly equal to one. We often omit the stars, because we always mean the reduced units, unless we specify other units.

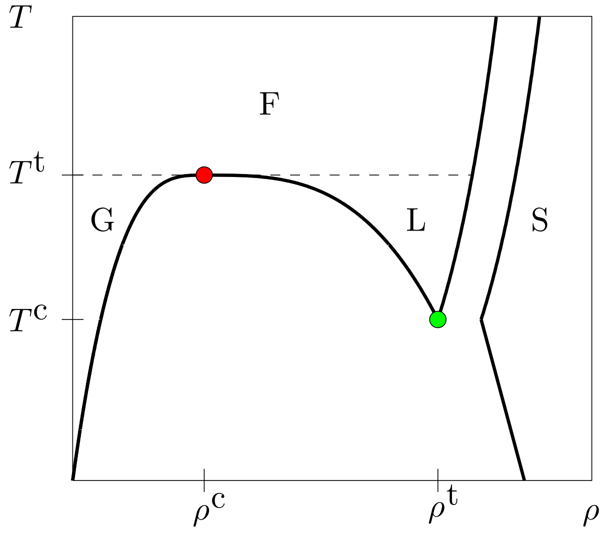

Figure 3.5: Phase diagram of a simple fluid.

Finally, let us take a look inside the physics of the simulation, in order to understand how the parameters T and ρ are to set up. We explained in Chapter 1, that a fluid is a system of particles, which are moved according to the given interactions. Even though the particles of a solid also interact, moving particles would be quite unusual – intuitively, a solid system is either too cold or too dense to flow. Indeed, *solid* and *fluid* are different *phase states* of matter, where *fluid* is a generic term for *liquid* and *gas*. Figure 3.5 shows the *phase diagram*, which helps to distinguish between different phase states. In such diagram, the temperature T and the density ρ of the system determine the state of matter (G stands for gas, L for liquid, S for solid, F for fluid). The solid lines represent the *coexistence lines*, where two phase states are present simultaneously. The green circle at $(\rho^{\text{t}}, T^{\text{t}})$ designates the *triple point*, where all three states are present. The red circle at $(\rho^{\text{c}}, T^{\text{c}})$ stands for the *critical point*, where a part of the matter is in the gaseous state and another part in the liquid state. The dashed line just separates visually the supercritical fluid from the other fluid states. We use the phase diagram as a guide for setting up a simulation in the NVT-ensemble. While we can carefree simulate a gas or a liquid, we avoid the solid state as well as the coexistence lines by choosing appropriate temperature and density. The safest for simulation is the supercritical fluid, therefore we prefer this phase state in the following section.

3.2 Simulated Data for Two-dimensional Fluids

Before we apply our regularization method on a real-world (ill-posed) inverse problem, we want to test it first under better conditions. We wrote our own code for two-dimensional molecular simulations, in order to quickly obtain insight into the dependence between the RDF and the underlying interaction potentials. We combined the programming languages C++ and Perl to implement the Monte Carlo and the Levenberg-Marquardt methods, which solve the direct and the inverse problems, respectively. For each inverse problem, we choose a certain exact solution $\overline{\mathrm{x}}$ and use $\mathrm{y}^{(\nu)} := \mathrm{F}^{(\nu)}[\overline{\mathrm{x}}]$ as the given data. Since the measurements become preciser (ν smaller) for a larger number N of particles, we find that $N = 128$ is an acceptable value. Surely, a simulated RDF contains some statistical noise, as modeled by the noisy map $\mathrm{F}^{(\nu)}$, but its magnitude is so small that we can consider the data $\mathrm{y}^{(\nu)}$ as nearly exact and the inverse problem as well-posed. We remind that such problem still can be ill-conditioned, as we demonstrated earlier in Chapter 2.

The preliminary formulation of the inverse problem was to obtain the Lennard-Jones parameters (ε and σ) as well as the temperature T and the density ρ for a simple fluid of monatomic molecules. However, after we test few possible norms for the data (Lebesgue, Sobolev, eventually weighted with characteristic functions), the derivative $\mathrm{DF}^{(\nu)}[\overline{\mathrm{x}}]$ reveals a correlation between the parameters. Indeed, it is one aspect of the direct problem – ε and σ can be chosen as the energy/temperature scale and the length/density scale, respectively. It is intuitively clear because of the reduced units, where we can choose $\varepsilon^{\mathrm{unit}} := \varepsilon$ and $\sigma^{\mathrm{unit}} := \sigma$, such that $\varepsilon^* = \sigma^* = 1$. We show this more rigorously in Theorem P7 in Appendix A.4. For this reason, we prefer to set $\varepsilon = \sigma = 1$ at this stage of testing and consider $\mathrm{x} = (\rho, \mathrm{T})^T$ as the basic parameters of the fluid.

In the first test, we want to know whether the parameters can also be obtained from the RDF, if the method starts with a very bad initial guess $\mathrm{x}^{(0)}$ far from the exact solution $\overline{\mathrm{x}} = (\overline{\rho}, \overline{\mathrm{T}})^T$. We choose $\overline{\mathrm{x}}$ from an equidistant grid on the area $[0.2, 0.9] \times [0.8, 2]$ and always use $\mathrm{x}^{(0)} := (0.55, 1)^T$ as the initial value. Since

$$\begin{aligned}(\rho^{\mathrm{c}}, \mathrm{T}^{\mathrm{c}}) &\approx (0.35, 0.5),\\ (\rho^{\mathrm{t}}, \mathrm{T}^{\mathrm{t}}) &\approx (0.8, 0.4),\end{aligned}$$

for the two-dimensional Lennard-Jones fluid [CM-1992], the test area corresponds to the (supercritical) fluid state, including the vicinity of the fluid-solid coexistence line (see again Figure 3.5). In order to solve the inverse problem, we combine the Levenberg-Marquardt method and the “pure” (and fast) Newton method where the regularization parameter is zero. We observe that the noise has no significant influence on the iterates $\mathrm{x}^{(k)}$ as long as

$$\|\mathrm{y}^{(\nu)} - \mathrm{F}^{(\nu)}[\mathrm{x}^{(k)}]\|_{\mathbb{Y}} \gg \nu$$

holds. For these iterates, there is no need for regularization, until they reach the area where the residual norm is of nearly the same order as ν and the (slower) Levenberg-Marquardt method finds a better application. In few steps, we obtain the parameters from the test area with relative errors

$$\left(\frac{|\overline{\rho} - \rho|}{|\overline{\rho}|}, \frac{|\overline{\mathrm{T}} - \mathrm{T}|}{|\overline{\mathrm{T}}|}\right)^T \approx (2.3 \cdot 10^{-3}, 8.1 \cdot 10^{-3})^T,$$

what is a nearly perfect reconstruction.

Already during these first numerical solutions of the inverse problem, we observe some useful facts, which allow to simplify the application of the Levenberg-Marquardt method in the following:

- The variations $\Delta\mathrm{x}$, which are necessary for the numerical differentiation and must fulfill the condition (3.20), can be chosen constant.
- The noise in the map $\mathrm{F}^{(\nu)}$ is nearly constant in the whole test area, such that we can choose a uniform bound ν for the noise there.
- For any initial guess, the Newton method is able to move the iterates close enough to the exact solution, such that the Levenberg-Marquardt method can take over.

Further, investigating the impact of the parameter variations on the RDF, we discover that for x near the fluid-solid coexistence line, it holds that

$$\left\|\mathrm{F}^{(\nu)}\left[\mathrm{x}+|\Delta\rho|\mathrm{e}^{(1)}\right]-\mathrm{F}^{(\nu)}[\mathrm{x}]\right\|_{\mathbb{Y}} \gg \left\|\mathrm{F}^{(\nu)}\left[\mathrm{x}-|\Delta\rho|\mathrm{e}^{(1)}\right]-\mathrm{F}^{(\nu)}[\mathrm{x}]\right\|_{\mathbb{Y}}.$$

In other words, the RDF is sensitive to the fluid-solid phase transition. For this reason, we keep the temperature and the density as parameters of the RDF in the following tests. In experiments, the data is usually measured near the triple point, thus we set the density near the mentioned coexistence line, but definitely in the fluid state. In this fashion, we hope to obtain representative results even in this very simple, preliminary setting.

The second test concerns a fluid of diatomic homonuclear molecules with the bond length ℓ. For the sake of simplicity, we assume that the bond is rigid and obtain the parameter $\mathrm{x}=(\mathrm{T},\rho,\ell)^T$ with relative errors near

$$(1.5\cdot 10^{-4}, 4.1\cdot 10^{-3}, 9.3\cdot 10^{-4})^T.$$

Inspired by the high quality of this reconstruction, we decide to extend the model to $\mathrm{x}=(\mathrm{T},\rho,\ell,\mathrm{k}_\ell)^T$ by considering the bond as a flexible spring with stiffness k_ℓ. However, we observe that

$$\left\|\mathrm{F}^{(\nu)}\left[\mathrm{x}+\Delta\mathrm{k}_\ell\mathrm{e}^{(4)}\right]-\mathrm{F}^{(\nu)}[\mathrm{x}]\right\|_{\mathbb{Y}} \lesssim 2\nu$$

for any variation $\Delta\mathrm{k}_\ell$, such that we cannot determine the corresponding derivative of $\mathrm{F}^{(\nu)}$ reliably. We discussed this situation more generally in Chapter 2, where we stressed that even in a well-posed, finite-dimensional problem, an ill-conditioned matrix can occur. If the influence of a parameter on the map is so small, that the variation condition is fulfilled only for very large variation, if ever, then the matrix $\mathrm{DF}^{(\nu)}$ is close to singular, as we can see in this concrete example,

$$\|\mathrm{D}_4\mathrm{F}^{(\nu)}[\mathrm{x}]\|_{\mathbb{Y}} = \frac{\|\mathrm{F}^{(\nu)}[\mathrm{x}+\Delta\mathrm{k}_\ell\mathrm{e}^{(4)}]-\mathrm{F}^{(\nu)}[\mathrm{x}]\|_{\mathbb{Y}}}{|\Delta\mathrm{k}_\ell|} \lesssim \frac{2\nu}{|\Delta\mathrm{k}_\ell|} \xrightarrow{|\Delta\mathrm{k}_\ell|\to\infty} 0.$$

Obviously, the bond stiffness k_ℓ is a very weak parameter and should be excluded from the model, otherwise the problem is severely ill-conditioned.

In the third test, we consider a diatomic molecule with a rigid bond, a bigger atom a and a smaller atom b, that is, $\sigma_{\mathtt{a,a}} > \sigma_{\mathtt{b,b}}$. We use the parameters of the atom a as scales, such that $\varepsilon_{\mathtt{a,a}} = \sigma_{\mathtt{a,a}} = 1$, and set the exact parameters of the atom b to $\varepsilon_{\mathtt{b,b}} = \sigma_{\mathtt{b,b}} = 0.5$. The mixed parameters $\varepsilon_{\mathtt{a,b}}$ and $\sigma_{\mathtt{a,b}}$ are obtained for each iterate via the Lorentz-Berthelot rules (see Appendix B.2). That is, the parameter in this case is $\mathrm{x}=(\mathrm{T},\rho,\ell_{\mathtt{a,b}},\varepsilon_{\mathtt{b,b}},\sigma_{\mathtt{b,b}})^T$, and our method leads to a good solution with the relative errors

$$(1.7\cdot 10^{-3}, 1.5\cdot 10^{-2}, 1.5\cdot 10^{-2}, 5.9\cdot 10^{-3}, 2.7\cdot 10^{-2})^T.$$

We notice that the quality of the reconstructions drops with growing number of parameters and suffers even from the low noise in the data $\mathrm{y}^{(\nu)}$. Since we cope with the (truly) noisy data from experiments in the next sections, we make no further tests of the Levenberg-Marquardt method.

In all above reconstructions, the singular value analysis highlights ρ as the strongest parameter and also shows the correlations between the other parameters. Since the previous fluids are quite simple, for a better visualization, we determine the singular values in the case of a more complex fluid, with respect to all (also very weak) parameters. For this

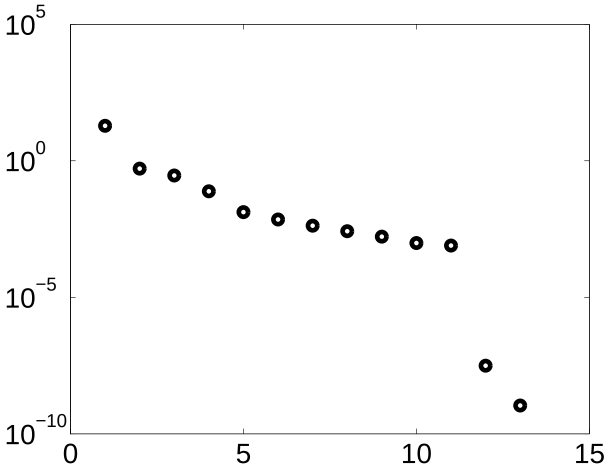

Figure 3.6: Singular values for the two-dimensional carbon dioxide model.

purpose, we consider a fluid of flexible molecules with three atoms arranged linearly, as in a molecule of carbon dioxide (bending angle $\theta_{\mathtt{O,C,O}} = \pi$). Such molecules can be bended, while the bonds `OC` and `CO` can be stretched independently. We set the Lennard-Jones parameters close to a common molecular model [HY-1995] for $\mathtt{CO}_2$, in particular, the oxygen atom `O` is bigger than the carbon atom `C`:

$$\begin{aligned} \varepsilon_{\mathtt{O,O}} &= 1.00, & \varepsilon_{\mathtt{O,C}} &= 0.60, & \varepsilon_{\mathtt{C,C}} &= 0.35, \\ \sigma_{\mathtt{O,O}} &= 1.00, & \sigma_{\mathtt{O,C}} &= 0.97, & \sigma_{\mathtt{C,C}} &= 0.90. \end{aligned}$$

We use short ($\ell_{\mathtt{O,C}} = \ell_{\mathtt{C,O}} = 0.035$) and stiff ($\mathrm{k}_{\mathtt{O,C}} = \mathrm{k}_{\mathtt{C,O}} \approx 10^4$, $\mathrm{k}_{\mathtt{O,C,O}} \approx 10^5$) bonds in order to prevent the high density from disrupting the molecules. During simulations, we observe that the bending stiffness $\mathrm{k}_{\mathtt{O,C,O}}$ turns out to be a very weak parameter. Apparently, the bonds `OC` and `OC` hold the atoms close together, such that repulsive forces between the two oxygen atoms prevail over the nonbonded interactions of the smaller carbon atom and prevent the molecule from bending. For the rest of parameters, we find the variations and approximate the derivative of the RDF in a dense fluid. The singular values of the derivative reveal how ill-posed the problem is and that the last two values are extremely small (see Figure 3.6). As usual, we represent the singular vectors as a pictogram

$\Phi.\hat{}2 =$

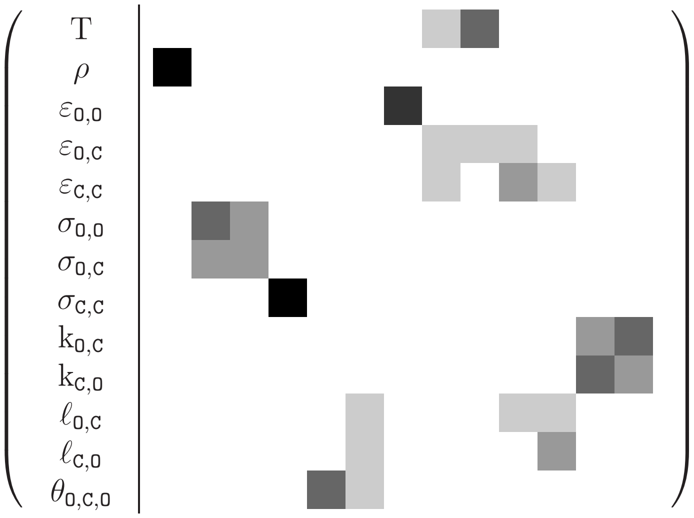

,

where the first column shows the thirteen parameters of the model. Again, we see that the density ρ is the strongest parameter. Then, the strong parameters $\sigma_{\mathtt{O,O}}$, $\sigma_{\mathtt{O,C}}$ and $\sigma_{\mathtt{C,C}}$

follow, where we can clearly see that the first one, which describes the nonbonded interactions between oxygen atoms, is leading. The parameters $\ell_{\mathtt{O,C}}$, $\ell_{\mathtt{C,O}}$ and $\theta_{\mathtt{O,C,O}}$, which determine the overall shape of the molecule, are somewhat weaker and conclude the group of the parameters corresponding to the length (size of system, atoms and bonds). Indeed, all remaining (and rather weak) parameters T, $\varepsilon_{\ldots}$, $\mathrm{k}_{\mathtt{O,C}}$ and $\mathrm{k}_{\mathtt{C,O}}$ describe the energy (of the system, atoms and bonds). This separation in two groups mirrors the clearly inferior contribution of the attractive forces to the structure of a dense fluid, where the molecules are kept together by pressure and where the repulsive forces overwhelm the thermal fluctuations. Further, we see that the two stiffness coefficients $\mathrm{k}_{\mathtt{O,C}}$ and $\mathrm{k}_{\mathtt{C,O}}$ are the weakest parameters, because they correspond to the lowest singular values in Figure 3.6. Removing these two parameters from the model would decrease the condition number of the derivative matrix and improve the quality of the reconstructions.

3.3 Experimental Data for Liquid Argon

Now we apply the Levenberg-Marquardt method on the particular inverse problem under realistic conditions where the fluid is three-dimensional and the noisy data is measured not by simulation, but by an experiment. First, we have to update our solver of the direct problem, in order to obtain RDFs with acceptable quality. While a hundred of molecules suffice to represent a two-dimensional fluid, this is not the case for a three-dimensional fluid. Therefore, we consider in the following simulations large systems with $N = 8192$ atoms (in the canonical ensemble). Further, we engage an established software package for molecular dynamics – GROMACS [BSD-1995], [LHS-2001], [SLHGMB-2005], [HKSL-2008]. Second, the noise in the experimental data $\mathrm{y}^{(\delta)}$ comes not only from the noisy map $\mathrm{F}^{(\nu)}$, but also from the discrepancy between the physical model of the RDF and the reality. The magnitude κ of this discrepancy is much larger than ν, such that the overall noise level $\delta := \kappa + \nu$ cannot be ignored and the solver of the inverse problem needs regularization.

In [YKWK-1973], we find an experimentally measured RDF of liquid argon `Ar` together with the physical setting of the system,

$$\begin{array}{rclll} \mathrm{T} & = & 85 & [\mathrm{K}] & \text{(temperature)}, \\ \rho & = & 0.02125 & [\text{Å}^{-3}] & \text{(density)}, \\ \mathrm{M} & = & 39.948 \cdot 10^{-3} \cdot N_A^{-1} & [\mathrm{kg}] & \text{(atom mass)}. \end{array}$$

For the sake of simplicity, we choose the unit mass $\mathrm{M}^{\mathrm{unit}} := \mathrm{M}$ and use the standard values of the Lennard-Jones parameters as the other units,

$$\begin{array}{rcccll} \varepsilon^{\mathrm{unit}} & := & \overline{\varepsilon} & = & 119.8 \cdot k_B & [\mathrm{J}], \\ \sigma^{\mathrm{unit}} & := & \overline{\sigma} & = & 3.405 & [\text{Å}]. \end{array}$$

Then, we can derive the setting of the system in the reduced units,

$$\mathrm{T} \approx 0.71, \quad \rho \approx 0.84, \quad \overline{\varepsilon} = 1, \quad \overline{\sigma} = 1,$$

what is very close to the triple point

$$(\rho^{\mathrm{t}}, \mathrm{T}^{\mathrm{t}}) \approx (0.85, 0.68)$$

of the three-dimensional Lennard-Jones fluid [HV-1969]. The measured data $\mathrm{y}^{(\delta)} \in \mathbb{Y}$ is given by $m = 400$ values on the grid with step $\Delta r = 0.02$ (see Figure 3.7). In the following,

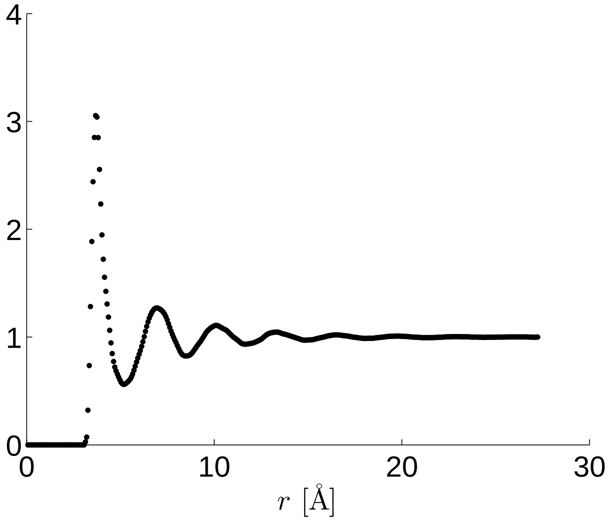

Figure 3.7: The RDF of the liquid argon.

we focus on the reconstructions of the interaction potentials and their parameters, while we consider the temperature and the density as fixed parameters of the system. We discuss the Lennard-Jones potential alongside more general models for interactions between argon atoms and devote a separate section to each model.

3.3.1 Lennard-Jones Model

In the Lennard-Jones model, the interaction potential is obtained via

$$\mathrm{H}_i^{\mathrm{LJ}}[\mathrm{x}] := 4\varepsilon\left(\left(\frac{\sigma}{r_i}\right)^{12} - \left(\frac{\sigma}{r_i}\right)^{6}\right), \quad 1 \le i \le m, \tag{3.24}$$

from $n = 2$ parameters, that is $\mathrm{x} = (\varepsilon, \sigma)^T$. According to the chosen reduced units, the exact parameter vector is $\overline{\mathrm{x}} = (1, 1)^T$. Since the preliminary tests in the previous section show that the Newton method can move the iterates close enough to the exact solution, it would suffice to test the Levenberg-Marquardt method in the vicinity of $\overline{\mathrm{x}}$. Therefore, we choose $\mathrm{x}^{(0)}$ randomly from the sphere

$$\|\overline{\mathrm{x}} - \mathrm{x}^{(0)}\|_{\mathbb{X}} = 0.015\|\overline{\mathrm{x}}\|_{\mathbb{X}}. \tag{3.25}$$

Further, we estimate the noise level in $\mathrm{F}^{(\nu)}[\mathrm{x}^{(0)}]$ and consider it as constant $\nu := 10^{-3}$ during the iteration. Since we assume that the noise level δ is given by experiment, but the above mentioned paper yields only an RMSD-estimate, we use $\overline{\mathrm{x}}$ once, in order to estimate the noise level with respect to our norm,

$$\delta := \|\mathrm{y}^{(\delta)} - \mathrm{F}^{(\nu)}[\overline{\mathrm{x}}]\|_{\mathbb{Y}} \approx 1.5 \cdot 10^{-2}.$$

Now we improve the initial vector via the Levenberg-Marquardt method (3.22) and the Morozov discrepancy principle with $\mu = 0.9$, until the residual norm $\|\mathrm{y}^{(\delta)} - \mathrm{F}^{(\nu)}[\mathrm{x}^{(k)}]\|_{\mathbb{Y}}$ crosses the level $\tau\delta$, $\tau := 1/\mu$. We run the reconstruction multiple times, in order to test different $\mathrm{x}^{(0)}$ and to determine the approximate solution by averaging the single results. In each run, both the residual norm and the parameter error decay monotonically (see Figure 3.8 for an example).

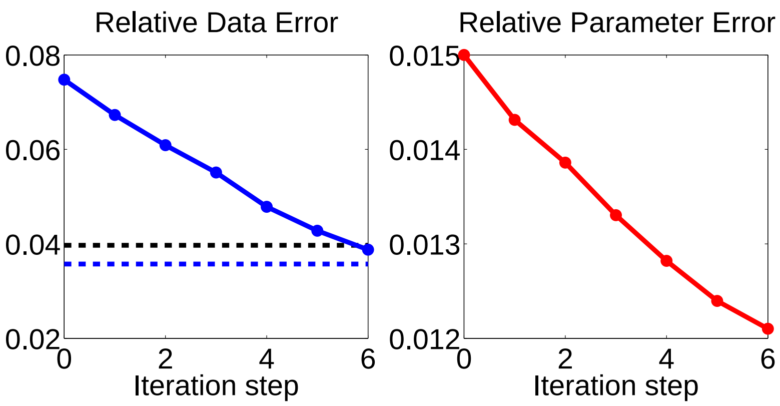

Figure 3.8: Relative errors of the iterates (red line) and of the data (blue line) for argon. The blue and black dashed lines represent the noise levels δ and $\tau\delta$, respectively.

In average, the iteration terminates after $k^{\text{stop}} = 7$ steps with a relative error near

$$(0.0156, 0.0017)^T.$$

We observe that the second parameter is almost perfectly reconstructed, while the first parameter is more or less ignored by the method (see the initial condition (3.25)). This imbalance could be expected – if we look at the condition numbers, we see that

$$\operatorname{cond}(\mathrm{DF}^{(\nu)}) \equiv \frac{\sigma_1}{\sigma_2} \gtrsim 25, \quad k \geq 1,$$

that is, in the vicinity of the exact solution, we can consider the stronger parameter (probably σ) to be at least 25 times stronger than the other one. The SVD of the derivative $\mathrm{DF}^{(\nu)} = \Psi\Sigma\Phi^*$ reveals that the parameters are perfectly uncorrelated, because

$$\Phi.\hat{}2 \approx \begin{pmatrix} & \blacksquare \\ \blacksquare & \end{pmatrix}, \quad k \geq 1,$$

and confirms that σ is a stronger parameter than ε. A similar statement can be derived in the following, statistical way. For each approximate solution $\mathrm{x}^{(k^{\text{stop}})}$, we can estimate

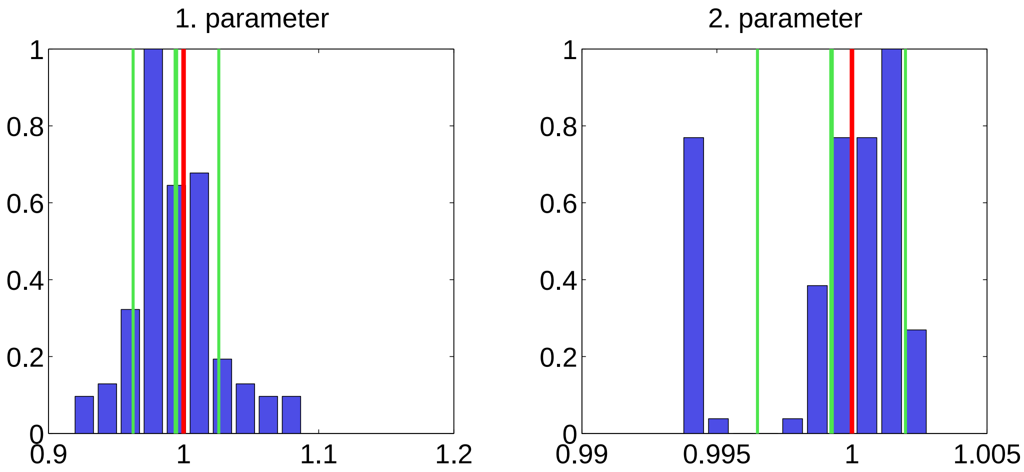

Figure 3.9: The blue bars represent the solution candidates. The red line designates the exact solution. The green lines represent the mean and the standard deviation.

the absolute errors by

$$\overline{\mathrm{x}} - \mathrm{x}^{(k^{\mathrm{stop}})} \approx \epsilon := \left(\mathrm{A}^{(k^{\mathrm{stop}} *2)} \mathrm{A}^{(k^{\mathrm{stop}})}\right)^{-1} \mathrm{A}^{(k^{\mathrm{stop}} *2)} (\mathrm{y}^{(\delta)} - \mathrm{F}^{(\nu)}[\mathrm{x}^{(k^{\mathrm{stop}})}]),$$

and consider all parameter vectors x from $\mathrm{x}^{(k^{\mathrm{stop}})} + [-|\epsilon_1|, |\epsilon_1|] \times [-|\epsilon_2|, |\epsilon_2|]$ as solution candidates. Averaging the latter over all $\mathrm{x}^{(k^{\mathrm{stop}})}$, we obtain

$$\mathbf{E}\,[\mathrm{x}] \approx (0.994, 0.999)^T$$

with standard deviations near $(0.0317, 0.0027)^T$. In other words, σ is about 12 times preciser than ε. Moreover, the average solution is quite close to the exact solution (see Figure 3.9).

3.3.2 Power Series Model

The Lennard-Jones potential does not properly describe the interactions between argon atoms (see, for instance, [HM-2006]). Moreover, while the attractive term $-\frac{1}{r^6}$ is crucial, the repulsive term $\frac{1}{r^{12}}$ is empirical and is sometimes replaced by an exponential repulsion (see Appendix A.2). Therefore, we want to consider a more detailed parameterization by the power series

$$\mathrm{H}_i^{\mathrm{Series}}[\mathrm{x}] := 4\mathrm{x}_1 \left(\sum_{p=7}^{24} \mathrm{x}_{p-2} \left(\frac{\mathrm{x}_2}{r_i}\right)^p - \left(\frac{\mathrm{x}_2}{r_i}\right)^6 + \mathrm{x}_4 \left(\frac{\mathrm{x}_2}{r_i}\right)^5 + \mathrm{x}_3 \left(\frac{\mathrm{x}_2}{r_i}\right)^4 \right), \qquad 1 \le i \le m,$$

with $n = 22$ parameters. Obviously, x_1 and x_2 have the same meaning as ε and σ in the Lennard-Jones model (3.24), respectively. The new model contains the terms of lower orders 5 and 4, which are admissible due to the property (3.3) of potentials, and further terms of higher and intermediate orders, which meet the property (3.2). The exact solution is unknown, thus we just consider the SVD near the guess

$$\mathrm{x}^{(0)} := (1, 1, 0, \ldots, 0)^T,$$

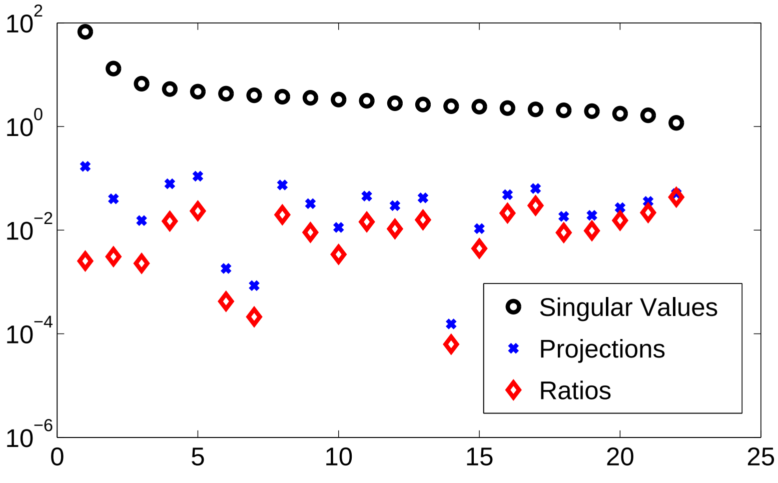

Figure 3.10: Picard plot for the power series model.

which corresponds to the exact solution for the Lennard-Jones model. The singular vectors

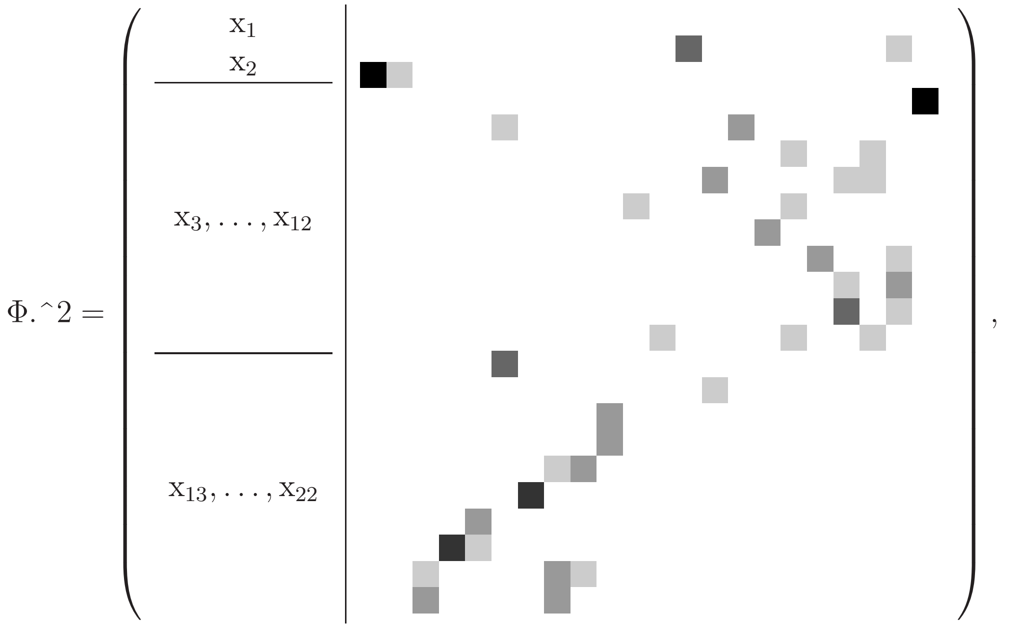

of the derivative $\mathrm{DF}[\mathrm{x}^{(0)}]$ show that the parameter x_2 is leading. The rest of the parameters can be approximately divided in two groups describing the high-order and the low-order terms. Similar to the Lennard-Jones model, they must describe the repulsion and the attraction of the fluid's particles, respectively. From this viewpoint, the parameter x_1, corresponding to the depth of the potential well (where repulsive and attractive terms are in balance) must indeed separate the two groups we mentioned above. Finally, from the Picard plot (Figure 3.10), we conclude that the inverse problem is not ill-posed, because the singular values decay slowly.

3.3.3 Spline Model

Here we pursue another approach where the discretized interaction potential $\mathrm{u} \in \mathbb{R}^m$ is represented directly by its $n = 77$ values u_j on the subgrid

$$s_j = 0.5 + 0.04(j-1), \quad 1 \leq j \leq n.$$

Let the parameterization $\mathrm{H}^{\mathrm{Spline}}$ yield the natural cubic spline interpolant u corresponding to the given parameters $\mathrm{x}_j := \mathrm{u}_j$. The resulting map $\mathrm{F}^{\mathrm{Spline}} := \mathrm{G} \circ \mathrm{H}^{\mathrm{Spline}}$ approximately covers also the Lennard-Jones case, such that we can use

$$\mathrm{x}_j^{(0)} := \mathrm{H}_j^{\mathrm{LJ}}[(1,1)]$$

as a guess. Even though the exact solution is unknown, we expect that the SVD reveals, at which grid points the Lennard-Jones-like potential $\mathrm{u}^{(0)} := \mathrm{H}^{\mathrm{Spline}}[\mathrm{x}^{(0)}]$ must be improved to describe the interactions between argon atoms better. As usual, we put the singular vectors of the derivative $\mathrm{DF}[\mathrm{x}^{(0)}]$ into the matrix

$\Phi.\hat{}2 =$

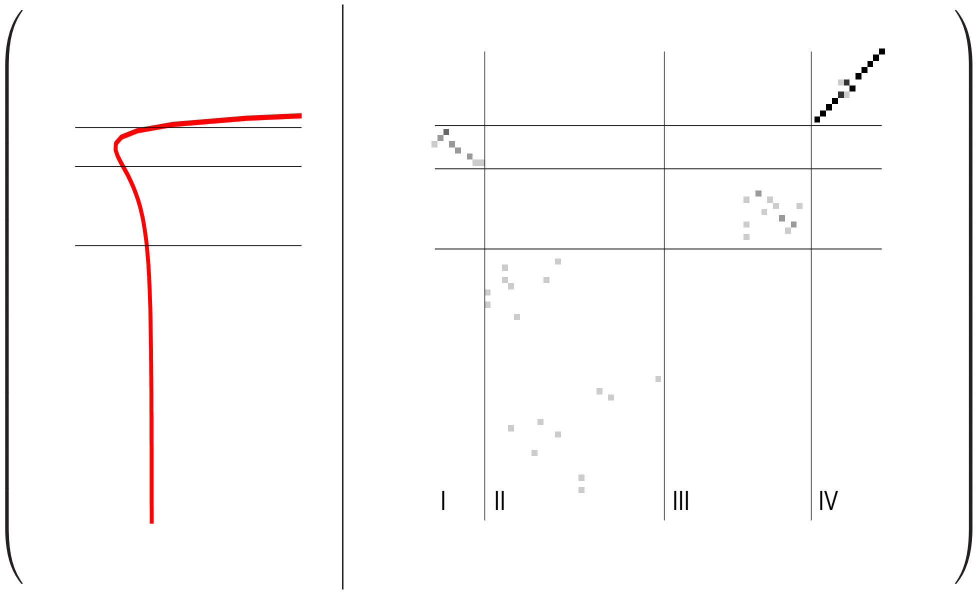

.

Since the parameters are nothing but the values of the potential function, we put the potential $\mathrm{u}^{(0)}$ sideways into the first column for the sake of a better view. We see immediately that in principle, the matrix can be separated in four parts arranged by the order of columns, where each part corresponds to a group of parameters with a clear physical interpretation:

(I. group) A couple of parameters with indices j between $s_j \approx \overline{\sigma}$ and $\mathrm{u}_j^{(0)} \approx -\overline{\varepsilon}$, describe the repulsive part of the potential well and are decisive in our generalized model. In this context, the Lennard-Jones model with parameters $(\overline{\varepsilon}, \overline{\sigma})$ is an example of appropriate model reduction.

(II. group) A handful of parameters describe the attractive tail $(1.5\overline{\sigma} \lesssim s_j < 3.5\overline{\sigma})$ of the potential and play a major role in the model. From this point of view, cutting off the potential in a computer simulation, typically at $s_j \approx 2.5\overline{\sigma}$, is a further model reduction and should be used with caution.

(III. group) A few parameters with indices, corresponding to the attractive part of the potential well, appear less important. This is interesting, because it suggests that a particular behaviour of the potential function between the minimum of the well and the tail does not really matter.

(IV. group) A handful of parameters, describing the repulsive part of the potential, are rather irrelevant. Of course, the repulsion keeps the particles of a fluid apart from each other, such that shorter distances are hardly reached and the potential is never evaluated on the corresponding interval $(0 < s_j \lesssim \overline{\sigma})$.

Moreover, the Picard plot (see Figure 3.11) shows that the inverse problem is not ill-posed for the first three parameter groups. In contrast, the singular values corresponding to the IV. group decay very fast, such that the discrete Picard criterion is not met. Considering the above analysis, a reconstruction of the core part of the potential from RDF is meaningless.

We conclude the discussion of models for liquid argon with an overall comparison of the two generalized models. Their singular value analysis shows that the Lennard-Jones

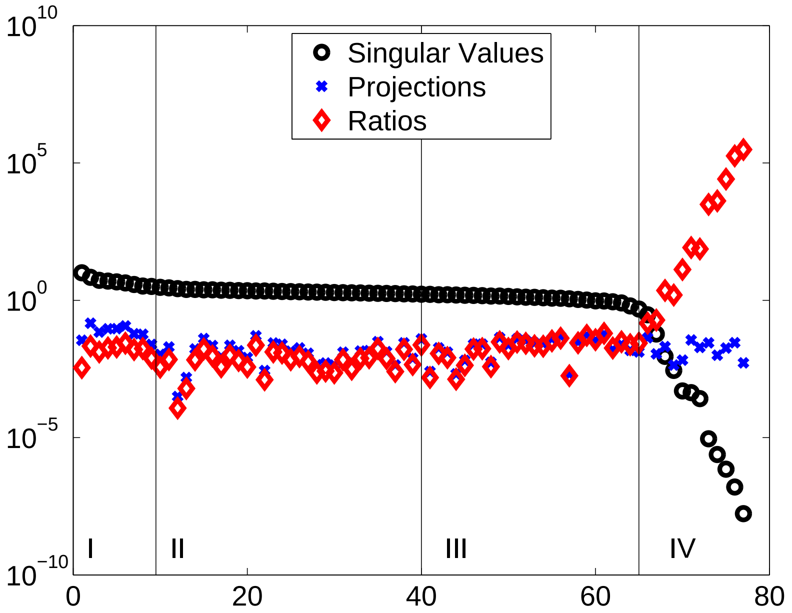

Figure 3.11: Picard plot for the spline model.

potential provides a quite simple, but good representation of the interaction potential. The spline model is better coupled to the desired object – the potential function on a grid – and appears to be more informative. In turn, a parametric approach of the power series model is better conditioned than a total discretization of the potential. In order to derive a better generalized model, one has to join the advantages of the single models by using the similarities in their characterizations. Indeed, according to the power series model, the high-order repulsion terms play an important role in the modeling of interactions. The spline model points that it is due to their contribution to the potential well and classifies the actual values of the potential in the core part as irrelevant. Further, each model indicates that the attractive tail of the potential does not really need a detailed parameterization. In summary, a better model should use only few parameters to fit the exact shape of the potential well and obtain both the core and the tail part by extrapolation.

3.4 Experimental Data for Liquid Nitrogen

In [NJH-1980], the RDF of liquid nitrogen $\mathtt{N}_2$ is measured by an experiment with settings near to the triple point,

$$\begin{array}{lcll} \mathrm{T} & = & 65 & [\mathrm{K}] \quad \text{(temperature)}, \\ \rho & = & 0.01851 & [\mathring{\mathrm{A}}^{-3}] \quad \text{(density)}, \\ \mathrm{M} & = & 2m_{\mathtt{N}} = 28.014 \cdot 10^{-3} \cdot N_A^{-1} & [\mathrm{kg}] \quad \text{(molecule mass)}. \end{array}$$

Further literature provides the standard values of the bonded and nonbonded interaction parameters,

$$\begin{array}{lclll} \overline{\varepsilon}_{\mathtt{N},\mathtt{N}} & = & 37.3 \cdot k_B & [\mathrm{J}], & \\ \overline{\sigma}_{\mathtt{N},\mathtt{N}} & = & 3.310 & [\mathring{\mathrm{A}}] & [\text{CP-1975}], \\ \overline{\ell}_{\mathtt{N},\mathtt{N}} & \approx & 1.090 & [\mathring{\mathrm{A}}] & [\text{BLQ-1973}], \\ \overline{\mathrm{k}}_{\mathtt{N},\mathtt{N}} & \approx & 37.3 \cdot \overline{\ell}_{\mathtt{N},\mathtt{N}}^{-5.71} & [\mathrm{mdyn} \cdot \mathring{\mathrm{A}}^{-1}] & [\text{TLJOT-1969}]. \end{array}$$

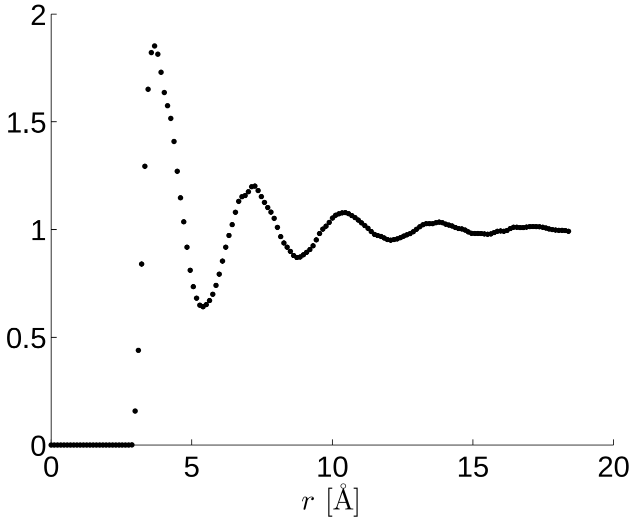

Figure 3.12: The RDF of the liquid nitrogen.

We choose $\varepsilon^{\text{unit}} := \overline{\varepsilon}_{\mathtt{N,N}}$, $\sigma^{\text{unit}} := \overline{\sigma}_{\mathtt{N,N}}$, and define the unit mass as the mass of a nitrogen molecule (two nitrogen atoms),

$$\mathrm{M}^{\text{unit}} := 2m_{\mathtt{N}} = 28.014 \cdot 10^{-3} \cdot N_A^{-1} \quad [\text{kg}].$$

That is, in the reduced units, we have

$$\mathrm{T} \approx 1.74, \quad \rho \approx 0.67, \quad \overline{\varepsilon}_{\mathtt{N,N}} = 1, \quad \overline{\sigma}_{\mathtt{N,N}} = 1, \quad \overline{\ell}_{\mathtt{N,N}} \approx 0.33, \quad \overline{k}_{\mathtt{N,N}} \approx 5 \cdot 10^5.$$

The measured data $\mathrm{y}^{(\delta)} \in \mathbb{Y}$ is given by $m = 160$ values on the grid with step $\Delta r \approx 0.035$ (see Figure 3.12).

The above parameters provide a model of the nitrogen molecule, where the Lennard-Jones potential

$$u_{\mathtt{N,N}}(r) = 4\overline{\varepsilon}_{\mathtt{N,N}} \left(\left(\frac{\overline{\sigma}_{\mathtt{N,N}}}{r} \right)^{12} - \left(\frac{\overline{\sigma}_{\mathtt{N,N}}}{r} \right)^{6} \right)$$

describes the nonbonded interactions, and the bonded atoms interact via harmonic potential

$$v_{\mathtt{N,N}}(\ell) = \frac{1}{2} \overline{\mathrm{k}}_{\mathtt{N,N}} (\ell - \overline{\ell}_{\mathtt{N,N}})^2.$$

We consider the weak parameter $\mathrm{k}_{\mathtt{N,N}}$ as fixed and work with $n = 3$ parameters, that is, $\mathrm{x} = (\varepsilon_{\mathtt{N,N}}, \sigma_{\mathtt{N,N}}, \ell_{\mathtt{N,N}})^T$. Exactly as for the liquid argon, we estimate the noise levels $\delta \approx 2.4 \cdot 10^{-2}$ and ν, where the latter can be regarded as constant, $\nu := 10^{-3}$. We choose a start vector $\mathrm{x}^{(0)}$ randomly from the sphere

$$\|\overline{\mathrm{x}} - \mathrm{x}^{(0)}\|_{\mathbb{X}} = 0.035 \|\overline{\mathrm{x}}\|_{\mathbb{X}} \tag{3.26}$$

and update it iteratively via Levenberg-Marquardt method with $\mu = 0.9$. We test different $\mathrm{x}^{(0)}$ and determine the approximate solution by averaging the single results. Figure 3.13 shows an example of the monotone decay of the relative errors, as we observe it in each test.

In average, the iteration terminates after $k^{\text{stop}} = 5$ steps with a relative error near

$$(0.032, 0.007, 0.073)^T. \tag{3.27}$$

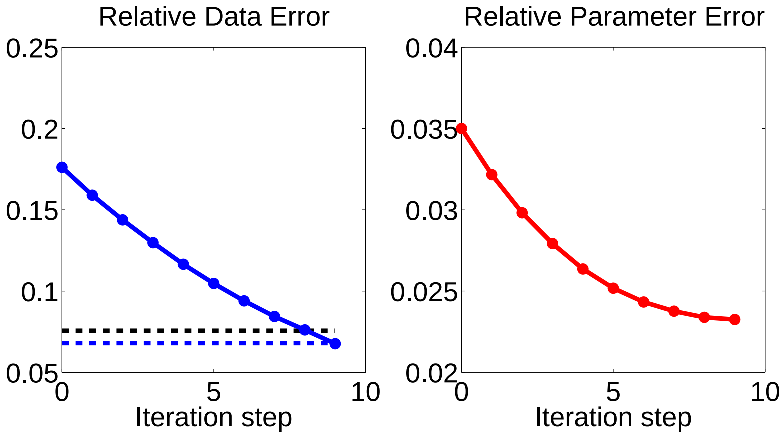

Figure 3.13: Relative errors of the iterates (red line) and of the data (blue line) for nitrogen. The blue and black dashed lines represent the noise levels δ and $\tau\delta$, respectively.

We see that the reconstruction of the second parameter is nearly perfect. In contrast, the first and the third parameters are in principle ignored by the method – the initial guess has a comparable quality due to the initial condition (3.26). The singular vectors

$$\Phi.\hat{}2 \approx \begin{pmatrix} & & \blacksquare \\ \blacksquare & & \\ & \blacksquare & \end{pmatrix}, \quad k \geq 1,$$

of the derivative $\mathrm{DF}^{(\nu)}$ reveal that the parameters are uncorrelated. Further, a look at the condition numbers shows that

$$\mathrm{cond}(\mathrm{DF}^{(\nu)}) \equiv \frac{\sigma_1}{\sigma_3} \gtrsim 20, \quad k \geq 1,$$

that is, in the vicinity of the exact solution, σ is at least 20 times stronger than ε. Again, we derive a similar statement in the statistical way, by estimating the absolute errors ϵ and by averaging all solution candidates

$$\mathrm{x} \in \mathrm{x}^{(k^{\mathrm{stop}})} + \bigtimes_{j=1}^{n} [-|\epsilon_j|, |\epsilon_j|]$$

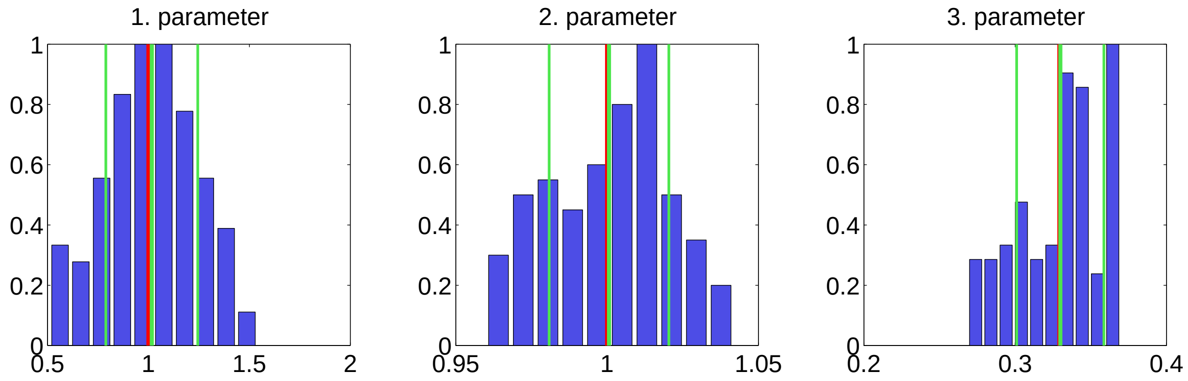

Figure 3.14: The blue bars represent the solution candidates. The red line designates the exact solution. The green lines represent the mean and the standard deviation.

over all approximate solutions $\mathrm{x}^{(k^{\text{stop}})}$. The average solution is given by

$$\mathbf{E}[\mathrm{x}] \approx (1.017, 1.00065, 0.3298)^T$$

with standard deviations near $(0.228, 0.020, 0.029)^T$. We see that σ is about 11 times preciser than ε. Moreover, we repeatedly observe that the quality of the solution rises through averaging significantly, such that even the weak parameters are very close to the exact solution (see Figure 3.14). Especially, the relative error of the average solution is much smaller than the average relative error (3.27).

We note that the resulting approximate solution, even for the good parameter $\sigma_{\mathtt{N},\mathtt{N}}$, is not as good as for the argon parameter σ. We believe that the reason is the particular physical setting of the system (near the triple point), such that it becomes difficult to simulate the "true" nitrogen (large noise level δ). However, we do not intend to present the "best" parameter vector. We rather look forward a regularization method, which is able to yield a better parameter vector, everytime the measurements (in experiment or simulation) become more precise and we deal with a lower the noise level δ.

3.5 Summary

In the above tests, we observe a good correspondence between reconstructions from simulated and experimental data. The most effects are common for the two- and three-dimensional, well- and ill-posed formulations of the inverse problem. For instance, the singular value analysis of the models reaches a level, where a physical interpretation of the results takes place. In a simple fluid, we see that weak parameters (describing energies, like temperature, energy of bonded/nonbonded interactions) can be recognized on the smallest singular values. In contrast, the parameters describing the lengths, that is, length of the bond, atom size or density, correspond to the largest singular values and can be called strong. In a molecular fluid, we observe that including too many weak parameters into the model severely increases the condition number of the problem, such that the potentially high precision of the strong parameters can be lost. That is, we are able to answer the Question II (see p. 11), because the condition number, or the singular values, can be used as a measure of the loss of the microscopic details. This loss can be lowered by excluding some weak parameters from the model or minimized by reducing the model to the minimal set of the most relevant parameters.

It is important to see that the Levenberg-Marquardt method converges in many practical cases and yields meaningful approximate solutions, although our approach is purely mathematical. An even more important result of this chapter is that the theory of inverse problems is applicable to the particular problem. We want to use this theory in the following, in order to analyze some established inversion methods derived from a deep understanding of the physical background of the problem and properties of the data. We hope this insight helps us to improve the Levenberg-Marquardt method, and in particular, to answer the question:

Question I.3: Is there a systematic way to derive an appropriate initial guess for the inversion method?

Chapter 4

Physical Approximations

In the previous chapters, we worked with the abstract map $G : U \to Y$ yielding an RDF $y = G[u]$ for a given potential u. Even though we motivated the models for u and y almost purely mathematically, they were enough for the application of our inversion method. For this reason, we did not provide a concrete expression for the RDF by arguing that G is not suitable for a theoretical convergence analysis of the method. In this chapter, we look deeper into the physical background of the map in order to develop a reasonable approximate description, which could be easier to analyze. Nonetheless, we do not intend to bore the reader with all physics related with the particular inverse problem. Therefore, we mainly pay attention to simple heuristics, which can be briefly sketched and understood on intuitive level. Their details and backgrounds can be looked up in Appendix A.

4.1 Insight into the Physics

4.1.1 Radial Distribution Function

We remind that an RDF y and an interaction potential u are functions of the distance r between two atoms in the system of N atoms with coordinates $(\vec{r}^{(i)})_{i=1}^{N} \subset \mathbb{R}^d$. The value $u(r)$ represents the potential energy of the atom pair,

$$E(\vec{r}^{(i)}, \vec{r}^{(j)}) = u(|\vec{r}^{(i)} - \vec{r}^{(j)}|).$$

The potential energy of the whole system is the sum of these values over all atom pairs,

$$E(\vec{r}_1, \dots, \vec{r}_N) = \sum_{i=1}^{N} \sum_{j>i}^{N} E(\vec{r}^{(i)}, \vec{r}^{(j)}) = \sum_{i=1}^{N} \sum_{j>i}^{N} u(|\vec{r}^{(i)} - \vec{r}^{(j)}|). \tag{4.1}$$

In the NVT-ensemble, any state of the system is given by atom coordinates distributed according to the probability density

$$\mathcal{P}(\vec{r}^{(1)}, \dots, \vec{r}^{(N)}) = \frac{1}{Z(N)} \exp\left(-\frac{E(\vec{r}^{(1)}, \dots, \vec{r}^{(N)})}{k_B T}\right), \tag{4.2}$$

where $Z(N)$ is a normalization constant. That is, integration of $\mathcal{P}$ over a region in $\mathbb{R}^{dN}$ gives us the probability to find N atoms in this region. The RDF y represents the part of this probability density concerning the atom pairs, where the rest of the system is integrated out. One of the atoms can be considered as fixed $\vec{r}^{(1)} := 0$ (a reference atom) and another one is picked out randomly from the rest of the system, such that the distance equals r. Without loss of generality, we can choose $\vec{r}^{(2)} := r\vec{e}^{(1)}$. For a fixed number density ρ, the value

$$y(r) = G[u](r) = \frac{N(N-1)}{\rho^2} \int \mathcal{P}(0, r\vec{e}^{(1)}, \vec{r}^{(3)}, \ldots, \vec{r}^{(N)}) d\vec{r}^{(3)} \ldots d\vec{r}^{(N)} \tag{4.3}$$

corresponds in principle to the number of atoms, which can be found at the distance r from the reference atom. This interpretation is in full accordance with the intuitive definition of the RDF via counting neighbour atoms in Chapter 1.

Inserting the definitions of the distribution (4.2) and energy (4.1) in (4.3) and using the properties of the exponential function, we find out that RDF is a combination of products and convolutions,

$$\begin{aligned} y[N](r) &= C\gamma(r) \int \prod_{i=1}^{N-2} \gamma(|\vec{r}^{(i+2)}|)\gamma(|\vec{r}^{(i+2)} - r\vec{e}^{(1)}|) \\ &\times \prod_{j>i}^{N-2} \gamma(|\vec{r}^{(i+2)} - \vec{r}^{(j+2)}|) d(\vec{r}^{(3)}, \ldots, \vec{r}^{(N)}), \end{aligned} \tag{4.4}$$

where only the function

$$\gamma(r) := \exp\left(-\frac{E(0, r\vec{e}^{(1)})}{k_B T}\right) = \exp\left(-\frac{u(r)}{k_B T}\right) \tag{4.5}$$

participates. The scaling constant C ensures

$$\lim_{r\to\infty} y[N](r) = 1,$$

which is an indispensable part of the RDF property (SY2) in our definition (3.6). Comparing (4.5) with the expression for $\mathcal{P}$, we conclude that γ is also a kind of distribution function reduced to the pairs of atoms. We purposely supplied the function y in (4.4) with the parameter N – it is easily seen that

$$y[2](r) = \gamma(r) \tag{4.6}$$

and for this reason, we call γ the *two-atom RDF* in the following. In the coarse-graining papers, γ is called exclusively the *low-density limit* of the RDF, because

$$\lim_{\rho\to 0} y(r) = \gamma(r) \tag{4.7}$$

(see Theorem P7 in Appendix A). In combination with (4.6), this property suggests that at low densities, two atoms can represent all pairs. However, we prefer to consider (4.7) as an extra, escorting the other properties we derive in this chapter for the two-atom RDF.

4.1.2 Inversion Methods

The expression in (4.5), which serves us as a definition of the two-atom RDF, is used in the actually best inversion methods for the particular problem, the Iterative Boltzmann Inversion (IBI) and the Inverse Monte Carlo (IMC). They are extensively applied in the coarse graining for last 25 years. In this section, we summarize the observations collected by other scientists during their application. At the same time, we begin with their mathematical interpretation, such that we can use the theory of inverse problems for analysis.

The *Iterative Boltzmann Inversion* (IBI) is an iterative method, broadly used to obtain an interaction potential from the given RDF without any parameterization (see, for example, [RPM-2003]). In our terms, the method is designed to solve the discretized problem (3.14), namely,

$$\overline{\mathrm{y}} = \mathrm{G}[\overline{\mathrm{u}}],$$

via the fixed-point iteration

$$\begin{aligned} \mathrm{u}_i^{(0)} &:= -k_B T \ln \overline{\mathrm{y}}_i, && (4.8)\\ \mathrm{h}_i^{(k)} &:= k_B T \ln \frac{\mathrm{G}_i[\mathrm{u}^{(k)}]}{\overline{\mathrm{y}}_i}, && (4.9)\\ \mathrm{u}_i^{(k+1)} &:= \mathrm{u}_i^{(k)} + \mathrm{h}_i^{(k)}, \quad k \geq 0, \quad 1 \leq i \leq m. && (4.10) \end{aligned}$$

The initial guess $\mathrm{u}^{(0)}$ has a very intuitive and physically meaningful motivation in view of the two-atom RDF (4.5). Indeed, for fluids with a very low density, an RDF $\mathrm{y} = \mathrm{G}[\mathrm{u}]$ is well approximated by

$$\gamma = \exp\left(-\frac{\mathrm{u}}{k_B T}\right),$$

therefore, for the given RDF $\overline{\mathrm{y}}$, one can approximate the potential via inversion of the exponential function, as it is done in (4.8). The resulting potential $\mathrm{u}^{(0)}$ is referred to as the *potential of mean force*. The quality of this approximation may be questioned for fluids with high density, but it is used only for initialization of the method. Not to mention that the potential of mean force is more realistic than, for example, $\mathrm{u}^{(0)} := 0$, which corresponds to absence of any interactions in the fluid. A more appropriate model of interactions is easier to refine – one updates the initial guess iteratively, until the update $\mathrm{h}^{(k)}$ vanishes, which is equivalent to $\mathrm{G}[\mathrm{u}^{(k)}] = \overline{\mathrm{y}}$. According to the Henderson theorem, the last iterate is the sought interaction potential.

The clear advantage of the IBI is the speed – the method needs one evaluation of the map G per step, while a Newton-type method would need $m = \dim(\mathbb{U})$ partial derivatives of the map, which could be very time consuming. However, one should not be deceived by the seemingly straightforward appearance of the method, because the practical implementation of the IBI requires a couple of improvements [RJLKA-2009]. Particularly, one should forbid the division by zero in the expression for the update – component $\mathrm{h}_i^{(k)}$, corresponding to $\overline{\mathrm{y}}_i = 0$, is usually set to zero. In order to stabilize the method, the iterates $\mathrm{u}^{(k)}$ should be smoothed and extrapolated. Further stabilization can be reached through multiplication of the update $\mathrm{h}^{(k)}$ with a damping prefactor $\lambda \in (0,1)$. Apparently, there is also an attemt to prevent the semiconvergence – the method terminates in the k-th step, if

$$\left(\int_{r_a}^{r_b} \exp(-r)(\overline{y} - G[u^{(k)}](r))^2 dr \approx\right) \quad \Delta r \sum_{i=a}^{b} \exp(-r_i)(\overline{\mathrm{y}}_i - \mathrm{G}_i[\mathrm{u}^{(k)}])^2 < \epsilon \qquad (4.11)$$

for some fixed a, b and ϵ [RMM-2002]. The term on left hand side represents a norm on the space $\mathbb{Y}$, and the exponential function plays the role of a weight function, which emphasizes the higher importance of the data at small distances. It is interesting that we derived the same weight function w_Y in (3.12) from a completely different and purely mathematical viewpoint.

In [Soper-1996], one can find reasons why the IBI should converge (in the absence of the noise), provided the existence of a solution. The reasoning follows a rather physical argumentation and avoids the functional space notation by referring instead to the observed behaviour of the method in practice. There is no rigorous convergence proof, at least not for noisy data, and indeed, the iteration has sometimes convergence problems. For instance, this is the case, if the method is applied to molecular fluids, where one computes the mixed potential $\mathrm{u}_{\mathsf{a},\mathsf{b}}$ just from the mixed RDF $\mathrm{y}_{\mathsf{a},\mathsf{b}}$, without respecting the evident correlation with other RDFs, $\mathrm{y}_{\mathsf{a},\mathsf{a}}$ and $\mathrm{y}_{\mathsf{b},\mathsf{b}}$ [RJLKA-2009]. Further, in the presence of the noise, one can question whether the actual stabilization of the method is a regularization in the sense of Chapter 2. A regularization affects the update rather implicitly by modification of the inversion than by direct damping. Finally, it is not clear how to choose the damping prefactor or how the stopping rule (4.11) is coupled to the noise in the data.

The *Inverse Monte Carlo* (IMC) is another iterative method of the Newton-type, using the derivatives of the map G to update the iterates. Therefore, the method is slower, if compared with the IBI, but it is also more precise and can even work with parameterized interaction potentials. For convenience, we present here the description without the parameterization, as it can be found in the original paper [LL-1995]. In the IMC, one modifies the RDFs $y \in Y$ via

$$y \mapsto J[y] := (r \mapsto Cy(r)r^2)$$

and solves the corresponding discrete inverse problem

$$\overline{\mathrm{s}} = \mathrm{K}[\overline{\mathrm{u}}], \tag{4.12}$$

where

$$\begin{aligned} \overline{\mathrm{s}} &:= \mathrm{J}[\overline{\mathrm{y}}], \\ \mathrm{K} &:= \mathrm{J} \circ \mathrm{G} \end{aligned}$$

and $C > 0$ is a certain constant. In accordance with the IBI, the method can be initialized via approximation

$$\mathrm{u}_i^{(0)} := -k_B T \ln \overline{\mathrm{y}} = -k_B T \ln \frac{\overline{\mathrm{s}}_i}{C r_i^2}, \quad 1 \le i \le m.$$

Eventually, some iterations of the IBI are applied on $\mathrm{u}^{(0)}$, in order to get a better initial guess. Then, the IMC updates such a guess via

$$\mathrm{u}^{(k+1)} := \mathrm{u}^{(k)} + \mathrm{h}^{(k)},$$

where the update $\mathrm{h}^{(k)}$ is a solution of the linear system

$$\overline{\mathrm{s}} - \mathrm{K}[\mathrm{u}^{(k)}] = \mathrm{A}^{(k)}\mathrm{h}^{(k)}. \tag{4.13}$$

The computation of the system matrix $\mathrm{A}^{(k)} \in \mathbb{R}^{m \times m}$ is the key feature of the IMC. The modified target allows one to simplify analytically the derivative of $K := J \circ G$ (see Theorem P6 in Appendix A.3), such that one can develope a computational procedure for $\mathrm{A}^{(k)}$, similar to that for sampling of the RDF.

The decisive advantage of the IMC is the rigorosity. First, the system matrix $\mathrm{A}^{(k)}$ is a pure discretization of the derivative $DK[u^{(k)}]$. In contrast to the Levenberg-Marquardt method, there is no need to approximate DK via finite differences. Second, the linear system (4.13) enables the method to regard all data correlations, in contrast to the IBI. The procedure for computation of the system matrix is implemented in the software package VOTCA [RJLKA-2009], but the developers confess that it requires much more snapshots of the trajectory. That is, much longer computer simulations are needed to reach an accuracy comparable with that of the IBI update. Despite the rigorous derivation of the updates, the convergence of the IMC remains an issue. In practice, the method experiences convergence problems, if the initial guess is too rough [MFKV-2007].

The modified map $K = J \circ G$ has the same problem as the original map G – the resulting system matrix in (4.13) is ill-conditioned due to some almost vanishing columns, what leads to instability of the method. Usually, such stability issues are solved ad hoc via removing the problematic columns and/or smoothing/damping of the update $\mathrm{h}^{(k)}$ [RJLKA-2009]. In [MFKV-2007], however, the authors prefer a Tikhonov regularization approach, where the corresponding minimization problem takes the form

$$\min_{\mathrm{h}\in\mathbb{X}} \|\bar{\mathrm{s}} - \mathrm{K}[\mathrm{u}^{(k)}] - \mathrm{A}^{(k)}\mathrm{h}^{(k)}\|_{\mathbb{S}}^2 + \lambda^2\|\mathrm{W}\mathrm{h}^{(k)}\|_{\mathbb{X}}^2,$$

such that the penalty term is controlled by the parameter $\lambda > 0$. Here, $\|\cdot\|_{\mathbb{S}}$ denotes a suitable norm for some (not further specified) space $\mathbb{S} \supseteq \operatorname{ran}(\mathrm{K})$ of discretized and modified RDFs. The matrix $\mathrm{W} \in \mathbb{R}^{m\times m}$ has the diagonal shape or represents the second derivative operator in order to force the update to be smooth. However, a systematic choice strategy for λ and W is not provided, by arguing that trial and error would suffice. Later, in [MBVDK-2009], the authors comment that the SVD of the matrix $\mathrm{A}^{(k)}$ allows one to identify, which changes in the potential lead to negligible changes in the data. Seemingly, they make decisions solely on the size of the singular values without taking a Picard plot into account.

We conclude this review of the physically motivated inversion methods with a short summary of their features. The most pleasing feature of the two methods is their successful applicability in practice. Further, we see that these are iterative methods for solution of the particular nonlinear inverse problem and they have one common aspect with regard to the Question I.3 (see p. 61). Namely, the actually existing methods posess a systematic way to derive an appropriate initial guess. In other aspects, the methods are completely different. The design of the IMC drags our attention to the procedure for computation of the derivative.

Question I.4: How much time does a method spend to compute the derivative?

However, even if the IMC obtains the derivative faster than the usual approach over finite differences, the IBI do not need any differentiation at all. This feature makes the IBI to the fastest actually known solution method for the particular inverse problem. On the other hand, the simple design of the IBI allows only ad hoc stabilization by damping the updates, what is a weak point of the method with regard to the Question I.1 (see p. 33). In contrast, the IMC, as a Newton-type method, can be easily regularized and extended with some well-studied parameter choice strategy. Finally, the IBI appears to be suitable only for simple fluids, what poses an additional criterion for a serious inversion method, which should also be applicable to realistic fluids.

Question I.5: Can we extend the application area of a method to molecular fluids?

These experiences motivate us to investigate the two new questions in the following.

4.2 Approximation of the RDF

4.2.1 Role in the Iterative Boltzmann Inversion

At the first sight, the Iterative Boltzmann Inversion (IBI) is not a Newton-type method, because it does not need any differentiation, but we still can discuss it as an iterative method. Using

$$\ln \frac{\mathrm{G}_i[\mathrm{u}^{(k)}]}{\overline{\mathrm{y}}_i} = \ln \mathrm{G}_i[\mathrm{u}^{(k)}] - \ln \overline{\mathrm{y}}_i$$

and the physical fact G[0] = 1 (see Appendix A.2), we can see the method (4.8)-(4.10) as the fixed-point iteration

$$\mathrm{u}^{(k+1)} := f[\mathrm{u}^{(k)}], \quad k \geq -1,$$

with the start vector $\mathrm{u}^{(-1)} := 0$ and the iteration function

$$f[\mathrm{u}] := (\mathrm{u}_i + k_B T \ln \mathrm{G}_i[\mathrm{u}] - k_B T \ln \overline{\mathrm{y}}_i)_{i=1}^{m}.$$

In order to analyze the convergence of the method, as it is convenient in the applied mathematics, we consider the derivative

$$(Df[\mathrm{u}])_{i,j} = \frac{\partial f_i[\mathrm{u}]}{\partial \mathrm{u}_j} \quad = \quad \delta_{i,j} + k_B T \frac{1}{\mathrm{G}_i[\mathrm{u}]} \frac{\partial \mathrm{G}_i[\mathrm{u}]}{\partial \mathrm{u}_j},$$

and notice that it does not depend on the given RDF $\overline{\mathrm{y}}$. The IBI never determines the "direction" towards the target RDF (no need for derivative) and it is surprising, because a method should actually "know" where to go. It appears that only the iteration function is responsible for convergence. Indeed, the function

$$f[\mathrm{u}] = \mathrm{u} + \Gamma^{-1}[\overline{\mathrm{y}}] - \Gamma^{-1}[\mathrm{G}[\mathrm{u}]] \tag{4.14}$$

is based on the map

$$\Gamma[\mathrm{u}] := \exp\left(-\frac{\mathrm{u}}{k_B T}\right), \tag{4.15}$$

which serves originally as a source of the initial guess. Also [Soper-1996] mentions this fact. In other words, the built-in approximation of the RDF G[u] by the two-atom RDF Γ[u] is the workhorse of the IBI and might be also used in a more general context. For instance, we can more easily study the properties of G by considering Γ, which is a much simpler link between potentials from U and RDFs from Y.

Theorem A3:
For any $\alpha_0 \geq 0$ and $\Delta\alpha_0 \geq 0$, the map $\Gamma : S_U(\alpha_0, \Delta\alpha_0) \to S_Y(\alpha_0, \Delta\alpha_0)$ is bijective.

Proof: It is obvious that Γ is injective, therefore it remains to show that $\Gamma(S_U(\alpha_0, \Delta\alpha_0)) = S_Y(\alpha_0, \Delta\alpha_0)$. Indeed, for any potential $u \in S_U(\alpha_0, \Delta\alpha_0)$, the corresponding two-atom RDF $\gamma := \Gamma[u]$ is in $S_Y(\alpha_0, \Delta\alpha_0)$:

(SY1) Due to the property (SU1) of u, there exist $A_0^{\inf}, A_0^{\sup} \in (0, \infty)$ and $r^{\mathrm{core}} \in (0, \infty)$, such that

$$A_0^{\inf} r^{-\alpha_0 + \Delta\alpha_0} \leq u(r) \leq A_0^{\sup} r^{-\alpha_0 - \Delta\alpha_0}, \quad \forall r \in (0, r^{\mathrm{core}}].$$

Since $a \mapsto \exp(-a)$ is a monotonically falling function, we obtain

$$\exp\left(-\underbrace{\frac{1}{k_B T}A_0^{\sup}}_{=:B_0^{\inf}} r^{-\alpha_0-\Delta\alpha_0}\right) \leq \gamma(r) \leq \exp\left(-\underbrace{\frac{1}{k_B T}A_0^{\inf}}_{=:B_0^{\sup}} r^{-\alpha_0+\Delta\alpha_0}\right).$$

(SY2) Due to the property (SU2) of u, there exist $A_\infty \in (0,\infty)$, $\alpha_\infty \in (d,\infty)$ and $r^{\mathrm{cut}} \in (r^{\mathrm{core}},\infty)$, such that

$$|u(r)| \leq A_\infty r^{-\alpha_\infty}, \quad \forall r \in (r^{\mathrm{cut}},\infty).$$

Since $|\exp(a)-1| \leq C|a|$ for small a and a constant $C \in (0,\infty)$, we have then

$$|\gamma(r)-1| \leq \underbrace{\frac{1}{k_B T}A_\infty C}_{=:B_\infty} r^{-\overbrace{\alpha_\infty}^{=:\beta_\infty}}, \quad \forall r \in (r^{\mathrm{cut}},\infty).$$

(SY3) Due to the property (SU3) of u, there exists a unique $r^{\min} \in (r^{\mathrm{core}}, r^{\mathrm{cut}}]$, such that

$$-\infty < u(r^{\min}) = \min_{r\in(0,\infty)} u(r) < 0.$$

We set $r^{\mathrm{peak}} := r^{\min}$. Then,

$$\gamma(r^{\mathrm{peak}}) = \exp\left(-\frac{1}{k_B T}u(r^{\min})\right) > e^0 = 1,$$

and the monotonicity of the exponential function yields

$$\begin{aligned}\max_{r\in(0,\infty)} \gamma(r) &= \exp\left(-\frac{1}{k_B T}\min_{r\in(0,\infty)} u(r)\right)\\ &= \exp\left(-\frac{1}{k_B T}u(r^{\min})\right)\\ &= \gamma(r^{\mathrm{peak}}).\end{aligned}$$

Conversely, for any RDF $y \in S_Y(\alpha_0,\Delta\alpha_0)$, the corresponding potential of mean force

$$v := \Gamma^{-1}[y] = -k_B T \ln(y)$$

is in $S_U(\alpha_0,\Delta\alpha_0)$:

(SU1) Due to the property (SY1) of y, there exist $B_0^{\inf}, B_0^{\sup} \in (0,\infty)$ and $r^{\mathrm{core}} \in (0,\infty)$, such that

$$\exp\left(-B_0^{\inf} r^{-\alpha_0-\Delta\alpha_0}\right) \leq y(r) \leq \exp\left(-B_0^{\sup} r^{-\alpha_0+\Delta\alpha_0}\right), \quad \forall r \in (0, r^{\mathrm{core}}].$$

Since $b \mapsto -\ln(b)$ is a monotonically falling function, we obtain

$$\underbrace{k_B T B_0^{\sup}}_{=:A_0^{\inf}} r^{-\alpha_0+\Delta\alpha_0} \leq v(r) \leq \underbrace{k_B T B_0^{\inf}}_{=:A_0^{\sup}} r^{-\alpha_0-\Delta\alpha_0}, \quad \forall r \in (0, r^{\mathrm{core}}].$$

(SU2) Due to the property (SY2) of y, there exist $B_\infty \in (0,\infty)$, $\beta_\infty \in (d,\infty)$ and $r^{\text{cut}} \in (r^{\text{core}},\infty)$, such that

$$|y(r) - 1| \le B_\infty r^{-\beta_\infty}, \quad \forall r \in (r^{\text{cut}},\infty).$$

Since $|\ln(1+b)| \le C|b|$ for small b and a constant $0 < C < \infty$, we have then

$$|v(r)| \le \underbrace{k_B T B_\infty C}_{=:A_\infty} r^{-\overbrace{\beta_\infty}^{=:\alpha_\infty}}, \quad \forall r \in (r^{\text{cut}},\infty).$$

(SU3) Due to the property (SY3) of y, there exists a unique $r^{\text{peak}} \in (r^{\text{core}}, r^{\text{cut}}]$, such that

$$1 < y(r^{\text{peak}}) = \max_{r\in(0,\infty)} y(r) < \infty.$$

We set $r^{\min} := r^{\text{peak}}$. Then, the monotonicity of the logarithm yields

$$v(r^{\min}) = -k_B T \ln(y(r^{\text{peak}})) < -k_B T \ln(1) = 0$$

and

$$\begin{aligned}\min_{r\in(0,\infty)} v(r) &= -k_B T \ln\left(\max_{r\in(0,\infty)} y(r)\right)\\ &= -k_B T \ln(y(r^{\text{peak}}))\\ &= v(r^{\min}).\end{aligned}$$

From the above considerations, it follows that the sets $\Gamma(S_U(\alpha_0,\Delta\alpha_0))$ and $S_Y(\alpha_0,\Delta\alpha_0)$ are included in each other, such that they must be equal. □

The above theorem is a simplified version of the Henderson theorem. It shows that the map Γ yields a one-to-one correspondence between potentials and RDFs. The IBI could benefit from this correspondence, because the set S_U has some linear structure (sum of potentials is a potential), in contrast to S_Y. For any $\overline{u}, u \in S_U$, the value of the iteration function

$$f[u] = \underbrace{u}_{\in S_U} + \underbrace{\Gamma^{-1}[G[\overline{u}]]}_{\in S_U} - \underbrace{\Gamma^{-1}[G[u]]}_{\in S_U}$$

is at least in U. We can expect that the third term is nearly as large as the second term, such that the actual update of the potential u is rather small. Further, we remind that f defines the next iterate $u^{(k+1)} = f[u^{(k)}]$, which is usually smoothed, extrapolated and stabilized by damping the changes in the potential. Taking these refinements into account, it is plausible that in practice, the refined value $f[u]$ is again in S_U. In other words, the map $f : U \to U$ may never leave the set S_U of potentials.

Further, Theorem A3 motivates us to regard the approximation $\Gamma \approx G$ as good enough to assume also $D\Gamma \approx DG$. Then, the derivative DG can be approximately expressed in terms of G,

$$DG[u](v) \approx D\Gamma[u](v) = -\frac{1}{k_B T}\Gamma[u]v \approx -\frac{1}{k_B T}G[u]v, \quad \forall v \in U, \tag{4.16}$$

without any kind of numerical differentiation. This could be an explanation why the IBI does not need this derivative. Finally, we summarize all previous findings respective the two-atom RDF.

Two-atom approximation:
The two-atom RDF, as a map $\Gamma : U \to Y$,

- approximates the RDF, that is,
$$\Gamma \approx G, \tag{4.17}$$
- approximates the derivative of the RDF, that is,
$$D\Gamma \approx DG, \tag{4.18}$$
- yields a one-to-one correspondence between RDFs and potentials, that is,
$$S_U \overset{\Gamma}{\longleftrightarrow} S_Y. \tag{4.19}$$

Now we improve the classical solution approach for the well-posed problem

$$\overline{y} = G[\overline{u}]$$

by applying this two-atom approximation, which appears to be useful for an iterative method. Especially, we ensure that the numerical method works only in the space U of potentials by considering the equation

$$\overline{v} = I[\overline{u}],$$

where

$$\begin{aligned} I &:= \Gamma^{-1} \circ G : U \to U, \\ \overline{v} &:= \Gamma^{-1}[\overline{y}] \in U. \end{aligned}$$

Then, we can solve the modified problem via the Newton method, which is nothing else than a fixed-point iteration with the iteration function

$$f^{\text{Newton}}[u] := u + DI[u]^{-1}(\overline{v} - I[u]).$$

We can simplify the derivative via

$$\begin{aligned} DI[u] &\overset{\text{def}}{=} D\left[\Gamma^{-1}[G[u]]\right] \\ &\overset{(4.15)}{=} -k_B T D\left[\ln G[u]\right] \\ &= -k_B T \frac{1}{G[u]} DG[u] \\ &\overset{(4.16)}{\approx} -k_B T \left(-\frac{1}{k_B T}\right) \cdot \mathbb{1} \\ &= \mathbb{1}, \end{aligned}$$

such that our iteration function

$$\begin{aligned} f^{\text{Newton}}[u] &\approx u + \overline{v} - I[u] \\ &\overset{\text{def}}{=} u + \Gamma^{-1}[\overline{y}] - \Gamma^{-1}[G[u]] \\ &\overset{(4.14)}{=} f[u] \end{aligned}$$

becomes identical with that of the IBI.

We just derived the IBI from the classical theory of the inverse problems by using only the insight in the physical background of the problem, provided to us by the two-atom RDF. We conclude that the nature of the map Γ itself plays the decisive role in the success of the method. In other words, the approximation of the RDF via two-atom RDF is used throughout the iteration. Since the practitioners observe that the IBI succeeds for quite dense fluids ($\rho \gg 0$), we feel confirmed in our discomfort to call Γ the "low-density limit". It remains to find out why the two-atom RDF is still a good approximation of the RDF in the case of high density.

4.2.2 First Coordination Shell

We want to understand the meaning of the two-atom RDF as a function in Y and as an approximation of the RDF. We learned that the two-atom RDF gives a good representation for the RDF of a very dilute system (ρ low), which corresponds to the gaseous state of matter. But we also saw that the application area of the two-atom RDF is broader than just the case of low density. In the following, we consider the extreme case of the crystalline argon, where the density ρ is so high, that the matter becomes solid. Further, we study again the RDF of a dense system (ρ high) on example of liquid argon and compare the quality of our approximation for different phase states.

From the theory of the solid state [AM-2007], we know that atoms of the argon crystal sit on the *face-centered cubic (fcc) Bravais lattice* (see Figure 4.1)

$$\frac{1}{2}a(n_1(e^{(2)}+e^{(3)})+n_2(e^{(3)}+e^{(1)})+n_3(e^{(1)}+e^{(2)})), \quad n \in \mathbb{Z}^3,$$

where

$$a \approx 5.26 \quad [\text{Å}].$$

Since the atoms of the solid argon are attached to the lattice, they cannot move as freely as they would do in the liquid state. That is, for each fixed atom, its nearest neighbours are found at the distance $s_1 = \frac{a}{\sqrt{2}}$. These neighbours build the first *coordination shell* and their number

$$N_1^{\text{solid}} = 12$$

is called the first *coordination number*. Similarly, the k-th coordination shell and the k-th coordination number can be defined for $k \geq 2$.

Further, we consider the liquid argon near the fluid-solid coexistence line, that is, where the atoms can theoretically move freely, but due to the high density, still remember their

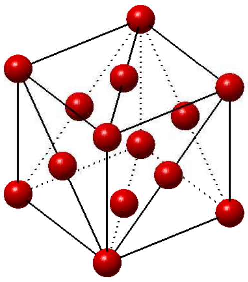

Figure 4.1: Atoms of the fcc Bravais lattice on the smallest cube.

positions in the crystal. We measure the RDF y and observe that we can define the k-th coordination shell by $[\ell_{k-1}, \ell_k]$, where $\ell_0 = 0$ and $(\ell_k)_{k\geq 1}$ are the positions of the local minima of the RDF, sorted in the ascending order. These shells describe approximately the deviations of the argon atoms from their crystalline positions. Then, we can define the analogon of the coordination numbers for the liquid state via

$$N_k^{\text{liquid}} := \rho \int_{\ell_{k-1}}^{\ell_k} y(r) |\partial B(r)| dr, \tag{4.20}$$

where $\partial B(r)$ denotes the sphere of the radius r around origin. In simple words, the integral over the k-th peak of the RDF gives the number of the atoms in the k-th coordination shell (see Theorem P4 in Appendix A.3). The same experimental RDF of the liquid argon, which we used for parameter reconstructions, yields

$$N_1^{\text{liquid}} \approx 12.$$

We are not surprised, because the RDF is measured near the triple point, where argon is simultaneously in the solid, liquid and the gaseous state.

Now we take a look at the corresponding two-atom RDF. Since the standard Lennard-Jones parameters $\overline{x} := (\overline{\varepsilon}, \overline{\sigma})^T$ for argon are known, we can easily compute

$$\gamma^{\text{LJ}} := \Gamma[H^{\text{LJ}}[\overline{x}]].$$

Comparing it with the experimental RDF (see Figure 4.2), we see that γ^{LJ} resembles well the overall shape of the function, but looses the information about all coordination shells, except the first one. We do not know where the first coordination shell ends – the upper bound ℓ_1 is smeared out to a long tail. Even if we borrow this information from above consideration, expression (4.20) counts 23 neighbours. It seems to be contraintuitive, because a two-atom RDF corresponds rather to a dilute gas, where few atoms try to fill a large container. This should lead to larger distances between atoms than in a liquid, but we count more atoms in the volume of interest, because the peak is obviously too high. The reason is the presence of the density prefactor in formula (4.20), while the two-atom RDF is independent from the density. As for counting the atoms, γ^{LJ} fails on its low-density property. However, the first part of the experimentally measured peak, from the core region to the maximum, appears to be properly modeled by the two-atom RDF (see Figure 4.2). It remains to show that this information suffices for our purposes.

We have a good reason to expect the redundancy of the lost coordination shells in the two-atom RDF. Let us visualize the idea on the discrete formulation of our inverse problem,

$$\mathrm{y} = \mathrm{G}[\mathrm{u}].$$

According to the Henderson theorem we discussed in Chapter 1, for constant N, V and T, there is a one-to-one correspondence between the sets of potentials and RDFs, which are embedded in the discrete setting into spaces of equal dimension m. As a bijective transformation between these sets, Γ is a simplified version of that correspondence. Its representation is so simple, that we can see which value of the potential u corresponds to which value of the two-atom RDF $\gamma := \Gamma[\mathrm{u}]$. In the case where the potential is parameterized, that is, $\mathrm{u} = \mathrm{H}[\mathrm{x}]$ for some $\mathrm{x} \in \mathbb{R}^n$ and $n \ll m$, we can expect a one-to-one correspondence between n components of x and n components of $\gamma = \Gamma[\mathrm{H}[\mathrm{x}]]$. In other words, we suppose that most of the components of γ (and y due to (4.4)) contain redundant information.

We test our hypothesis analytically on the Lennard-Jones potential with parameters $x = (\varepsilon, \sigma)^T$,

$$u^{\mathrm{LJ}}(r) = H^{\mathrm{LJ}}[x](r) = 4\varepsilon(\sigma^{12}r^{-12} - \sigma^6 r^{-6}), \quad r \in (0, \infty).$$

From a short analysis

$$\begin{aligned} u^{\mathrm{LJ}}(r) &= 0 \quad \Leftrightarrow \quad r = \sigma, \\ Du^{\mathrm{LJ}}(r) &= 0 \quad \Leftrightarrow \quad r = \sqrt[6]{2}\sigma, \\ u^{\mathrm{LJ}}\left(\sqrt[6]{2}\sigma\right) &= -\varepsilon, \\ D^2u^{\mathrm{LJ}}\left(\sqrt[6]{2}\sigma\right) &> 0, \end{aligned}$$

we conclude that

$$\begin{aligned} \varepsilon &= -\min_{r\in(0,\infty)} u^{\mathrm{LJ}}(r), \\ \sigma &= \min\{r \in (0,\infty) | u^{\mathrm{LJ}}(r) = 0\}. \end{aligned}$$

In other words, the parameterization map

$$H^{\mathrm{LJ}} : S_X \to H^{\mathrm{LJ}}(S_X)$$

is bijective. Further, according to definition (4.15) of the two-atom RDF,

$$\begin{aligned} \min_{r\in(0,\infty)} u(r) \quad &= \quad -k_B T \ln \max_{r\in(0,\infty)} \Gamma[u](r), \\ u(r) = 0 \quad &\Leftrightarrow \quad \Gamma[u](r) = 1. \end{aligned}$$

That is, the inverse problem

$$\gamma^{\mathrm{LJ}} = \Gamma^{\mathrm{LJ}}[x]$$

with the bijective map

$$\Gamma^{\mathrm{LJ}} := \Gamma \circ H^{\mathrm{LJ}} : S_X \xrightarrow{H^{\mathrm{LJ}}} \underbrace{H^{\mathrm{LJ}}(S_X)}_{\subseteq S_U} \xrightarrow{\Gamma} \underbrace{\Gamma(H^{\mathrm{LJ}}(S_X))}_{\subseteq S_Y} \tag{4.21}$$

has a unique solution given by

$$x = \left(k_B T \ln \left(\max_{r\in(0,\infty)} \gamma^{\mathrm{LJ}}(r)\right), \min\left\{r \in (0,\infty) | \gamma^{\mathrm{LJ}}(r) = 1\right\}\right)^T. \tag{4.22}$$

According to this formula, in order to obtain the two Lennard-Jones parameters, we need only two characteristics of the data – the height and the position of the first peak.

Since our hypothesis is confirmed in the framework of the two-atom approximation, we can expect a similar redundancy in the data for the more general problem

$$y^{\mathrm{LJ}} = F^{\mathrm{LJ}}[x],$$

where the map

$$F^{\mathrm{LJ}} := G \circ H^{\mathrm{LJ}} : S_X \xrightarrow{H^{\mathrm{LJ}}} \underbrace{H^{\mathrm{LJ}}(S_X)}_{\subseteq S_U} \xrightarrow{G} \underbrace{G(H^{\mathrm{LJ}}(S_X))}_{\subseteq S_Y}$$

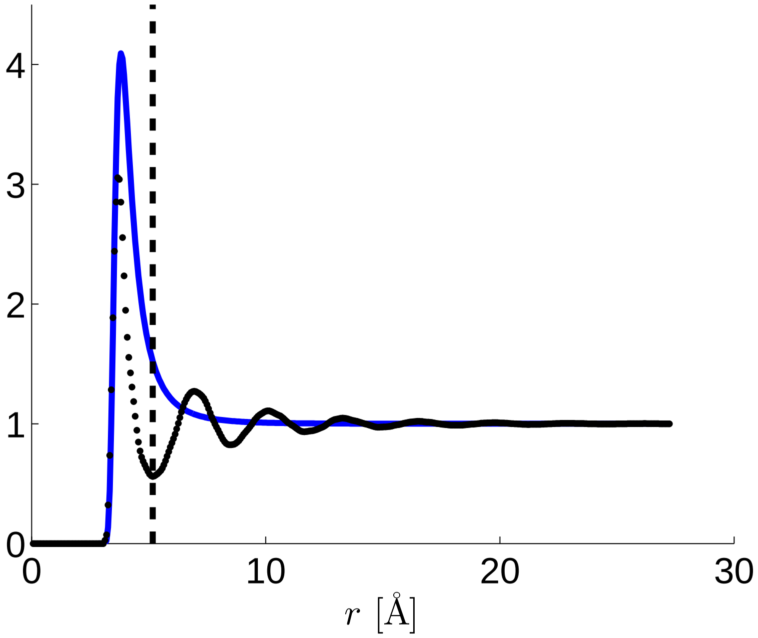

Figure 4.2: The RDF of the liquid argon (black dots) and the corresponding two-atom RDF (blue solid line). The black dashed line at $r = \ell_1$ separates the first coordination shell.

is bijective due to the Henderson theorem. Indeed, in order to apply the solution formula (4.22), we need just the part of the data from the first coordination shell, which is present in both $\gamma^{\mathrm{LJ}} \in \operatorname{ran}(\Gamma^{\mathrm{LJ}})$ and $y^{\mathrm{LJ}} \in \operatorname{ran}(F^{\mathrm{LJ}})$. Disregarding the two-atom approximation,

$$\operatorname{ran}(\Gamma^{\mathrm{LJ}}) \not\approx \operatorname{ran}(F^{\mathrm{LJ}}),$$

but we can assume that

$$\operatorname{ran}(P \circ \Gamma^{\mathrm{LJ}}) \approx \operatorname{ran}(P \circ F^{\mathrm{LJ}}), \tag{4.23}$$

where the map $P : S_Y \to S_Y$ truncates the RDF at the first peak,

$$P[y](r) := \begin{cases} y(r), & 0 < r \leq \arg\max_{s \in (0,\infty)} y(s), \\ 1, & \text{otherwise.} \end{cases} \tag{4.24}$$

In accordance with our redundancy assumption, a Lennard-Jones fluid cannot have two different RDFs, that are equal after truncation, because the relevant data is not truncated. In other words, we assume that $P|_{\operatorname{ran}(\Gamma^{\mathrm{LJ}})}$ is injective. Altogether, formula (4.22) defines the bijective solution map

$$\Lambda^{\mathrm{LJ}} := (P \circ \Gamma^{\mathrm{LJ}})^{-1} : \operatorname{ran}(P \circ \Gamma^{\mathrm{LJ}}) \to S_X. \tag{4.25}$$

Due to (4.23), we can apply this map, at least formally, to the truncated data

$$P\left[y^{\mathrm{LJ}}\right] \in \operatorname{ran}(P \circ F^{\mathrm{LJ}}).$$

We understand that this would yield rather approximate results, because the two necessary characteristics of the data are hidden in the RDF due to the many convolutions of the two-atom RDF (see equation (4.4)). However, we apply $\Lambda^{\mathrm{LJ}} \circ P$ to the experimental RDF of liquid argon and obtain the following approximate Lennard-Jones parameters

$$\begin{array}{rcll} \varepsilon & \approx & 94.9 \cdot k_B & [\mathrm{J}], \\ \sigma & \approx & 3.370 & [\mathring{\mathrm{A}}], \end{array} \tag{4.26}$$

which are in good agreement with the standard values

$$\begin{array}{rcll} \overline{\varepsilon} & = & 119.8 \cdot k_B & [\mathrm{J}], \\ \overline{\sigma} & = & 3.405 & [\mathring{\mathrm{A}}]. \end{array}$$

Moreover, in accordance with the tests in Chapter 3, we have a better reconstruction for the parameter σ than for ε.

Finally, we return to the crystalline argon, where a reference atom also has the first coordination shell filled with nearest atoms at the distance $s_1 = \frac{a}{\sqrt{2}}$. In order to calculate the density of the crystal, we build a large cube from $n \times n \times n$ smallest argon cubes (see Figure 4.1). We determine the volume of the cube and the number of contained atoms,

$$\begin{array}{rcl} V(n) & = & n^3 a^3, \\ N(n) & = & (n+1)^3 + 3n^2(n+1), \end{array}$$

in dependence of n and obtain the density in the limit

$$\rho^{\mathrm{solid}} = \lim_{n \to \infty} \frac{N(n)}{V(n)} = \frac{4}{a^3} = \frac{\sqrt{2}}{s_1^3}. \tag{4.27}$$

Considering the parameter σ as unknown, we take advantage of the good correspondence between concepts of the first coordination shell for the solid and liquid argon. As we learned above, the distance between nearest neighbours in the argon crystal is given by s_1. Then, we saw that an atom in the liquid argon has a preferred distance $r^{\min} = \sqrt[6]{2}\sigma$ to the nearest atoms, because the energy of an atom pair is minimal at this distance. However, we cannot demand

$$s_1 \overset{!}{=} r^{\min}$$

due to different densities of the solid and the liquid. For instance, the experimental RDF of the liquid argon is measured at the density $\rho^{\mathrm{liquid}} = 0.02125$ $[\mathring{\mathrm{A}}^{-3}]$. Therefore, we have to "liquify" the crystal by rescaling the distance s_1, such that $\rho^{\mathrm{solid}}(s_1) = \rho^{\mathrm{liquid}}$. According to (4.27), we obtain that the correct value of s_1 is rather

$$s_1^{\mathrm{correct}} = \sqrt[3]{\frac{\sqrt{2}}{\rho^{\mathrm{liquid}}}},$$

what leads to

$$\sigma = \frac{r^{\min}}{\sqrt[6]{2}} \approx \frac{s_1^{\mathrm{correct}}}{\sqrt[6]{2}} = \frac{1}{\sqrt[3]{\rho^{\mathrm{liquid}}}} \approx 3.610 \quad [\mathring{\mathrm{A}}].$$

The value of the parameter σ is overestimated. We note that the estimated σ depends only on the density of the liquid. Since this dependence does not require any data from solid state, we can expect that the above formula can be applied also to other materials, which crystallize into the fcc lattice. Evidently, σ grows as the density drops, but a particular liquid can have a very low density. Therefore, we fix the density to its most meaningful value ρ^{t} at the triple point, such that we can write the above formula in the more general form

$$\sigma \approx \frac{1}{\sqrt[3]{\rho^{\mathrm{t}}}}.$$

Especially for the Lennard-Jones model of argon, we have

$$\rho^{\mathrm{t}} = \frac{\rho^{\mathrm{t}*}}{\sigma^3} \approx 0.02138 \quad [\mathring{\mathrm{A}}^{-3}],$$

what leads to a bit better estimate $\sigma \approx 3.603$ [Å].

However, such overestimate cannot be used as a safe initial guess for σ in a molecular dynamics simulation. Indeed, assuming larger atoms at the experimental density is equivalent to exact atoms at larger density (see Theorem P7 in Appendix A.4). Near the fluid-solid coexistence line, this will result in a “frozen” start configuration. In the contrary, the two-atom approximation underestimates the Lennard-Jones parameters (see (4.26)), such that a stable initial guess for an iterative inversion method is guaranteed. In this regard, we remind on the Question I.3 (see p. 61), which can be answered positively for all discussed inversion methods, at least in the case of a simple fluid.

4.2.3 Derivatives of the RDF

Now we drag our attention to the two-atom approximation (4.18), which copes with the derivative of the RDF. We expect that the Levenberg-Marquardt method can benefit from this approximation as the Iterative Boltzmann Inversion (IBI) does, for instance, if we could speed up (or bypass) the numerical differentiation via finite differences. For the sake of simplicity, we consider a fluid with Lennard-Jones interactions. In this special case, the two-atom approximation takes the form

$$\Gamma^{\mathrm{LJ}}[x] \overset{(4.17)}{\approx} F^{\mathrm{LJ}}[x], \tag{4.28}$$

$$D\Gamma^{\mathrm{LJ}}[x] \overset{(4.18)}{\approx} DF^{\mathrm{LJ}}[x], \tag{4.29}$$

what leads to

$$\begin{aligned}
\frac{\partial F^{\mathrm{LJ}}[x](r)}{\partial \varepsilon} &\overset{(4.29)}{\approx} \frac{\partial \Gamma^{\mathrm{LJ}}[x](r)}{\partial \varepsilon} \\
&= -4\frac{1}{k_B T}\sigma^6 r^{-6}(\sigma^6 r^{-6} - 1)\Gamma^{\mathrm{LJ}}[x](r) \\
&\overset{(4.28)}{\approx} -4\frac{1}{k_B T}\sigma^6 r^{-6}(\sigma^6 r^{-6} - 1)F^{\mathrm{LJ}}[x](r), \qquad (4.30)\\
\frac{\partial F^{\mathrm{LJ}}[x](r)}{\partial \sigma} &\overset{(4.29)}{\approx} \frac{\partial \Gamma^{\mathrm{LJ}}[x](r)}{\partial \sigma} \\
&= -24\frac{1}{k_B T}\varepsilon\sigma^5 r^{-6}(2\sigma^6 r^{-6} - 1)\Gamma^{\mathrm{LJ}}[x](r) \\
&\overset{(4.28)}{\approx} -24\frac{1}{k_B T}\varepsilon\sigma^5 r^{-6}(2\sigma^6 r^{-6} - 1)F^{\mathrm{LJ}}[x](r). \qquad (4.31)
\end{aligned}$$

These expressions represent the derivatives as rescaled RDFs and they are very similar to expression (4.16), that we obtained for the IBI. It remains to show that these approximations have a similar quality, then we can completely remove the finite differences from our inversion method.

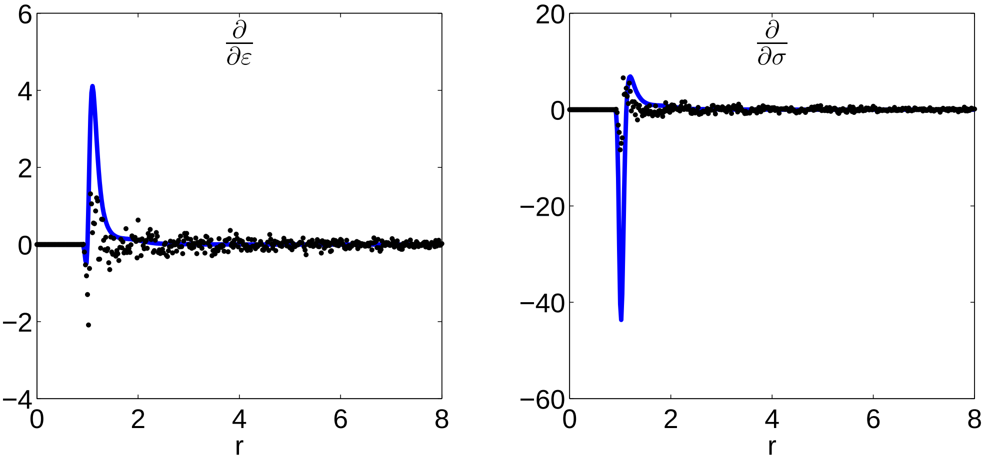

Figure 4.3: Comparison of the discrete (black dots) and approximated derivatives (blue solid lines) of the RDF.

We consider again the example of liquid argon, in order to visualize the effect of the approximations (4.30) and (4.31). Even though the argon RDF $F^{\mathrm{LJ}}[\overline{x}]$ is given on a grid, the plot of the data has a rather smooth shape (see Figure 4.2). However, the partial derivatives (black dots in Figure 4.3), obtained from the finite differences, are far from smoothness. The reason is condition (3.20) for estimation of the variations, which aims the best precision of the derivative at risk of noisy components. In particular, while we would expect

$$\lim_{r\to\infty} DF^{\mathrm{LJ}}[x](r) \approx \lim_{r\to\infty} D\Gamma^{\mathrm{LJ}}[x](r) = -\frac{1}{k_B T} \lim_{r\to\infty} \underbrace{Du^{\mathrm{LJ}}(r)}_{\to 0}\, \underbrace{\Gamma^{\mathrm{LJ}}[x](r)}_{\to 1} = 0, \tag{4.32}$$

the noise conceals this asymptotic behaviour. In contrast, our two-atom approximations (blue lines in Figure 4.3) provide a smooth version of the derivatives at cost of precision, that is, they do not match the height of the peaks. Such smoothing can have a regularizing effect, because the statistical noise is replaced by deterministic uncertainty, which respects all common properties of F and Γ, for instance, (4.32). We emphasize that the most information (see the strong negative peak in Figure 4.3) is stored in the derivative $\frac{\partial \Gamma^{\mathrm{LJ}}}{\partial \sigma}$ near the core region, on the interval corresponding to the first coordination shell. In other words, the derivative of the map representing the two-atom RDF, confirms its quality by recognizing σ as the strongest parameter of the model.

Similarly, we can use the two-atom approximation to derive from a Newton-type method a simplified, derivative-free method for any interaction parameter or even for the temperature of the system. We demonstrate the derivation of such numerical method for the temperature reconstruction. In the above problem settings, we looked for a potential or its parameters, matching the given RDF measured at given temperature and density. Here we want to find the *inverse temperature* $\beta := \frac{1}{k_B T} \in S_X$ with

$$y = F[\beta]$$

for the given RDF $y \in S_Y$, potential $u \in S_U$ and density. Also in this formulation, the map F yields an RDF for each value of β via (long) computer simulation, while the two-atom RDF is obtained (very fast) via the map

$$\Gamma[\beta](r) = e^{-\beta u(r)},$$

which can be used again as a correspondence between S_X and S_Y. On the first sight, Γ is not bijective in this context, because

$$1 = \dim(S_X) < \dim(S_Y).$$

But we can force bijectivity by choosing an appropriate evaluation point r^{eval}. Evidently, the point should be far from the regions, where $y(r)$ or $u(r)$ vanish, otherwise Γ cannot be inverted safely. We choose

$$r^{\text{eval}} := \arg\max_r y(r), \tag{4.33}$$

which corresponds to the potential value $u^{\text{eval}} = \min_r u(r) =: -\varepsilon$. This choice is motivated by our observation in Chapter 3 that ε and the temperature T are equivalent energetic parameters of the RDF. We emphasize that r^{eval} is bound to the potential value via the two-atom approximation (4.17),

$$\max_r y(r) \approx \max e^{-\beta u(r)} = e^{-\beta \min_r u(r)} = e^{\beta\varepsilon}.$$

In comparison, we could bind the evaluation point directly to the potential via

$$r^{\text{eval}} := \arg\min_r u(r),$$

but it is a worse idea, because the potentials contain (in our model) no information about temperature and will be not updated during the iteration. Once r^{eval} is chosen, our inverse problem takes the form

$$y^{\text{eval}} = F[\beta](r^{\text{eval}}),$$

such that we have in principle

$$\dim(S_X) = \dim(S_U) = \dim(S_Y) = 1.$$

The map $\Gamma[\beta] = e^{\beta\varepsilon}$, adapted to this new formulation, has the inverse

$$\Gamma^{-1}[y^{\text{eval}}] = \frac{1}{\varepsilon} \ln y^{\text{eval}}.$$

This explicit expression allows us to proceed the same way we derived the IBI from the Newton method. We ensure that the iteration works only in S_X by overcoming to the equation

$$z = K[\beta], \tag{4.34}$$

where

$$\begin{aligned} K &:= \Gamma^{-1} \circ F, \\ z &:= \Gamma^{-1}[y^{\text{eval}}]. \end{aligned}$$

The iteration function of the corresponding Newton method is

$$\begin{aligned} \Psi[\beta] &= \beta + DK[\beta]^{-1}(z - K[\beta]) \\ &= \beta + \left(\frac{1}{\varepsilon F[\beta]} DF[\beta]\right)^{-1} \left(\frac{\ln y^{\text{eval}}}{\varepsilon} - \frac{\ln F[\beta]}{\varepsilon}\right). \end{aligned}$$

Applying the two-atom approximation (4.18), we obtain

$$DF[\beta](x) \approx D\Gamma[\beta](x) = \varepsilon\Gamma[\beta]x \approx \varepsilon F[\beta]x, \quad \forall x \in S_X,$$

and the iteration function gets rid of the derivative,

$$\Psi[\beta] = \beta - \frac{1}{\varepsilon}\ln\frac{F[\beta]}{y^{\mathrm{eval}}}.$$

For infinite temperature, RDF has the value 1 at the evaluation point, therefore we can set $\beta^{(-1)} := 0$, and the iteration takes finally the desired form,

$$\begin{aligned} \beta^{(0)} &:= \frac{1}{\varepsilon}\ln y^{\mathrm{eval}}, \\ \beta^{(k+1)} &:= \beta^{(k)} - \frac{1}{\varepsilon}\ln\frac{F[\beta^{(k)}]}{y^{\mathrm{eval}}}. \end{aligned} \tag{4.35}$$

In the above realizations of the two-atom approximation in iterative inversion methods, we get rid of the derivatives in the sense that there is no need for finite differences or additional simulations to compute varied RDFs. Especially, modified with the new way to compute the derivatives from the actual RDF, the Levenberg-Marquardt method needs just one evaluation of the map F per step. With regard to the Question I.4 (see p. 67), the modified method is as fast as the IBI.

4.2.4 Role in the Levenberg-Marquardt Method

In this section, we look back to the Levenberg-Marquardt method we presented in Chapter 2. During the application of the method to the particular inverse problem in Chapter 3 and the approximation of the underlying model with the simple map Γ, we elaborated enough understanding to discuss the convergence. We remind that the Levenberg-Marquardt method converges, if condition (2.32) is fulfilled, what is much easier to check for the two-atom RDF. This will ensure the convergence for the fluids with low density and, according to the considerations of the previous sections, we can expect a transfer of this result to the dense fluids.

Since we are primarily interested in applicability of the method, we use our observations from Chapter 3, in order to constrain the interaction potentials to a suitable subset $T_U \subseteq S_U$. As we have seen in the applications, the change of the potential during the iteration is controllable, such that we can demand the set T_U to be bounded. Especially, the singular value analysis of the interactions in the liquid argon shows that the behaviour of the potential in the core region is rather unimportant, such that we can restrict our consideration to $T_U \subseteq S_U(0,0)$. According to the definition, a potential from this set is given on a certain interval $(0, r^{\mathrm{core}}]$ by an energy value $A_0 \in (0,\infty)$ (see property (SU1)). Further, due to property (SU3), the minimal interaction energy is finite,

$$u(r^{\mathrm{min}}) > -\infty.$$

Regarding the desired boundedness of the set T_U, it becomes natural to assume the existence of

$$\begin{aligned} E^{\mathrm{max}} &:= \max_{u\in T_U}\max_{r} u(r) < \infty, \\ E^{\mathrm{min}} &:= \min_{u\in T_U}\min_{r} u(r) > -\infty. \end{aligned}$$

Summarizing the above requirements, we conclude that for fixed $E^{\max} \in (0,\infty)$ and $E^{\min} \in (-\infty, 0)$, the set

$$T_U := \{u \in S_U(0,0) | E^{\min} < u < E^{\max}\} \tag{4.36}$$

is bounded and contains all potentials of interest.

Theorem A4:
There exists a constant $C > 0$, such that

$$\|\Gamma[u_1] - \Gamma[u_0] - D\Gamma[u_0](u_1 - u_0)\|_Y \leq C\|u_1 - u_0\|_{C((0,\infty))}\|\Gamma[u_1] - \Gamma[u_0]\|_Y, \quad \forall u_0, u_1 \in T_U.$$

Proof: For all $k \in \mathbb{N}$, we have

$$D^k\Gamma[u] = \left(-\frac{1}{k_BT}\right)^k \exp\left(-\frac{1}{k_BT}u\right) = \left(-\frac{1}{k_BT}\right)^k \Gamma[u].$$

Then, for all $r \in (0,\infty)$, we obtain the estimate

$$\begin{aligned}
&|\Gamma[u_1](r) - \Gamma[u_0](r) - D\Gamma[u_0](r) \cdot (u_1(r) - u_0(r))| \\
&\quad\leq \frac{1}{2} \max_{u \in T_U} \max_s |D^2\Gamma[u](s)| \cdot |u_1(r) - u_0(r)|^2 \\
&\quad= \frac{1}{2}\left(\frac{1}{k_BT}\right)^2 \max_{u \in T_U} \max_s \exp\left(-\frac{1}{k_BT}u(s)\right) \cdot |u_1(r) - u_0(r)|^2 \\
&\quad= \frac{1}{2k_B^2T^2} \exp\left(-\frac{1}{k_BT}E^{\min}\right) \cdot |u_1(r) - u_0(r)|^2.
\end{aligned}$$

Further, we introduce $\gamma_i := \Gamma[u_i]$ for $i \in \{0,1\}$ and

$$\begin{aligned}
\Lambda : \Gamma[T_U] &\rightarrow T_U, \\
\gamma &\mapsto -k_BT \ln \gamma.
\end{aligned}$$

Then, we see that

$$\begin{aligned}
\Lambda\Gamma[u] &= u, \\
D\Lambda[\gamma] &= -\frac{k_BT}{\gamma}
\end{aligned}$$

and for all $r \in (0,\infty)$, we estimate

$$\begin{aligned}
|u_1(r) - u_0(r)| &= |\Lambda[\gamma_1](r) - \Lambda[\gamma_0](r)| \\
&\leq \max_{\gamma \in \Gamma[T_U]} \max_s |D\Lambda[\gamma](s)| \cdot |\gamma_1(r) - \gamma_0(r)| \\
&= \max_{u \in T_U} \max_s \frac{k_BT}{\exp\left(-\frac{1}{k_BT}u(s)\right)} \cdot |\gamma_1(r) - \gamma_0(r)| \\
&= k_BT \exp\left(\frac{1}{k_BT}E^{\max}\right) \cdot |\Gamma[u_1](r) - \Gamma[u_0](r)|.
\end{aligned}$$

Finally, we combine the two estimates,

$$
\begin{aligned}
&\|\Gamma[u_1] - \Gamma[u_0] - D\Gamma[u_0](u_1 - u_0)\|_Y^2 \\
&\quad = \int_0^\infty |\Gamma[u_1](r) - \Gamma[u_0](r) - D\Gamma[u_0](r)\cdot(u_1(r) - u_0(r))|^2 w_Y(r)dr \\
&\quad \leq C\int_0^\infty |u_1(r) - u_0(r)|^4 w_Y(r)dr \\
&\quad \leq C\int_0^\infty |u_1(r) - u_0(r)|^2 |\Gamma[u_1](r) - \Gamma[u_0](r)|^2 w_Y(r)dr \\
&\quad \leq C\|u_1 - u_0\|_{C((0,\infty))}^2 \int_0^\infty |\Gamma[u_1](r) - \Gamma[u_0](r)|^2 w_Y(r)dr \\
&\quad = C\|u_1 - u_0\|_{C((0,\infty))}^2 \|\Gamma[u_1] - \Gamma[u_0]\|_Y^2. \quad \square
\end{aligned}
$$

The above theorem answers the Question I.2 (see p. 33) concerning the convergence of the Levenberg-Marquardt method, at least in the framework of the two-atom approximation and for potentials from (4.36).

4.2.5 Application to Argon

We saw in Section 3.3 that the Levenberg-Marquardt method converges in the case of the liquid argon. Later we discussed the Iterative Boltzmann Inversion – the fastest known method, which requires a minimum of evaluations. This method is motivated by the two-atom approximation and we derived in the similar way a couple of improving modifications for the Levenberg-Marquardt method. First, the maps (4.25) and (4.24) provide (approximate) Lennard-Jones parameters

$$\Lambda^{\mathrm{LJ}} \circ P\mathrm{y}^{(\delta)} =: (\varepsilon^{(0)}, \sigma^{(0)})^T \quad \approx \quad (94.9 \cdot k_B, 3.370)^T \quad [(\mathrm{J}, \mathrm{Å})].$$

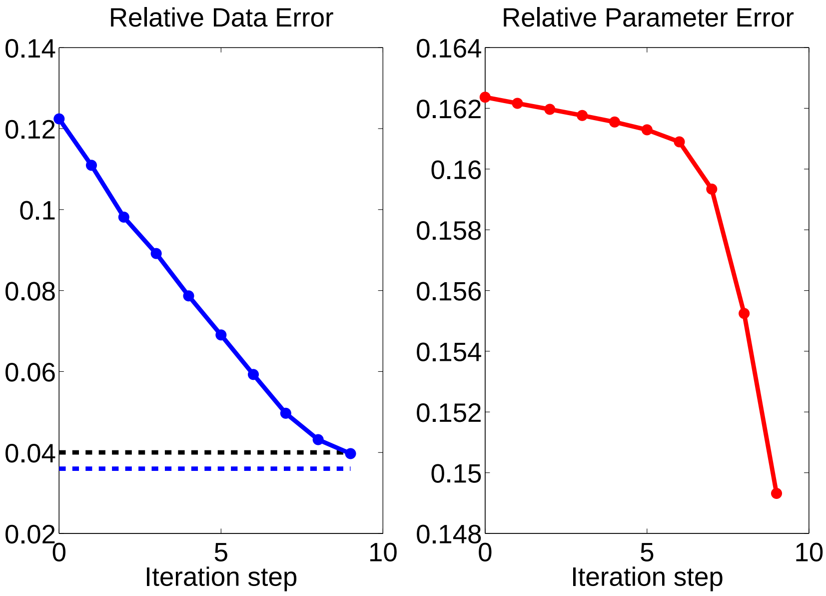

Figure 4.4: Relative errors of the iterates (red line) and of the data (blue line) from the reconstruction of the Lennard-Jones parameters of argon. The blue and black dashed lines represent the noise levels δ and $\tau\delta$, respectively.

for the liquid argon by using the given RDF $\mathrm{y}^{(\delta)} \in \mathbb{Y}$. We use these approximates to define $\varepsilon^{\mathrm{unit}} := \varepsilon^{(0)}$ and $\sigma^{\mathrm{unit}} := \sigma^{(0)}$, and obtain

$$\mathrm{T} \approx 0.90, \quad \rho \approx 0.81, \quad \overline{\mathrm{x}} \approx (1.262, 1.010)^T, \quad \mathrm{x}^{(0)} = (1,1)^T$$

in the reduced units. Second, (4.30) and (4.31) approximate the partial derivatives of F, what allows us to avoid the finite differences and the associated evaluations of the map. These modifications make the Levenberg-Marquardt method as fast as the Iterative Boltzmann Inversion. It remains to test whether the two-atom approximation affects the convergence of the method.

In the following, we always assume that argon atoms interact via Lennard-Jones potential. As before, we assume that the noise level $\delta = 1.5 \cdot 10^{-2}$ is given or can be estimated. We update the initial guess $\mathrm{x}^{(0)}$ by using the modified Levenberg-Marquardt method and Morozov discrepancy principle with $\mu = 0.9$, and stop when the residual norm crosses the level $\tau\delta$, $\tau = 1/\mu$. Both the residual norm and the relative parameter error fall monotonically (see Figure 4.4), such that the iteration terminates after $k^{\mathrm{stop}} = 9$ steps with the approximate solution

$$\mathrm{x}^{(9)} \approx (1.021, 1.016)^T$$

and relative errors

$$(1.9 \cdot 10^{-1}, 5.6 \cdot 10^{-3})^T.$$

We state that the initial guess is safe, because the method remains stable. Moreover, Figure 4.4 shows that the convergence rate gets higher as the iterates approach the exact solution. We can explain this effect by considering the regularization parameters (see Figure 4.5), which are chosen in each step of the iteration in order to damp the noise. Earlier, deriving the two-atom approximations (4.30) and (4.31), we suspected that these smooth versions of the derivatives can have a regularizing effect. Now we observe indeed that $\lambda^{(k)}$ as a function of k is rather smooth and decays monotonically, what never happened in the reconstructions involving finite differences. The regularization parameters loose an order in magnitude during this short iteration, where practically only the second decimal place of the leading parameter is polisched. In other words, the closer the method is to the solution, the less regularization it needs. Since the exact solution $\overline{\mathrm{x}}$ lies near the triple point of argon, where a part of the system behaves like a gas, it is only natural that

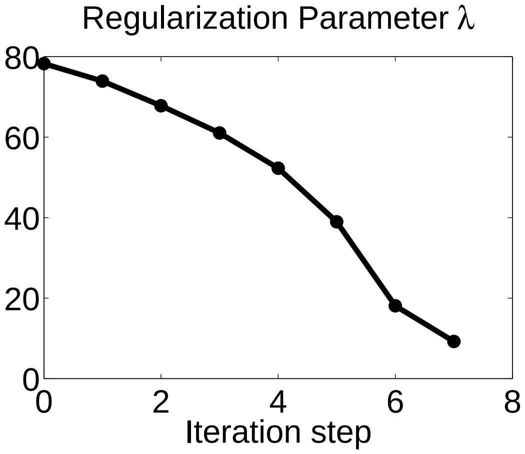

Figure 4.5: The regularization parameters $\lambda^{(k)}$ in the application of the modified Levenberg-Marquardt method to argon.

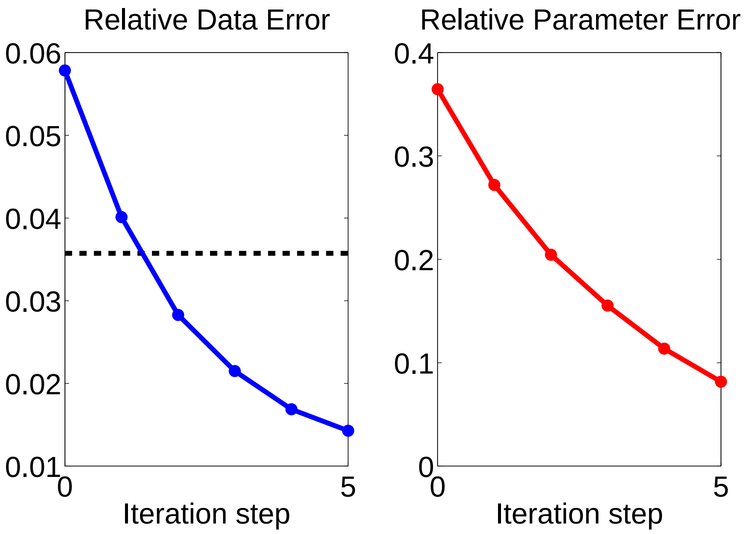

Figure 4.6: Relative errors of the iterates (red line) and of the data (blue line) from the reconstruction of the temperature in the given argon system. The black dashed line represents the noise level $\tau\delta = \delta$.

the quality of the two-atom approximation grows in its vicinity due to the low-density property (4.7).

In Section 4.2.3, we developed another "derivative-free" method (4.35) for reconstruction of the (inverse) temperature of a Lennard-Jones fluid. The method has a visual (and conceptual) similarity with the Iterative Boltzmann Inversion and obtains a proper update without any regularization, that is, it is not a Levenberg-Marquardt method anymore. However, we use further the stopping rule with $\tau = 1$ in order to prevent semi-convergence due to the noise ($\delta = 1.5 \cdot 10^{-2}$). We note again that the Lennard-Jones parameters ε and σ are given here and the exact temperature of the considered argon system is $\overline{\mathrm{T}} = 85$ [K]. By choosing

$$\varepsilon^{\mathrm{unit}} := \varepsilon, \quad \sigma^{\mathrm{unit}} := \sigma, \quad \mathrm{M}^{\mathrm{unit}} := \mathrm{M},$$

we obtain the setting of the system in the reduced units,

$$\rho \approx 0.84, \quad \varepsilon = 1, \quad \sigma = 1, \quad \overline{\mathrm{T}} \approx 0.71 \quad (\text{or } \overline{\beta} \approx 1.41).$$

According to our method, the iteration starts with the initial value

$$T^{(0)} \approx 0.90 \quad (\text{or } \beta^{(0)} \approx 1.12)$$

and terminates after $k^{\mathrm{stop}} = 5$ steps with the approximate solution

$$T^{(5)} \approx 0.77 \quad (\text{or } \beta^{(5)} \approx 1.30).$$

This is a good reconstruction of the exact temperature value, especially, if we remember that temperature is a weak parameter of the model (an energy parameter, equivalent to ε). Moreover, the monotone decay of the error curves in Figure 4.6 shows that we can expect better solutions for better estimates of the noise level δ.

4.2.6 More Coordination Shells

According to (4.4), any RDF $y = y[N](r)$ can be written in terms of the two-atom RDF, which appears to approximate the RDF very well. In the hope of finding an even better approximation (for instance, one respecting the density of the fluid), we discuss the role of the number N of atoms as a parameter of the RDF. From a certain physical viewpoint, N as well as the volume V of the system must be very large, or even infinite in some theoretical considerations, while the density $\rho = N/V$ always remains finite. In a simulation, where an RDF y is computed on some interval $(0, L/2)$, the number N must be finite – small enough to run the simulation sufficiently fast and large enough to guarantee a sufficiently large system size

$$L = \sqrt[d]{\frac{N}{\rho}},$$

such that $y(r) \to 1$ for $r \to L/2$. This choice provides us all "visible" peaks of the RDF, while the other peaks, which are probably present on $(L/2, \infty)$, are neglected, because they are "invisible" due to uncertainties of the measurement in the simulation/experiment. From the mathematical viewpoint, we choose a finite N_∞, such that

$$y[N](r) \approx y[N_\infty](r) =: y(r), \quad \forall r \in (0, L/2), \ \forall N \geq N_\infty,$$

is a valid approximation. Even more, we believe that ignoring of the infinitely many "invisible" peaks has a negligible impact on the "visible" peaks. Then, the following questions appear natural:

- Is there a small N, such that $y[N]$ describes the first one, two, three peaks of the RDF well enough for a matching procedure?
- Is this N small enough to compute the integrals in (4.4) numerically faster than to determine the RDF by computer simulation?

We already know one answer for these questions, because the two-atom RDF corresponds to $N = 2$, that is, $\gamma \equiv y[2]$. Due to the simplicity of γ, where no integration at all is needed, we could show by practically playing with the function, how good the approximation of the first peak can be. Therefore, we are encouraged to test, which quality the other "toy" RDFs $y[3]$ and $y[4]$ show. We notice that we need to integrate $d(N-2)$ times and decide to compute the functions in $d = 1$ dimension. As we can see in Figure 4.7, extra atoms fill the first coordination shell better. Even more, they also visit the second one, so that the second peak arises in the RDF and the two peaks grow as we add atoms. In contrast to a computer simulation, we obtain an information about two coordination shells, without averaging over very many (due to the low density) snapshots. The quality of this information must be higher than for two-atom RDF, because the first peak is reproduced better, such that its height and width can be fitted to the experimental data. Even though we cannot invert the map $\Gamma^{(3)} : u \mapsto y[3]$ directly, we would need only few iterations of the Levenberg-Marquardt method with just d integrals, in order to obtain an initial guess for the interaction potential fitting approximately the structure of the fluid with a density, which is never zero. [Ben-Naim-2006] also uses the RDF $y[3]$ to visualize the structure of a slightly dense gas in Section 2.5.3. Considering the need of all iterative methods for a proper start vector, the three-particle RDF may have a future as a source of a more stable initial guess, which takes the density of the fluid into account.

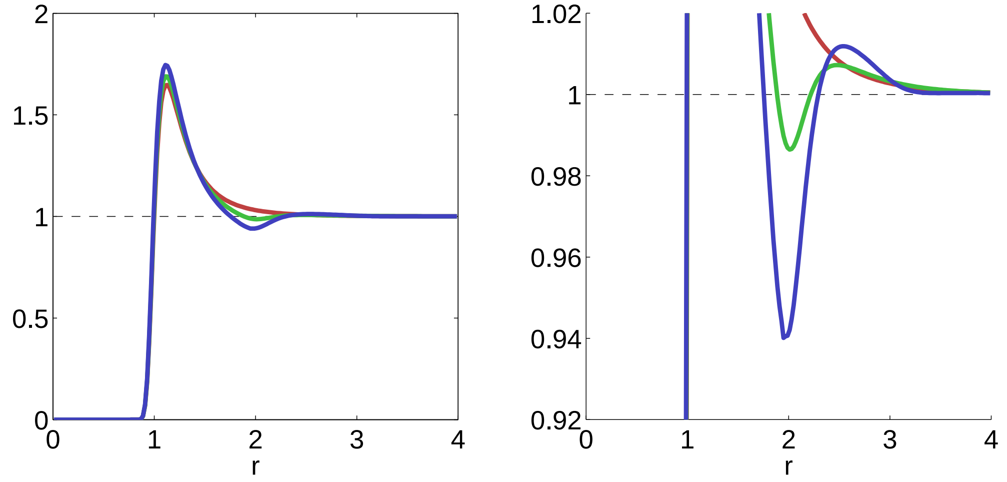

Figure 4.7: The RDFs $y[2](r)$, $y[3](r)$ and $y[4](r)$ in red, green and blue, respectively. The dashed line indicates the level $y = 1$. The left plot shows an overall comparison, while the right one shows the asymptotic behaviour. The parameters of the fluid are $T = 2$, $\rho = 0.3$, $\varepsilon = 1$, $\sigma = 1$.

We regard the three-atom RDF $y[3]$ as an intermediate approximate between $y[2]$ and y. For instance, we can use it to test the Iterative Boltzmann Inversion (IBI). Indeed, a method, working for any general RDF y, should also work for the low-density cases $y[2]$ and $y[3]$. As we explained above, the two-atom RDF $y[2]$ is already incorporated in the initial guess, such that the IBI would succeed per definition. It makes $y[3]$ to the simplest test case for the following comparison of the method with the classical Newton method.

We consider $N = 3$ atoms at temperature $T = 2$ and set the system size small enough, such that $\rho = 0.5$. We use the Lennard-Jones potential with parameters $\varepsilon = 1$ and $\sigma = 1$, determine the corresponding three-atom RDF and add to it some artificial Gaussian noise with standard deviation η. For the sake of comparability, we supply each method with the

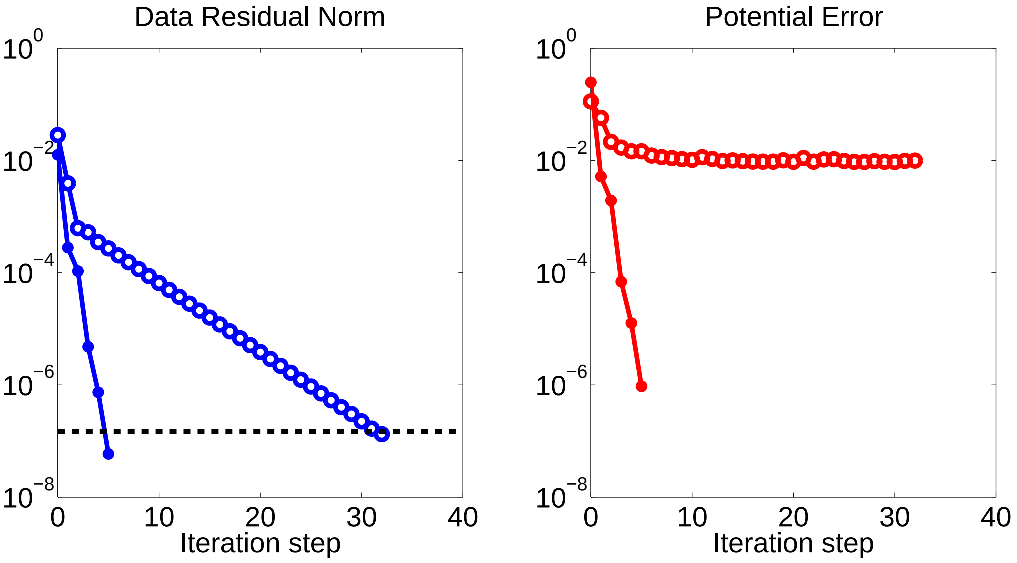

Figure 4.8: Newton method (dots) versus IBI (circles). Dashed line represents the noise level.

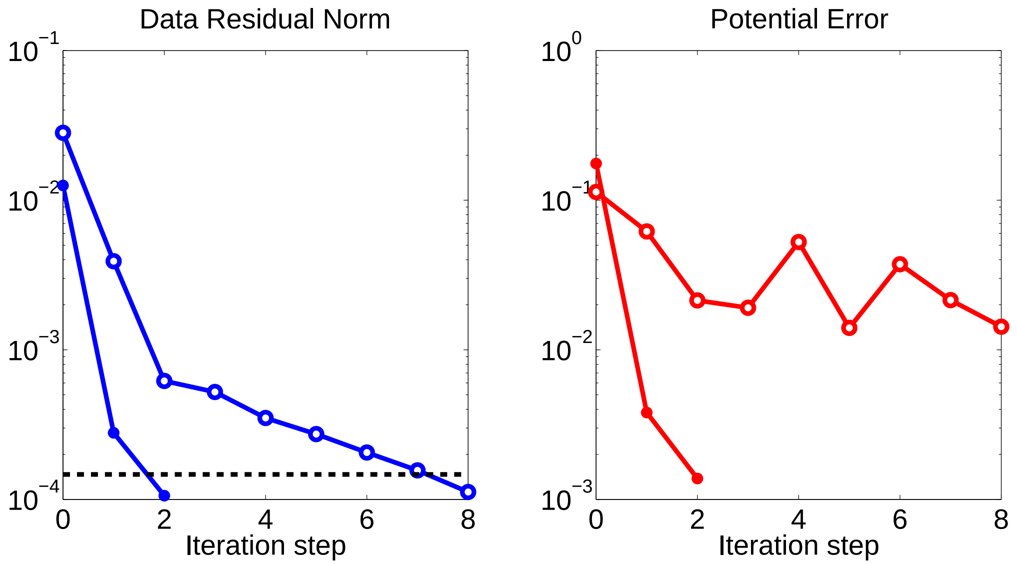

Figure 4.9: Newton method (dots) versus IBI (circles). Dashed line represents the noise level.

same initial guess, even though the Newton method works with just the parameters of the potential, while the IBI handles the complete potential tabulated on an equidistant grid with step $\Delta r = 0.02$. Further, we do not smooth the iterates and use the same stopping rule preventing optimization below the noise level. Figure 4.8 shows that, for low noise ($\eta = 10^{-8}$) or even without noise, the IBI converges to a rather suboptimal potential. In contrast, the Newton method unfolds its whole efficiency due to a small number of parameters.

We remind on the previous analysis where the iteration function suggested that the IBI just "knows" the direction towards the target RDF. In this theoretical and quite ideal setting, the Henderson theorem promises that the resulting potential is unique. Now, in practice, the iteration function can have another fixed point far from solution (see Figure 4.8). If the other fixed point does not fulfill our expectations about a physical

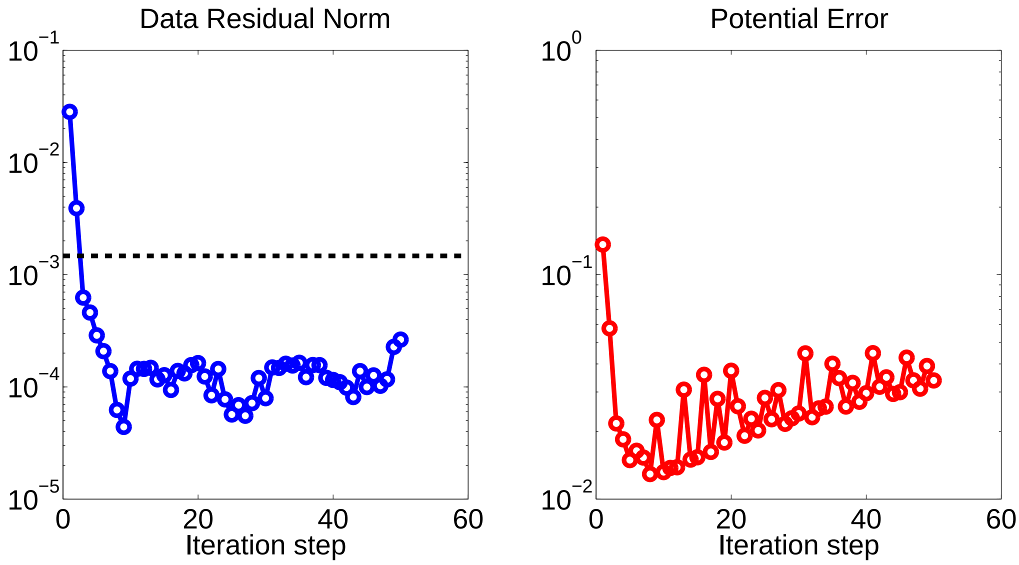

Figure 4.10: Semiconvergence of the IBI. Dashed line represents the noise level.

potential, a smart smoothing strategy can prevent that the iterates converge to it. Otherwise, the method does not really control the updates, what becomes more clear at a higher noise level ($\eta = 10^{-5}$). In this case, the IBI reveals an unpleasant behaviour – while the residual norm decreases monotonically, the potential error shows oscillations (see Figure 4.9). Finally, if we set $\eta = 10^{-4}$ and remove the stopping rule, we can observe the semiconvergence (see Figure 4.10). Indeed, the residual norm decreases, but the potential error begins to grow earlier, such that the potential becomes worse with further iteration steps. The Newton method, however, prevents such development by calculating the derivative in each step. Summarizing the above tests, we conclude that the two-atom approximation should be used with caution in an inversion method. It is advantageous for the initialization, but without proper stabilization and stopping rule, it can lead to unwanted effects already for a three-atom system.

4.2.7 Molecular Fluid

Regarding the quality of the two-atom approximation for a simple fluid, we question whether it can also be extended to a molecular fluid. Such an extension is desired for any realistic inversion method, as we stated earlier in Question 1.5. The Iterative Boltzmann Inversion (IBI) was already applied to the molecular case by fitting the RDFs separately for each type of interaction. However, this strategy does not respect the correlations between the targets, what leads to convergence problems [RJLKA-2009]. In our interpretation, the IBI is a direct consequence of the two-atom approximation, that is, our task reduces to the derivation of a "two-molecule" RDF.

We introduced the RDF in Chapter 1 as a distribution of the distance in each particle pair of the fluid. In principle, this concept is general enough to work for a molecular fluid as well as for a simple fluid. The only difference is that the term "particle" denotes now molecules, such that the term "distance" becomes ambiguous. While a distance between two atoms is a clear thing, a distance between two molecules can be defined in different manner. The most popular definitions of the molecular RDFs, namely the *center-of-mass* RDF and the *atom-atom* RDFs, consider the distance between the centers of mass and the distances between constituent atoms, respectively. Fortunately, the low-density limit of these RDFs can also be obtained [GG-1984] and it is obvious that the limit corresponds to an RDF for two molecules (see Appendix A.5 for details). Due to the total similarity and redundancy in the actual context, we omit the general definitions here and provide a detailed definition of the two-molecule RDFs in a relevant special case.

We shield the concept of the two-molecule RDF on the simplest diatomic molecule. We consider a fictive molecule `ab` consisting of a (heavier) atom `a` and a (lighter) atom `b` with masses $m_{\mathtt{a}} \geq m_{\mathtt{b}} > 0$. The two atoms are held together by a rigid bond of length $\ell_{\mathtt{a},\mathtt{b}}$. In order to compute the two-molecule approximation of the center-of-mass RDF $y_{\mathtt{ab},\mathtt{ab}}(r)$ or the atom-atom RDF $y_{\mathtt{a},\mathtt{b}}(r)$, we need two such molecules at distance r. In $d = 3$ dimensions, these are well-described by their centers of mass $\vec{R}_1, \vec{R}_2 \in \mathbb{R}^3$ and spatial orientations $\vec{z}_1, \vec{z}_2 \in S^2$. Since $|\vec{R}_1 - \vec{R}_2| = r$, the centers can be fixed to

$$\begin{aligned} \vec{R}_1 &= 0, \\ \vec{R}_2 &= r\vec{e}^{(1)}, \end{aligned}$$

without loss of generality. Then, we can write the coordinates of the atoms as

$$\begin{aligned}
\vec{r}_1 &= \vec{R}_1 + M_{\mathtt{b}}\ell_{\mathtt{a},\mathtt{b}}\vec{z}_1 && \text{(atom } \mathtt{a} \text{ of the 1. molecule)},\\
\vec{r}_2 &= \vec{R}_1 - M_{\mathtt{a}}\ell_{\mathtt{a},\mathtt{b}}\vec{z}_1 && \text{(atom } \mathtt{b} \text{ of the 1. molecule)},\\
\vec{r}_3 &= \vec{R}_2 + M_{\mathtt{b}}\ell_{\mathtt{a},\mathtt{b}}\vec{z}_2 && \text{(atom } \mathtt{a} \text{ of the 2. molecule)},\\
\vec{r}_4 &= \vec{R}_2 - M_{\mathtt{a}}\ell_{\mathtt{a},\mathtt{b}}\vec{z}_2 && \text{(atom } \mathtt{b} \text{ of the 2. molecule)},
\end{aligned}$$

where

$$M_{\mathtt{a}} := \frac{m_{\mathtt{a}}}{m_{\mathtt{a}} + m_{\mathtt{b}}}, \quad M_{\mathtt{b}} := \frac{m_{\mathtt{b}}}{m_{\mathtt{a}} + m_{\mathtt{b}}}$$

are their reduced masses. The molecular pair interaction potential

$$U^{(2)}(\vec{R}_1, \vec{R}_2, \vec{z}_1, \vec{z}_2) = u_{\mathtt{a},\mathtt{a}}(|\vec{r}_1 - \vec{r}_3|) + u_{\mathtt{a},\mathtt{b}}(|\vec{r}_1 - \vec{r}_4|) + u_{\mathtt{a},\mathtt{b}}(|\vec{r}_2 - \vec{r}_3|) + u_{\mathtt{b},\mathtt{b}}(|\vec{r}_2 - \vec{r}_4|)$$

is the sum of the interactions between atoms. Then, the two-molecule (atom-atom) RDF is defined by

$$y_{\mathtt{a},\mathtt{b}}[2](r) := \frac{1}{16\pi^2} \int_{S^2 \times S^2} \exp\left(-\frac{1}{k_B T} U^{(2)}(0, r\vec{e}_1 + \vec{v}_{1,\mathtt{a}} - \vec{v}_{2,\mathtt{b}}, \vec{z}_1, \vec{z}_2)\right) d\vec{z}_1 d\vec{z}_2, \tag{4.37}$$

where

$$\begin{aligned}
\vec{v}_{1,\mathtt{a}} &:= \vec{r}_1 - \vec{R}_1 = M_{\mathtt{b}}\ell_{\mathtt{a},\mathtt{b}}\vec{z}_1,\\
\vec{v}_{2,\mathtt{b}} &:= \vec{r}_4 - \vec{R}_2 = -M_{\mathtt{a}}\ell_{\mathtt{a},\mathtt{b}}\vec{z}_2
\end{aligned}$$

are the relative coordinates of atoms `a` and `b` in their molecules (see Appendix A.5 for general definitions).

In the following, we want to approximate the RDF of a molecular fluid with the two-molecule RDF (4.37). The computation of the latter requires integration over multiple dimensions, which must be carried out numerically and is clearly not so precise and fast as a simple evaluation of a function in the two-atom approximation. However, we saw earlier that incorporation of such approximation in an inversion method happens only at places where the importance of high precision is secondary. The first place is the initial guess, which must primarily be appropriate for the simulation of the fluid of interest. The second place is the computation of the derivative, which, especially in a regularization method, defines primarily a coarse direction for a small and controllable step towards the next iterate. We remind that the method would still evaluate the quality of the next iterate via the simulated RDF, such that the actual quality of the update would inevitably reveal a possibly too coarse approximation of the derivative. Further, with regard to the speed of the evaluating the approximate expression, a finite-differences derivative is obtained faster than for the RDF from a molecular simulation. From the viewpoint of the implementation, the integration in (4.37) requires three loops (over r, $\vec{z}_1$ and $\vec{z}_2$), where the loops over orientations may indeed appear time consumable. However, already first tests with the standard parameters for liquid nitrogen reveal that 450 points per variable yield a good approximation (see Figure 4.11) within few minutes on a desktop machine.

The first sight on Figure 4.11 may suggest that the two-molecule RDF yields only a coarse approximation of the first peak of the RDF, whose height is totally wrong. However, the position of the peak is quite precise and corresponds to the Lennard-Jones parameter σ, which is the strongest parameter of the model, as we observed in Section 3.4

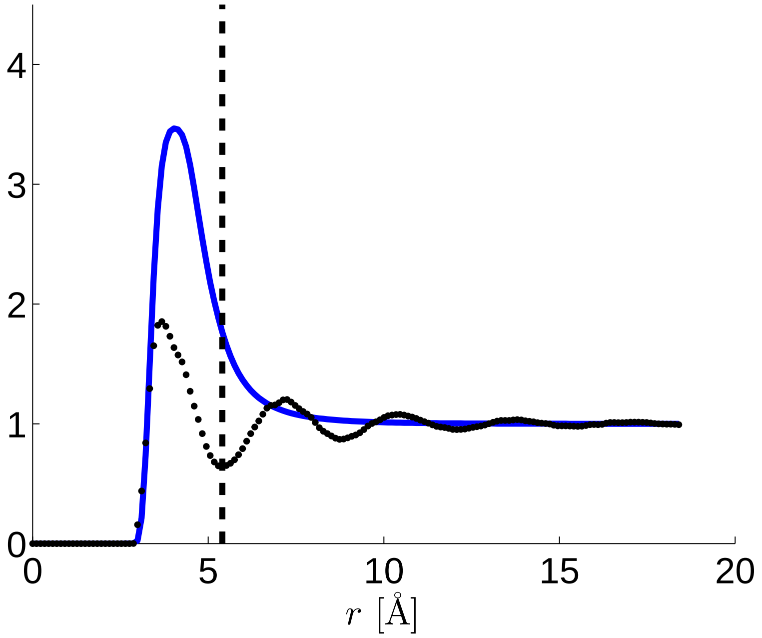

Figure 4.11: The RDF of the liquid nitrogen (black dots) and the corresponding two-molecule RDF (blue solid line). The black dashed line separates the first coordination shell.

for a simple fluid. The height of the peak is controlled by the rather weak Lennard-Jones parameter ε. In principle, we can expect that fitting of the two-molecule RDF to the first peak of the RDF yields a good initial guess for an inversion method. The fitting procedure would work with just the two-molecule RDF and a start vector with minimal requirements. As we saw in Chapter 3, a bit unlucky initialization can lead to an unwanted phase transition in the simulation. In the contrary, the explicit formula (4.37) is not sensitive to any phase-specific pecularities, such that we can initialize the fitting procedure with any meaningful guess. We develope in the next section an approach how to obtain such a guess by studying the geometry of the molecule.

4.3 Approximation of Molecular Parameters

4.3.1 Derivation of a Reconstruction Algorithm

We learned in the previos sections that the most relevant parameter of an atom is the Lennard-Jones parameter σ describing the size of the atom. This parameter, as the distance to the next neighbours of the atom, can be reliably obtained from the RDF of the fluid via map (4.25). There is a similar concept of the *van der Waals radius* – the radius of a sphere, which restricts the space occupied by an atom. The volume of the sphere interior is called the *excluded volume*, and the radius can be obtained from thermodynamical data. Since we work only with structural data (RDF), we adapt the above concept to our purposes and consider an atom as a sphere with diameter σ and volume $V(\sigma) = \frac{1}{6}\pi\sigma^3$. In contrast to atoms, molecules are rarely spherical, such that we have many possibilities to find an appropriate term for size. One of the simplest non-spherical models of a molecule would be the smallest ellipsoid around its center of mass, which contains all atoms of the molecule. However, such model requires three size parameters (the lengths of the ellipsoid's axes) to describe the molecule, therefore we prefer to discuss a special case where an ellipsoid becomes a sphere and the size of the molecule is just the diameter of this sphere. Considering the molecule as a spherical, effective particle interacting via Lennard-Jones potential, we can regard the molecular fluid as simple and use the solution map (4.25) to obtain the size of the molecule from the molecular RDF.

In the following, we want to reconstruct, at least approximately, all *molecular parameters* (atom sizes and bond lengths) from the given molecular RDF of the fluid. We know how to obtain the overall, effective size of the molecule, but due to our simple, spherical model, we loose the correspondence between the molecule and constituent atoms. Obviously, at most one parameter can be uniquely defined by the molecule size, therefore we need to couple the atom sizes and bond lengths by additional conditions. We do not aim the best numerical accuracy, thus we derive these coupling conditions approximately by following only the physical intuition about sizes. For instance, if the atomic number of atom `b` is significantly larger than that of the atom `a`, then we can demand a relation

$$V(\sigma_{\mathtt{b},\mathtt{b}}) \approx 2 \cdot V(\sigma_{\mathtt{a},\mathtt{a}}), \tag{4.38}$$

or we can set the atom sizes equal, if their atomic numbers are nearly equal. Further, the spherical model has the advantage that the size $\sigma_{\mathtt{a},\mathtt{a}}$ is at the same time the distance to the next neighbour of type `a`. This allows to define the next-neighbour-distance to an atom of type `b` via one of the *Lorentz-Berthelot rules*,

$$\sigma_{\mathtt{a},\mathtt{b}} \approx \frac{1}{2}(\sigma_{\mathtt{a},\mathtt{a}} + \sigma_{\mathtt{b},\mathtt{b}}) \tag{4.39}$$

(see Appendix B.2). For the estimation of the bond lengths, we can use the following heuristic. Choosing a bond length $\ell_{\mathtt{a},\mathtt{b}}$ near zero would be too small due to nonbonded repulsion, while setting it near the minimum $\sqrt[6]{2}\sigma_{\mathtt{a},\mathtt{b}}$ of the nonbonded potential would be redundant or, in other words, too large. Therefore, the mean value

$$\ell_{\mathtt{a},\mathtt{b}} \approx \frac{\sqrt[6]{2}}{2}\sigma_{\mathtt{a},\mathtt{b}} \tag{4.40}$$

is a coarse, but meaningful estimate. Finally, according to the coupling conditions (4.38), (4.39) and (4.40), there is a single relevant parameter, for example, $\sigma_{\mathtt{a},\mathtt{a}}$. Provided that the geometry of the molecule is given, there is a unique value of $\sigma_{\mathtt{a},\mathtt{a}}$, such that the proper constellation of spherical atoms fits into the spherical molecule of the given size.

According to the above discussion, we have now an approach for estimation of molecular parameters. We line it out by using the polystyrene example from Chapter 1 as a guide. We start in the left bottom corner of Figure 4.12, where a molecule (phenyl ring $\mathtt{C}_6\mathtt{H}_5$) is represented by the constituent atoms arranged in the correct geometrical constellation. We consider the size $\sigma_{\mathtt{C}_6\mathtt{H}_5,\mathtt{C}_6\mathtt{H}_5}$ of our molecule as unknown, while the density ρ, the temperature T and the center-of-mass RDF $y_{\mathtt{C}_6\mathtt{H}_5,\mathtt{C}_6\mathtt{H}_5}$ of the fluid are given. In the coarse graining, the mapping scheme would replace the molecule by the effective particle `a`, in accordance with the geometry of the molecule, such that only the center of mass matters and all atom coordinates become lost. An inversion procedure would set $y_{\mathtt{a},\mathtt{a}} := y_{\mathtt{C}_6\mathtt{H}_5,\mathtt{C}_6\mathtt{H}_5}$ and yield the parameters of the corresponding Lennard-Jones potential, $\varepsilon_{\mathtt{a},\mathtt{a}}$ and $\sigma_{\mathtt{a},\mathtt{a}}$, as if the fluid was simple. These numbers describe the relevant energy and the size of the spherical particle `a` in the right bottom corner of the figure. As we discussed in Chapter 1, effective particles are averages of molecules, such that they are typically softer and smaller than the underlying molecules, that is,

$$\sigma_{\mathtt{a},\mathtt{a}} \lesssim \sigma_{\mathtt{C_6H_5},\mathtt{C_6H_5}}.$$

We can use this observation for our needs, even though we do not intend to coarse-grain the fluid practically. Indeed, we learned in Section 4.2.2 that the parameters of the underlying potential can be easily estimated via (4.25) from the center-of-mass RDF,

$$(\tilde{\varepsilon}_{\mathtt{a},\mathtt{a}}, \tilde{\sigma}_{\mathtt{a},\mathtt{a}})^T := \Lambda^{\mathrm{LJ}} \circ P\left[y^{(\delta)}_{\mathtt{C_6H_5},\mathtt{C_6H_5}}\right], \tag{4.41}$$

such that the (unknown) effective size parameter is underestimated,

$$\tilde{\sigma}_{\mathtt{a},\mathtt{a}} \lesssim \sigma_{\mathtt{a},\mathtt{a}}.$$

We let $\tilde{\sigma}_{\mathtt{a},\mathtt{a}}$ describe the size of the spherical particle in the right upper corner of the figure, which is our approximation of the particle $\mathtt{a}$ and of the original molecule $\mathtt{C_6H_5}$. Clearly, the original atom sizes and bond lengths are lost, but we still know the geometry of the molecule and only need to decrease its size to the known value

$$\tilde{\sigma}_{\mathtt{C_6H_5},\mathtt{C_6H_5}} := \tilde{\sigma}_{\mathtt{a},\mathtt{a}} \lesssim \sigma_{\mathtt{a},\mathtt{a}} \lesssim \sigma_{\mathtt{C_6H_5},\mathtt{C_6H_5}}.$$

Using the coupling conditions (4.38), (4.39) and (4.40), we can reduce the unknown parameters $\tilde{\sigma}_{\mathtt{C},\mathtt{C}}$, $\tilde{\sigma}_{\mathtt{C},\mathtt{H}}$, $\tilde{\sigma}_{\mathtt{H},\mathtt{H}}$, $\tilde{\ell}_{\mathtt{C},\mathtt{C}}$ and $\tilde{\ell}_{\mathtt{C},\mathtt{H}}$ to a single relevant parameter, for example, $\tilde{\sigma}_{\mathtt{C},\mathtt{C}}$. It remains to fit this parameter to the given size $\tilde{\sigma}_{\mathtt{C_6H_5},\mathtt{C_6H_5}}$ (see the left upper corner in Figure 4.12), what leads in principle to a linear equation with one unknown, which defines nearly all molecular parameters. Finally, due to small influence of energy parameters on the fluid's structure, we can set the remaining parameters to

$$\tilde{\varepsilon}_{\mathtt{C},\mathtt{C}} := \tilde{\varepsilon}_{\mathtt{C},\mathtt{H}} := \tilde{\varepsilon}_{\mathtt{H},\mathtt{H}} := \tilde{\varepsilon}_{\mathtt{a},\mathtt{a}}. \tag{4.42}$$

Per construction, this strategy yields a unique and meaningful approximation of molecular parameters.

We can use the approximation derived above as a guess

$$\tilde{x}^{(0)} := (\tilde{\varepsilon}_{\mathtt{C},\mathtt{C}}, \tilde{\varepsilon}_{\mathtt{C},\mathtt{H}}, \tilde{\varepsilon}_{\mathtt{H},\mathtt{H}}, \tilde{\sigma}_{\mathtt{C},\mathtt{C}}, \tilde{\sigma}_{\mathtt{C},\mathtt{H}}, \tilde{\sigma}_{\mathtt{H},\mathtt{H}}, \tilde{\ell}_{\mathtt{C},\mathtt{C}}, \tilde{\ell}_{\mathtt{C},\mathtt{H}})^T$$

for molecular parameters, which should be appropriate for a simulation due to smaller atom sizes. Similarly to the simple fluid, we describe the computation of the corresponding RDF as the nonlinear map

$$F_{\mathtt{C_6H_5},\mathtt{C_6H_5}} : S_X \to S_Y, \quad x \mapsto y_{\mathtt{C_6H_5},\mathtt{C_6H_5}},$$

whose evaluation can be time consuming and instable, if $\tilde{x}^{(0)}$ is unlucky. Therefore, we want to refine our guess by involving the two-molecule approximation

$$F_{\mathtt{C_6H_5},\mathtt{C_6H_5}} \approx \Gamma_{\mathtt{C_6H_5},\mathtt{C_6H_5}},$$

where the map

$$\begin{aligned} \Gamma_{\mathtt{C_6H_5},\mathtt{C_6H_5}} : S_X &\to S_Y, \\ x &\mapsto y_{\mathtt{C_6H_5},\mathtt{C_6H_5}}[2], \end{aligned}$$

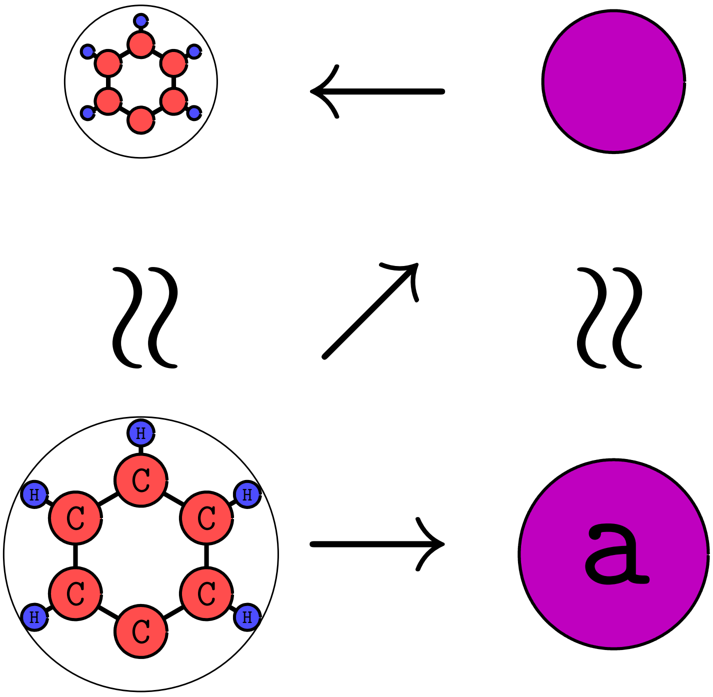

Figure 4.12: Visualization of the fitting of the atom sizes to the molecule size.

provides the two-molecule RDF for the given fluid and can be evaluated for any $\tilde{x} \in S_X$ without any phase-specific complications. We hope that this refinement helps us to obtain molecular parameters, which are appropriate for simulation and initialization of inversion methods, as it was the case for the two-atom approximation. Although $\Gamma_{\mathtt{C_6H_5},\mathtt{C_6H_5}}$ cannot be inverted directly like Γ, we can fit its values to the entries of the given molecular RDF $y^{(\delta)}_{\mathtt{C_6H_5},\mathtt{C_6H_5}}$, that correspond to the first coordination shell. That is, for a certain map $P_{\mathtt{C_6H_5},\mathtt{C_6H_5}}$ truncating the molecular RDF at the end of the first peak, we solve the inverse problem

$$P_{\mathtt{C_6H_5},\mathtt{C_6H_5}}\left[y^{(\delta)}_{\mathtt{C_6H_5},\mathtt{C_6H_5}}\right] = P_{\mathtt{C_6H_5},\mathtt{C_6H_5}} \circ \Gamma_{\mathtt{C_6H_5},\mathtt{C_6H_5}}[x]$$

with an inversion method of our choice and obtain an approximate solution $\tilde{x}^{(\tilde{k}^{\text{stop}})}$. That is, the given molecular RDF $y^{(\delta)}_{\mathtt{C_6H_5},\mathtt{C_6H_5}} \in Y$ provides us the inital guess $x^{(0)} := \tilde{x}^{(\tilde{k}^{\text{stop}})}$ for the parameter vector x as well as the energy and the length units

$$\begin{aligned} \varepsilon^{\text{unit}} &:= \tilde{\varepsilon}_{\mathtt{a},\mathtt{a}}, \\ \sigma^{\text{unit}} &:= \tilde{\sigma}_{\mathtt{a},\mathtt{a}}. \end{aligned}$$

In other words, we can apply now an inversion method also to the detailed inverse problem

$$y^{(\delta)}_{\mathtt{C_6H_5},\mathtt{C_6H_5}} = F_{\mathtt{C_6H_5},\mathtt{C_6H_5}}[x].$$

Summarizing the above discussion, we can write down the final algorithm for reconstruction of the molecular parameters:

Reconstruction algorithm. Requirements and goals:
Requirements:

(a) the center-of-mass RDF $y^{(\delta)}_{\mathtt{a},\mathtt{a}} \in S_Y$ of a molecule $\mathtt{a}$ consisting of atoms $\mathtt{a}_1, \dots, \mathtt{a}_N$ sorted by their atomic number;

(b) the geometry of the molecule, that is, a vector $\omega \in [0, \infty)^n$ with $\|\omega\|_2 \neq 0$, such that for each molecule size $\sigma_{\mathtt{a},\mathtt{a}} \in (0, \infty)$, there exists $x \in S_X$ with

$$\sigma_{\mathtt{a},\mathtt{a}} = \langle \omega | x \rangle_2. \tag{4.43}$$

Goal:
Determine the vector $\overline{x} \in S_X$ of molecular parameters, such that

$$y^{(\delta)}_{\mathtt{a},\mathtt{a}} \approx F_{\mathtt{a},\mathtt{a}}[\overline{x}]. \tag{4.44}$$

Reconstruction algorithm. Stage I:
Estimate the parameters of the effective particle via two-atom approximation

$$(\tilde{\varepsilon}_{\mathtt{a},\mathtt{a}}, \tilde{\sigma}_{\mathtt{a},\mathtt{a}})^T := \Lambda^{\mathrm{LJ}} \circ P\left[y^{(\delta)}_{\mathtt{a},\mathtt{a}}\right]. \tag{4.45}$$

Set $\tilde{\varepsilon}_{\mathtt{a}_i,\mathtt{a}_j} := \tilde{\varepsilon}_{\mathtt{a},\mathtt{a}}$. Then, by using the coupling conditions

$$\tilde{\sigma}_{\mathtt{a}_i,\mathtt{a}_i} = \begin{cases} \sqrt[3]{2} \cdot \tilde{\sigma}_{\mathtt{a}_j,\mathtt{a}_j}, & i \gg j, \\ \tilde{\sigma}_{\mathtt{a}_j,\mathtt{a}_j}, & i \approx j, \end{cases} \tag{4.46}$$

$$\tilde{\sigma}_{\mathtt{a}_i,\mathtt{a}_j} = \frac{1}{2}(\tilde{\sigma}_{\mathtt{a}_i,\mathtt{a}_i} + \tilde{\sigma}_{\mathtt{a}_j,\mathtt{a}_j}), \tag{4.47}$$

$$\tilde{\ell}_{\mathtt{a}_i,\mathtt{a}_j} = \frac{\sqrt[6]{2}}{2} \tilde{\sigma}_{\mathtt{a}_i,\mathtt{a}_j}, \tag{4.48}$$

determine the unique solution $\tilde{x} := (\tilde{\varepsilon}_{\dots}, \tilde{\sigma}_{\dots}, \tilde{\ell}_{\dots})^T$ of (4.43) for $\sigma_{\mathtt{a},\mathtt{a}} = \tilde{\sigma}_{\mathtt{a},\mathtt{a}}$.

Reconstruction algorithm. Stage II:
Define a proper truncation map $P_{\mathtt{a},\mathtt{a}}$ by localizing the first peak of the RDF visually. Then, by starting with $\tilde{x}^{(0)} := \tilde{x}$, obtain the approximate solution $\tilde{x}^{(\tilde{k}^{\mathrm{stop}})}$ of

$$P_{\mathtt{a},\mathtt{a}}\left[y^{(\delta)}_{\mathtt{a},\mathtt{a}}\right] = P_{\mathtt{a},\mathtt{a}} \circ \Gamma_{\mathtt{a},\mathtt{a}}[x] \tag{4.49}$$

via $\tilde{k}^{\mathrm{stop}}$ steps of the Levenberg-Marquardt method.

Reconstruction algorithm. Stage III:
Starting with $x^{(0)} := \tilde{x}^{(\tilde{k}^{\mathrm{stop}})}$, obtain the approximate solution $x^{(k^{\mathrm{stop}})}$ of

$$y^{(\delta)}_{\mathtt{a},\mathtt{a}} = F_{\mathtt{a},\mathtt{a}}[x] \tag{4.50}$$

via k^{stop} steps of the Levenberg-Marquardt method.

4.3.2 Application to Nitrogen

We demonstrate the workflow of our reconstruction algorithm on the example of liquid nitrogen from Section 3.4. Provided a center-of mass RDF $y^{(\delta)}_{\mathtt{N}_2,\mathtt{N}_2}$, we can assume that the fluid consists of spherical molecules $\mathtt{N}_2$ interacting via the Lennard-Jones potential and estimate the parameter $\tilde{\sigma}_{\mathtt{N}_2,\mathtt{N}_2}$ via (4.45). Then, according to our definition of the molecule size, the following relation to atom size and bond length must hold,

$$\tilde{\sigma}_{\mathtt{N}_2,\mathtt{N}_2} \overset{!}{=} \frac{1}{2}\tilde{\sigma}_{\mathtt{N},\mathtt{N}} + \tilde{\ell}_{\mathtt{N},\mathtt{N}} + \frac{1}{2}\tilde{\sigma}_{\mathtt{N},\mathtt{N}} = \tilde{\ell}_{\mathtt{N},\mathtt{N}} + \tilde{\sigma}_{\mathtt{N},\mathtt{N}}$$

(see Figure 4.13). But sometimes, we have not a center-of-mass RDF, but an atom-atom RDF $y^{(\delta)}_{\mathtt{N},\mathtt{N}}$, which describes rather the distribution of the distance between all nitrogen atoms in the reference molecule to a single atom of the next-neighbour molecule. Therefore, we do as if the fluid would consist of spherical molecules $\mathtt{N}_2$ and free atoms $\mathtt{N}$ interacting via Lennard-Jones potential with parameters nearly given by

$$(\tilde{\varepsilon}_{\mathtt{N}_2,\mathtt{N}}, \tilde{\sigma}_{\mathtt{N}_2,\mathtt{N}}) := \Lambda^{\mathrm{LJ}} \circ P\left[y^{(\delta)}_{\mathtt{N},\mathtt{N}}\right] \approx (40 \cdot k_B, 3.261) \quad [(\mathrm{J}, \mathrm{Å})].$$

Then, we obtain the size of the atoms via rule (4.39),

$$\tilde{\sigma}_{\mathtt{N}_2,\mathtt{N}} \approx \frac{1}{2}(\tilde{\sigma}_{\mathtt{N}_2,\mathtt{N}_2} + \tilde{\sigma}_{\mathtt{N},\mathtt{N}}) \approx \frac{1}{2}\tilde{\ell}_{\mathtt{N},\mathtt{N}} + \tilde{\sigma}_{\mathtt{N},\mathtt{N}}.$$

In other words, we can consider the requirements of the reconstruction algorithm as fulfilled. The first stage yields

$$\begin{aligned}
\tilde{\varepsilon}_{\mathtt{N},\mathtt{N}} &:= \tilde{\varepsilon}_{\mathtt{N}_2,\mathtt{N}_2} \approx 40 \cdot k_B \quad [\mathrm{J}],\\
\tilde{\sigma}_{\mathtt{N},\mathtt{N}} &:= \frac{4}{4+\sqrt[6]{2}}\tilde{\sigma}_{\mathtt{N}_2,\mathtt{N}} \approx 2.546 \quad [\mathrm{Å}],\\
\tilde{\ell}_{\mathtt{N},\mathtt{N}} &:= \frac{2\sqrt[6]{2}}{4+\sqrt[6]{2}}\tilde{\sigma}_{\mathtt{N}_2,\mathtt{N}} \approx 1.429 \quad [\mathrm{Å}].
\end{aligned}$$

We compare our estimates with the known standard parameter values,

$$\begin{aligned}
\overline{\varepsilon}_{\mathtt{N},\mathtt{N}} &= 37.3 \cdot k_B \quad [\mathrm{J}],\\
\overline{\sigma}_{\mathtt{N},\mathtt{N}} &= 3.310 \quad [\mathrm{Å}],\\
\overline{\ell}_{\mathtt{N},\mathtt{N}} &= 1.090 \quad [\mathrm{Å}],
\end{aligned}$$

and observe that the atom size is underestimated (as expected) and the other parameters are meaningful approximations.

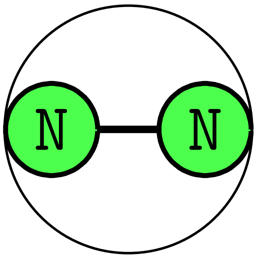

Figure 4.13: The spherical model of the nitrogen molecule.

In the second stage, we inspect the atom-atom RDF (see Figure 4.14) and introduce the map

$$P_{\mathtt{N,N}}[y](r) := \begin{cases} y(r), & 0 < r \leq \arg\min_{s\in(0,\infty)} \frac{\partial y(s)}{\partial s}, \\ 1, & \text{otherwise}, \end{cases} \tag{4.51}$$

truncating the RDF at the small shoulder after the first peak. Then we solve the inverse problem (4.49) iteratively, by starting with the guess $\tilde{x}^{(0)} := (\tilde{\varepsilon}_{\mathtt{N,N}}, \tilde{\sigma}_{\mathtt{N,N}}, \tilde{\ell}_{\mathtt{N,N}})^T$. As the fitting procedure, we engage the Levenberg-Marquardt method with $\mu = 0.9$ and the following stopping rule. As soon as the reduction of the residual is not visible due to the map noise, that is,

$$(1-\mu)\left\| P_{\mathtt{N,N}}\left[y^{(\delta)}_{\mathtt{N,N}}\right] - P_{\mathtt{N,N}} \circ \Gamma_{\mathtt{N,N}}[\tilde{x}^{(k)}]\right\|_Y \approx 2\nu,$$

the choice of the regularization parameter becomes ambiguous, such that it makes sense to stop. With these settings, the method terminates after $k^{\text{stop}} = 34$ steps and we obtain

$$\begin{array}{rcll} \tilde{\varepsilon}^{(34)}_{\mathtt{N,N}} & \approx & 40.9 \cdot k_B & [\mathrm{J}], \\ \tilde{\sigma}^{(34)}_{\mathtt{N,N}} & \approx & 3.239 & [\text{Å}], \\ \tilde{\ell}^{(34)}_{\mathtt{N,N}} & \approx & 3.5 & [\text{Å}]. \end{array}$$

We emphasize that the second stage of our algorithm yields a much better reconstruction than the first stage by working exclusively with the two-molecule RDF. Even though the parameters $\varepsilon_{\mathtt{N,N}}$ and $\ell_{\mathtt{N,N}}$ drift away, we obtain a nearly perfect underestimate of the leading parameter $\sigma_{\mathtt{N,N}}$.

Earlier in this chapter, we discussed critically the actual inversion methods, the Iterative Boltzmann Inversion (IBI) and the Inverse Monte Carlo, which are initialized or based entirely on the low-density approximation of the RDF. Particularly, [MFKV-2007] reported that the quality of such initialization drops for more complex molecular fluids,

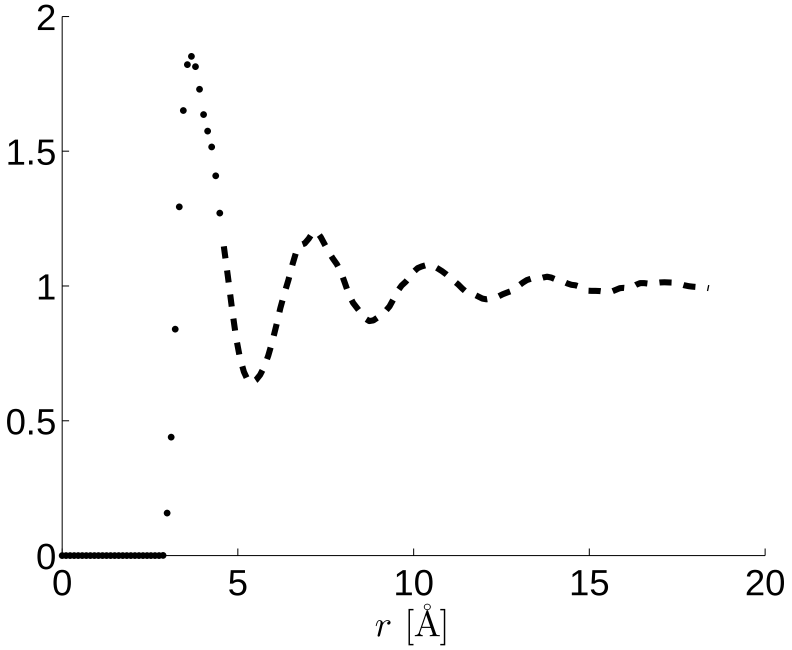

Figure 4.14: The first peak with shoulder (black dots) and the rest (dashed line) of the atom-atom RDF of the liquid nitrogen.

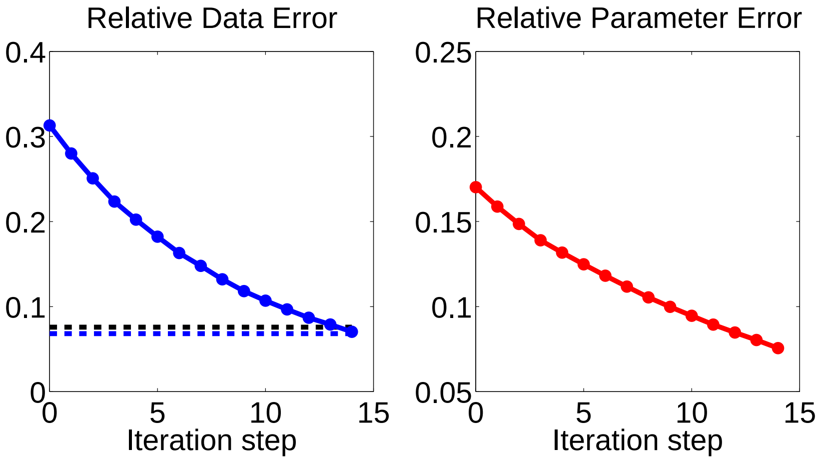

Figure 4.15: Relative errors of the iterates (red line) and of the data (blue line) for nitrogen. The blue and black dashed lines represent the noise levels δ and $\tau\delta$, respectively.

but remains crucial for the convergence of the inversion methods. Since we saw that the low-density RDF used there means just a two-atom RDF (not two-molecule RDF), we can easily explain the dropping quality by a fundamental inability of an atom (effective particle) to represent a non-spherical molecule. This can be visualized on the above reconstruction where the two-atom approximation extracts from the molecular RDF the approximate particle size 3.261 [Å]. This number might be a safe underestimate of size of the nitrogen atom, 3.310 [Å], but in fact it is an approximation of the molecule size. Accidentally, the bond is rather small, such that the size of the single atoms is quite near to the size of the molecule, but our reconstruction suggests a slightly lower value, 3.239 [Å]. For a more complex molecule, the difference of the two estimates would be more evident. While the two-atom RDF describes in the best case an averaged molecule (effective particle), the two-molecule RDF carries the information about the real geometry of the molecule. Therefore, we believe that the two-molecule RDF is a more suitable approximation of the RDF for molecular fluids and can improve the convergence of an inversion method. In this sense, we consider the two-molecule approximation as an answer to the Question I.5 (see p. 67).

Even though the above reconstruction shows that the strongest parameter $\sigma_{\mathtt{N,N}}$ is well approximated, this is evidently not the case for the bond length $\ell_{\mathtt{N,N}}$. There is a need for discussion, because the small shoulder directly after the first peak of the given RDF (see Figure 4.14) arises due to the given molecule geometry (see, for instance, [HM-2006]). Indeed, while in one nitrogen molecule, the first atom has a preferred distance (near $\sigma_{\mathtt{N,N}}$) to the other nitrogen molecule, the second atom is always at the distance $\ell_{\mathtt{N,N}}$ from the first one due to the bond. That is, the first coordination shell has a “second preferred distance” near $\sigma_{\mathtt{N,N}} + \ell_{\mathtt{N,N}}$. The simulations during the iteration show that the two-molecule RDF also posesses this shoulder, until the method “decides” to optimize the first peak primarily. Due to the chosen weighted Lebesgue-norm $\|\cdot\|_{\mathbb{Y}}$, the variation of the peak (parameter $\sigma_{\mathtt{N,N}}$) has much more impact on the RDF than the variation of the shoulder (parameter $\ell_{\mathtt{N,N}}$). In other words, this norm is not able to recognize what one can easily see with the naked eye and therefore, it is at least contraintuitive.

Until we find a better data norm, we can keep in mind that the two-molecule approximation provides a meaningless guess for the bond length and estimate it by the geometrically motivated formula (4.40), which yields

$$\ell_{\mathtt{N,N}} \approx \frac{\sqrt[6]{2}}{2}\sigma_{\mathtt{N,N}} \approx 1.818 \quad [\text{Å}].$$

Then, we have a complete initial guess for the final stage of our reconstruction algorithm, where we work with molecular RDFs obtained by computer simulations. According to the above discussion, the given atom-atom RDF $y^{(\delta)}_{\mathtt{N,N}}$ provides us the energy and the length units

$$\begin{array}{rcccl} \varepsilon^{\text{unit}} & := & \varepsilon_{\mathtt{N_2,N}} & \approx & 40 \cdot k_B \;\; [\text{J}], \\ \sigma^{\text{unit}} & := & \sigma_{\mathtt{N_2,N}} & \approx & 3.261 \quad [\text{Å}], \end{array}$$

and the inital guess $x^{(0)} := (\tilde{\varepsilon}^{(34)}_{\mathtt{N,N}}, \tilde{\sigma}^{(34)}_{\mathtt{N,N}}, \tilde{\ell}^{(34)}_{\mathtt{N,N}})^T$. In the reduced units, we have then

$$T \approx 1.62, \quad \rho \approx 0.64, \quad k_{\mathtt{N,N}} \approx 4 \cdot 10^5 \tag{4.52}$$

and

$$\begin{array}{rcl} \overline{x} & \approx & (0.931, 1.015, 0.334)^T, \\ x^{(0)} & \approx & (1.020, 0.993, 0.558)^T. \end{array}$$

The Levenberg-Marquardt method with $\mu = 0.9$ terminates in the step $k^{\text{stop}} = 14$ with the approximate solution

$$x^{(14)} \approx (1.016, 1.017, 0.399)^T.$$

The error curves in Figure 4.15 attest that the iterates converge monotonically, such that we can consider the inital guess derived above as stable. The relative errors

$$(9.1 \cdot 10^{-2}, 1.7 \cdot 10^{-3}, 1.9 \cdot 10^{-1})^T$$

of the last iterate show that the second parameter, the atom size $\sigma_{\mathtt{N,N}}$, is reconstructed very precisely. In contrast, the first and the third parameter are just acceptable, if we consider that the method did a good work on improving the start vector $x^{(0)}$ towards the exact solution $\overline{x}$. We observe here the same problem as before, namely that the method does not really optimize the bond length, because $\ell_{\mathtt{N,N}} > 0$ leads just to some shoulders in the RDF, which are nearly ignored by the method due to the chosen norm.

4.4 Approximation of the Lennard-Jones Potential

The singular value analysis of the RDF in Chapter 3 revealed the most important parameters of the interactions in a fluid. These are the “attraction energy” and the “repulsion distance”, which allow to reduce the underlying potential to the simple Lennard-Jones model with parameters ε and σ, respectively. Disregarding the apparent simplicity, analytical discussion of the the two-parametric interaction potential

$$u^{\text{LJ}}(r) = 4\varepsilon\left(\left(\frac{\sigma}{r}\right)^{12} - \left(\frac{\sigma}{r}\right)^{6}\right)$$

soon becomes difficult. For instance, the singular value analysis of the corresponding two-atom RDF is impossible, as we see later in this section.

Fortunately, the Lennard-Jones model yields such a handy and successful potential for computer simulations, that a further simplification may be indeed brought into discussion.

The idea to simplify the interaction potential for a pen-and-paper analysis already came up earlier in the perturbation theory [Zwanzig-1954]. There, one uses the observation that the structure of a fluid at high density is mainly defined by the repulsive part of the potential, such that the attractive part can be considered as a (small) perturbation. In this context, the *soft-sphere potential*

$$u^{\mathrm{SS}}(r) = 4\varepsilon \left(\frac{\sigma}{r}\right)^{\alpha}, \quad \alpha > 6, \tag{4.53}$$

emerges, that is nothing but the first term in the Lennard-Jones potential for $\alpha = 12$. Its primary properties are the fast growth towards infinity for small distances and the fast decay to zero for large distances, such that an even coarser model with the same properties becomes possible. The *hard-sphere potential* has an extraordinarily simple form

$$u^{\mathrm{HS}}(r) = \begin{cases} A_0, & 0 < r < \sigma, \\ 0, & \sigma \le r < \infty, \end{cases} \tag{4.54}$$

where the constant $A_0 > 0$ is very large and is often considered as infinite in theoretical discussions. At this level of simplicity, one can easily extend the interaction model with attractive forces by considering the *square-well potential*

$$u^{\mathrm{SW}}(r) = \begin{cases} A_0, & 0 < r < \sigma, \\ -\varepsilon, & \sigma \le r < \gamma\sigma, \\ 0, & \gamma\sigma \le r < \infty. \end{cases} \tag{4.55}$$

Usually, $\gamma = 1.5$ and the parameters ε and σ play the same roles as in the Lennard-Jones potential. This is probably the simplest adequate interaction potential for a fluid, because it fulfills property (SU3), in contrast to the soft- and hard-sphere potentials. For a detailed discussion of appropriate interaction potentials, we refer to Appendix A.2.

In this section, we combine the two-atom approximation $\Gamma \approx G$ with the above potentials. Our aim is to find out which properties of a Lennard-Jones fluid can be recognized in this extremely simple framework. In other words, we consider each of the above parameterizations H of interactions as an approximation of H^{LJ} and discuss whether

$$\Gamma \circ H \approx G \circ H^{\mathrm{LJ}}$$

holds in the sense of the singular values. We cut off the Lennard-Jones potential at the usual distance $r^{\mathrm{cut}} = 2.5\sigma$ for the sake of comparability with other potentials, which have a finite support. For a two-parametric model, we can write down the singular values and vectors explicitly, that is, we consider the two-atom RDF as a function $\Gamma[x] \in L^2((0, r^{\mathrm{cut}}))$, parameterized with vector $x \in \mathbb{R}^2$. Then, we can investigate the behaviour of such function via the singular value decomposition of the operator

$$\begin{aligned} A &:= D\Gamma[x] = \left(\frac{\partial \Gamma[x]}{\partial x_1}, \frac{\partial \Gamma[x]}{\partial x_2}\right) \\ &= \Psi\Sigma\Phi^* := (\psi^{(1)}, \psi^{(2)}, \ldots) \begin{pmatrix} \sigma_1 & 0 \\ 0 & \sigma_2 \\ \hline 0 & 0 \\ 0 & 0 \\ \cdots & \cdots \end{pmatrix} (\varphi^{(1)}, \varphi^{(2)})^T, \end{aligned}$$

where $\sigma_1 \geq \sigma_2 \geq 0$. In order to obtain the operators Σ and Φ, we look for the eigenvalues of the operator

$$M := A^* A = \begin{pmatrix} \xi & \zeta \\ \zeta & \eta \end{pmatrix},$$

where

$$\begin{aligned} \xi &:= \langle D_1\Gamma[x] | D_1\Gamma[x] \rangle_{L^2((0,r^{\mathrm{cut}}))}, \\ \eta &:= \langle D_2\Gamma[x] | D_2\Gamma[x] \rangle_{L^2((0,r^{\mathrm{cut}}))}, \\ \zeta &:= \langle D_1\Gamma[x] | D_2\Gamma[x] \rangle_{L^2((0,r^{\mathrm{cut}}))}. \end{aligned}$$

These are the solutions of the quadratic equation

$$0 \overset{!}{=} \det(M - \lambda \mathbb{1}) \equiv \lambda^2 - (\xi + \eta)\lambda + (\xi\eta - \zeta^2),$$

and more precisely,

$$\lambda^{(\pm)} = \frac{1}{2}\left(\xi + \eta \pm \sqrt{(\xi - \eta)^2 + 4\zeta^2}\right).$$

Evidently, $\lambda^{(+)} \geq \lambda^{(-)}$ and due to the Cauchy-Schwarz inequality, $\lambda^{(-)} \geq 0$. Further, for $\zeta \neq 0$, we obtain the corresponding eigenvectors $\varphi^{(\pm)}$ from the equation

$$\begin{aligned} 0 &\overset{!}{=} (M - \lambda^{(\pm)}\mathbb{1})\varphi^{(\pm)} \\ &= \begin{pmatrix} \xi - \lambda^{(\pm)} & \zeta \\ \zeta & \eta - \lambda^{(\pm)} \end{pmatrix} \varphi^{(\pm)} \\ &= \begin{pmatrix} 0 & \zeta - \frac{1}{\zeta}(\xi - \lambda^{(\pm)})(\eta - \lambda^{(\pm)}) \\ \zeta & \eta - \lambda^{(\pm)} \end{pmatrix} \varphi^{(\pm)} \\ &= \begin{pmatrix} 0 & -\frac{1}{\zeta}\det(M - \lambda\mathbb{1}) \\ \zeta & \eta - \lambda^{(\pm)} \end{pmatrix} \varphi^{(\pm)} \\ &= \begin{pmatrix} 0 & 0 \\ \zeta & \eta - \lambda^{(\pm)} \end{pmatrix} \varphi^{(\pm)}, \end{aligned}$$

that is,

$$\varphi^{(\pm)} = \frac{1}{\sqrt{(\eta - \lambda^{(\pm)})^2 + \zeta^2}} \begin{pmatrix} \eta - \lambda^{(\pm)} \\ -\zeta \end{pmatrix}.$$

In the following subsections, we study the quantities

$$\sigma_1 = \sqrt{\lambda^{(+)}}, \quad \sigma_2 = \sqrt{\lambda^{(-)}}, \quad \varphi^{(1)} = \varphi^{(+)}, \quad \varphi^{(2)} = \varphi^{(-)},$$

for the parameter $x := (\varepsilon, \sigma)^T$ near the typical value $(1, 1)^T$.

If the interactions are given by the Lennard-Jones potential, we obtain

$$\begin{aligned}
H^{\mathrm{LJ}}[\varepsilon,\sigma](r) &= 4\varepsilon(\sigma^{12}r^{-12}-\sigma^6 r^{-6}),\\
\Gamma^{\mathrm{LJ}}[\varepsilon,\sigma](r) &= \exp(-4\beta\varepsilon(\sigma^{12}r^{-12}-\sigma^6 r^{-6})),\\
\frac{\partial\Gamma^{\mathrm{LJ}}[\varepsilon,\sigma](r)}{\partial\varepsilon} &= -4\beta\sigma^6 r^{-6}(\sigma^6 r^{-6}-1)\Gamma^{\mathrm{LJ}}[\varepsilon,\sigma](r),\\
\frac{\partial\Gamma^{\mathrm{LJ}}[\varepsilon,\sigma](r)}{\partial\sigma} &= -24\beta\varepsilon\sigma^5 r^{-6}(2\sigma^6 r^{-6}-1)\Gamma^{\mathrm{LJ}}[\varepsilon,\sigma](r),\\
\xi &= 4^2\beta^2\int_0^{r^{\mathrm{cut}}}\left(\sigma^6 r^{-6}(\sigma^6 r^{-6}-1)\right)^2\left(\Gamma^{\mathrm{LJ}}[\varepsilon,\sigma](r)\right)^2 dr,\\
\eta &= 24^2\beta^2\frac{\varepsilon^2}{\sigma^2}\int_0^{r^{\mathrm{cut}}}\left(\sigma^6 r^{-6}(2\sigma^6 r^{-6}-1)\right)^2\left(\Gamma^{\mathrm{LJ}}[\varepsilon,\sigma](r)\right)^2 dr,\\
\zeta &= 4\cdot 24\beta^2\frac{\varepsilon}{\sigma}\int_0^{r^{\mathrm{cut}}}\left(\sigma^6 r^{-6}\right)^2(\sigma^6 r^{-6}-1)(2\sigma^6 r^{-6}-1)\left(\Gamma^{\mathrm{LJ}}[\varepsilon,\sigma](r)\right)^2 dr,
\end{aligned}$$

where the parameter $\beta=\frac{1}{k_B T}$ denotes the inverse temperature again. Even though the map Γ^{LJ} is quite simple, we cannot obtain the above integrals analytically and have to make use of numerical integration. In order to compute the integrals fast and with an appropriate precision, we apply the rectangle quadrature with adaptive gridsteps on each subinterval, where the integrands have a constant sign. Figure 4.16 shows the ratio $\frac{\sigma_1}{\sigma_2}$ of the resulting singular values as a function of the inverse temperature on the equidistant grid $\beta\in\{0.1,0.2,\ldots,70\}$. It is interesting that this function shows a clear minimum at $\beta^{\min}\approx 36$. This could mean that the roles of the two singular values are switching there, therefore we want to know which one corresponds to which parameter. Since the entries of the singular vectors not always allow to determine the leading parameter with respect to the definitions (2.30) and (2.31), and since we have only two parameters, we define that ε is leading, if

$$|\varphi_1^{(1)}|>|\varphi_2^{(1)}|,$$

and σ is leading, if the inequality is reversed. The singular vectors indicate that the two Lennard-Jones parameters are differently important for different temperatures – while σ is leading for $\beta<\beta^{\min}$, ε is leading for $\beta>\beta^{\min}$. We are curious whether the other interaction models will resemble this switch.

If the interactions are given by the soft-sphere potential, we obtain

$$\begin{aligned}
H^{\mathrm{SS}}[\varepsilon,\sigma](r) &= 4\varepsilon\left(\frac{\sigma}{r}\right)^\alpha,\quad \alpha>6,\\
\Gamma^{\mathrm{SS}}[\varepsilon,\sigma](r) &= \exp\left(-4\beta\varepsilon\left(\frac{\sigma}{r}\right)^\alpha\right),\\
\frac{\partial\Gamma^{\mathrm{SS}}[\varepsilon,\sigma](r)}{\partial\varepsilon} &= -4\beta\frac{\sigma^\alpha}{r^\alpha}\Gamma^{\mathrm{SS}}[\varepsilon,\sigma](r),\\
\frac{\partial\Gamma^{\mathrm{SS}}[\varepsilon,\sigma](r)}{\partial\sigma} &= -4\alpha\beta\varepsilon\frac{\sigma^{\alpha-1}}{r^\alpha}\Gamma^{\mathrm{SS}}[\varepsilon,\sigma](r),\\
\xi &= 16\beta^2\sigma^{2\alpha}I,\\
\eta &= 16\alpha^2\beta^2\varepsilon^2\sigma^{2\alpha-2}I,\\
\zeta &= 16\alpha\beta^2\varepsilon\sigma^{2\alpha-1}I,
\end{aligned}$$

where the integral

$$I:=\int_0^{r^{\mathrm{cut}}}\frac{1}{r^{2\alpha}}\exp\left(-8\beta\varepsilon\left(\frac{\sigma}{r}\right)^\alpha\right)dr$$

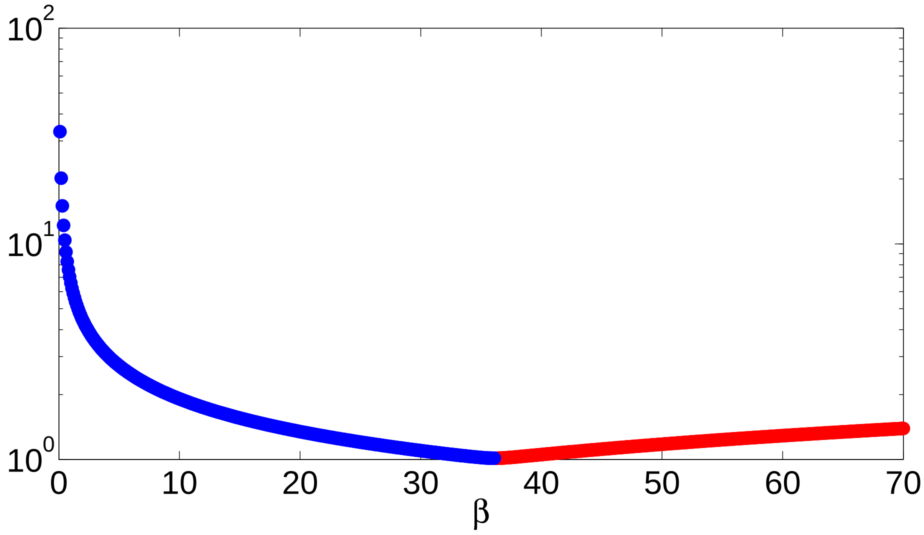

Figure 4.16: The ratio of the singular values for the Lennard-Jones potential. σ is leading in the blue part of the curve, ε – in the red one.

is obviously finite, such that we can divide the entries of the matrix M by $16\beta^2\sigma^{2\alpha-2}I$ without influence on its SVD. We obtain the eigenvalues of the rescaled matrix from the equation

$$0 \overset{!}{=} \det \begin{pmatrix} \sigma^2 - \lambda & \alpha\varepsilon\sigma \\ \alpha\varepsilon\sigma & \alpha^2\varepsilon^2 - \lambda \end{pmatrix} = (\sigma^2 - \lambda)(\alpha^2\varepsilon^2 - \lambda) - (\alpha\varepsilon\sigma)^2 = \lambda(\lambda - (\sigma^2 + \alpha^2\varepsilon^2)),$$

that is, the singular values are

$$\sigma_1 = \sqrt{\sigma^2 + \alpha^2\varepsilon^2}, \quad \sigma_2 = 0$$

and the columns of the matrix

$$\Phi = \begin{pmatrix} \sigma & -\alpha\varepsilon \\ \alpha\varepsilon & \sigma \end{pmatrix}$$

show the corresponding singular vectors. Typically $\sigma = \varepsilon = 1$, but α is large, especially, if we consider the potential as the repulsive part of the Lennard-Jones potential, where $\alpha = 12$. That is, numerically

$$\Phi.\hat{}2 \approx \begin{pmatrix} \square & \blacksquare \\ \blacksquare & \square \end{pmatrix},$$

as we already saw in Section 3.3.1. In other words, the parameter σ is much stronger than the parameter ε. However, their singular values are independent from the inverse temperature β, the ratio $\frac{\sigma_1}{\sigma_2}$ is infinite and cannot be compared with results for the Lennard-Jones potential. It is not really surprising, because the soft-sphere potential is not really a two-parametric model. Indeed, since ε does not describe the depth the potential well, the purely repulsive potential u^{SS} posesses rather only one parameter $\varepsilon\sigma^\alpha$.

If the interactions are described by the square-well potential, we have

$$\begin{aligned} H^{\mathrm{SW}}[\varepsilon,\sigma](r) &= \begin{cases} A_0, & 0 < r < \sigma, \\ -\varepsilon, & \sigma \le r < \gamma\sigma, \\ 0, & \gamma\sigma \le r < \infty, \end{cases} \\ \Gamma^{\mathrm{SW}}[\varepsilon,\sigma](r) &= \begin{cases} e^{-\beta A_0}, & 0 < r < \sigma, \\ e^{\beta\varepsilon}, & \sigma \le r < \gamma\sigma, \\ 1, & \gamma\sigma \le r < \infty, \end{cases} \\ \frac{\partial \Gamma^{\mathrm{SW}}}{\partial \varepsilon} &= \begin{cases} 0, & 0 < r < \sigma, \\ \beta e^{\beta\varepsilon}, & \sigma \le r < \gamma\sigma, \\ 0, & \gamma\sigma \le r < \infty, \end{cases} \\ \xi &= \beta^2 e^{2\beta\varepsilon}(\gamma - 1)\sigma. \end{aligned}$$

The derivative with respect to σ requires a more sophisticated treatment – we use the equality

$$\Gamma^{\mathrm{SW}}[\varepsilon,\sigma](r) = \Gamma^{\mathrm{SW}}[\varepsilon,1](r/\sigma)$$

and by introducing $s := r/\sigma$, we obtain

$$\begin{aligned} \frac{\partial \Gamma^{\mathrm{SW}}[\varepsilon,\sigma](r)}{\partial \sigma} &= \frac{\partial}{\partial \sigma}\Big(\Gamma^{\mathrm{SW}}[\varepsilon,1](s) \Big) \\ &= \frac{\partial \Gamma^{\mathrm{SW}}[\varepsilon,1](s)}{\partial s} \frac{\partial s}{\partial \sigma} \\ &= -\frac{r}{\sigma^2}\frac{\partial}{\partial s} \begin{cases} e^{-\beta A_0}, & 0 < s < 1, \\ e^{\beta\varepsilon}, & 1 \le s < \gamma, \\ 1, & \gamma \le s < \infty \end{cases} \\ &= -\frac{r}{\sigma^2}((e^{\beta\varepsilon} - e^{-\beta A_0}) \cdot \delta(s-1) + (1 - e^{\beta\varepsilon}) \cdot \delta(s-\gamma)) \\ &= -\frac{r}{\sigma}((e^{\beta\varepsilon} - e^{-\beta A_0}) \cdot \delta(r-\sigma) + (1 - e^{\beta\varepsilon}) \cdot \delta(r-\gamma\sigma)). \end{aligned}$$

We see that discontinuous H^{SW} leads to discontinuous Γ^{SW}, such that the two Dirac-δ functions appear, what makes our study impossible. Moreover, our attemts to work with appropriate continuous sequences $H_k^{\mathrm{SW}} \to H^{\mathrm{SW}}$ and $\Gamma_k^{\mathrm{SW}} \to \Gamma^{\mathrm{SW}}$ yield infinite values of the integral η in the limit $k \to \infty$, $A_0 \to \infty$. Therefore, we conclude that an approximation of the Lennard-Jones potential in the sense of singular values should be at least differentiable. However, we do not intend to derive a new model for interactions, so we put aside the analytical consideration and discuss the problem in its natural, discretized form, which is not so precise but more practicable.

For each parameterization $\mathrm{H} \in \{\mathrm{H}^{\mathrm{LJ}}, \mathrm{H}^{\mathrm{SW}}\}$ of the interactions, we differentiate the discretized two-atom map Γ via the finite difference operator

$$\mathrm{D}_j\Gamma_i[\mathrm{x}] := \frac{\Gamma_i[\mathrm{x} + \Delta\mathrm{x}_j \mathrm{e}^{(j)}] - \Gamma_i[\mathrm{x}]}{\Delta\mathrm{x}_j}, \quad 1 \le i \le m, 1 \le j \le 2,$$

where $\Delta\mathrm{x} = \Delta r(1,1)^T$ and Δr is the gridstep of the discretization. Then, we consider the curve corresponding to the singular values/vectors of the matrix $\mathrm{A} = \mathrm{D}\Gamma$ in comparison with the curve from Figure 4.16. Each of the new curves shows the same switch of the

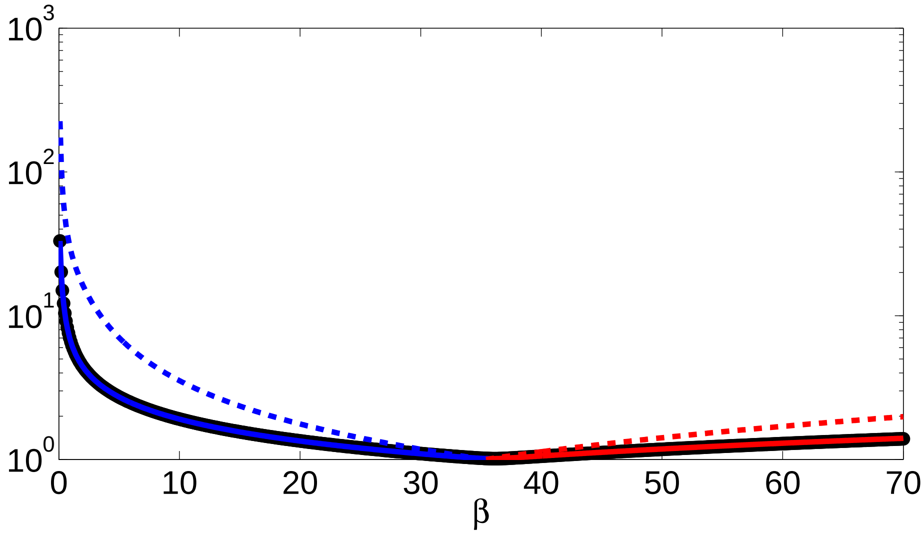

Figure 4.17: The ratio of singular values obtained by finite differences for the Lennard-Jones potential (solid line) and the square-well potential (dashed line). The curve from Figure 4.16 is plotted as the reference (black dots). σ is leading in the blue part of the curve, ε – in the red one.

leading parameter, and the Lennard-Jones data fits the reference curve almost perfectly for a sufficiently small gridstep Δr (see Figure 4.17). The curve corresponding to the square-well model reveals a similar behaviour at $\beta \to 0$ and $\beta \to \infty$. Moreover, this curve reaches its minimum near $\beta^{\min}$.

Singular values characterize the derivatives and therefore, the behaviour of the maps Γ^{LJ} and Γ^{SW}. Thus, we conclude that in practice, we can claim

$$\begin{aligned} \Gamma^{\mathrm{SW}} &\approx \Gamma^{\mathrm{LJ}}, \\ D\Gamma^{\mathrm{SW}} &\approx D\Gamma^{\mathrm{LJ}}, \end{aligned}$$

or simply

$$\mathrm{H}^{\mathrm{SW}} \approx \mathrm{H}^{\mathrm{LJ}} \tag{4.56}$$

in the sense of resembling the behaviour of the two-atom RDF. In other words, within the framework of the two-atom approximation $\Gamma \approx G$, the square-well and the Lennard-Jones potentials are nearly equivalent, two-parametric models for interactions in a simple fluid. We expect that approximation (4.56) also holds for molecular fluids and can be used for further numerical analysis of the RDF. Indeed, we used the bijectivity of H^{LJ} in Section 4.3, in order to estimate the Lennard-Jones parameters $\varepsilon^{\mathrm{LJ}}$ and σ^{LJ}. For a molecular fluid, however, such estimation appears impossible and our inversion method fails to reconstruct the bond length due to the Lebesgue-norm suited to simple fluids. In contrast, the simple form of the bijective map H^{SW} makes possible to estimate the necessary parameters $\varepsilon^{\mathrm{SW}}$, σ^{SW} etc. from the molecular RDF analytically. Finally, analysis of the molecular RDF in dependence on the square-well parameters can yield indications for a better norm, more appropriate for molecular fluids.

4.5 Summary

In this chapter, we derived the two-atom approximation as the essential feature of the physically motivated inversion methods, the Iterative Boltzmann Inversion (IBI) and the Inverse Monte Carlo (IMC). Then, in the framework of this approximation, we proved the convergence of the purely mathematical, regularizing Levenberg-Marquardt (LM) method and derived a significantly improved modification. Finally, we provided theoretical and empirical statements, which confirm that the modified LM method incorporates all advantages of the physical and mathematical derivations. Summarizing our observations in the following table,

Question\Method	LM	IBI	IMC	Modified LM
I.1. Regularization?	Yes	Maybe	Yes	Yes
I.2. Convergence?	Yes	Maybe	Maybe	Yes
I.3. Initial guess?	No	Yes	Yes	Yes
I.4. Derivative-free?	No	Yes	No	Yes
I.5. Molecular fluid?	Yes	Yes	Yes	Yes

we see that, step by step, we answered the Question I we posed in Chapter 1 for the particular inverse problem (see p. 11).

Chapter 5

Conclusion

5.1 Results

In this work, we successfully applied a mathematical theory to the inverse problem

$$y = G[u],$$

where one looks for a potential u corresponding to the given radial distribution function (RDF) y. We motivated in Chapter 1 that this problem arises in the coarse graining, when one looks for a mesoscopic potential, whose (mesoscopic) RDF fits the given microscopic RDF. Coarse graining is a physical approach taking advantage of the mapping from the microscopic to the mesoscopic scale, in order to speed up the simulation of soft matter. An inversion method solving the above equation is an essential part of the approach, and the quality of the approximate solutions is responsible for preservation of the microscopic details. In order to improve the quality of coarse graining, we determined the guideline for our investigations by posing two questions, which appear natural for the particular inverse problem:

Question I: Can we develop a better inversion method?

Question II: Can we measure/lower/minimize the loss of microscopic details owing to inversion?

In order to answer the first question, we discussed its components. First, in Chapter 2, we reviewed the theory of inverse problems, where we motivated that an "inversion method" should be stable against moderate discrepancies between the measured data and the underlying model. This stability can be reached by regularization:

Question I.1: Does the inversion method contain regularization?

Since regularization modifies the original inverse problem, it is important that the method converges:

Question I.2: Does the inversion method converge?

Then, we presented the regularizing Levenberg-Marquardt (LM) method as an example of the Newton-type methods from the applied mathematics. This method is also proved to converge under a certain condition.

Further, in Chapter 3, we applied the LM to the particular inverse problem. We reconstructed the parameters $x \in S_X$ of various parameterizations $u := H[x] \in S_U$ from the given data $y := G[u] \in S_Y$. During adaptation of the method to the problem, we derived rigorous definitions for sets/spaces $S_X \hookrightarrow X$, $S_U \hookrightarrow U$ and $S_Y \hookrightarrow Y$ of parameters, potentials and RDFs, respectively. Although the term "data" has a very general meaning in the theory, its application to the structural data (RDF) yields good reconstructions in many examples: Since we solve the nonlinear inverse problem iteratively, a "good" inversion method requires a "good" initial guess:

Question I.3: Is there a systematic way to derive an appropriate initial guess for the inversion method?

Then, we analyzed in Chapter 4 the actually existing inversion methods with the same theoretical criteria, for the sake of fair comparison. These methods, called the Iterative Boltzmann Inversion (IBI) and the Inverse Monte Carlo (IMC), are broadly and successfully applied in the coarse graining for solving the particular inverse problem. The developers of the methods are aware of the discrepancies in the data and created a number of stabilizing modifications, including the regularization of the IMC. Even though the convergence of the two methods is an issue, they reveal an intuitive physical understanding of the structural data, which allows an admissible approximation of the complex physical model G with a handy map Γ:

Two-atom approximation:
The two-atom RDF, as a map $\Gamma : U \to Y$,

- approximates the RDF, that is,
$$\Gamma \approx G,$$
- approximates the derivative of the RDF, that is,
$$D\Gamma \approx DG,$$
- yields a one-to-one correspondence between RDFs and potentials, that is,
$$S_U \overset{\Gamma}{\longleftrightarrow} S_Y.$$

Obviously, this approximation supplies the actual methods with a good initial guess by applying the inverse of Γ to the given microscopic RDF. Another advantage of the approximation became clear first after we saw that the actual inversion methods can be interpreted as Newton-type methods. Such method computes the derivative of the RDF in each iteration, what is typically a time consuming procedure, such that a runtime analysis makes sense:

Question I.4: How much time does a method spend to compute the derivative?

While the LM engages finite differences, the IMC contains an alternative procedure with physical motivation and eventually better performance. However, the effort for computing the two-atom RDF is negligible, such that the usage of the approximation in the IBI increases the convergence speed of the method significantly. But for molecular fluids, the IBI becomes unstable and the initial guess looses its quality. We believe that the reason is the high discrepancy between the molecular data (microscopic RDF) and the simple model of the fluid:

Question I.5: Can we extend the application area of a method to molecular fluids?

Finally, we used the quality of the physical two-atom approximation as a link between the functional spaces for potentials and RDFs, in order to modify the purely mathematical LM. In this fashion, we derived a novel, stable inversion method with appropriate initial guess and the convergence speed of the IBI. Further, in this approximate framework, we proved the convergence condition for the LM on a meaningful subset $T_U \subseteq S_U$ of potentials. Then, we applied the modified LM and observed a good quality of the initial guess and a convergence speed, equal to that of the IBI. Inspired by the above insight from the physical theory of simple fluids, we found a generalization of the two-atom RDF in the theory of molecular fluids – the two-molecule RDF. Moreover, we provided a reconstruction algorithm using the two-molecule RDF and the geometry of the underlying molecule to derive an appropriate initial guess for an inversion method also in the case of molecular fluids. As a substantial part of this algorithm, the LM finds a successful application to the liquid nitrogen and answers the Question I.

During the application of the LM in Chapter 3, we answered also the Question II concerning the microscopic details, that is, molecular parameters. In the case where the interaction potential is parameterized, singular value analysis reveals the weak parameters, whose influence on the RDF is nearly negligible. Moreover, the condition number measures the "badness" of the problem, such that we can raise or optimize the quality of the solution by excluding the weak parameters from consideration. According to our results in Chapter 4, we can even improve the applicability of such numerical analysis by approximating the Lennard-Jones potential by the square-well potential.

5.2 Impact on the Coarse Graining

Let us look back on the particular inverse problem

$$y = F[x]$$

from Chapter 1, where

$$F : X \xrightarrow{H} U \xrightarrow{G} Y,$$

maps the parameters $x \in X$ of a potential $u \in U$ to the corresponding RDF $y \in Y$. Solving of this problem is an essential part of the coarse graining and now, at the end of our work, we recognize that it requires a much more complex description, including appropriate functional spaces as well as simplified representatives of the maps between them. We visualize the state of our development in Figure 5.1 and discuss its content in the following.

First, we pay attention to the three-dimensional character of the mentioned figure. On the red axis, the spaces X, U and Y represent the parameters, potentials and RDFs, respectively. We used these spaces throughout our work to model a simple fluid, which is a coarser (mesoscopic) description, if compared to the modeling of a molecular fluid. The latter contains atoms of many types, such that a fine (microscopic) description via cartesian product $\mathcal{X}^q$ is required, where a parameter vector from $\mathcal{X}$, in contrast to X, contains not only the properties of atoms, but also the bond parameters, like lengths and angles. As a direct consequence, $\mathcal{U}^q$ and $\mathcal{Y}^q$ represent the variety of potentials and RDFs on the microscopic scale, respectively. The two different scales are marked on the green axis. The blue axis allows us to distinguish these (actually unknown) exact spaces from the approximate sets, which are described rigorously. For instance, the set S_Y is defined by properties (SY1)-(SY3), which yield an approximate model of the RDF by declaring its core region, first peak and tail. Even though this set is embedded in the space Y, the latter might take also the other peaks of the RDF into account. The same separation in exact and approximate descriptions also takes place on the microscopic scale, such that, for instance, the set $S_{\mathcal{X}}^Q$ emerges with $Q \leq q$. The case $Q < q$ covers the eventual reduction of the model, which has nothing to do with leaving the microscopic scale and describes a molecule approximately by a selection of molecular parameters.

Second, we discuss closer the connections between the different spaces, which are sketched in Figure 5.2. We consider the familiar example with coarse graining of the polystyrene in two dimensions, where the 11-atomic molecule $\mathtt{C}_6\mathtt{H}_5$ (with parameters from $\mathcal{X}^q$) is replaced by one spherical atom (with parameters from X). We assume that the bonds are rigid and the single atoms interact via the Lennard-Jones potential. The resulting interaction potentials from $\mathcal{U}^q$ and U reveal that in principle, we replace an n-polygon by a sphere, what appears as a good approximation for the present case $n = 6$. However, the corresponding center-of-mass RDFs from $\mathcal{Y}^q$ and Y differ already in the first peak. While the molecular RDF has a double peak due to polygonal geometry of the molecule, the atomistic RDF can have only one peak due to pure Lennard-Jones interactions. We motivate in our work that this discrepancy should not be ignored. Similar to the simple fluid, whose interactions can be obtained via the two-atom RDF from S_Y, we compute the molecular interactions via the two-molecule RDF from $S^Q_{\mathcal{Y}}$. The latter is able to fit the double peak, and the corresponding potential from $S^Q_{\mathcal{U}}$ reveals a penta- or hexagonal geometry of the approximate molecule (with parameters from $S^Q_{\mathcal{X}}$). In other words, the two-molecule approximation (TMA) proposes to replace the six `C`-atoms by a spherical atom, but keep the five `H`-atoms in order to save the polygonal geometry of the molecule and remain on the microscopic scale. We see now that the two-atom approximation (TAA) suggests a more aggressive averaging of the interactions, such that all but mesoscopic parameters of the original molecule are lost. Since the coarse graining benefits from reduced number of atoms and suffers from loss of microscopic details, it remains to decide between efficient TAA ($11 \mapsto 1$ atom(s)) and precise TMA ($11 \mapsto 7$ atoms). At this place, we remind on the square-well approximation from Section 4.4. Evindently, the above analysis is much easier to do for the square-well potential than for the Lennard-Jones potential. For a bunch of eligible mapping schemes, we can quickly determine how large the condition number is, how strong the single interaction parameters are, and choose the “best” mapping scheme. Further, we can use the square-well approximation as a source of automatic initial guess or as a “real-time” guide during a full-blooded analysis of the dependence of the RDF on molecular parameters.

Third, we use Figure 5.1 to explain how the inversion methods of our interest work. Many actions in the figure are explicitly invertible:

(I) The mapping of the molecules to the mesoscopic atoms can be inverted by backmapping – reinsertion of the molecules on the given atom positions, even though it is a quite advanced procedure (see Section 1.3).

(II) Parameterization is usually bijective, such that the parameters of the given potential can be easily obtained by fitting (see Section 4.2.2).

(III) The two-particle approximations (TAA and TMA) provide simple maps between our models for RDFs and potentials, where the atomistic map is bijective (see Section 4.2.1) and we can expect the same for the molecular one.

(IV) Truncation of the redundant peaks from the RDF leads to a subset embedded in a space where the original RDF comes from (see Section 4.2.2).

(V) Reduction is per se not bijective, but a proper coupling of the molecular parameters allows to reconstruct the original molecule from its size partially (see Section 4.3).

However, one cannot invert the simulation in a similar explicit way – no one generates a final particle configuration from the given RDF and runs the molecular dynamics backwards

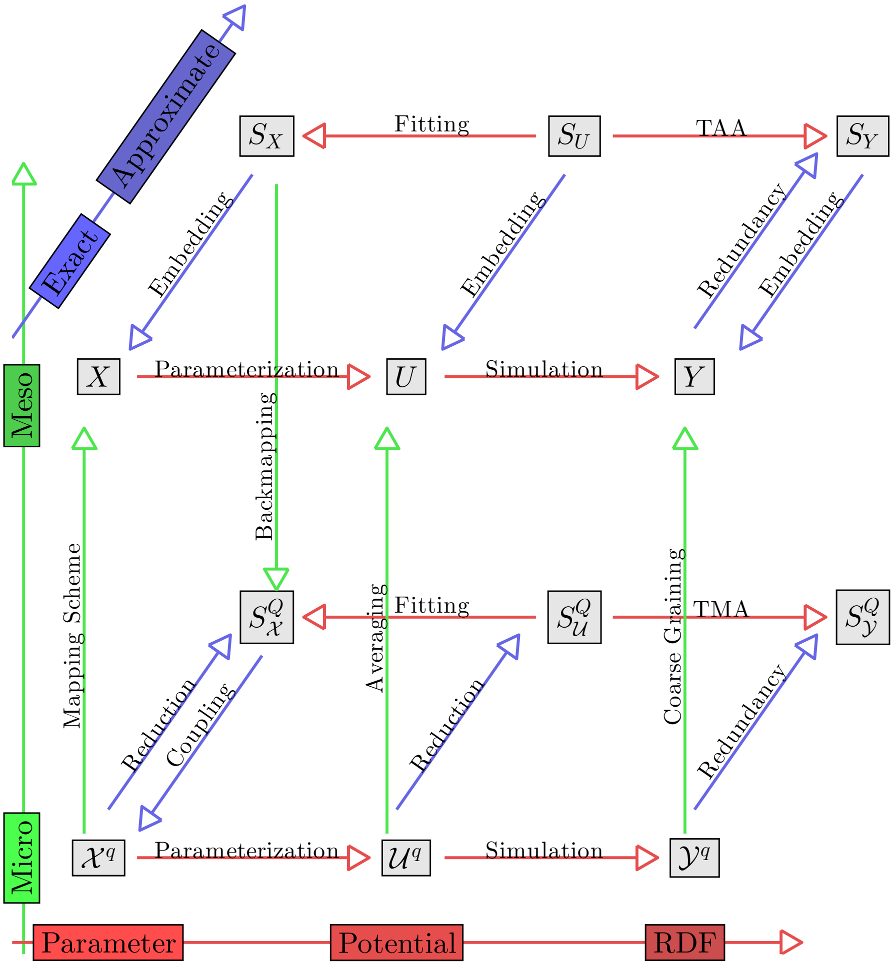

Figure 5.1: A visualization of the relations between considered spaces.

to restore the initial configuration. The iteration function of the Iterative Boltzmann Inversion (IBI) suggests that the method restores the underlying potential from U by fitting the given center-of-mass RDF from $\mathcal{Y}$. In our terms, however, the IBI makes the following detour

$$\mathcal{Y} \longrightarrow [Y \longrightarrow S_Y \longrightarrow S_U \hookrightarrow U \longrightarrow],$$

where the brackets denote the loop. In the coarse graining, one assumes implicitly that $\mathcal{Y} \subseteq Y$, in other words, for each center-of-mass RDF, there is a potential, such that the corresponding simple fluid has the same RDF. The other inclusion, $Y \subseteq \mathcal{Y}$ is evident, such that one regards the two spaces as identical. The modified Levenberg-Marquardt method avoids the scale transition arising through this identification and provides two alternatives:

$$[Y \longrightarrow S_Y \longrightarrow S_U \longrightarrow S_X \hookrightarrow X \longrightarrow U \longrightarrow]$$

for simple fluids and

$$\left[\mathcal{Y}^q \longrightarrow S_{\mathcal{Y}}^Q \longrightarrow S_{\mathcal{U}}^Q \longrightarrow S_{\mathcal{X}}^Q \longrightarrow \mathcal{X}^q \longrightarrow \mathcal{U}^q \longrightarrow\right]$$

for molecular fluids. One can still use the method for coarse graining by supplying the first version with assumption $\mathcal{Y} = Y$, what would lead to a novel, parameterized and regularized version of the IBI

$$\mathcal{Y} \longrightarrow [Y \longrightarrow S_Y \longrightarrow S_U \longrightarrow S_X \hookrightarrow X \longrightarrow U \longrightarrow].$$

Another possibility is to consider the mesoscopic potential from U as an average of the microscopic interactions described by potentials from $\mathcal{U}^q$. Then, provided a proper averaging $\mathcal{U}^q \to U$, one can derive an inversion method searching for microscopic potentials/parameters, such that the corresponding molecular RDF and the atomistic RDF corresponding to the averaged potential fit the given molecular RDF simultaneously. In this fashion, the molecular parameters match the structure of the fluid on both microscopic and mesoscopic scales. Moreover, one computes a mesoscopic (averaged) potential together with the underlying geometry of the molecule, which differs from the original molecule and can serve as a quality estimate and a further measure for loss of microscopic details.

Finally, this work proposes a new kind of the structure-based coarse graining, that puts accent on an accurate resembling of the microscopic structure by using only the Lennard-Jones potentials. Indeed, our study of a tabulated potential shows how ill-posed the inversion is already for the simple argon fluid. As a consequence, whole regions of the potential have nearly no impact on the structure of the fluid. That is, even if we obtain a sophisticated mesoscopic potential that resembles the given microscopic RDF, many features of the potential, for instance, a second attractive well, might play a negligible role in the transfer of the microscopic features to the mesoscopic scale. The accuracy of the new approach lies in a refined structure of the mesoscopic particles, which are now non-spherical molecules consisting of atoms with intuitively clear features – size σ and attractiveness ε – parameters of the Lennard-Jones (or square-well) potential. The price for this is a lower mapping ratio, as in the above example of polystyrene, where the structure suggests to map eleven atoms to seven instead of one effective particle. This causes a higher computational effort, but the advantage of a parameterized model for effective interactions is evident.

5.3 Outlook

We finish this conclusion by discussing the limitations of our approach and by providing a small outlook on promising ways to circumvent them. Particularly, the two-atom RDF, which becomes to a fruit fly for our research, is only an approximation of the experimentally measured RDF and resembles only a **part** of the first peak. An approximate framework is certainly not wrong in a topic with physical background, but its capabilities are limited, as we saw in the study of the liquid nitrogen. At this place, the three-atom RDF opens a perspective for a more rigorous (numerical) analysis, because it is able to model the **whole** first peak of the RDF. The effort due to growing number of atoms can be cancelled out by considering the square-well interactions, whose singular values resemble that of the Lennard-Jones potential.

A possible topic for future discussion is the usage of the finite differences

$$\frac{F[\cdot + \Delta x] - F[\cdot]}{\Delta x}$$

in the inversion method, where F computes the RDF or its atomistic/molecular approximation. The derivative of the two-atom RDF suggests that an ad hoc strategy for choice of the variation Δx can lead to a noisy approximation of DF, what impairs the convergence behaviour of the method. Therefore, it makes sense to use the two-particle RDFs, in order to find an optimal variation. Such search is a classical problem in the numerical

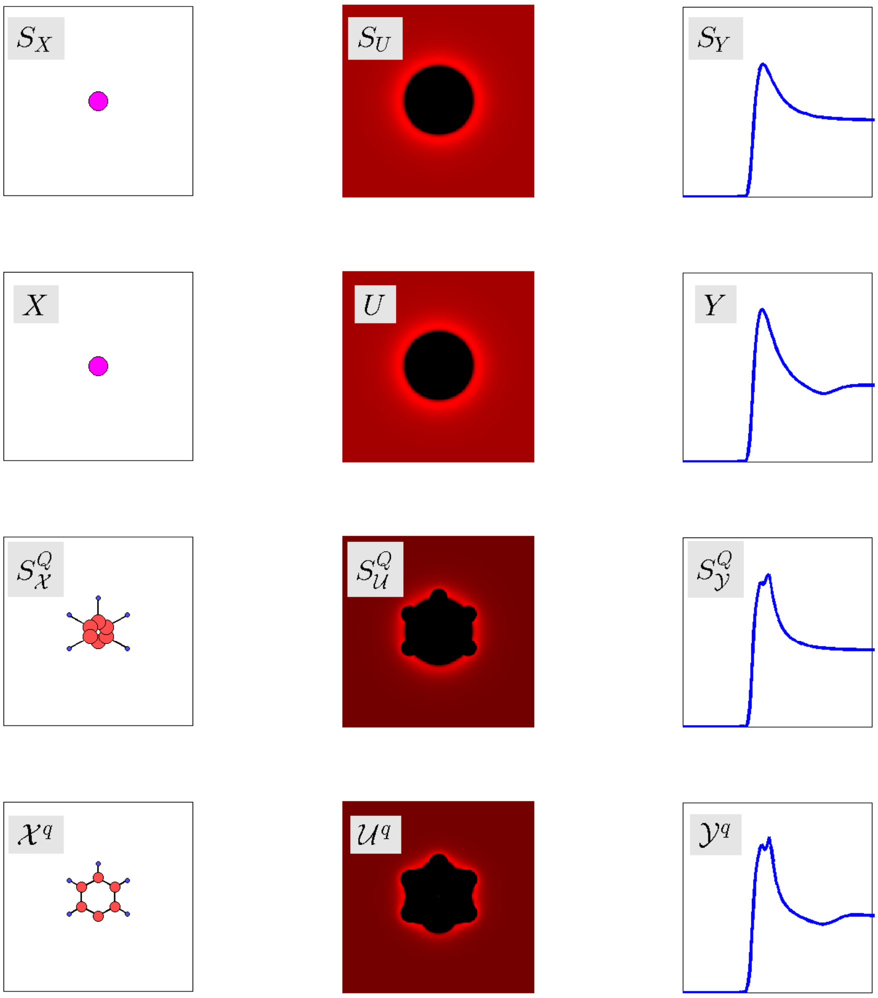

Figure 5.2: A visualization of the elements from considered spaces.

differentiation, and the theory of inverse problems provides some fundamental solution approaches based on regularization [EHN-1996].

Another open problem is a further specification of the set $S_{\mathcal{Y}} \subseteq \mathcal{Y}$ of molecular RDFs, as it was derived for the atomistic RDFs. On the one hand, the two-particle approximations confirm that the properties of the RDFs from $S_Y \subseteq Y$ are meaningful and general enough for inclusion $S_{\mathcal{Y}} \subseteq S_Y$. On the other hand, we saw that our inversion method using the two-molecule approximation cannot distinguish between simple and molecular fluid, what leads to a loss of microscopic information (the bond length in the nitrogen molecule). In the end, it is because of the Lebesque-norm on Y, which is not able to recognize the shoulder in the first peak of the molecular RDF. However, we believe that the poor norm arises from the poor description of molecular RDFs by assuming $S_{\mathcal{Y}} = S_Y$. In order to derive further properties of the RDF, we can study the composition of the coordination shells, because they directly affect the specific shape of the peaks in a molecular RDF. Since the underlying physics is quite general, we can analyze simple or molecular Lennard-Jones fluids in two, three and four dimensions. We emphasize that the question here is not, whether the Lennard-Jones potential is a correct potential in other dimensions, but what the map $G : U \to Y$ does with the potential to compute the RDF, in dependence of the dimension. The Monte Carlo method allows us to simulate easily molecules with rigid bonds, such that we can focus on the link between the molecular geometry and the coordination shells. This approach may appear as troublesome, but, considering the redundancy in the RDF, a good description of the first coordination shell should suffice. Further, due to the good correspondence between a dense liquid and a solid, there is not much puzzling possible, because the next-neighbour-molecules cannot be too far from their positions on the crystal lattice.

In order to circumvent the direct analysis of the space $\mathcal{Y}$, we can also take an established mathematical path. Namely, we had a similar problem with modeling the interactions via discretized potential in Chapter 3 and saw that a suitable parameterization $H : X \to U$ of the potential renders the problem well-posed. Therefore, instead of looking for a sophisticated definition/norm for RDFs, we can consider first a parameterization $I : \mathcal{Z} \to \mathcal{Y}$, where $\dim(\mathcal{Z}) < \infty$. For instance, we could follow the idea from [MGM-2005], where the distributions of the bond length and angles in a polymer are represented as a linear combination of Gaussian distributions. The adaptation for our case would be to consider a parameterization of the potential of mean force. It is interesting that the latter can be obtained from the molecular RDF with help of the two-atom approximation and is therefore a potential from U. Evidently, we could not exhaust the properties of the two-particle approximations in every sense, such that room for future work is available.

Appendix A

Radial Distribution Function

In this appendix, we give a comprehensive introduction to the concept of the radial distribution function. This function has the ability to describe the structure of the given system of particles and can be derived from the dynamic equations of the system. However, the physical behaviour of the particles as well as the mathematical formulation of the equations depend strongly on the system size. While the system can be considered as infinitely large in theoretical discussions, we can simulate only few thousands of particles in practice. Therefore, we consider the theory for these two cases as a preliminary knowledge and provide a short overview before we start with the subject.

A.1 Introduction to Statistical Physics

For the sake of simplicity, we do not consider any quantum effects, such that we can start with the classical mechanics, as it can be found, for instance, in [LAL-1970]. In the mechanics, we discuss the motion (time evolution) of physical bodies. A body, whose shape (color, size, orientation) may be neglected in the given problem setting, is called a *particle*. We consider a system of $N \in \mathbb{N}$ identical particles with mass $M \in (0, \infty)$. Let

$$R :\equiv (R_1, \dots, R_N)^T, P :\equiv (P_1, \dots, P_N)^T : [0, \infty) \to \mathbb{R}^{dN}, \quad 1 \le I \le N,$$

describe the time-dependent coordinates and momenta of the particles, respectively. In the Hamilton formalism, we assume that the total energy of the system can be expressed as the *Hamiltonian* – a function

$$H : \mathbb{R}^{dN} \times \mathbb{R}^{dN} \to \mathbb{R}$$

of the instantaneous particle coordinates $\underline{R} := (\vec{R}_1, \dots, \vec{R}_N)^T$ and momenta $\underline{P} := (\vec{P}_1, \dots, \vec{P}_N)^T$, which does not depend on time explicitly. The time evolution of the system is then given by the *Hamilton equations*

$$\begin{aligned} \dot{R}(t) &= \left. \frac{\partial H(R(t), \underline{P})}{\partial \underline{P}} \right|_{\underline{P}=P(t)}, \\ \dot{P}(t) &= - \left. \frac{\partial H(\underline{R}, P(t))}{\partial \underline{R}} \right|_{\underline{R}=R(t)}. \end{aligned} \tag{A.1}$$

In principle, provided an initial state $(R(0), P(0))^T \in \mathbb{R}^{2dN}$ of the system, we can determine the *trajectory* $((R(t), P(t))^T)_{t \ge 0} \subset \mathbb{R}^{2dN}$ of the system. The Hamilton equations imply a conservation law – the total time derivative vanishes,

$$\dot{H}(R(t), P(t)) = \left.\frac{\partial H(\underline{R}, P(t))}{\partial \underline{R}}\right|_{\underline{R}=R(t)} \dot{R}(t) + \left.\frac{\partial H(R(t), \underline{P})}{\partial \underline{P}}\right|_{\underline{P}=P(t)} \dot{P}(t) = 0, \tag{A.2}$$

that is, the total energy of the system remains constant (conserved) during the motion of constituent particles.

In the most popular special case, the total energy can be separated, with respect to coordinates and momenta, in the sum

$$H(\underline{R}, \underline{P}) = E^{\text{kin}}(\underline{P}) + E^{\text{pot}}(\underline{R}) \tag{A.3}$$

of the *kinetic energy*

$$E^{\text{kin}}(\underline{P}) := \frac{1}{2M} |\underline{P}|^2 \tag{A.4}$$

and the *potential energy* $E^{\text{pot}}(\underline{R})$. Then, the Hamilton equations imply that coordinates and momenta are coupled via

$$\begin{aligned} M\dot{R}(t) &\overset{(A.1)}{=} M \left.\frac{\partial H(R(t), \underline{P})}{\partial \underline{P}}\right|_{\underline{P}=P(t)} \\ &\overset{(A.3)}{=} M \left.\frac{\partial E^{\text{kin}}(\underline{P})}{\partial \underline{P}}\right|_{\underline{P}=P(t)} \\ &\overset{(A.4)}{=} P(t). \end{aligned} \tag{A.5}$$

Further,

$$\begin{aligned} M\ddot{R}(t) &\overset{(A.5)}{=} \dot{P}(t) \\ &\overset{(A.1)}{=} - \left.\frac{\partial H(\underline{R}, P(t))}{\partial \underline{R}}\right|_{\underline{R}=R(t)} \\ &\overset{(A.3)}{=} -\nabla E^{\text{pot}}(R(t)) \end{aligned}$$

yields the *Newton equations*

$$M\ddot{R}(t) = F(R(t)), \tag{A.6}$$

where the function

$$F(\underline{R}) := -\nabla E^{\text{pot}}(\underline{R}) \tag{A.7}$$

describes *forces* acting on the particles due to their coordinates. Now the trajectory can be determined from the initial state $(R(0), \dot{R}(0))^T \in \mathbb{R}^{2dN}$.

In the statistical mechanics, we consider the evolution of very large systems where the number N of particles reaches realistic, proportional to the Avogadro number, values of order 10^{23}. The number of the corresponding Hamilton equations becomes overwhelming, but such a system still obeys the laws of mechanics. This allows us to derive a suitable evolution equation for the distribution of the particles, as it was done in [Español-2004]. Let us denote the trajectory of the system with $X(t) := (R(t), P(t))^T$ and an instantaneous state with $\underline{X} := (\underline{R}, \underline{P})^T$. Then, we can summarize the Hamilton equations to

$$\dot{X}(t) = L \cdot \nabla H(X(t)), \tag{A.8}$$

where

$$L := \begin{pmatrix} 0 & \mathbb{1} \\ -\mathbb{1} & 0 \end{pmatrix}.$$

If we know the initial state $X(0)$, then formally,

$$X(t) =: \Gamma_t X(0)$$

defines the time evolution operator Γ_t with natural properties

$$\Gamma_0 \equiv \mathbb{1}, \quad \Gamma_t \Gamma_s \equiv \Gamma_{t+s}, \quad \forall t, s,$$

and a kind of volume-conserving property,

$$|\det(\Gamma_t)| = 1, \quad \forall t. \tag{A.9}$$

In a large system, we consider the evolution of the time-dependent probability density $\mathcal{P} : \mathbb{R}^{2dN} \times [0, \infty) \to \mathbb{R}$ of states. Instead of an initial state, we know a certain distribution of the initial state, given by the probability density $\mathcal{P}^{\text{init}} : \mathbb{R}^{2dN} \to \mathbb{R}$, such that

$$\mathcal{P}(\underline{X}, 0) = \mathcal{P}^{\text{init}}(\underline{X})$$

holds for all states $\underline{X}$ in an arbitrary set $\Omega \subset \mathbb{R}^{2dN}$ with $|\Omega| > 0$. Since the evolution is deterministic, the probabilities

$$\mathbf{P}\left[X(0) \in \Omega\right] = \mathbf{P}\left[X(t) \in \Gamma_t \Omega\right]$$

are equal and we can write this equality in terms of the probability density,

$$\int_\Omega \mathcal{P}(\underline{X}, 0) d\underline{X} = \int_{\Gamma_t \Omega} \mathcal{P}(\underline{X}, t) d\underline{X}.$$

Then, using the Jacobi transformation formula and (A.9), we obtain

$$\int_\Omega \mathcal{P}(\underline{X}, 0) d\underline{X} = \int_\Omega \mathcal{P}(\Gamma_t \underline{X}, t) d\underline{X}.$$

Since Ω was arbitrary, the equality holds also for the integrands, especially for $\underline{X} = X(0)$, what yields the *Liouville theorem*

$$\mathcal{P}(X(0), 0) = \mathcal{P}(X(t), t), \tag{A.10}$$

that is, the probability density remains constant along the trajectory. The total time derivative

$$\begin{aligned}
0 &= \frac{d\mathcal{P}(X(t), t)}{dt} \\
&= \frac{\partial \mathcal{P}(X(t), t)}{\partial t} + \left.\frac{\partial \mathcal{P}(\underline{X}, t)}{\partial \underline{X}}\right|_{\underline{X}=X(t)} \cdot \dot{X}(t) \\
&= \frac{\partial \mathcal{P}(X(t), t)}{\partial t} + \left.\frac{\partial \mathcal{P}(\underline{X}, t)}{\partial \underline{X}}\right|_{\underline{X}=X(t)} \cdot L \cdot \nabla H(X(t)) \\
&\overset{D=\nabla^T}{=} \frac{\partial \mathcal{P}(X(t), t)}{\partial t} + DH(X(t)) \cdot L^T \cdot \nabla \mathcal{P}(X(t), t) \\
&= \frac{\partial \mathcal{P}(X(t), t)}{\partial t} - DH(X(t)) \cdot L \cdot \nabla \mathcal{P}(X(t), t)
\end{aligned}$$

leads to the *Liouville equation*

$$\frac{\partial \mathcal{P}(\underline{X},t)}{\partial t} = -\mathbb{L}\mathcal{P}(\underline{X},t), \tag{A.11}$$

where

$$\mathbb{L} \;:\equiv\; -DH \cdot L \cdot \nabla \tag{A.12}$$

is the *Liouville operator*.

Now we let the time go to infinity in order to see the state into which our large system evolves. Considering the complexity of the interactions in such a system, we can assume that the evolution is unstable/chaotic. That is, the system visits all possible states, such that any initial state/distribution appears meaningless. We say that after sufficiently long *relaxation time*, the system reaches the *equilibrium* – there is the stationary (or equilibrium) probability density

$$\mathcal{P}^{\mathrm{eq}}(\underline{X}) := \lim_{t\to\infty} \mathcal{P}(\underline{X},t), \quad \forall \underline{X} \in \mathbb{R}^{2dN}. \tag{A.13}$$

For any observable $A = A(\underline{X})$, we can consider its *time average*

$$\overline{A} := \lim_{\Theta\to\infty} \frac{1}{\Theta} \int_0^\Theta A(X(t))dt \tag{A.14}$$

or its *ensemble average*

$$\langle A\rangle := \int A(\underline{X})\mathcal{P}^{\mathrm{eq}}(\underline{X})d\underline{X}. \tag{A.15}$$

In practice, we often assume the *Ergodic hypothesis*,

$$\langle A\rangle = \overline{A}. \tag{A.16}$$

For instance, we shall need it in Appendix B dedicated to computer simulation.

The above formulation mirrors the fact that we actually consider not one system corresponding to a certain initial state, but a whole family (*ensemble*) of systems completely determined by a small set of *dynamical invariants*. The latter are the components of the vector-valued function $J = J(\underline{X})$ with the total time derivative

$$\dot{J}(X(t)) = 0. \tag{A.17}$$

In other words, we assume that there is a function f with

$$\mathcal{P}^{\mathrm{eq}}(\underline{X}) = f(J(\underline{X})) \tag{A.18}$$

and derive it in the following. Clearly, for any given value $\tilde{J}$ of J at equilibrium, there is a set

$$\Omega^{\mathrm{eq}}(\tilde{J}) := \{\underline{X} | J(\underline{X}) = \tilde{J}\}$$

of compatible states with the volume

$$Q^{\mathrm{eq}}(\tilde{J}) := |\Omega^{\mathrm{eq}}(\tilde{J})|.$$

Therefore, we can write the distribution $f^{\mathrm{eq}} = f^{\mathrm{eq}}(\tilde{J})$ of all possible values of the dynamical invariants at equilibrium in terms of the equilibrium probability density, that is,

$$\begin{aligned} f^{\mathrm{eq}}(\tilde{J}) &= \int \mathcal{P}^{\mathrm{eq}}(\underline{X})\delta(J(\underline{X}) - \tilde{J})d\underline{X} \\ &\overset{(A.18)}{=} \int f(J(\underline{X}))\delta(J(\underline{X}) - \tilde{J})d\underline{X} \\ &\overset{\text{Dirac-}\delta}{=} \int f(\tilde{J})\delta(J(\underline{X}) - \tilde{J})d\underline{X} \\ &= f(\tilde{J})Q^{\mathrm{eq}}(\tilde{J}). \end{aligned}$$

Inserting this into (A.18), we obtain the probability density

$$\mathcal{P}^{\mathrm{eq}}(\underline{X}) = \frac{1}{Q^{\mathrm{eq}}(J(\underline{X}))} f^{\mathrm{eq}}(J(\underline{X})) \tag{A.19}$$

governed exclusively by the dynamical invariants.

For instance, the Hamiltonian H is a dynamical invariant due to (A.2), and we can define an ensemble of closed systems of N particles in a container of volume V with energy $E = H(X(0))$, which is called the *microcanonical* ensemble. At equilibrium, the distribution f^{eq} of the energy E is time-independent and must be consistent with the given initial value, that is,

$$f^{\mathrm{eq}}(E) = \delta(H(\underline{X}) - E).$$

Using (A.19), we can derive the *microcanonical* probability density

$$\mathcal{P}^{\mathrm{mc}}(\underline{X}) = \frac{1}{Q^{\mathrm{mc}}(E)}\delta(H(\underline{X}) - E), \tag{A.20}$$

where the volume

$$Q^{\mathrm{mc}}(E) := \int \delta(H(\underline{X}) - E)d\underline{X} \tag{A.21}$$

is called the *microcanonical partition function*.

There are also other ensembles and we can derive them from the microcanonical ensemble. Following [LL-1980], we split a large closed system in two subsystems, such that they can exchange the energy. We let one system, described by tuple (N, V, E), be significantly smaller than the other one, descibed by tuple $(N_\infty, V_\infty, E_\infty)$. The larger system is called the *heat bath* – it will determine the evolution of the smaller subsystem by giving energy, if the system is ″colder″, and by taking energy, if the system is ″warmer″. The *temperature* is given by

$$T := \frac{1}{\frac{\partial S(E)}{\partial E}}, \tag{A.22}$$

where

$$S(E) := k_B \ln(Q^{\mathrm{mc}}(E)) \tag{A.23}$$

is the *entropy* and k_B is the *Boltzmann constant*. If the exchange of energy stops, that is, if

$$T = T_\infty,$$

the subsystems are in the *thermal equilibrium* with each other. Clearly, the heat bath plays the decisive role in the value of the equilibrium temperature, therefore it is also called the *thermostat*. The ensemble governed by invariants (N, V, T) is called the *canonical* ensemble. The canonical probability density and partition function are

$$\begin{aligned} \mathcal{P}^{\mathrm{c}}(\underline{X}) &= \frac{1}{(2\pi\hbar)^{dN} N! Q^{\mathrm{c}}} \exp(-\beta H(\underline{X})), && \text{(A.24)} \\ Q^{\mathrm{c}} &:= \frac{1}{(2\pi\hbar)^{dN} N!} \int \exp(-\beta H(\underline{X})) d\underline{X}, && \text{(A.25)} \end{aligned}$$

respectively, where

$$\beta := \frac{1}{k_B T} \tag{A.26}$$

is called the *inverse temperature*.

The function $\mathcal{P}^{\mathrm{c}}$ is often separated into the distribution of the particle coordinates and momenta. The first part of the distribution,

$$\begin{aligned} \mathcal{P}^{\mathrm{c}}(\underline{R}) &= \int \mathcal{P}^{\mathrm{c}}(\underline{R}, \underline{P}) d\underline{P} \\ &= \frac{\int \exp(-\beta H(\underline{R}, \underline{P})) d\underline{P}}{\int \exp(-\beta H(\underline{R}, \underline{P})) d\underline{R} d\underline{P}} \\ &= \frac{\int \exp(-\beta E^{\mathrm{kin}}(\underline{P})) d\underline{P}}{\int \exp(-\beta E^{\mathrm{kin}}(\underline{P})) d\underline{P}} \cdot \frac{\exp(-\beta E^{\mathrm{pot}}(\underline{R}))}{\int \exp(-\beta E^{\mathrm{pot}}(\underline{R})) d\underline{R}} \\ &= \frac{1}{Z^{\mathrm{c}}} \exp(-\beta E^{\mathrm{pot}}(\underline{R})), && \text{(A.27)} \end{aligned}$$

plays an important role in the theory of equilibrium fluids and will be considered later in this appendix. The normalization integral over the coordinates (configurations)

$$Z^{\mathrm{c}} := \int \exp(-\beta E^{\mathrm{pot}}(\underline{R})) d\underline{R} \tag{A.28}$$

is called the *configuration integral* and can only be obtained in simplified circumstances. The second part of the distribution concerning the momenta,

$$\begin{aligned} \mathcal{P}^{\mathrm{c}}(\underline{P}) &= \int \mathcal{P}^{\mathrm{c}}(\underline{R}, \underline{P}) d\underline{R} \\ &= \frac{\int \exp(-\beta H(\underline{R}, \underline{P})) d\underline{R}}{\int \exp(-\beta H(\underline{R}, \underline{P})) d\underline{R} d\underline{P}} \\ &= \frac{\int \exp(-\beta E^{\mathrm{pot}}(\underline{R})) d\underline{R}}{\int \exp(-\beta E^{\mathrm{pot}}(\underline{R})) d\underline{R}} \cdot \frac{\exp(-\beta E^{\mathrm{kin}}(\underline{P}))}{\int \exp(-\beta E^{\mathrm{kin}}(\underline{P})) d\underline{P}} \\ &= \frac{1}{\int \exp(-\beta E^{\mathrm{kin}}(\underline{P})) d\underline{P}} \exp(-\beta E^{\mathrm{kin}}(\underline{P})). && \text{(A.29)} \end{aligned}$$

is the *Maxwell-Boltzmann velocity distribution*. Its normalization integral can be obtained explicitly

$$\begin{aligned} \int \exp(-\beta E^{\mathrm{kin}}(\underline{P})) d\underline{P} &= \left(\int_{-\infty}^{\infty} \exp\left(-\frac{\beta p^2}{2M} \right) dp \right)^{dN} \\ &= \left(\sqrt{\frac{2M}{\beta}} \int_{-\infty}^{\infty} \exp\left(-q^2 \right) dq \right)^{dN} \\ &= \left(\frac{2\pi M}{\beta} \right)^{dN/2} = \left(\frac{2\pi\hbar}{\Lambda} \right)^{dN}, && \text{(A.30)} \end{aligned}$$

where

$$\Lambda := \sqrt{\frac{2\pi\beta\hbar^2}{M}} \tag{A.31}$$

is the *de Broglie thermal wavelength* and $\hbar$ is the *Planck constant*.

We emphasize that different ensembles are just different descriptions of systems in the equilibrium. For example, in the thermal equilibrium, the total energy is conserved (no exchange) and the microcanonical ensemble can be used to describe the subsystems. We defined the temperature by considering the special splitting of a large closed system, but it is also defined for all other ensembles. Additionally, we can consider the exchange of volume and particles between subsystems, in order to define the *pressure*

$$P := -\frac{\partial E(V)}{\partial V} \tag{A.32}$$

and the *chemical potential*

$$\mu := \frac{\partial E(N)}{\partial N}. \tag{A.33}$$

The ensemble governed by invariants (μ, V, T) is called the *grand canonical* ensemble. One can show that the probability density of dynamical states in the grand canonical ensemble is

$$\mathcal{P}^{\mathrm{gc}}(\underline{X}; N) = \frac{1}{(2\pi\hbar)^{dN} N! Q^{\mathrm{gc}}} \exp(-\beta(H(\underline{X}) - \mu N)), \tag{A.34}$$

where

$$Q^{\mathrm{gc}} := \sum_{N=0}^{\infty} \frac{e^{\beta\mu N}}{(2\pi\hbar)^{dN} N!} \int \exp(-\beta H(\underline{X})) d\underline{X} \tag{A.35}$$

is the *grand canonical partition function*. It is convenient to introduce the *activity*

$$a := \frac{e^{\beta\mu}}{\Lambda^d}, \tag{A.36}$$

and use the (intuitively clear) relation to the canonical probability density,

$$\mathcal{P}^{\mathrm{gc}}(\underline{X}; \tilde{N}) = \mathbf{P}\left[N = \tilde{N}\right] \cdot \mathcal{P}^{\mathrm{c}}(\underline{X})\big|_{N=\tilde{N}}, \tag{A.37}$$

where

$$\begin{aligned}
\mathbf{P}\left[N = \tilde{N}\right] &= \int \mathcal{P}^{\mathrm{gc}}(\underline{X}; \tilde{N}) d\underline{X} \\
&= \frac{1}{(2\pi\hbar)^{d\tilde{N}} \tilde{N}! Q^{\mathrm{gc}}} \int \exp(-\beta(H(\underline{X}) - \mu\tilde{N})) d\underline{X} \\
&= \frac{e^{\beta\mu\tilde{N}}}{(2\pi\hbar)^{d\tilde{N}} \tilde{N}! Q^{\mathrm{gc}}} \int \exp(-\beta H(\underline{X}))\big|_{N=\tilde{N}} d\underline{X} \\
&= \frac{e^{\beta\mu\tilde{N}}}{(2\pi\hbar)^{d\tilde{N}} \tilde{N}! Q^{\mathrm{gc}}} \left(\frac{2\pi\hbar}{\Lambda}\right)^{d\tilde{N}} Z^{\mathrm{c}}\big|_{N=\tilde{N}} \\
&= \frac{a^{\tilde{N}}}{\tilde{N}! Q^{\mathrm{gc}}} Z^{\mathrm{c}}\big|_{N=\tilde{N}}
\end{aligned} \tag{A.38}$$

is the probability that the system contains precisely $\tilde{N}$ particles. A similar relation can be derived for the partition functions,

$$Q^{\mathrm{gc}} = \sum_{N=0}^{\infty} \frac{a^N}{N!} Z^{\mathrm{c}}. \tag{A.39}$$

In the statistical thermodynamics, we leave the probability densities and describe different ensembles exclusively through the dynamical invariants, which are called in the new context the *thermodynamic quantities*. It is usual to separate the quantities in the *extensive* (additive), like

$$\begin{aligned} N &= N_1 + N_2, \\ V &= V_1 + V_2, \\ E &= E_1 + E_2, \\ S &= S_1 + S_2, \end{aligned}$$

and *intensive* (non-additive), like

$$\begin{aligned} T &= T_1 = T_2, \\ P &= P_1 = P_2, \\ \mu &= \mu_1 = \mu_2. \end{aligned}$$

Further, the extensive quantities N, V, S are seen as *conjugated* to the intensive quantities μ, P, T, respectively. The corner stones of the thermodynamics are the *thermodynamic potentials* – functions, which allow to derive the quantities from their conjugated counterparts. For instance,

$$F := E - TS = -k_B T \ln Q^{\mathrm{c}}, \tag{A.40}$$

$$\Phi := F - \mu N = -PV = -k_B T \ln Q^{\mathrm{gc}} \tag{A.41}$$

are the thermodynamic potentials of the canonical and grand canonical ensembles, respectively. Conveniently, the entropy $S(E)$ can be also seen as the thermodynamic potential of the microcanonical ensemble (see (A.23)), but often, the energy $E(S)$ is preferred. Any thermodynamic quantity can be obtained from the total differentials

$$dE = TdS - PdV + \mu dN, \tag{A.42}$$

$$dF = -SdT - PdV + \mu dN, \tag{A.43}$$

$$d\Phi = -SdT - PdV - Nd\mu. \tag{A.44}$$

Equation (A.42) is often referred to as the *first law of thermodynamics*. One of the most important tasks of thermodynamics is to find the *equation of state* for the given system, that is, an equation of the form

$$f(T, P, \rho) = 0,$$

coupling the temperature T, pressure P and the *(number) density*

$$\rho := \frac{N}{V}. \tag{A.45}$$

Example "Ideal Gas":
Ideal gas is the system of particles without interactions, that is, where the potential energy $E^{\text{pot}} \equiv 0$ and from the mechanical point of view, only the momenta of particles can be considered. From the thermodynamic viewpoint, due to missing interactions, many integrals become trivially obtainable, for instance,

$$\begin{aligned}
Z^{\text{c}} &= V^N, \\
Q^{\text{c}} &= \frac{V^N}{\Lambda^{dN} N!}, \\
Q^{\text{gc}} &= \sum_{N=0}^{\infty} \frac{a^N}{N!} V^N = e^{aV}, \\
F &= -k_B T \ln\left(\frac{V^N}{\Lambda^{dN} N!}\right) \\
&\overset{\textit{Stirling}}{\approx} -k_B T(N \ln V - dN \ln \Lambda - N \ln N + N), \\
\Phi &= -k_B T \ln e^{aV} = -k_B T a V.
\end{aligned}$$

Then, the first law of thermodynamics yields the equation of state for the ideal gas,

$$P \overset{\text{(A.43)}}{=} - \left.\frac{\partial F}{\partial V}\right|_{N,T\equiv\text{const}} = \rho k_B T. \tag{A.46}$$

Even more, we have

$$P \overset{\text{(A.41)}}{=} -\frac{1}{V}\Phi = a k_B T$$

and by comparing to (A.46), we state that the ideal gas activity $a = \rho$. ◇

We can see in the above example that, disregarding the different abstraction levels, the classical dynamics and the statistical thermodynamics do not loose the link to each other. Using this link, one can show a more exact equation of state,

$$P = \rho k_B T - \frac{1}{Vd}\left\langle \sum_{I=1}^{N} \vec{R}_I \cdot \vec{\nabla}_I E^{\text{pot}}(\underline{R}) \right\rangle, \tag{A.47}$$

known as the *virial equation*. Setting $E^{\text{pot}} \equiv 0$, we see that it is consistent with our example.

A.2 Definition of the RDF for a Simple Fluid

Now, when we understand the dynamics of a large system towards the equilibrium state, we can start with the subject of this appendix. We want to describe the structure of liquids and gases, which are systems of many moving particles. Liquid, gas and solid are the three classical states of matter (*phases*). Liquid and gas are also called *fluid* for their ability to flow and take the shape of a container. However, while a gas tries to fill the whole container at cost of the density, a liquid keeps its density nearly constant. The densities of both a liquid and a solid are of the same order and much higher than in a gas. Since the particles of a solid do not move almost ($|E^{\text{kin}}| \ll |E^{\text{pot}}|$), we consider only fluid phase in the following. For the sake of simplicity, we restrict our consideration to the simple fluids, where the particles are spherical.

Following [HM-2006], we model a *simple fluid* as a large system of $N \in \mathbb{N}$ identical particles with mass $M \in (0, \infty)$ and the Hamiltonian of the form (A.3), so that we can forget their momenta and just work with their coordinates $\underline{R} \in \mathbb{R}^{dN}$ and the potential energy. The latter is nothing else than N-body interaction potential, thus we approximate it via the sum

$$E^{\text{pot}}(\underline{R}) := \frac{1}{2} \sum_{I=1}^{N} \sum_{J \neq I}^{N} U^{(2)}(\vec{R}_I, \vec{R}_J) \tag{A.48}$$

of the pair interactions given by potentials $U^{(2)} : \mathbb{R}^d \times \mathbb{R}^d \to \overline{\mathbb{R}}$. In the following, we assume that the interaction potential is translationally invariant, that is,

$$U^{(2)}(\vec{X}, \vec{Y}) = U^{(2)}(\vec{X} + \vec{Z}, \vec{Y} + \vec{Z}), \quad \forall \vec{Z} \in \mathbb{R}^d, \tag{A.49}$$

and rotationally invariant, that is,

$$U^{(2)}(\vec{X}, \vec{Y}) = U^{(2)}(A\vec{X}, A\vec{Y}), \quad \forall A \in \mathrm{SO}(d). \tag{A.50}$$

In this case, we obtain

$$\begin{aligned} U^{(2)}(\vec{X}, \vec{Y}) &\overset{\text{(A.49)}}{=} U^{(2)}(0, \vec{Y} - \vec{X}) \\ &\overset{\text{(A.50)}}{=} U^{(2)}(0, |\vec{Y} - \vec{X}|\vec{e}_1), \end{aligned}$$

that is, via

$$U(r) := U^{(2)}(0, r\vec{e}_1), \tag{A.51}$$

we define a *radial* potential $U : (0, \infty) \to \mathbb{R}$ with

$$U^{(2)}(\vec{X}, \vec{Y}) = U(|\vec{X} - \vec{Y}|), \quad \forall \vec{X}, \vec{Y} \in \mathbb{R}^d.$$

The physics has a collection of common interaction potentials, but not all of them are proper for modeling of the liquid state. Such potential U must at least reflect the *Pauli exclusion principle*, that is,

$$\lim_{r \to 0} U(r) = \infty,$$

and vanish, if two particles are too far from each other, that is,

$$\lim_{r \to \infty} U(r) = 0.$$

For example, the *hard-sphere potential*

$$U^{\text{HS}}(r) := \begin{cases} \infty, & 0 < r < \sigma, \\ 0, & \sigma \leq r, \end{cases} \tag{A.52}$$

is often used for fluid phase simulations. The parameter $\sigma > 0$ represents the size of the particles, such that two particles cannot be closer than their sizes allow. However, fluid is quite not a liquid, until the potential has an attractive part keeping the particles together and forming a stable liquid phase. In contrast, the *square-well potential*

$$U^{\text{SW}}(r) := \begin{cases} \infty, & 0 < r < \sigma, \\ -\varepsilon, & \sigma \leq r < \gamma\sigma, \\ 0, & \gamma\sigma \leq r, \end{cases} \tag{A.53}$$

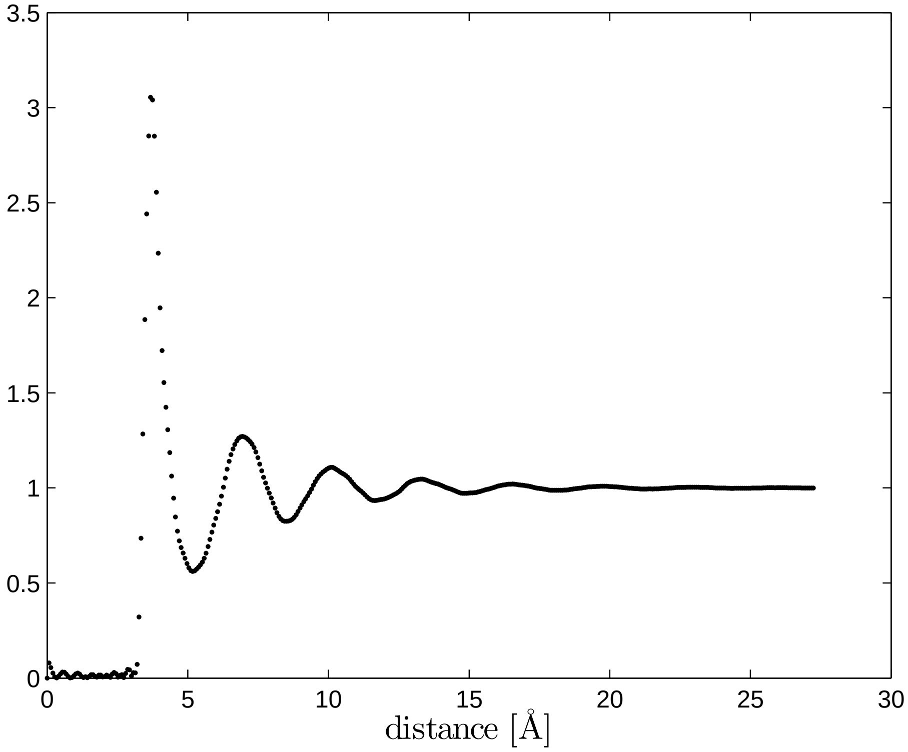

Figure A.1: A radial distribution function of liquid argon, obtained in a neutron scattering experiment [YKWK-1973].

has an attractive well with depth $\varepsilon > 0$ and width $\sigma(\gamma - 1) > 0$. Another appropriate choice for liquid simulations is the *hard-core Yukawa potential*

$$U^{\mathrm{Y}}(r) := \begin{cases} \infty, & 0 < r < \sigma, \\ -\frac{\varepsilon\sigma}{r} \exp\left(-\lambda\left(\frac{r}{\sigma} - 1\right)\right), & \sigma \leq r, \end{cases} \tag{A.54}$$

with $\lambda > 0$. Due to quantum-mechanical reasons, the leading term in the series expansion of the attractive interaction between neutral particles is of order $\mathcal{O}(r^{-6})$ for large r, what suggests the *Buckingham potential*

$$U^{\mathrm{B}}(r) := Ae^{-Br} - \frac{C}{r^6} \tag{A.55}$$

and the famous *Lennard-Jones potential*

$$U^{\mathrm{LJ}}(r) := 4\varepsilon\left(\left(\frac{\sigma}{r}\right)^{12} - \left(\frac{\sigma}{r}\right)^{6}\right). \tag{A.56}$$

We notice that all potentials are piecewise smooth, real-valued functions on $(0, \infty)$ with negative, but finite minimal values.

Even though the interaction potential allows us to derive the equations of motion for the particles, we are not interested in the exact dynamics and rather look at the system from the statistical viewpoint. We assume the fluid to be at equilibrium, where the dynamical states obey a certain probability density $\mathcal{P}^{\mathrm{eq}}$. Similar to the interaction potential, which specifies the energy for the given particle coordinates and takes a radially symmetric form in our model, the distribution can posess some symmetries, which allow us to reduce the distribution to a function, which is translationally and rotationally invariant. The latter is called the *radial distribution function* (RDF). This function describes the distribution of the distance between pairs of particles and can be determined experimentally for a concrete matter by neutron or x-ray scattering (see Figure A.1).

In order to give an explicit definition of the RDF, we have to choose one of the ensembles from the framework of statistical mechanics. Therefore, the "definitions" may be also read as derivations. We present the definition of the RDF in the grand canonical ensemble (or *μVT-ensemble*, after governing invariants), where

I) the chemical potential μ is constant,

II) the fluid is contained in a region $\Omega \subseteq \mathbb{R}^d$ of constant volume V, e.g.

$$\{\vec{R}_I\}_{1\le I\le N} \subset \Omega := \left[-\frac{L}{2}, \frac{L}{2}\right]^d, \quad V = L^d, \quad L > 0,$$

III) the temperature T is constant,

and in the canonical ensemble (or *NVT-ensemble*), where

I) the particle number N is constant

and the properties II) and III) are inherited from the grand canonical ensemble. Clearly, different ensembles provide different models (expressions), but in the *thermodynamic limit*, that is, when $N \to \infty$ and $V \to \infty$ with the constant density ρ, the two descriptions become identical and agree with experimental data. We note that $V \to \infty$ leads to $L \to \infty$ and $\Omega \to \mathbb{R}^d$, that is, Ω becomes translationally and rotationally invariant. However, the infinity is unreachable in practice, so that the experimental RDF is given on a finite interval – we can see this in Figure A.1, where the interparticle distances hardly reach 30 [Å]. Thus, in our theoretical considerations, we often work with finite N and V, mostly assuming them large enough and occasionally infinite. Further, we shall switch between the ensembles in order to use their specific advantages. For these reasons, we prove the following theorems not in the mathematically rigorous manner, but in the framework of the convenient calculus that is often used in the physical literature for argumentation.

The simplest derivation of the RDF can be made in the canonical ensemble. From the statistical mechanics, we know the equilibrium probability density $\mathcal{P}^{\mathrm{c}}$ as a function of particle coordinates $\underline{R} \in \mathbb{R}^{dN}$. The function contains redundant information – since the particles of considered fluid are identical, we can interchange any I-th particle and any J-th particle, that is,

$$\mathcal{P}^{\mathrm{c}}(\vec{R}_1, \dots, \vec{R}_I, \dots, \vec{R}_J, \dots, \vec{R}_N) = \mathcal{P}^{\mathrm{c}}(\vec{R}_1, \dots, \vec{R}_J, \dots, \vec{R}_I, \dots, \vec{R}_N). \tag{A.57}$$

Further, we are not always interested in all details of the distribution, therefore we define simplified probability densities, where the unnecessary information is removed by integration. For each $1 \le n \le N$, the *(reduced) n-particle density* is

$$\rho^{(n)}(\vec{R}_1, \dots, \vec{R}_n) := \frac{N!}{(N-n)!} \int \mathcal{P}^{\mathrm{c}}(\underline{R}) d\vec{R}_{n+1} \dots d\vec{R}_N \tag{A.58}$$

and the *n-particle distribution function* is

$$g^{(n)}(\vec{R}_1, \dots, \vec{R}_n) := \frac{\rho^{(n)}(\vec{R}_1, \dots, \vec{R}_n)}{\rho^{(1)}(\vec{R}_1) \dots \rho^{(1)}(\vec{R}_n)}. \tag{A.59}$$

The following results deal with the properties of the reduced distributions, which describe the properties of the fluid. In this regard, we remind on our assumption that the interaction potential U as well as the region Ω are translationally and rotationally invariant. However, it can still happen that under these symmetric conditions, the *symmetry breaking* takes place, that is, configurations of the particles and related properties of the fluid are not symmetric. For instance, at the liquid-solid phase transition, the particles of the system form a lattice, which preserves partially the translational symmetry, while the rotational symmetry is completely out. Therefore, we assume in the following that no such phenomenon occurs.

Theorem P1:
The n-particle density is translationally and rotationally invariant.
Proof: Any rotation and any translation in $\mathbb{R}^d$ can be described as the transformation

$$\begin{aligned} \Phi : \mathbb{R}^d &\rightarrow \mathbb{R}^d, \\ \vec{X} &\mapsto A\vec{X} + \vec{Z} \end{aligned} \tag{A.60}$$

with $A \in \mathrm{SO}(d)$ and $\vec{Z} \in \mathbb{R}^d$. Then,

$$\begin{aligned} E^{\mathrm{pot}}(\Phi(\vec{R}_1), \dots, \Phi(\vec{R}_N)) &\overset{(A.48)}{=} \frac{1}{2}\sum_{i=1}^{N}\sum_{j\neq i}^{N} U(|\Phi(\vec{R}_i) - \Phi(\vec{R}_j)|) \\ &\overset{(A.60)}{=} \frac{1}{2}\sum_{i=1}^{N}\sum_{j\neq i}^{N} U(|A\vec{R}_i + \vec{Z} - A\vec{R}_j - \vec{Z}|) \\ &\overset{A\in\mathrm{SO}(d)}{=} \frac{1}{2}\sum_{i=1}^{N}\sum_{j\neq i}^{N} U(|\vec{R}_i - \vec{R}_j|) \\ &\overset{(A.48)}{=} E^{\mathrm{pot}}(\underline{R}), \end{aligned} \tag{A.61}$$

that is, the potential energy is translationally and rotationally invariant. Similarly,

$$\begin{aligned} \rho^{(n)}(\vec{R}_1, \dots, \vec{R}_n) &\overset{(A.58)}{=} \frac{1}{Z^{\mathrm{c}}}\frac{N!}{(N-n)!}\int \exp\left(-\beta E^{\mathrm{pot}}(\underline{R})\right) d\vec{R}_{n+1}\dots d\vec{R}_N \\ &\overset{(A.61)}{=} \frac{1}{Z^{\mathrm{c}}}\frac{N!}{(N-n)!}\int \exp\Big(-\beta E^{\mathrm{pot}}(\Phi(\vec{R}_1), \dots, \Phi(\vec{R}_N))\Big) d\vec{R}_{n+1}\dots d\vec{R}_N \\ &\quad \text{Substitution(s):} \\ &\quad \vec{S}_i := \Phi(\vec{R}_i), \\ &\quad d\vec{S}_i = d\vec{R}_i, \quad n+1 \leq i \leq N \\ &\overset{\mathrm{JTF}}{=} \frac{1}{Z^{\mathrm{c}}}\frac{N!}{(N-n)!} \\ &\quad \cdot \int \exp\Big(-\beta E^{\mathrm{pot}}(\Phi(\vec{R}_1), \dots, \Phi(\vec{R}_n), \vec{S}_{n+1}, \dots, \vec{S}_N)\Big) \\ &\quad \cdot d\vec{S}_{n+1}\dots d\vec{S}_N \\ &\overset{(A.58)}{=} \rho^{(n)}(\Phi(\vec{R}_1), \dots, \Phi(\vec{R}_n)). \quad \square \end{aligned}$$

Corollary:
For all $\vec{R} \in \mathbb{R}^d$, we have

$$\rho^{(1)}(\vec{R}) = \frac{N}{V} = \rho, \tag{A.62}$$

that is, the one-particle density is just the density of the fluid.
Proof:

$$\begin{aligned}
\rho^{(1)}(\vec{R}) &\overset{\text{P1}}{=} \rho^{(1)}(0) \\
&= \frac{1}{V}\int_\Omega \rho^{(1)}(0)d\vec{R}_1 \\
&\overset{\text{P1}}{=} \frac{1}{V}\int_\Omega \rho^{(1)}(\vec{R}_1)d\vec{R}_1 \\
&\overset{\text{(A.58)}}{=} \frac{1}{V}\int_\Omega \left(N\int \mathcal{P}^{\mathrm{c}}(\underline{R})d\vec{R}_2\dots d\vec{R}_N\right)d\vec{R}_1 \\
&\overset{\text{(A.27)}}{=} \frac{N}{V} = \rho. \quad \square
\end{aligned}$$

Theorem P2:
$\rho^{(n)}$ is a function of $\frac{n(n-1)}{2}$ scalar arguments.
Proof: Per definition, $\rho^{(n)}$ is a function of n vectors $\vec{R}_1, \dots, \vec{R}_n$, where the latter can be freely rotated and shifted in space, without changing the value of the function (according to Theorem P1). We take these n vectors as vertices of an $(n-1)$-simplex. This geometric figure is fully determined by the lengths of its edges $|\vec{R}_J - \vec{R}_I|$, $1 \le I \le n$, $I+1 \le J \le n$.
$\square$

According to Theorem P1, we have

$$\rho^{(2)}(\vec{R}_1, \vec{R}_2) = \rho^{(2)}(0, |\vec{R}_1 - \vec{R}_2|\vec{e}^{(1)}), \quad \forall \vec{R}_1, \vec{R}_2 \in \mathbb{R}^d. \tag{A.63}$$

Further, Theorem P2 implies directly that the pair distribution function

$$g^{(2)} \overset{\text{(A.62)}}{\equiv} \frac{1}{\rho^2}\rho^{(2)}$$

depends on only one scalar argument. In other words, there is the *radial distribution function* (RDF) $g : (0, \infty) \to \mathbb{R}$ with

$$g^{(2)}(\vec{R}_1, \vec{R}_2) = g(|\vec{R}_1 - \vec{R}_2|), \quad \forall \vec{R}_1, \vec{R}_2 \in \mathbb{R}^d.$$

Respective (A.63), the RDF is given by

$$g(r) := g^{(2)}(0, r\vec{e}^{(1)}). \tag{A.64}$$

We caution that this definition only makes sense under the above assumption of symmetry.

The definition of the RDF in the grand canonical ensemble can be obtained in the similar way. While in the canonical ensemble, the number of particles is an implicit parameter of all distributions and quantities, in the grand canonical ensemble, where the chemical potential μ and not N is constant, the number of particles is an explicit variable of the distribution. Relation (A.37) between the two ensembles suggests to define the *(reduced) n-particle density* for each $1 \leq n \leq N$ via

$$\rho^{\mathrm{gc},(n)}(\vec{R}_1, \ldots, \vec{R}_n) := \sum_{\tilde{N}=n}^{\infty} \mathbf{P}\left[N = \tilde{N}\right] \cdot \rho^{(n)}(\vec{R}_1, \ldots, \vec{R}_n)\Big|_{N=\tilde{N}}. \tag{A.65}$$

Then, we can adopt the expressions (A.59) for the n-particle distribution function and (A.64) for the RDF.

Example "Ideal Gas":
Since the potential energy $E^{\mathrm{pot}} \equiv 0$, we obtain

$$\begin{aligned} Z^{\mathrm{c}} &= \int \exp(-\beta E^{\mathrm{pot}}(\underline{R}))d\underline{R} = V^N, \\ P^{\mathrm{c}}(\underline{R}) &= \frac{1}{Z^{\mathrm{c}}}\exp(-\beta E^{\mathrm{pot}}(\underline{R})) = \frac{1}{V^N}, \\ \rho^{(2)}(\vec{R}_1, \vec{R}_1) &= N(N-1)\int P^{\mathrm{c}}(\underline{R})d\vec{R}_3 \ldots d\vec{R}_N \\ &= \frac{N(N-1)V^{N-2}}{V^N} = \frac{N(N-1)}{V^2}, \\ g(r) &= \frac{1}{\rho^2}\rho^{(2)}(0, r\vec{e}^{(1)}) = 1 - \frac{1}{N}. \end{aligned}$$

that is, in the thermodynamic limit,

$$g(r) = 1 \tag{A.66}$$

for the ideal gas. ◇

A.3 General Properties of the RDF

The two ensembles provide us a powerful calculus, which can be applied to derive some general properties of the RDF. Due to equivalence of the two descriptions, we can switch between the ensembles, in order to use their specific advantages for the particular derivation.

Theorem P3:
We can write the pair distribution function $g^{(2)}$ and the RDF in terms of ensemble averages of Dirac δ-functions,

$$g^{(2)}(\vec{X}, \vec{Y}) = \frac{1}{\rho^2}\sum_{I=1}^{N}\sum_{J\neq I}^{N}\left\langle \delta(\vec{X} - \vec{R}_I)\delta(\vec{Y} - \vec{R}_J)\right\rangle, \tag{A.67}$$

$$g(r) = \frac{V}{N^2}\sum_{I=1}^{N}\sum_{J\neq I}^{N}\left\langle \delta(r\vec{e}^{(1)} - \vec{R}_J + \vec{R}_I)\right\rangle. \tag{A.68}$$

Proof:

$$\begin{aligned}
g^{(2)}(\vec{X},\vec{Y}) &\overset{\text{(A.59)}}{=} \frac{\rho^{(2)}(\vec{X},\vec{Y})}{\rho^{(1)}(\vec{X})\rho^{(1)}(\vec{Y})} \\
&\overset{\text{(A.62)}}{=} \frac{1}{\rho^2}\rho^{(2)}(\vec{X},\vec{Y}) \\
&\overset{\text{(A.58)}}{=} \frac{1}{\rho^2}N(N-1)\int \mathcal{P}^{\text{c}}(\vec{X},\vec{Y},\vec{R}_3,\dots,\vec{R}_N)d\vec{R}_3\dots d\vec{R}_N \\
&\overset{\text{Dirac-}\delta}{=} \frac{1}{\rho^2}N(N-1)\int \delta(\vec{X}-\vec{R}_1)\delta(\vec{Y}-\vec{R}_2)\mathcal{P}^{\text{c}}(\underline{R})d\underline{R} \\
&\overset{\text{(A.57)}}{=} \frac{1}{\rho^2}\sum_{I=1}^{N}\sum_{J\neq I}^{N}\int \delta(\vec{X}-\vec{R}_I)\delta(\vec{Y}-\vec{R}_J)\mathcal{P}^{\text{c}}(\underline{R})d\underline{R} \\
&\overset{\text{(A.15)}}{=} \frac{1}{\rho^2}\sum_{I=1}^{N}\sum_{J\neq I}^{N}\left\langle \delta(\vec{X}-\vec{R}_I)\delta(\vec{Y}-\vec{R}_J)\right\rangle, \\
g(r) &\overset{\text{(A.64)}}{=} g^{(2)}(0,r\vec{e}^{(1)}) \\
&\overset{\text{P1}}{=} \frac{1}{V}\int g^{(2)}(\vec{W},r\vec{e}^{(1)}+\vec{W})d\vec{W} \\
&\overset{\text{(A.67)}}{=} \frac{1}{V}\int \frac{1}{\rho^2}\sum_{I=1}^{N}\sum_{J\neq I}^{N}\left\langle \delta(\vec{W}-\vec{R}_I)\delta(r\vec{e}^{(1)}+\vec{W}-\vec{R}_J)\right\rangle d\vec{W} \\
&\overset{\text{Dirac-}\delta}{=} \frac{V}{N^2}\sum_{I=1}^{N}\sum_{J\neq I}^{N}\left\langle \delta(r\vec{e}^{(1)}-\vec{R}_J+\vec{R}_I)\right\rangle. \quad \square
\end{aligned}$$

The above theorem shows that $g(r)$ tests for each particle pair, if they are at distance r in average. Further, the next theorem reveals that the RDF also counts the particles during testing.

Theorem P4:

$$\rho\int g(r)|\partial B(r)|dr = N-1.$$

Proof:

$$\begin{aligned}
\int g(r)|\partial B(r)|dr &= \frac{N(N-1)}{\rho^2}\int \mathcal{P}^{\text{c}}(0,r\vec{e}_1,\vec{R}_3,\dots,\vec{R}_N)|\partial B(r)|dr d\vec{R}_3\dots d\vec{R}_N \\
&\overset{\text{JTF}}{=} \frac{N(N-1)}{\rho^2}\int \mathcal{P}^{\text{c}}(0,\vec{R}_2,\dots,\vec{R}_N)d\vec{R}_2\dots d\vec{R}_N \\
&\overset{\text{JTF}}{=} \frac{N(N-1)}{V\rho^2}\int \mathcal{P}^{\text{c}}(\vec{R}_1,\dots,\vec{R}_N)d\vec{R}_1\dots d\vec{R}_N \\
&\overset{\text{(A.27)}}{=} \frac{N-1}{\rho}. \quad \square
\end{aligned}$$

Further, we can obtain the pressure P and the potential energy E^{pot} from the given RDF.

Theorem P5:

$$\begin{aligned} P &= \rho k_B T - \frac{\rho^2}{2d}\int_0^\infty DU(r)g(r)|\partial B(r)|r dr, && \text{(A.69)} \\ \left\langle E^{\text{pot}}\right\rangle &= \frac{N^2}{2V}\int_0^\infty U(r)g(r)|\partial B(r)|dr. && \text{(A.70)} \end{aligned}$$

Proof: We use the virial equation to write the pressure P in the form

$$\begin{aligned} P &\overset{(A.47)}{=} \rho k_B T - \frac{1}{Vd}\left\langle \frac{1}{2}\sum_{I=1}^{N}\sum_{J\neq I}^{N} DU(|\vec{R}_{IJ}|)|\vec{R}_{IJ}|\right\rangle \\ &\overset{(A.15)}{=} \rho k_B T - \frac{1}{2Vd}\sum_{I=1}^{N}\sum_{J\neq I}^{N}\int DU(|\vec{R}_{IJ}|)|\vec{R}_{IJ}|\mathcal{P}^{\text{c}}(\underline{R})d\underline{R} \\ &\overset{(A.57)}{=} \rho k_B T - \frac{N(N-1)}{2Vd}\int DU(|\vec{R}_{21}|)|\vec{R}_{21}|\mathcal{P}^{\text{c}}(\underline{R})d\underline{R} \\ &\overset{(A.59)}{=} \rho k_B T - \frac{N(N-1)}{2Vd}\frac{\rho^2}{N(N-1)}\int DU(|\vec{R}_{21}|)|\vec{R}_{21}|g^{(2)}(\vec{R}_1,\vec{R}_2)d\vec{R}_1 d\vec{R}_2 \\ &\overset{\text{P1}}{=} \rho k_B T - \frac{\rho^2}{2Vd}\int DU(|\vec{R}_{21}|)|\vec{R}_{21}|g^{(2)}(0,|\vec{R}_{21}|\vec{e}_1)d\vec{R}_1 d\vec{R}_2 \\ &\overset{\text{JTF}}{=} \rho k_B T - \frac{\rho^2}{2d}\int DU(|\vec{R}|)|\vec{R}|g^{(2)}(0,|\vec{R}|\vec{e}_1)d\vec{R} \\ &\overset{\text{JTF}}{=} \rho k_B T - \frac{\rho^2}{2d}\int_0^\infty DU(r)g(r)|\partial B(r)|r dr. \end{aligned}$$

Similarly, we obtain

$$\begin{aligned} \left\langle E^{\text{pot}}\right\rangle &\overset{(A.48)}{=} \left\langle \frac{1}{2}\sum_{I=1}^{N}\sum_{J\neq I}^{N} U(|\vec{R}_{IJ}|)\right\rangle \\ &\overset{(A.15)}{=} \frac{1}{2}\sum_{I=1}^{N}\sum_{J\neq I}^{N}\int U(|\vec{R}_{IJ}|)\mathcal{P}^{\text{c}}(\underline{R})d\underline{R} \\ &\overset{(A.57)}{=} \frac{N(N-1)}{2}\int U(|\vec{R}_{21}|)\mathcal{P}^{\text{c}}(\underline{R})d\underline{R} \\ &= \frac{N(N-1)}{2}\int U(|\vec{R}_{21}|)\left(\int \mathcal{P}^{\text{c}}(\underline{R})d\vec{R}_3\dots d\vec{R}_N\right)d\vec{R}_1 d\vec{R}_2 \\ &\overset{(A.59)}{=} \frac{N(N-1)}{2}\frac{\rho^2}{N(N-1)}\int U(|\vec{R}_{21}|)g^{(2)}(\vec{R}_1,\vec{R}_2)d\vec{R}_1 d\vec{R}_2 \\ &\overset{\text{P1}}{=} \frac{\rho^2}{2}\int U(|\vec{R}_{21}|)g^{(2)}(0,|\vec{R}_{21}|\vec{e}_1)d\vec{R}_1 d\vec{R}_2 \\ &\overset{\text{JTF}}{=} \frac{\rho^2 V}{2}\int U(|\vec{R}|)g^{(2)}(0,|\vec{R}|\vec{e}_1)d\vec{R} \\ &\overset{\text{JTF}}{=} \frac{N^2}{2V}\int_0^\infty U(r)g(r)|\partial B(r)|dr. \quad \square \end{aligned}$$

In a similar way, we can derive another important relation between the RDF and the underlying interaction potential.

Theorem P6:
The RDF can be written as a rescaled ensemble average of the function

$$S(r;\underline{R}) := \frac{1}{2}\sum_{I=1}^{N}\sum_{J\neq I}^{N}\delta(r-|\vec{R}_{IJ}|),$$

more precisely,

$$\langle S(r;\underline{R})\rangle = \frac{2\pi r^2 N^2}{V}g(r).$$

The advantage of this respresentation is that we can determine the functional derivative of the latter average with respect to the potential U, that is,

$$\frac{\partial\langle S(r;\underline{R})\rangle}{\partial U(s)} = -\beta(\langle S(r;\underline{R})S(s;\underline{R})\rangle - \langle S(r;\underline{R})\rangle\langle S(s;\underline{R})\rangle). \tag{A.71}$$

Proof: Evidently, the function $S(r;\underline{R})$ is nothing else than the instantaneous system configuration in terms of Dirac δ-functions. Indeed, similar to Theorem P5, we can write the instantaneous potential energy via

$$\begin{aligned}
E^{\text{pot}}(\underline{R}) &\overset{\text{(A.48)}}{=} \frac{1}{2}\sum_{I=1}^{N}\sum_{J\neq I}^{N}U(|\vec{R}_{IJ}|)\\
&\overset{\text{Dirac-}\delta}{=} \frac{1}{2}\sum_{I=1}^{N}\sum_{J\neq I}^{N}\int_0^\infty U(r)\delta(r-|\vec{R}_{IJ}|)dr\\
&= \int_0^\infty U(r)S(r;\underline{R})dr.
\end{aligned}$$

Moreover, the ensemble average over the instantaneous configurations yields a rescaled RDF, more precisely,

$$\begin{aligned}
\langle S(r;\underline{R})\rangle &= \frac{1}{2}\sum_{I=1}^{N}\sum_{J\neq I}^{N}\left\langle \delta(r-|\vec{R}_{IJ}|)\right\rangle\\
&\overset{\text{(A.15)}}{=} \frac{1}{2}\sum_{I=1}^{N}\sum_{J\neq I}^{N}\int \delta(r-|\vec{R}_{IJ}|)\mathcal{P}^{\text{c}}(\underline{R})d\underline{R}\\
&\overset{\text{(A.57)}}{=} \frac{N(N-1)}{2}\int \delta(r-|\vec{R}_{21}|)\mathcal{P}^{\text{c}}(\underline{R})d\underline{R}\\
&\overset{\text{JTF}}{=} \frac{VN(N-1)}{2}\int \delta(r-|\vec{R}_2|)\mathcal{P}^{\text{c}}(0,\vec{R}_2,\ldots,d\vec{R}_N)d\vec{R}_2\ldots d\vec{R}_N\\
&\overset{\text{JTF}}{=} \frac{VN(N-1)}{2}\int \delta(r-s)4\pi s^2\mathcal{P}^{\text{c}}(0,s\vec{e}_1,\vec{R}_3,\ldots,d\vec{R}_N)dsd\vec{R}_3\ldots d\vec{R}_N\\
&\overset{\text{Dirac-}\delta}{=} \frac{4\pi r^2VN(N-1)}{2}\int \mathcal{P}^{\text{c}}(0,r\vec{e}_1,\vec{R}_3,\ldots,d\vec{R}_N)d\vec{R}_3\ldots d\vec{R}_N\\
&= \frac{4\pi r^2VN(N-1)}{2}\frac{\rho^2}{N(N-1)}g(r)\\
&= \frac{2\pi r^2N^2}{V}g(r).
\end{aligned}$$

Then, the derivative of the ensemble average is given by

$$\begin{aligned}\frac{\partial\langle S(r;\underline{R})\rangle}{\partial U(s)} &= \frac{\partial}{\partial U(s)}\int S(r;\underline{R})\mathcal{P}^{\mathrm{c}}(\underline{R})d\underline{R}\\ &= \frac{\partial}{\partial U(s)}\left(\frac{\int S(r;\underline{R})\exp(-\beta E^{\mathrm{pot}}(\underline{R}))d\underline{R}}{Z^{\mathrm{c}}}\right)\\ &= \frac{\partial}{\partial U(s)}\left(\frac{\int S(r;\underline{R})\exp\left(-\beta\int_0^\infty U(r)S(r;\underline{R})dr\right)d\underline{R}}{\int\exp\left(-\beta\int_0^\infty U(r)S(r;\underline{R})dr\right)d\underline{R}}\right)\\ &= -\beta(\langle S(r;\underline{R})S(s;\underline{R})\rangle-\langle S(r;\underline{R})\rangle\langle S(s;\underline{R})\rangle).\quad\square\end{aligned}$$

The above results are obtained in the simple formalism of the canonical ensemble and provide nice tools for computer simulation of the fluid or for analysis of experimental data. However, using the rather complicated model of the grand canonical ensemble, we can derive even more powerful statement.

Theorem P7:
If we assume, that the activity $a=\rho$ for $\rho\to 0$, then

$$\lim_{\rho\to 0} g^{\mathrm{gc},(n)}(\vec{R}_1,\ldots,\vec{R}_n)=\exp(-\beta E^{\mathrm{pot}}(\vec{R}_1,\ldots,\vec{R}_n)).$$

Proof: We write the distribution function as the series

$$\begin{aligned}g^{\mathrm{gc},(n)}(\vec{R}_1,\ldots,\vec{R}_n) &\overset{\mathrm{P1}}{=} \frac{1}{\rho^n}\rho^{\mathrm{gc},(n)}(\vec{R}_1,\ldots,\vec{R}_n)\\ &\overset{(\mathrm{A.65})}{=} \frac{1}{\rho^n}\sum_{\tilde{N}=n}^{\infty}\mathbf{P}\left[N=\tilde{N}\right]\cdot\rho^{(n)}(\vec{R}_1,\ldots,\vec{R}_n)\Big|_{N=\tilde{N}}\\ &\overset{(\mathrm{A.38})}{=} \frac{1}{\rho^n}\sum_{\tilde{N}=n}^{\infty}\frac{a^{\tilde{N}}}{\tilde{N}!Q^{\mathrm{gc}}}\,Z^{\mathrm{c}}|_{N=\tilde{N}}\,\rho^{(n)}(\vec{R}_1,\ldots,\vec{R}_n)\Big|_{N=\tilde{N}}\\ &\overset{(\mathrm{A.58})}{=} \frac{1}{\rho^n}\sum_{\tilde{N}=n}^{\infty}\frac{a^{\tilde{N}}}{\tilde{N}!Q^{\mathrm{gc}}}\,Z^{\mathrm{c}}|_{N=\tilde{N}}\\ &\qquad\cdot\frac{\tilde{N}!}{(\tilde{N}-n)!\,Z^{\mathrm{c}}|_{N=\tilde{N}}}\int\exp(-\beta E^{\mathrm{pot}}(\vec{R}_1,\ldots,\vec{R}_{\tilde{N}}))d\vec{R}_{n+1}\ldots d\vec{R}_{\tilde{N}}\\ &\overset{(\mathrm{A.58})}{=} \frac{1}{\rho^n}\frac{1}{Q^{\mathrm{gc}}}\sum_{\tilde{N}=n}^{\infty}\frac{a^{\tilde{N}}}{(\tilde{N}-n)!}\int\exp(-\beta E^{\mathrm{pot}}(\vec{R}_1,\ldots,\vec{R}_{\tilde{N}}))d\vec{R}_{n+1}\ldots d\vec{R}_{\tilde{N}}.\end{aligned}$$

Under the assumption $a=\rho$, the density disappears from the first term of the series. That is, if we let the density ρ go to zero, the remaining terms vanish. Similarly, for $\rho\to 0$, only the first term of the series

$$\begin{aligned}Q^{\mathrm{gc}} &\overset{(\mathrm{A.39})}{=} \sum_{N=0}^{\infty}\frac{a^N}{N!}Z^{\mathrm{c}}\\ &\overset{(\mathrm{A.28})}{=} \sum_{N=0}^{\infty}\frac{a^N}{N!}\int\exp(-\beta E^{\mathrm{pot}}(\vec{R}_1,\ldots,\vec{R}_N))d\vec{R}_1\ldots d\vec{R}_N\end{aligned}$$

remains and equals 1, because the potential energy of an empty system is zero. □

We remark that $a = \rho$ for the ideal gas, as we have shown in Section A.1. In the case, where the density goes to zero, the interactions between particles are very rare, so that the system behaves nearly like the ideal gas and the assumption of Theorem P7 can be considered as given. The direct consequence of the above theorem is the equation

$$\begin{aligned}\lim_{\rho\to 0} g(r) &= \lim_{\rho\to 0} g^{(2)}(0, r\vec{e}^{(1)}) \\ &= \exp(-\beta E^{\text{pot}}(0, r\vec{e}^{(1)})) \\ &= \exp(-\beta U(r)), \end{aligned} \tag{A.72}$$

called the *low-density limit* of the RDF.

A.4 Special Case of the Lennard-Jones Potential

While the previous results are valid for the general interaction potential and show how much information can be retrieved from the RDF, we also test a special case of the Lennard-Jones potential (A.56), in order to obtain a deeper insight into the nature of the distribution. To do so, we use the formalism of the canonical ensemble and assume that our system has a large, but finite size

$$L = \sqrt[d]{V} = \sqrt[d]{\frac{N}{\rho}}.$$

We consider the RDF

$$g(r) = \frac{N(N-1)}{\rho^2} \int \mathcal{P}^{\text{c}}(0, r\vec{e}_1, \vec{R}_3, \ldots, \vec{R}_N) d\vec{R}_3 \ldots d\vec{R}_N, \quad r \in \left[0, \frac{L}{2}\right],$$

as a function of the distance, parameterized with T, L and the parameters ε, σ of the Lennard-Jones potential

$$U(r; \varepsilon, \sigma) = 4\varepsilon \left(\left(\frac{\sigma}{r}\right)^{12} - \left(\frac{\sigma}{r}\right)^{6} \right).$$

The following properties of the potential attract our attention:

$$\begin{aligned} U(r; a\varepsilon, \sigma) &= 4a\varepsilon \left(\left(\frac{\sigma}{r}\right)^{12} - \left(\frac{\sigma}{r}\right)^{6} \right) \\ &= aU(r; \varepsilon, \sigma), \\ U(r; \varepsilon, b\sigma) &= 4\varepsilon \left(\left(\frac{b\sigma}{r}\right)^{12} - \left(\frac{b\sigma}{r}\right)^{6} \right) \\ &= U\left(\frac{r}{b}; \varepsilon, \sigma\right). \end{aligned}$$

Then, the potential energy takes the form

$$E^{\text{pot}}(\underline{R}; \varepsilon, \sigma) = \frac{1}{2} \sum_{I=1}^{N} \sum_{J\neq I}^{N} U(|\vec{R}_I - \vec{R}_J|; \varepsilon, \sigma)$$

and satisfies the relations

$$
\begin{aligned}
E^{\mathrm{pot}}(\underline{R}; a\varepsilon, \sigma) &= aE^{\mathrm{pot}}(\underline{R}; \varepsilon, \sigma), && \text{(A.73)}\\
E^{\mathrm{pot}}(\underline{R}; \varepsilon, b\sigma) &= E^{\mathrm{pot}}\left(\frac{1}{b}\underline{R}; \varepsilon, \sigma\right). && \text{(A.74)}
\end{aligned}
$$

This motivates us to rewrite the RDF of the Lennard-Jones fluid in the parameterized form,

$$
\begin{aligned}
g(s; T, L, \varepsilon, \sigma) &= \frac{N(N-1)}{\rho^2}\int_{\Omega^{N-2}} \mathcal{P}^{\mathrm{c}}(0, Ls\vec{e}_1, \vec{R}_3, \ldots, \vec{R}_N; T, L, \varepsilon, \sigma)d\vec{R}_3 \ldots d\vec{R}_N\\
&= \frac{(N-1)L^{2d}}{N}\int_{\Omega^{N-2}} \mathcal{P}^{\mathrm{c}}(0, Ls\vec{e}_1, \vec{R}_3, \ldots, \vec{R}_N; T, L, \varepsilon, \sigma)d\vec{R}_3 \ldots d\vec{R}_N\\
&\overset{\mathrm{JTF}}{=} \frac{(N-1)L^{Nd}}{N}\int_{\Omega^{N-2}/L} \mathcal{P}^{\mathrm{c}}(0, Ls\vec{e}_1, L\vec{S}_3, \ldots, L\vec{S}_N; T, L, \varepsilon, \sigma)d\vec{S}_3 \ldots d\vec{S}_N
\end{aligned}
$$

for all $s \in \left[0, \frac{1}{2}\right]$.

Theorem P8:
The RDF of the Lennard-Jones fluid (as a function of s) depends on only two parameters – the first one is either T or ε, the second one is either L or σ.
Proof: Let us also parameterize the probability density of the canonical ensemble and the configuration integral,

$$
\begin{aligned}
\mathcal{P}^{\mathrm{c}}(\underline{R}; T, L, \varepsilon, \sigma) &= \frac{1}{Z^{\mathrm{c}}(T, L, \varepsilon, \sigma)}\exp(-\beta E^{\mathrm{pot}}(\underline{R}; \varepsilon, \sigma)),\\
Z^{\mathrm{c}}(T, L, \varepsilon, \sigma) &= \int_{\Omega^N} \exp(-\beta E^{\mathrm{pot}}(\underline{R}; \varepsilon, \sigma))d\underline{R}\\
&\overset{\mathrm{JTF}}{=} L^{Nd}\int_{\Omega^N/L} \exp(-\beta E^{\mathrm{pot}}(L\underline{S}; \varepsilon, \sigma))d\underline{S}. && \text{(A.75)}
\end{aligned}
$$

Then, we see that

$$
\begin{aligned}
Z^{\mathrm{c}}(T, L, a\varepsilon, b\sigma) &\overset{\text{(A.75)}}{=} L^{Nd}\int_{\Omega^N/L} \exp(-\beta E^{\mathrm{pot}}(L\underline{S}; a\varepsilon, b\sigma))d\underline{S}\\
&\overset{\substack{\text{(A.73),}\\ \text{(A.74)}}}{=} L^{Nd}\int_{\Omega^N/L} \exp\left(-a\beta E^{\mathrm{pot}}\left(\frac{L}{b}\underline{S}; \varepsilon, \sigma\right)\right)d\underline{S}\\
&= b^{Nd}\left(\frac{L}{b}\right)^{Nd}\int_{\Omega^N/L} \exp\left(-a\beta E^{\mathrm{pot}}\left(\frac{L}{b}\underline{S}; \varepsilon, \sigma\right)\right)d\underline{S}\\
&\overset{\text{(A.75)}}{=} b^{Nd}Z^{\mathrm{c}}\left(\frac{T}{a}, \frac{L}{b}, \varepsilon, \sigma\right) && \text{(A.76)}
\end{aligned}
$$

and

$$\begin{aligned}
g(s;T,L,a\varepsilon,b\sigma) &= \frac{(N-1)L^{Nd}}{NZ^{\mathrm{c}}(T,L,a\varepsilon,b\sigma)} \\
&\quad \cdot \int_{\Omega^{(N-2)}/L} \exp(-\beta E^{\mathrm{pot}}(0,Ls,LS_3,\ldots,LS_N;a\varepsilon,b\sigma)) \\
&\quad \cdot dS_3\ldots dS_N \\
&\overset{(A.76)}{=} \frac{(N-1)\left(\frac{L}{b}\right)^{Nd}}{NZ^{\mathrm{c}}\left(\frac{T}{a},\frac{L}{b},\varepsilon,\sigma\right)} \\
&\quad \cdot \int_{\Omega^{(N-2)}/L} \exp(-\beta E^{\mathrm{pot}}(0,Ls,LS_3,\ldots,LS_N;a\varepsilon,b\sigma)) \\
&\quad \cdot dS_3\ldots dS_N \\
&\overset{\substack{(A.73),\\(A.74)}}{=} \frac{(N-1)\left(\frac{L}{b}\right)^{Nd}}{NZ^{\mathrm{c}}\left(\frac{T}{a},\frac{L}{b},\varepsilon,\sigma\right)} \\
&\quad \cdot \int_{\Omega^{(N-2)}/L} \exp\left(-a\beta E^{\mathrm{pot}}\left(0,\frac{L}{b}s,\frac{L}{b}S_3,\ldots,\frac{L}{b}S_N;\varepsilon,\sigma\right)\right) \\
&\quad \cdot dS_3\ldots dS_N \\
&= g\left(s;\frac{T}{a},\frac{L}{b},\varepsilon,\sigma\right)
\end{aligned}$$

for all $s \in \left[0,\frac{1}{2}\right]$. In particular,

$$\begin{aligned}
g(s;T,L,\varepsilon,\sigma) &= g\left(s;\frac{T}{\varepsilon},\frac{L}{\sigma},1,1\right), \\
g(s;T,L,\varepsilon,\sigma) &= g\left(s;1,1,\frac{\varepsilon}{T},\frac{\sigma}{L}\right). \quad \square
\end{aligned}$$

A.5 Definition of the RDF for a Molecular Fluid

The definition of the RDF can be extended also to the case of the *molecular* fluid whose particles are identical but should not be considered as spherical, for example, the rod-shaped molecules of nitrogen $\mathtt{N}_2$ and carbon dioxide $\mathtt{CO}_2$, or the bended molecule of water $\mathtt{H}_2\mathtt{O}$. In this case, we have to model also the *bonded interactions* inside the molecules, for instance, by potentials of the form

$$\begin{aligned}
v_i^{\mathrm{bond}}(\ell) &= \frac{1}{2}k_i^{\mathrm{bond}}(\ell-\ell_i)^2, \\
v_i^{\mathrm{bend}}(\theta) &= \frac{1}{2}k_i^{\mathrm{bend}}(\theta-\theta_i)^2, \\
v_i^{\mathrm{tors}}(\phi) &= \frac{1}{2}k_i^{\mathrm{tors}}(\phi-\phi_i)^2.
\end{aligned}$$

In other words, we model a *molecule* as a composition of diverse spherical particles arranged by constants

$$\begin{aligned}
\{\ell_i : 1 \le i \le N^{\mathrm{bond}}\} &\subset \mathbb{R}, \\
\{\theta_i : 1 \le i \le N^{\mathrm{bend}}\} &\subset \mathbb{R}, \\
\{\phi_i : 1 \le i \le N^{\mathrm{tors}}\} &\subset \mathbb{R},
\end{aligned}$$

called *bond lengths*, *bending angles* and *torsion angles*, respectively. We call the constituent particles *atoms* and label them with numbers $\{1, \dots, N^{\text{atom}}\}$. The following theory is not affected by the chosen labeling, because we shall work with the maps

$$\begin{aligned} \tau : \{1, \dots, N^{\text{atom}}\} &\to \{1, \dots, N^{\text{type}}\}, \\ \nu : \{1, \dots, N^{\text{atom}}\} &\to \{1, \dots, N\}, \end{aligned}$$

assigning the given atom label to one of N^{type} types and one of N molecules. For example, two water molecules would be represented by

Label i	Type $\tau(i)$	Atom	Molecule $\nu(i)$
1	1	`H`	1
2	2	`O`	1
3	1	`H`	1
4	1	`H`	2
5	2	`O`	2
6	1	`H`	2

Surely, similar to the simple fluid, we could also describe the system through the atom coordinates

$$\{\vec{r}_i : 1 \le i \le N^{\text{atom}}\} \subset \mathbb{R}^d,$$

masses $(m_a)_{a=1}^{N^{\text{type}}}$ and the interaction potential

$$u_{a,b}^{(2)} : \mathbb{R}^d \times \mathbb{R}^d \to \overline{\mathbb{R}}$$

for each pair of atoms of a-th and b-th types, $1 \le a, b \le N^{\text{type}}$. However, this description would contain many redundant degrees of freedom – the shape of the molecules can be often considered as *rigid*, that is, the changes of the shape due to the bonded interactions are negligible, when averaged over all molecules of the fluid. On the other hand, the bond lengths, bending angles and torsion angles would not suffice for a good description – they do not specify the "positions" of the molecules. The latter, following [GG-1984], can be defined by the coordinates of molecular centers of mass

$$\vec{R}_I := \frac{1}{M} \sum_{i:\nu(i)=I} m_{\tau(i)} \vec{r}_i \in \mathbb{R}^d, \quad 1 \le I \le N,$$

and by the molecular orientations

$$W_I \in Q \subset \mathbb{R}^q, \quad 1 \le I \le N,$$

where

$$M := \sum_{i:\nu(i)=1} m_{\tau(i)}$$

is the total mass of the first molecule (molecules are identical). It is easily seen that for a suitable $Q \subset \mathbb{R}^q$, the set of variables allows to determine the positions $\{\vec{r}_i\}$ of the atoms. In $d = 3$ dimensions, the orientation of a rigid body (molecule) is given by Euler angles

$$(\psi, \varphi, \gamma) \in (0, \pi) \times (-\pi, \pi) \times (0, 2\pi),$$

that is, $Q \simeq S^2 \times S^1$ and $|Q| = 8\pi^2$. If the molecule has symmetries, the degrees of freedom reduce – for a rod-shaped molecule, the spherical coordinates

$$(\psi, \varphi) \in (0, \pi) \times (-\pi, \pi)$$

will suffice, that is, $Q \simeq S^2$ and $|Q| = 4\pi$. Finally, the potential energy for a pair of molecules is the sum of potential energies between building atoms, so that we can define the molecular pair interaction potential as

$$\begin{aligned} U^{(2)} : \mathbb{R}^d \times \mathbb{R}^d \times \mathbb{R}^q \times \mathbb{R}^q &\to \overline{\mathbb{R}}, \\ (\vec{R}_I, \vec{R}_J, W_I, W_J) &\mapsto \sum_{i:\nu(i)=I} \sum_{j:\nu(j)=J} u^{(2)}_{\tau(i),\tau(j)}(\vec{r}_i, \vec{r}_j). \end{aligned}$$

Summarizing the above definitions in other words, we just carried out a *scale transition*. We could model the molecular fluid on the *microscopic scale* – we would cope with the bonded interactions v_i^{bond}, v_i^{bend}, v_i^{tors} and non-bonded interactions $u^{(2)}_{a,b}$ of single atoms (*microscopic* particles) $\{\vec{r}_i\}$ with masses $\{m_a\}$. But in this case, we could not assume translationally and rotationally invariant interactions in the sense of definitions (A.49) and (A.50), which hold on the microscopic scale and implicitly require a single potential for all interactions. We remind that the concept of the RDF holds only under this assumption. Therefore, we prefer to consider the molecular fluid on a *mesoscopic scale*, as a family of $N \in \mathbb{N}$ identical molecules (*mesoscopic* particles) $\{(\vec{R}_I, W_I)\}$ with mass M and interaction potential $U^{(2)}$. Indeed, a non-spherical molecule, "averaged" over all orientations, has a nearly spherical shape. For fixed molecular orientations $\{W_I\}$, we obtain the relations

$$\begin{aligned} U^{(2)}(\vec{R}_I, \vec{R}_J, W_I, W_J) &= U^{(2)}(\vec{R}_I + \vec{Z}, \vec{R}_J + \vec{Z}, W_I, W_J), \quad \forall \vec{Z} \in \mathbb{R}^d, \\ U^{(2)}(\vec{R}_I, \vec{R}_J, W_I, W_J) &= U^{(2)}(A\vec{R}_I, A\vec{R}_J, W_I, W_J), \quad \forall A \in \mathrm{SO}(d), \end{aligned}$$

which could serve as the mesoscopic equivalents of the translational and rotational invariance of the interaction potential, respectively. Evidently, there is no corresponding radial potential due to the presence of the molecular orientations, but now we can follow the way the RDF was derived for simple fluids. We generalize the probability density of the canonical ensemble to the "angular" version

$$\mathcal{P}^{\text{ang}}(\underline{R}, \underline{W}) := \frac{1}{Z^{\text{ang}}} \exp(-\beta E^{\text{pot}}(\underline{R}, \underline{W})), \tag{A.77}$$

where $\underline{R}$ are the coordinates, $\underline{W}$ orientations ("angles") of molecules and

$$Z^{\text{ang}} := \int \exp(-\beta E^{\text{pot}}(\underline{R}, \underline{W})) d\underline{R} d\underline{W}. \tag{A.78}$$

is the *configuration integral*. Then, for each $1 \le n \le N$, we can define in the common way the *angular n-particle distribution function*

$$\rho^{\text{ang},(n)}(\vec{R}_1, \dots, \vec{R}_n, W_1, \dots, W_n) := \frac{N!}{(N-n)!} \int \mathcal{P}^{\text{ang}}(\underline{R}, \underline{W}) \prod_{i=n+1}^{N} d\vec{R}_i dW_i, \tag{A.79}$$

the *angular n-particle distribution function*

$$g^{\text{ang},(n)}(\vec{R}_1, \dots, \vec{R}_n, W_1, \dots, W_n) := \frac{\rho^{\text{ang},(n)}(\vec{R}_1, \dots, \vec{R}_n, W_1, \dots, W_n)}{\rho^{\text{ang},(1)}(\vec{R}_1, W_1) \dots \rho^{\text{ang},(1)}(\vec{R}_n, W_n)}, \tag{A.80}$$

and average the latter over all orientations, in order to obtain the *n-particle distribution function* in the form

$$g^{(n)}(\vec{R}_1,\dots,\vec{R}_n) := \frac{1}{|Q|^n}\int g^{\mathrm{ang},(n)}(\vec{R}_1,\dots,\vec{R}_n,W_1,\dots,W_n)\prod_{i=1}^{n} dW_i. \tag{A.81}$$

The complex constitution of the molecules allows to define different kinds of the RDF. For example, in the liquid $\mathtt{CO}_2$, we can measure the distribution $g_{\mathtt{O},\mathtt{O}}$ between oxygen atoms, $g_{\mathtt{C},\mathtt{C}}$ between carbon atoms, $g_{\mathtt{C},\mathtt{O}}$ between different kinds of atoms, or we can measure the distribution between centers of mass of the $\mathtt{CO}_2$ molecules. The *center-of-mass radial distribution function* is

$$g(r) := g^{(2)}(0, r\vec{e}^{(1)}) \tag{A.82}$$

and the *atom-atom radial distribution function* for atoms of types a and b is

$$g_{a,b}(r) := \frac{1}{\mathcal{N}(a)(\mathcal{N}(a)-1)}\sum_{i\in\mathcal{T}(a)}\sum_{j\in\mathcal{T}(b)\setminus\{i\}} g^{(2)}(0, r\vec{e}^{(1)} + \vec{v}_i - \vec{v}_j), \tag{A.83}$$

where

$$\vec{v}_i := \vec{r}_i - \vec{R}_{\nu(i)}, \quad 1 \le i \le N^{\mathrm{atom}},$$

are the relative coordinates of atoms and

$$\begin{aligned} \mathcal{N}(a) &:= |\mathcal{T}(a)|, \\ \mathcal{T}(a) &:= \{i : \tau(i) = a\}. \end{aligned}$$

In principle, by using the grand canonical formalism, one can derive the *low-density limit* for the molecular RDF,

$$\lim_{\rho\to 0} g^{\mathrm{ang},(2)}(\vec{R}_1,\vec{R}_2,W_1,W_2) = \exp(-\beta U^{(2)}(\vec{R}_1,\vec{R}_2,W_1,W_2)). \tag{A.84}$$

The derivation is analogous to the case of the simple fluid.

A.6 Theory of Coarse Graining

In the previous section, we saw how important it can be to find a small set of meaningful variables describing the given fluid. We also demonstrated this in the preliminary section, where we derived some different levels of description of a fluid system. But that derivation carried rather explanatory and therefore, intuitive character. In this section, we present the general approach from the theory of coarse graining, as it can be found by [Español-2009]. We let the probability density $\rho^{\mathrm{eq}} = \rho^{\mathrm{eq}}(x)$ describe the equilibrium distribution at the microscopic level. Each mesoscopic variable $(X_I)_{I=1}^{N}$ is expressed as a function of the microscopic variables $(x_i)_{i=1}^{n}$, that is, at a mesoscopic level, the system is described by a *downscaling* map

$$\begin{aligned} V : \mathbb{R}^n &\to \mathbb{R}^N, \\ x &\mapsto X. \end{aligned}$$

Our goal is to derive a dynamic equation for the probability density $\mathcal{P}(X,t)$ of mesoscopic states.

For each mesoscopic state X, there is a whole submanifold of all compatible microscopic states, which has the volume

$$Q(X) := \int \rho^{\mathrm{eq}}(x)\delta(V(x) - X)dx.$$

We introduce the constrained average

$$\mathbf{E}_X[a] := \frac{1}{Q(X)} \int a(x)\rho^{\mathrm{eq}}(x)\delta(V(x) - X)dx$$

of a phase function a over the relevant submanifold corresponding to the given mesoscopic state X. In a nutshell, this average maps $a = a(x)$ on its mesoscopic version $A = A(X)$. The volume $Q(X)$ can be seen as the mesoscopic partition function, such that

$$S(X) = k_B \ln Q(X)$$

can be interpreted as the mesoscopic entropy. Further, following [Zwanzig-1960], we define the projection operators

$$\begin{aligned} \mathbb{P}a(x) &:= \mathbf{E}_{V(x)}[a], \\ \mathbb{Q}a(x) &:= (\mathbb{1} - \mathbb{P})a(x) = a(x) - \mathbf{E}_{V(x)}[a], \end{aligned}$$

which split any phase function

$$a = \mathbb{P}a + \mathbb{Q}a,$$

in the relevant and the irrelevant part, respectively. Of course,

$$\mathbb{P}^2 \equiv \mathbb{P}, \quad \mathbb{Q}^2 \equiv \mathbb{Q}, \quad \mathbb{P}\mathbb{Q} \equiv 0,$$

such that $\mathbb{P}$ and $\mathbb{Q}$ are true projection operators. According to [Zwanzig-1961], we can derive the Fokker-Planck equation for the set of relevant variables and, due to above definitions, write it in the form

$$\frac{\partial \mathcal{P}(X,t)}{\partial t} = -\frac{\partial}{\partial X}\left(\left(K(X) + M(X)\frac{\partial S(X)}{\partial X}\right)\mathcal{P}(X,t)\right) + k_B \frac{\partial}{\partial X}\left(M(X)\frac{\partial \mathcal{P}(X,t)}{\partial X}\right),$$

where

$$K(X) := \mathbf{E}_X[\mathbb{L}V]$$

is the (reversible) *drift* term,

$$M(X) := \frac{1}{k_B}\int_0^\infty \mathbf{E}_X\left[(\mathbb{L}V - \mathbf{E}_X[\mathbb{L}V])\exp(\mathrm{i}\mathbb{Q}\mathbb{L}\tilde{t})\,(\mathbb{L}V - \mathbf{E}_X[\mathbb{L}V])\right]d\tilde{t}$$

is the (irreversible) *friction* term (a symmetric and positive definite operator) and $\mathbb{L}$ is the Liouville operator (A.12). The Fokker-Planck equation can be transformed into the following stochastic differential equation

$$d\mathcal{X} = \left(K(\mathcal{X}) + M(\mathcal{X})\frac{\partial S(\mathcal{X})}{\partial \mathcal{X}} + k_B\frac{\partial M(\mathcal{X})}{\partial \mathcal{X}}\right)dt + B(\mathcal{X})d\mathcal{W}_t,$$

where $\mathcal{W}_t$ is the multicomponent Wiener process and the covariance term B fulfills the fluctuation-dissipation theorem

$$B(\mathcal{X})B(\mathcal{X})^T = 2k_B M(\mathcal{X}).$$

Now, eliminating the fluctuations (which are of order k_B) in the formal limit $k_B \to 0$, one obtains a deterministic dynamic equation of the form

$$\frac{dX}{dt} = K(X) + M(X)\frac{\partial S(X)}{\partial X}.$$

Futher simplifications become possible, if the microscopic dynamical invariants $j(x)$ can be expressed in terms of the relevant (coarse grained) variables $X = V(x)$, that is,

$$j(x) = J(V(x)).$$

For example, if the total energy of the system is $e(x) = E(V(x))$, then the mesoscopic dynamics can be written if the form, known as the *General Equation for the Non-Equilibrium Reversible-Irreversible Coupling (GENERIC)*,

$$\frac{dX}{dt} = \mathbb{L}(X)\frac{\partial E(X)}{\partial X} + M(X)\frac{\partial S(X)}{\partial X},$$

which is indeed, as the name suggests, a generalization of the reversible Hamilton equations (A.8).

In this section, we derived a dynamic equation for the probability density $\mathcal{P}(X,t)$ of mesoscopic variables X for the given set of microscopic variables and downscaling map. The presented framework especially yields a theoretical justification of the structure-based coarse graining, which is outlined in Chapter 1 in a more practical form, suitable for computer simulations. There, atom groups are coarse grained to certain effective particles, that is, the coordinates of atoms are the microscopic variables and the coordinates of the effective particles are the mesoscopic ones. The above theory guarantees the existence of the corresponding effective dynamic equation. Although the downscaling map is given, one skips the derivation of the GENERIC and assumes that the effective interactions, determined from various atomistic RDFs, represent the mesoscopic Hamiltonian (the reversible part of the dynamics) in the right way. Moreover, since the dynamics of particles in the simulation cannot be purely Hamiltonian (see the next appendix), there are always certain friction terms, so that one can assume a correct irreversible part of the dynamics. The mentioned assumptions can be tested for a small representative example – if the results of the coarse grained simulation show the quality of the detailed atomistic simulation, one can state that the underlying GENERIC was matched.

Appendix B

Molecular Simulation

Although the results of simulations are often as good as the experimental measurements, there are some differences in the accompanying theory from the mathematical viewpoint. Therefore, we decided to supply our work with the short appendix about molecular simulation, composed from the selected topics of [FS-2002].

B.1 Simulation Methods

In the *Monte Carlo* (MC) method, the dynamics of the molecules is given by the canonical probability density (A.27). According to the distribution, the "probability" to find the system in a configuration $\underline{R}^{(i)}$ is given by

$$\mathbf{P}[\underline{R}^{(i)}] := \frac{1}{Z^{\mathrm{c}}} \exp(-\beta E^{\mathrm{pot}}(\underline{R}^{(i)})).$$

Let $\mathbf{P}[\underline{R}^{(i)} \to \underline{R}^{(j)}]$ denote the probability of the transition from the i-th state to the j-th state. For the sake of simplicity, we consider a system with a finite number of states. At the equilibrium, each state is equiprobable, so that the *master equation*

$$\sum_{j \neq i} \mathbf{P}[\underline{R}^{(i)}]\mathbf{P}[\underline{R}^{(i)} \to \underline{R}^{(j)}] \overset{!}{=} \sum_{j \neq i} \mathbf{P}[\underline{R}^{(j)}]\mathbf{P}[\underline{R}^{(j)} \to \underline{R}^{(i)}], \quad \forall i,$$

can be imposed. In a nutshell, the left hand side summarizes, for the system in the i-th state, the probability to leave this state ("outcoming flow"). The right hand side is the probability for a transition from any other state to the i-th state ("incoming flow"). The equation holds especially, if we have the *detailed balance*

$$\mathbf{P}[\underline{R}^{(i)}]\mathbf{P}[\underline{R}^{(i)} \to \underline{R}^{(j)}] = \mathbf{P}[\underline{R}^{(j)}]\mathbf{P}[\underline{R}^{(j)} \to \underline{R}^{(i)}], \quad \forall i, j,$$

that is, if every transition, happened with a certain probability, can be unmade by the next transition, which has the same probability. In order to fulfill the above condition, we can choose the transition probabilities, for instance, according to the *Metropolis criterion*

$$\mathbf{P}[\underline{R}^{(i)} \to \underline{R}^{(j)}] := \min\{1, \exp(-\beta(E^{\mathrm{pot}}(\underline{R}^{(j)}) - E^{\mathrm{pot}}(\underline{R}^{(i)})))\}.$$

Indeed, for $E^{\mathrm{pot}}(\underline{R}^{(j)}) \leq E^{\mathrm{pot}}(\underline{R}^{(i)})$, we have

$$\begin{aligned}
\mathbf{P}[\underline{R}^{(i)}]\mathbf{P}[\underline{R}^{(i)} \to \underline{R}^{(j)}] &= \frac{1}{Z^{\mathrm{c}}} \exp(-\beta E^{\mathrm{pot}}(\underline{R}^{(i)})) \cdot 1 \\
&= \frac{1}{Z^{\mathrm{c}}} \exp(-\beta E^{\mathrm{pot}}(\underline{R}^{(j)})) \cdot \exp(-\beta(E^{\mathrm{pot}}(\underline{R}^{(i)}) - E^{\mathrm{pot}}(\underline{R}^{(j)}))) \\
&= \mathbf{P}[\underline{R}^{(j)}]\mathbf{P}[\underline{R}^{(j)} \to \underline{R}^{(i)}]
\end{aligned}$$

and the opposite case is analogous. In simple words, the criterion allows all transitions, which lower the energy, while the states with higher energy can be only reached with a smaller probability decreasing exponentially with respect to the growing energy. In practice, the method chooses randomly a particle from the system, moves it slightly in a random direction, measures the change in the potential energy and decides whether the move should be accepted or rejected (undone).

In the *molecular dynamics* (MD) method, the molecules are moved along their trajectories $((R(t),P(t))^T)_{t\geq 0}\subset\mathbb{R}^{2dN}$, according to the Newton equation (A.6). We write here the latter for convenience in the form

$$\begin{aligned} M\dot{R}(t) &= P(t), \\ \dot{P}(t) &= F(R(t)). \end{aligned}$$

In order to derive a numerical solution scheme (an *integrator*), one describes the time evolution of any phase function $A=A(R(t),P(t))$ in terms of the Liouville operator (A.12), that is,

$$\dot{A}=\dot{R}\frac{\partial A}{\partial R}+\dot{P}\frac{\partial A}{\partial P}=\mathbb{L}A. \tag{B.1}$$

This is an ordinary differential equation with the formal solution

$$A(R(t),P(t))=e^{\mathbb{L}t}A(R(0),P(0)).$$

Then, one splits the Liouville operator in two parts,

$$\mathbb{L}=\underbrace{\dot{R}\frac{\partial}{\partial R}}_{=:\mathbb{L}_R}+\underbrace{\dot{P}\frac{\partial}{\partial P}}_{=:\mathbb{L}_P},$$

and, using the Taylor expansion, shows that $e^{\mathbb{L}_R t}$ and $e^{\mathbb{L}_P t}$ correspond to a shift of coordinates and momenta, respectively, that is,

$$\begin{aligned} e^{\mathbb{L}_R t}A(R(0),P(0)) &= A(R(0)+t\dot{R}(0),P(0)), \\ e^{\mathbb{L}_P t}A(R(0),P(0)) &= A(R(0),P(0)+t\dot{P}(0)). \end{aligned}$$

Thank *Trotter identity*, one can split the operator $e^{\mathbb{L}t}$ in these two parts, more precisely,

$$e^{\mathbb{L}t}\approx\left(e^{\mathbb{L}^{\mathrm{mom}}\frac{1}{2}\tau}e^{\mathbb{L}^{\mathrm{coord}}\tau}e^{\mathbb{L}^{\mathrm{mom}}\frac{1}{2}\tau}\right)^k,$$

where $\tau=\frac{t}{k}$ and k sufficiently large. Then, step by step, one can determine the action of the decomposed operator,

$$\begin{aligned} e^{\mathbb{L}^{\mathrm{mom}}\frac{1}{2}\tau}\begin{pmatrix} R(0) \\ P(0) \end{pmatrix} &= \begin{pmatrix} R(0) \\ P(0)+\frac{1}{2}\tau\dot{P}(0) \end{pmatrix} \\ &= \begin{pmatrix} R(0) \\ P(0)+\frac{1}{2}\tau F(R(0)) \end{pmatrix}, \end{aligned}$$

$$\begin{aligned} e^{\mathbb{L}^{\mathrm{coord}}\tau}\begin{pmatrix} R(0) \\ P(0)+\frac{1}{2}\tau F(R(0)) \end{pmatrix} &= \begin{pmatrix} R(0)+\tau\dot{R}(\frac{1}{2}\tau) \\ P(0)+\frac{1}{2}\tau F(R(0)) \end{pmatrix} \\ &= \begin{pmatrix} R(0)+\tau\frac{1}{M}P(\frac{1}{2}\tau) \\ P(0)+\frac{1}{2}\tau F(R(0)) \end{pmatrix} \\ &= \begin{pmatrix} R(0)+\tau\frac{1}{M}P(0)+\tau^2\frac{1}{2M}F(R(0)) \\ P(0)+\frac{1}{2}\tau F(R(0)) \end{pmatrix}, \end{aligned}$$

$$
\begin{aligned}
e^{\mathbb{L}^{\mathrm{mom}}\frac{1}{2}\tau}\begin{pmatrix} R(0)+\tau\frac{1}{M}P(0)+\tau^2\frac{1}{2M}F(R(0)) \\ P(0)+\frac{1}{2}\tau F(R(0)) \end{pmatrix}
&= \begin{pmatrix} R(0)+\tau\frac{1}{M}P(0)+\tau^2\frac{1}{2M}F(R(0)) \\ P(0)+\frac{1}{2}\tau F(R(0))+\frac{1}{2}\tau\dot{P}(\tau) \end{pmatrix} \\
&= \begin{pmatrix} R(0)+\tau\frac{1}{M}P(0)+\tau^2\frac{1}{2M}F(R(0)) \\ P(0)+\frac{1}{2}\tau F(R(0))+\frac{1}{2}\tau F(R(\tau)) \end{pmatrix}.
\end{aligned}
$$

Summarizing the above results, one obtains the *Velocity-Verlet* integrator, which computes, for the given $(\vec{R}_I^{(0)},\vec{P}_I^{(0)})_{I=1}^N$, the trajectory of the particles via

$$
\begin{aligned}
\vec{R}_I^{(k+1)} &= \vec{R}_I^{(k)}+\frac{1}{M}\tau\vec{P}_I^{(k)}+\frac{1}{2M}\tau^2\vec{F}_I^{(k)}, \\
\vec{P}_I^{(k+1)} &= \vec{P}_I^{(k)}+\frac{1}{2}\tau\left(\vec{F}_I^{(k+1)}+\vec{F}_I^{(k)}\right),
\end{aligned}
$$

where the time step τ is sufficiently small.

Obviously, the integrator does not affect the number N of particles and the volume V of the system. Further, the dynamics driven by the operator $\mathbb{L}$ conserves the Hamiltonian, it is easily shown by inserting equation (A.2) into (B.1). For these reasons, the Velocity-Verlet integrator, derived from the energy-conserving Liouville operator, is a standard numerical scheme for molecular simulations in the microcanonical (N,V,E)-ensemble. Although all ensembles are equivalent at equilibrium, a microcanonical simulation will yield a trajectory with a (nearly) constant, but unpredictable temperature $\tilde{T}$. Since one usually wants to determine the RDF of the fluid for the given temperature T and cannot leave it to the chance, that $\tilde{T}=T$, one introduces a *thermostat* – an additional virtual system, which enforces the given temperature by exchanging the energy with the fluid. In practice, the dynamic equations are modified according to the concrete needs, because there is no universal thermostat. For instance, the *DPD-thermostat* (for Dissipative Particle Dynamics) models the force term as the sum

$$
F = F^{\mathrm{C}} + F^{\mathrm{D}} + F^{\mathrm{R}},
$$

where the usual *conservative* forces

$$
F^{\mathrm{C}} = -\nabla E^{\mathrm{pot}}
$$

are upgraded with two virtual terms, F^{D} and F^{R}, representing the *dissipative* and the *random* forces, respectively. We decided to present this thermostat, because it really appears to model the dynamics of a fluid in the canonical ensemble. In [EW-1995], the authors show that the probability density $\mathcal{P}$ of a system with the DPD-thermostat obeys the following Fokker-Planck equation

$$
\frac{\partial\mathcal{P}(\underline{R},\underline{P},t)}{\partial t} = -\mathbb{L}\mathcal{P}(\underline{R},\underline{P},t)+\mathbb{M}\mathcal{P}(\underline{R},\underline{P},t),
$$

where $\mathbb{L}$ is the Liouville operator (with resprect to the conservative forces) and the operator $\mathbb{M}$ describes the action of dissipative and random forces. Further, they find the relation between the dissipative and random forces, for which the above equation has a stationary solution – the probability density $\mathcal{P}^{\mathrm{c}}(\underline{R},\underline{P})$ of the canonical ensemble.

B.2 Interaction Potentials

In a computer simulation, for efficiency reasons, only next-neighbour interactions can be considered, that is, the interaction potential is cut off at certain distance $r = r^{\text{cut}}$ and continuated with zero. Typically $r^{\text{cut}} \approx 2.5\sigma$, sometimes greater values are taken. Thus, the attractive part of the potential should converge to zero fast enough, say $\mathcal{O}(r^{-\alpha})$. From (A.69) and (A.70), we can estimate the amounts of pressure and energy, which are lost through the cut off, and demand them to be finite. Since the RDF is typically bounded, we obtain that

$$\begin{aligned}
|P^{\text{cut}}| &\leq \int_{r^{\text{cut}}}^{\infty} |Du(r)y(r)||\partial B(r)|r dr \\
&\leq \int_{r^{\text{cut}}}^{\infty} \frac{C}{r^{\alpha+1}} r^d dr \\
&= C \int_{r^{\text{cut}}}^{\infty} \frac{1}{r^{\alpha+1-d}} dr \\
&= C \left[\frac{1}{r^{\alpha-d}} \right]_{r^{\text{cut}}}^{\infty} \\
&< \infty
\end{aligned}$$

and

$$\begin{aligned}
|E^{\text{cut}}| &\leq \int_{r^{\text{cut}}}^{\infty} |u(r)y(r)||\partial B(r)| dr \\
&\leq \int_{r^{\text{cut}}}^{\infty} \frac{C}{r^{\alpha}} r^{d-1} dr \\
&= C \int_{r^{\text{cut}}}^{\infty} \frac{1}{r^{\alpha-d+1}} dr \\
&= C \left[\frac{1}{r^{\alpha-d}} \right]_{r^{\text{cut}}}^{\infty} \\
&< \infty
\end{aligned}$$

for a certain constant $C > 0$, if and only if $\alpha > d$. In other words, the interaction potential used in a simulation must be *short-ranged* – tend to zero fast enough at large distances.

In a simulation with Lennard-Jones potential, one describes the interactions for the a-th atom type by "pure" parameters $\varepsilon_{a,a}$ and $\sigma_{a,a}$. However, if the atoms of different types `a` and `b` interact, the "mixed" parameters $\varepsilon_{\mathtt{a,b}}$ and $\sigma_{\mathtt{a,b}}$ are needed. In order to keep the number of input parameters low, one can estimate them via the *Lorentz-Berthelot rules*:

$$\begin{aligned}
\sigma_{\mathtt{a,b}} &= \frac{1}{2}\Big(\sigma_{\mathtt{a,a}} + \sigma_{\mathtt{b,b}} \Big), \\
\varepsilon_{\mathtt{a,b}} &= \sqrt{\varepsilon_{\mathtt{a,a}} \cdot \varepsilon_{\mathtt{b,b}}}.
\end{aligned}$$

The first estimate is an arithmetic mean, which is rigorous for hard-sphere interactions. The second one appears to mimic the first one by using the geometric mean.

B.3 Radial Distribution Function

In Appendix A, we defined the RDF via (A.64) and stressed that the definition holds actually for a translationally and rotationally invariant (symmetric) potential. In a molecular simulation, however, even a simple fluid may loose the underlying symmetry due to various approximations, for example, the one-particle density $\rho^{(1)}$ is not constant and not equal to ρ anymore. We observed in Appendix A.5 a far worse situation in the molecular fluid, whose interactions are per se not symmetric due to the presence of spatial orientations of molecules. There, in order to define the center-of-mass RDF, we cured the problem with an averaging over the orientations. We apply the same idea here, for example, the one-particle density yields the density, after averaging over the spatial translations,

$$\begin{aligned}\frac{1}{V}\int_{\Omega}\rho^{(1)}(\vec{W})d\vec{W} &\overset{(A.58)}{=} \frac{1}{V}N\int\mathcal{P}^{c}(\underline{R})d\underline{R}\\ &\overset{(A.27)}{=} \frac{N}{V}=\rho.\end{aligned}$$

Similarly, we average the RDF over both the translations and the rotations,

$$g(r)=\frac{1}{|\partial B(r)|}\int_{\partial B(r)}\frac{1}{V}\int_{\Omega}g^{(2)}(\vec{W},\vec{Z}+\vec{W})d\vec{W}d\vec{Z}. \tag{B.2}$$

Since we are primarily interested in the computation of

$$g^{(2)}(\vec{R}_1,\vec{R}_2)\overset{(A.59)}{=}\frac{\rho^{(2)}(\vec{R}_1,\vec{R}_2)}{\rho^{(1)}(\vec{R}_1)\rho^{(1)}(\vec{R}_2)}$$

or, more precisely, of $\rho^{(2)}$, which obviously contains more information than $\rho^{(1)}$, we approximate in the following

$$\rho^{(1)}\approx\rho. \tag{B.3}$$

Then, we can write

$$\begin{aligned}g^{(2)}(\vec{X},\vec{Y}) &\overset{(B.3)}{\approx} \frac{1}{\rho^2}\rho^{(2)}(\vec{X},\vec{Y})\\ &\overset{(A.58)}{=} \frac{1}{\rho^2}N(N-1)\int\mathcal{P}^{c}(\vec{X},\vec{Y},\vec{R}_3,\ldots,\vec{R}_N)d\vec{R}_3\ldots d\vec{R}_N\\ &\overset{\text{Dirac-}\delta}{=} \frac{1}{\rho^2}N(N-1)\int\delta(\vec{X}-\vec{R}_1)\delta(\vec{Y}-\vec{R}_2)\mathcal{P}^{c}(\underline{R})d\underline{R}\\ &\overset{(A.57)}{=} \frac{1}{\rho^2}\sum_{i=1}^{N}\sum_{j\neq i}^{N}\int\delta(\vec{X}-\vec{R}_i)\delta(\vec{Y}-\vec{R}_j)\mathcal{P}^{c}(\underline{R})d\underline{R}\\ &\overset{(A.15)}{=} \frac{1}{\rho^2}\sum_{i=1}^{N}\sum_{j\neq i}^{N}\left\langle\delta(\vec{X}-\vec{R}_i)\delta(\vec{Y}-\vec{R}_j)\right\rangle.\end{aligned} \tag{B.4}$$

It is impossible to retrieve the ensemble average, because we do not know the complete probability density $\mathcal{P}^{c}$. Therefore, we use relation (A.16) and obtain

$$\langle A\rangle=\lim_{\Theta\to\infty}\frac{1}{\Theta}\int_0^{\Theta}A(R(t))dt$$

for any observable $A:\mathbb{R}^{Nd}\to\mathbb{R}$. In practice, Θ is the **finite** simulation time needed for sampling of the RDF from n snapshots of the trajectory. In other words, $\Theta:=n\tau$, where τ is the time separating uncorrelated snapshots. Thus, we choose n large enough and approximate

$$\lim_{\Theta\to\infty} \frac{1}{\Theta}\int_0^{\Theta} \approx \frac{1}{n\tau}\int_0^{n\tau} . \tag{B.5}$$

It means also that the trajectory is discretized on the equidistant time grid

$$t_\ell = \ell\tau, \quad 0 \le \ell \le n-1.$$

Further, we are only capable to sample the RDF (B.2) on the equidistant space grid

$$r_k = k\Delta r, \quad 0 \le k \le m-1$$

with an arbitrary Δr and $m := \frac{L}{2\Delta r}$. Especially, we have to approximate

$$\partial B(r_k) \approx S_k := B(r_{k+1}) \setminus B(r_k). \tag{B.6}$$

Finally, we insert the above considerations in (B.2) and obtain

$$\begin{aligned}
g(r_k) &\overset{\text{(B.6)}}{\approx} \frac{1}{|S_k|}\int_{S_k}\frac{1}{V}\int_\Omega g^{(2)}(\vec{W},\vec{Z}+\vec{W})d\vec{W}d\vec{Z} \\
&\overset{\text{(B.4)}}{\approx} \frac{1}{|S_k|}\int_{S_k}\frac{1}{V}\int_\Omega \frac{1}{\rho^2}\sum_{i=1}^{N}\sum_{j\neq i}^{N}\left\langle \delta(\vec{W}-\vec{R}_i)\delta(\vec{Z}+\vec{W}-\vec{R}_j)\right\rangle d\vec{W}d\vec{Z} \\
&\overset{\text{Fubini}}{=} \frac{1}{|S_k|}\frac{V}{N^2}\sum_{i=1}^{N}\sum_{j\neq i}^{N}\int_{S_k}\left\langle \int_\Omega \delta(\vec{W}-\vec{R}_i)\delta(\vec{Z}+\vec{W}-\vec{R}_j)d\vec{W}\right\rangle d\vec{Z} \\
&\overset{\text{Dirac-}\delta}{=} \frac{1}{|S_k|}\frac{V}{N^2}\sum_{i=1}^{N}\sum_{j\neq i}^{N}\int_{S_k}\left\langle \delta(\vec{Z}+\vec{R}_i-\vec{R}_j)\right\rangle d\vec{Z} \\
&\overset{\text{(A.16)}}{=} \frac{1}{|S_k|}\frac{V}{N^2}\sum_{i=1}^{N}\sum_{j\neq i}^{N}\lim_{\Theta\to\infty}\frac{1}{\Theta}\int_0^{\Theta}\int_{S_k}\delta(\vec{Z}+\vec{R}_i(t)-\vec{R}_j(t))d\vec{Z}dt \\
&\overset{\text{Dirac-}\delta}{=} \frac{1}{|S_k|}\frac{V}{N^2}\sum_{i=1}^{N}\sum_{j\neq i}^{N}\lim_{\Theta\to\infty}\frac{1}{\Theta}\int_0^{\Theta} 1_{S_k}(\vec{R}_j(t)-\vec{R}_i(t))dt \\
&= \frac{1}{|S_k|}\frac{V}{N^2}\sum_{i=1}^{N}\sum_{j\neq i}^{N}\lim_{\Theta\to\infty}\frac{1}{\Theta}\int_0^{\Theta} 1_{[r_k,r_{k+1})}(|\vec{R}_i(t)-\vec{R}_j(t)|)dt \\
&\overset{\text{(B.5)}}{\approx} \frac{1}{|S_k|}\frac{V}{N^2}\sum_{i=1}^{N}\sum_{j\neq i}^{N}\frac{1}{n\tau}\int_0^{n\tau} 1_{[r_k,r_{k+1})}(|\vec{R}_i(t)-\vec{R}_j(t)|)dt \\
&\overset{\text{quadrature}}{\approx} \frac{1}{|S_k|}\frac{V}{N^2}\sum_{i=1}^{N}\sum_{j\neq i}^{N}\frac{1}{n}\sum_{\ell=0}^{n-1} 1_{[r_k,r_{k+1})}(|\vec{R}_i(t_\ell)-\vec{R}_j(t_\ell)|) \\
&= \frac{1}{|S_k|}\frac{V}{N^2}\frac{1}{n}\sum_{\ell=0}^{n-1}\sum_{i=1}^{N}\sum_{j>i}^{N} 2\cdot 1_{[r_k,r_{k+1})}(|\vec{R}_i(t_\ell)-\vec{R}_j(t_\ell)|)
\end{aligned}$$

for $0 \le k \le m-1$. Although the expression looks complicated, it suggests a handy numerical algorithm for calculation of the RDF. For large number N of particles, the translational and rotational averages damp the approximation errors, such that the RDF from a simulation has a quality comparable to the experimental data.

List of Symbols

$\mathbb{1}$	identity operator/matrix
α_0	behaviour of potentials in the core region
Å	Angstrøm, $1 \cdot 10^{-10}$ [m]
$A^\dagger$	Moore-Penrose inverse of operator A
$A^{(k)}$	derivative for the actual iterate
$\mathtt{a}, \mathtt{b}, \dots$	fictive/effective particles
β	inverse temperature of the system
β_0	behaviour of RDFs in the core region
$B(r)$	open ball of the radius r around origin
$B(X, Y)$	space of bounded operators from X to Y
$b^{(k)}$	right hand side of the actual linearization
$b^{(k,\delta)}$	noisy right hand side of the actual linearization
$C(\Omega)$	space of continuous functions on Ω
$\chi_1, \chi_2, \dots$	filter functions
$\mathrm{cond}(M)$	condition number of matrix M
D	derivative operator
D	finite difference
Δr	grid step for distances
$\Delta\mathrm{x}$	variation vector
d	dimension of the Euclidean space
$\partial B(r)$	sphere of the radius r around origin
δ	(overall) noise level
$\delta(\cdot)$	Dirac-δ function
$\mathrm{diag}(v)$	diagonal matrix with elements of vector v on the main diagonal
$\dim(X)$	dimension of space X
$\mathrm{dom}(F)$	domain of map F
$\mathbf{E}$	sample mean
ε	energy parameter of the Lennard-Jones potential
$\varepsilon^{\mathrm{unit}}$	unit energy
$\vec{\mathrm{e}}^{(1)}, \dots, \vec{\mathrm{e}}^{(d)}$	standard base of the Euclidean space
F	map from parameters to RDFs
$\vec{F}$	force
G	map from potentials to RDFs
Γ	map from potentials to two-atom RDFs
γ	two-atom RDF
H	parameterization
$h^{(k)}$	update for the actual iterate
$h^{(k,\lambda)}$	regularized update for the actual iterate
κ	noise level of experimental measurement

k_ℓ, k_θ, k_ϕ	stiffnesses for bond length, bending and torsion
k_B	Boltzmann constant, $1.3806505 \cdot 10^{-23}$ $[\mathrm{J} \cdot \mathrm{K}^{-1}]$
$\ker(F)$	kernel of map F
k^{stop}	step number, according to the stopping rule
L	system size
Λ	mapping scheme
λ	regularization parameter
$\lambda(\cdot,\cdot)$	parameter choice strategy
$L(X,Y)$	space of operators from X to Y
$L^2(\Omega)$	Lebesgue space of square-integrable functions on Ω
$L^2(\Omega,w)$	Lebesgue space of square-integrable with weight w functions on Ω
$\ell, \ell_{\mathtt{a},\mathrm{b}}, \ldots$	bond lengths
μ	reduction rate of the Morozov discrepancy principle
M^{unit}	unit mass
m	length of data vector
$m_i, m_{\mathtt{a}}$	masses of particles
N	number of particles
N_A	Avogadro number, $6.0221415 \cdot 10^{23}$ $[\mathrm{mol}^{-1}]$
n	length of solution vector, number of parameters
ν	noise level of computational implementation
P	truncation map for data
$\mathcal{P}$	probability density
Φ	matrix with right singular vectors as columns
ϕ	torsion angle
$\varphi^{(1)}, \varphi^{(2)}, \ldots$	right singular vectors
$\psi^{(1)}, \psi^{(2)}, \ldots$	left singular vectors
$\overline{\mathbb{R}}$	real numbers and $\{\pm\infty\}$
$\vec{R}_i, \vec{r}_i$	coordinates of particles
$R^{(\lambda)}$	regularization
r	distance between particles
r^{core}	core distance
r^{cut}	cut off distance
ρ	density of the system/fluid
ρ^{c}	critical point density
ρ^{t}	triple point density
$r_1, \ldots, r_m$	grid corresponding to data vector
r^{min}	preferred distance between two particles
r^{peak}	position of the highest peak in the RDF
$\mathrm{ran}(F)$	range of map F
$\sigma_1, \sigma_2, \ldots$	singular values
$\sigma, \sigma_{\mathtt{a},\mathrm{a}}, \ldots$	length parameters of the Lennard-Jones potential
σ^{unit}	unit length
S_U	set of potentials
S_X	set of parameters
S_Y	set of RDFs
T	temperature of the system
T^{c}	critical (point) temperature
T^{t}	triple point temperature

τ	safety factor in the stopping rule
$T^{(\lambda,\delta)}$	Tikhonov functional
t	time
θ	bending angle
U	Hilbert space of potentials
u	non-bonded potential
$u^{\min}$	preferred energy between two particles
V	volume of the system
Var	sample variance
v_ℓ, v_θ, v_ϕ	potentials for bond length, bending and torsion
w_U, w_Y	weight functions for potentials and RDFs
Ξ	Taylor remainder of the linearization
X	Hilbert space of parameters
x	parameter
$\overline{x}$	exact parameter/solution
$x^{(\delta)}$	best-approximate solution
$x^{(\lambda,\delta)}$	regularized solution
$x^{(k)}$	actual iterate
Y	Hilbert space of data
y	data (RDF)
$\overline{y}$	exact data (RDF)
$y_{\mathtt{a},\mathtt{b}}$	atom-atom RDF
$y_{\mathtt{ab},\mathtt{ab}}$	center-of-mass RDF
$y^{(\delta)}$	noisy data (RDF)
$y[N]$	N-atom RDF
y^{peak}	height of the highest peak in the RDF

List of Abbreviations

CPU	central processing unit
CSI	Cauchy-Schwarz inequality
fcc	face-centered cubic
HS	hard-sphere
IBI	Iterative Boltzmann Inversion
IMC	Inverse Monte Carlo method
JTF	Jacobi transformation formula
LJ	Lennard-Jones
LM	Levenberg-Marquardt method
RDF	radial distribution function
RMSD	root mean square distance
SS	soft-sphere
SVD	singular value decomposition
SW	square-well
TAA	two-atom approximation
TMA	two-molecule approximation
TSVD	truncated SVD

Bibliography

[AM-2007] N.W. Ashcroft und D.N. Mermin. *Festkörperphysik.* Oldenbourg Wissenschaftsverlag GmbH, München, 3. Auflage, 2007.

[Ben-Naim-2006] A. Ben-Naim. *Molecular Theory of Solutions.* Oxford University Press, New York, 2006.

[BLQ-1973] J. Barojas, D. Levesque and B. Quentrec. Simulation of Diatomic Homonuclear Liquids. *Physical Review A*, 1973, **7(3)**, 1092–1105.

[BSD-1995] H.J.C. Berendsen, D. van der Spoel and R. van Drunen. GROMACS: A message-passing parallel molecular dynamics implementation. *Computer Physics Communications*, 1995, **91**, 43–56.

[Cheney-2001] W. Cheney. *Analysis for Applied Mathematics.* Springer-Verlag, New York, 2001.

[CM-1992] F. Cuadros and A. Mulero. The radial distribution function for two-dimensional Lennard-Jones fluids: computer simulation results. *Chemical Physics*, 1992, **159**, 89–97.

[CP-1975] S.Y. Cheung and J.G. Powles. The properties of liquid nitrogen IV. A computer simulation. *Molecular Physics*, 1975, **30(3)**, 921–949.

[EHN-1996] H.W. Engl, M. Hanke and A. Neubauer. *Regularization of Inverse Problems.* Kluwer Academic Publishers, London, 1996.

[Español-2004] P. Español. Statistical Mechanics of Coarse-Graining. *Novel Methods in Soft Matter Simulations. Lecture Notes in Physics*, **640**, 69–115, Springer-Verlag, Berlin, 2004.

[Español-2009] P. Español, J.G. Anero and I. Zúñiga. Microscopic derivation of discrete hydrodynamics. *J. Chem. Phys.*, 2009, **131**, 244117.

[EW-1995] P. Español and P. Warren. Statistical Mechanics of Dissipative Particle Dynamics. *Europhys. Lett.*, 1995, **30(4)**, 191–196.

[Evans-1998] L.C. Evans. *Partial Differential Equations.* American Mathematical Society, USA, 1998.

[FS-2002] D. Frenkel and B. Smit. *Understanding Molecular Simulation: From Algorithms to Applications.* Academic Press, San Diego, 2nd edition, 2002.

[Groetsch-1993] C.W. Groetsch. *Inverse problems in the mathematical sciences.* Vieweg, 1993.

[GG-1984] C.G. Gray and K.E. Gubbins. *Theory of Molecular Fluids. Volume 1: Fundamentals.* Oxford University Press, New York, 1984.

[Hanke-1997] M. Hanke. A regularizing Levenberg-Marquardt scheme, with applications to inverse groundwater filtration problems. *Inverse Problems*, 1997, **12**, 79–95.

[Hanke-Bourgeois-2006] M. Hanke-Bourgeois. *Grundlagen der Numerischen Mathematik und des Wissenschaftlichen Rechnens.* Teubner, Wiesbaden, 2. Auflage, 2006.

[Hansen-1994] P.C. Hansen. Regularization Tools: A Matlab package for analysis and solution of discrete ill-posed problems. *Numerical Algorithms*, 1994, **6**, 1–35.

[Hansen-2010] P.C. Hansen. *Discrete Inverse Problems. Insight and Algorithms.* SIAM, Philadelphia, 2010.

[HAVK-2006] V.A. Harmandaris, N.P. Adhikari, N.F.A. van der Vegt and K. Kremer. Hierarchical Modeling of Polystyrene: From Atomistic to Coarse-Grained Simulations. *Macromolecules*, 2006, **39**, 6708–6719.

[Henderson-1974] R.L. Henderson. A uniqueness theorem for fluid pair correlation functions. *Physics Letters*, 1974, **49A**, 197–198.

[HKSL-2008] B. Hess, C. Kutzner, D. van der Spoel and E. Lindahl. GROMACS 4: Algorithms for Highly Efficient, Load-Balanced, and Scalable Molecular Simulation. *J. Chem. Theory Comput.*, 2008, **4(3)**, 435–447.

[HM-2006] J.P. Hansen and I.R. McDonald. *Theory of simple liquids.* Academic Press, London, 3rd edition, 2006.

[HRVK-2007] V.A. Harmandaris, D. Reith, N.F.A. van der Vegt and K. Kremer. Comparison between coarse-graining models for polymer systems: two mapping schemes for polystyrene. *Macromol. Chem. Phys.*, 2007, **208**, 2109–2120.

[HV-1969] J.P. Hansen and L. Verlet. Phase Transitions of the Lennard-Jones System. *Physical Review*, 1969, **184(1)**, 151–161.

[HY-1995] J.G. Harris and K.H. Yung. Carbon Dioxide's Liquid – Vapor Coexistence Curve and Critical Properties As Predicted by a Simple Molecular Model. *J. Phys. Chem.*, 1995, **99**, 12021–12024.

[LAL-1970] L.D. Landau, A.I. Achieser und E.M. Lifschitz. *Mechanik und Molekularphysik.* Akademie-Verlag, Berlin, 1970.

[Levelt-1960] J.M.H. Levelt. The reduced equation of state, internal energy and entropy of argon and xenon. *Physica*, 1960, **26**, 361–377.

[LGK-2005] H. Liu, S. Garde and S. Kumar. Direct determination of phase behavior of square-well fluids. *J. Chem. Phys.*, 2005, **123**, 174505.

[LHS-2001] E. Lindahl, B. Hess and D. van der Spoel. GROMACS 3.0: a package for molecular simulation and trajectory analysis. *J. Mol. Model.*, 2001, **7**, 306–317.

[LL-1980] L.D. Landau and E.M. Lifshitz. *Course of Theoretical Physics. Volume 5: Statistical Physics. Part 1.* Pergamon-Press, Frankfurt, 3rd edition, 1980.

[LL-1995] A.P. Lyubartsev and A. Laaksonen. Calculation of effective interaction potentials from RDF: A reverse Monte Carlo approach. *Physical Review E*, 1995, **52(4)**, 3730–3737.

[MBVDK-2009] T. Murtola, A. Bunker, I. Vattulainen, M. Deserno and M. Karttunen. Multiscale modeling of emergent materials: biological and soft matter. *Phys. Chem. Chem. Phys.*, 2009, **11**, 1869–1892.

[MFKV-2007] T. Murtola, E. Falck, M. Karttunen and I. Vattulainen. Coarse-grained model for phospholipid/cholesterol bilayer employing inverse Monte Carlo with thermodynamic constraints. *J. Chem. Phys.*, 2007, **126**, 075101.

[MGM-2005] G. Milano, S. Goudeau and F. Müller-Plathe. Multicentered Gaussian-Based Potentials for Coarse-Grained Polymer Simulations: Linking Atomistic and Mesoscopic Scales. *J. Polym. Sci. Part B: Polym. Phys.*, 2005, **43**, 871-885.

[MVYPBMM-2009] B. Mognetti, P. Virnau, L. Yelash, W. Paul, K. Binder, M. Müller and L. MacDowell. Coarse-grained models for fluids and their mixtures. *J. Chem. Phys.*, 2009, **130**, 044101.

[NCAKIVDA-2008] W. Noid, J. Chu, G. Ayton, V. Krishna, S. Izvekov, G. Voth, A. Das and H. Andersen. The multiscale coarse-graining method. I. A rigorous bridge between atomistic and coarse-grained models. *J. Chem. Phys.*, 2008, **128**, 244114.

[NJH-1980] A.H. Narten, E. Johnson and A. Habenschuss. Atom pair potentials of liquid nitrogen from diffraction data. *J. Chem. Phys.*, 1980, **73(3)**, 1248–1255.

[PDK-2008] C. Peter, L. Delle Site and K. Kremer. Classical simulations from the atomistic to the mesoscale and back: coarse graining an azobenzene liquid crystal. *Soft Matter*, 2008, **4**, 859–869.

[PK-2009] C. Peter and K. Kremer. Multiscale simulation of soft matter systems – from the atomistic to the coarse-grained level and back. *Soft Matter*, 2009, **5**, 4357–4366.

[PK-2010] C. Peter and K. Kremer. Multiscale simulation of soft matter systems. *Faraday Discussions*, 2010, **144**, 9–24.

[RMM-2002] D. Reith, H. Meyer and F. Müller-Plathe. CG-OPT: A software package for automatic force field design. *Computer Physics Communications*, 2002, **148**, 299–313.

[RPM-2003] D. Reith, M. Pütz and F. Müller-Plathe. Deriving Effective Mesoscale Potentials from Atomistic Simulations. *J. Comput. Chem.*, 2003, **24**, 1624–1636.

[RJLKA-2009] V. Rühle, C. Junghans, A. Lukyanov, K. Kremer and D. Andrienko. Versatile Object-Oriented Toolkit for Coarse-Graining Applications. *J. Chem. Theory Comput.*, 2009, **5**, 3211–3223.

[Schmid-2006] F. Schmid. Coarse-grained models of complex fluids at equilibrium and under shear. *Computer Simulations in Condensed Matter: from Materials to Chemical Biology.*, **2**, 211–258, Springer-Verlag, Berlin, 2006.

[Soper-1996] A.K. Soper. Empirical potential Monte Carlo simulation of fluid structure. *Chemical Physics*, 1996, **202**, 295–306.

[SLHGMB-2005] D. van der Spoel, E. Lindahl, B. Hess, G. Groenhof, A.E. Mark and H.J.C. Berendsen. GROMACS: Fast, Flexible, and Free. *J. Comput. Chem.*, 2005, **26(16)**, 1701–1718.

[TKHBB-1998] W. Tschöp, K. Kremer, O. Hahn, J. Batoulis and T. Bürger. Simulation of polymer melts. II. From coarse-grained models back to atomistic description. *Acta Polymer.*, 1998, **49**, 75–79.

[TLJOT-1969] T.H. Thomas, J.A. Ladd, V.I.P. Jones and W.J. Orville-Thomas. Force constants, bond lengths and vibrational frequencies of nitrogen-nitrogen bonds. *J. Mol. Structure*, 1969, **3**, 49–56.

[Varah-1983] J.M. Varah. Pitfalls in the numerical solution of linear ill-posed problems. *SIAM J. Sci. Stat. Comput.*, 1983, **4**, 164–176.

[YKWK-1973] J.L. Yarnell, M.J. Katz, R.G. Wenzel and S.H. Koenig. Structure Factor and Radial Distribution Function for Liquid Argon at 85° K. *Physical Review A*, 1973, **7**, 2130–2144.

[Zwanzig-1954] R. Zwanzig. High-Temperature Equation of State by a Perturbation Method. I. Nonpolar Gases. *Journal of Chemical Physics*, 1954, **22(8)**, 1420–1426.

[Zwanzig-1960] R. Zwanzig. Ensemble Method in the Theory of Irreversibility. *Journal of Chemical Physics*, 1960, **33(5)**, 1338–1341.

[Zwanzig-1961] R. Zwanzig. Memory Effects in Irreversible Thermodynamics. *Physical Review*, 1961, **124(4)**, 983–992.

Index